# Cooling $^{6}$Li to Quantum Degeneracy by $^{166}$Er in a Novel Ultracold Fermi-Bose Gas Mixture

Florian Johannes Kiesel

Tübingen
2025

# Cooling $^{6}$Li to Quantum Degeneracy by $^{166}$Er in a Novel Ultracold Fermi-Bose Gas Mixture

**Dissertation**
der Mathematisch-Naturwissenschaftlichen Fakultät
der Eberhard Karls Universität Tübingen
zur Erlangung des Grades eines
Doktors der Naturwissenschaften
(Dr. rer. nat.)

vorgelegt von
Florian Johannes Kiesel
aus Filderstadt

Tübingen
2025

Gedruckt mit Genehmigung der Mathematisch-Naturwissenschaftlichen Fakultät der
Eberhard Karls Universität Tübingen.

Tag der mündlichen Qualifikation: 29. Januar 2026
Dekan: Prof. Dr. Thilo Stehle
1. Berichterstatter: Prof. Dr. Christian Groß
2. Berichterstatter: Prof. Dr. apl. Sebastian Slama
3. Berichterstatter: Assistant Professor Richard Fletcher

## Zusammenfassung

Die Simulation hochkorrelierter Quantensysteme mit klassischen Computern übersteigt deren Rechenleistung bei steigender Systemgröße. In analogen Quantensimulatoren wird das betreffende System durch ein anderes Quantensystem in einer hochgradig kontrollierbaren und zugänglichen Umgebung nachgebildet. Auch wenn Quantensimulatoren mit ultrakalten Atomen bereits große Erfolge erzielt haben, bleibt es experimentell herausfordernd, Systeme sehr niedriger Temperaturen zu erzeugen, weshalb viele Quantenphänomene noch unerforscht geblieben sind. Neue Ansätze zur Realisierung immer niedrigerer Temperaturen, insbesondere in fermionischen Systemen, bleiben ein beständiges Ziel in der Atom-, Molekül- und Optischen Physik (AMO).

In der vorliegenden Arbeit wird ein neues Quantengasexperiment mit fermionischem $^{6}$Li und bosonischem $^{166}$Er vorgestellt und erste Ergebnisse zur sympathischen Kühlung von $^{6}$Li unter die quanten kritische Temperatur durch $^{166}$Er präsentiert. Der Versuchsaufbau wird detailliert beschrieben, wobei der Schwerpunkt auf dem Li-Teilsystem des Doppel-Spezies-Experiments liegt. Nebst herkömmlichen werden auch weiterentwickelte Laserkühltechniken zur Erzeugung einer magneto-optische Falle (MOT) von Li eingesetzt und zusammen mit den Vakuumteilsystemen, in denen sie angewendet werden, beschrieben. In diesem Zusammenhang wird eine kombinierte Technik aus optischem Pumpen und Transversalkühlung des Atomstrahls auf der $D_1$-Linie vorgestellt und anschließend eine Verbesserung der MOT-Laderate um eine Größenordnung demonstriert. Der Aufbau und einzelne Bestandteile des Lasersystems zur Erzeugung von resonantem Licht um $671\,\mathrm{nm}$ für die Laserkühlung von Li werden detailliert beschrieben und es werden Techniken zur Frequenzstabilisierung und Lichtverstärkung durch Injektionssynchronisation von Hochleistungslaserdioden vorgestellt. Ein besonderes Augenmerk wird hierbei auf die Einführung und Charakterisierung einer neuen laserdiodenunabhängigen Methode zur Injektionssynchronisation gelegt, bei der die spektral reine Lichtverstärkung durch eine periodische Stromoptimierung, durchgeführt von einem Mikrocontroller, erhalten bleibt. Dieses System wurde zur Patentierung angemeldet. In weiteren Schritten der optischen Kühlung von Li wird eine weiterentwickelte, auf Intensitätsrampen basierende, Graue-Mollasse-Kühltechnik vorgestellt, die Temperaturen von bis zu $13\,\mu\mathrm{K}$ ermöglicht. Die verfeinerte Graue-Molasse-Technik wird anschließend charakterisiert und mit Ergebnissen des herkömmlichen gepulsten Ansatzes verglichen, welcher typischerweise nur $50\,\mu\mathrm{K}$ erreicht. Die Kühlschritte zur Bereitstellung einer ultrakalten Li-Wolke in der Glaszelle beginnen mit dem Laden der optischen Dipolfalle durch Verdichtung der MOT und anschließendem Umladen mit Hilfe von Verdampfungskühlen in ein 1D-Transportgitter aus gegenläufigen $1064\,\mathrm{nm}$ Laserstrahlen. Durch Verstimmung eines der Gitterstrahlen wird optischer Transport über die Strecke von $1\,\mathrm{m}$ zur Glaszelle mit einem Wirkungsgrad von $74\%$ demonstriert. In einer kombinierten ErLi-Sequenz werden die beiden Elemente gemeinsam zur Glaszelle transportiert und dort in optische Dipolfallen, erzeugt duch $1064\,\mathrm{nm}$ Licht, geladen. Es wird neben sympathischem Kühlen von Li durch Verdampfungskühlung von Er auf $T/T_F = 0.77 \pm 0.10$ auch die Erzeugung eines Er-BEC beschrieben und präsentiert.

Zusammenfassend lässt sich sagen, dass in dieser Arbeit ein neues vielversprechendes Doppel-Spezies-Experiment vorgestellt und anschließend dessen Fähigkeit zum sympathischen Kühlen von Li durch Er bis in den quantendegenerierten Bereich demonstriert wird. Die vorliegenden Ergebnisse bilden eine aussichtsreiche Grundlage für das Erreichen höherer Quantendegeneration, um mit Hilfe von verfeinerter experimenteller Kontrolle bisher unerforschte Tieftemperaturbereiche in Quantensimulatoren zu erschließen.

# Abstract

Simulating highly correlated quantum systems with classical computers exceed their capabilities as the system size increases. In analog quantum simulators, the system of interest is mimicked by another quantum system in a highly controllable and accessible environment. Even though quantum simulations with ultracold atoms have been demonstrated successfully, ultra-low temperature regimes are experimentally challenging to achieve and still remain to be explored. New approaches to realizing ever lower temperatures, especially in Fermi systems, have been and continue to be a constant pursuit in Atomic, Molecular, and Optical Physics (AMO).

Within this thesis, a new quantum gas experiment of fermionic $^6$Li and bosonic $^{166}$Er is presented and first results on sympathetic cooling of Li to quantum degeneracy by Er are demonstrated. The experimental apparatus is described in detail with a focus on the Li subsystem of the dual-species experiment. Standard and further developed laser cooling techniques used to produce a Magneto-Optical Trap (MOT) of Li are characterized, along with their associated vacuum system stages. In this context, a combined Optical Pumping / Transversal Cooling (OP/TC) technique of the atomic beam on the $D_1$-line is presented, and an enhancement of the MOT loading rate by one order of magnitude is demonstrated. The architecture and building blocks of the laser system for providing resonant light at $671\,\mathrm{nm}$ for laser cooling of Li are detailed, and laser locking techniques for frequency stabilization and light amplification by injection locking of high-power laser diodes are presented. Special focus is placed on the introduction and characterization of a new laser-diode-independent injection locking technique, keeping spectrally pure amplified light by a periodic slave current optimization routine executed by a microcontroller. The system has been submitted for patent approval.

In further steps of optical cooling of Li, a non-standard free-space Gray Molasses (GM) technique based on intensity ramps, providing temperatures as low as $13\,\mu\mathrm{K}$, is presented. The non-standard technique is characterized and compared to the standard pulse GM approach, which typically achieves $50\,\mu\mathrm{K}$ only. Cooling steps for preparing an ultracold Li cloud in the glass cell start from an Optical Dipole Trap (ODT) loaded by a compressed Magneto-Optical Trap (cMOT) and consecutive evaporation into a 1D transport lattice of counter propagating $1064\,\mathrm{nm}$ laser beams. By detuning one of the lattice beams, optical transport over $1\,\mathrm{m}$ to the glass cell with an efficiency of $74\%$ is demonstrated.

In a combined ErLi sequence, the two species are transported to the glass cell together and loaded to $1064\,\mathrm{nm}$ ODTs. Sympathetic cooling of Li by forced evaporation of Er to $T/T_F = 0.77 \pm 0.10$ next to the production of an Er BEC are presented.

To conclude, this work introduces a new promising dual-species quantum gas experiment and its ability for providing sympathetic cooling of Li by Er to quantum degeneracy is demonstrated. These findings are an encouraging foundation for achieving higher degeneracies by refined experimental control in pursuit of penetrating unexplored temperature regimes in quantum simulators.

# Contents

# List of Figures

# List of Tables

---

*„Der Inhalt der Physik geht die Physiker an, die Auswirkungen alle Menschen.“*

Friedrich Dürrenmatt, Die Physiker

# Chapter 1

# Introduction

The $100^{\text{th}}$ anniversary of quantum mechanics is celebrated in 2025 and UNESCO has declared it the International Year of Quantum Science and Technology. In the beginning of the $20^{\text{th}}$ century, Planck [1] had successfully derived a formula describing black-body radiation by assuming quantized energy levels in matter and Einstein [2] had successfully derived an explanation for the photoelectric effect assuming quantization of energy in light. Even though these heuristic approaches were very successful in describing the respective phenomena, it took a good twenty years before the advent of an underlying theory started establishing. The findings of Heisenberg [3] and Schrödinger [4] were initially hard to accept, as they defy classical intuition. Especially quantum entanglement, which instantaneously correlates measurements on two or more particles, even if they are on opposite sides of the universe, triggered skepticism in the community [5]. The phenomena, which Einstein criticized as "spukhafte Fernwirkung", now is made use of in unhackable quantum communication protocols [6–8]. After one century has passed, the outstandingly successful quantum theory of the microscopic world has not lost its thrill to physicists.

Even though quantum mechanics in principle allows describing almost arbitrary physical systems by stating their (highly complex) Hamiltonians, already seemingly simple ones have turned out not to be solvable analytically [9, 10]. Employing modern supercomputers to numerically solve Hamiltonians of $N$ two-level particles quickly face capacity limits due to the exponential growth of the Hilbert space of size $2^N$ [11]. In 1982, this fact was pointed out by Feynman, and he proposed to instead of employing classical computers, computers or simulators that rely on quantum mechanical systems are the natural system to be made use of [12].

The quantum simulators Feynman dreamed about are categorized into *digital* and *analog* [13]. For digital quantum computers, a Hamiltonian is implemented by a set of discrete operations (gates) performed on the quantum bits (qubits) of the system [14]. In principle an arbitrary Hamiltonian can be implemented on a universal quantum computer [15, 16]. However, gate errors, heating and decoherence still strongly limit the experimentally realized performance of digital quantum computer devices [17]. In quantum error correction protocols a logical qubit is encoded in multiple physical qubits, protecting the quantum information [18, 19]. For this approach to work efficiently, the performance of the experimental platform must provide low enough physical error rates, the usage of a reasonable overhead in physical qubits and fast decoding [20]. The implementation of efficient error correction remains to be demonstrated.

In the analog quantum computing approach, the quantum system of interest is mimicked by a model Hamiltonian in another quantum system in a highly controllable experimental environment [10]. Although the Hamiltonians to be simulated are limited to experimentally achievable systems, physically meaningful experiments can still be carried without the need of resource demanding error correction [21]. Here, experimental results provide knowledge about the system, though in a different parameter regime.

Ultracold atomic gases provide a rapidly evolving experimental platform, making Feynman's vision come true [22, 23]. The Fermi-Hubbard system is among the popular Hamiltonians, which are tackled with analog quantum simulations using ultracold gases [24]. The Fermi-Hubbard model, developed in 1963 in condensed matter theory, describes electrons in crystal lattices at low temperatures [25, 26]. It considers only nearest-neighbor hopping from one lattice site to the next and onsite interaction of two fermions. Fermi-Hubbard systems are realized with optical lattices [27] and magnetically tunable Feshbach resonances [24, 28]. Single-site [29–31] and spin-state [32, 33] resolved imaging is achieved with quantum gas microscopes [34].

Using ultracold gas experiments, conventional superconductivity (BCS) [35, 36], Mott insulators [37, 38] and antiferromagnetic phase [39, 40] have been realized in a Fermi-Hubbard system. The so far unexplored phase diagram of doped Fermi-Hubbard systems is expected to be very rich, and to host exotic phases of matter such as the striped phase [41, 42] and d-wave superconductivity [43, 44]. These new states of matter are expected to be observed for low temperatures, that have not been experimentally realized so far. Recent advances in preparing systems at lower temperatures have started to enter the regime of $T/T_F \sim 0.06$ [40], where the appearance of a pseudogap [42, 45, 46] was observed [47].

Reaching ever lower temperatures to explore new quantum phenomena is a persistent pursuit in ultracold gases experiments. After initial laser cooling of atomic clouds to intermediate temperatures [48–50], the quantum degenerate regime is commonly reached by evaporative cooling [51] in optical dipole traps [52]. Evaporative cooling relies on fast thermalization of the gas after a high energy particle has left the system. In fermionic spin mixtures thermalization slows down dramatically at $T/T_F = 0.2$, as the number of scattering channels in the filling Fermi seas decreases [53]. In a sympathetic-cooling approach, bosons cool fermions, thermalization is improved and cooling stays efficient as bosons do not obey the Pauli principle [54]. The highest degeneracies in bulk systems were achieved in such Fermi-Bose mixtures experiments with $T/T_F = 0.05$ in $^6$Li$^{23}$Na [55] and $T/T_F = 0.03$ in $^6$Li$^7$Li [56].

Sympathetic cooling in Fermi-Bose mixtures is limited by the scaling of the respective heat capacities. For bosons the heat capacity follows a cubic power law in the quantum degenerate regime, whereas for fermions it is only a linear decrease [57]. For the same trapping conditions, the heat capacity mismatch makes sympathetic cooling inefficient at $T/T_F \approx 0.3$ [58]. Tuning the onset of the bosonic condensation is therefore the key to keeping sympathetic cooling efficient, in order to reach higher degeneracies in the fermionic system [59].

The Fermi-Bose mixture of $^6$Li and $^{166}$Er has great prerequisites for sympathetic cooling, to achieve even lower temperatures. Both $^6$Li and $^{166}$Er have been successfully cooled to quantum degeneracy individually [60–62]. The Fermi temperature to critical temperature ratio naturally benefits from the high mass imbalance of the alkali-lanthanide mixture. $^{166}$Er possesses a rich optical spectrum [63] with a tune-out wavelength near a narrow line at $841\,\mathrm{nm}$ [64], which can be made use of for species selective trapping, and to further increase $T_F/T_c$. Next to the enhanced cooling properties, the $^6$Li$^{166}$Er quantum gas mixture is a promising platform for studying polaron [65–68], impurity [69, 70] and Efimov physics [71–73]. On top of that, both elements posses stable isotopes of opposite quantum statistics, which allows for future flexibility of the experimental apparatus.

This work reports on a new quantum gas mixture experiment of $^{6}$Li and $^{166}$Er. The apparatus is designed as two independent single-species experiments integrated into a shared vacuum system, to account for the distinct experimental requirements of each element individually. The description of the system focuses on apparatus parts to provide an initial cold cloud of $^{6}$Li in a high optical access glass cell. Detailed descriptions of the Er part of the system is given in [74]. The vacuum and laser system are described, laser cooling performance of $^{6}$Li is characterized and highly efficient $1\,\mathrm{m}$ transport to the glass cell is demonstrated. Finally, this thesis reports on the realization of an ultracold mixture of $^{6}$Li$^{166}$Er and preliminary work on sympathetic cooling of $^{6}$Li by $^{166}$Er to quantum degeneracy in a $1064\,\mathrm{nm}$ optical dipole trap is demonstrated.

These findings mark a promising starting point for achieving even higher degeneracies by employing optical dipole traps at the tune-out wavelength. Furthermore, using the tune-out wavelength for providing an optical lattice for $^{6}$Li may allow the exploration of new phases in the Fermi-Hubbard model by cooling $^{6}$Li in a bath of $^{166}$Er.

## Outline

In this thesis, the setup and characterization of a novel dual-species experiment of fermionic $^6$Li and bosonic $^{166}$Er is reported. As the dual-species apparatus for producing ultracold atomic gases is quite complex, the focus is set mostly on the vacuum and laser system parts of the experimental setup concerning $^6$Li. Detailed descriptions of the Er part of the system is given in [74]. The presented experimental procedure relies on well established laser cooling techniques, that have been adapted and further developed to meet the requirements of the system. In the course of this thesis, a new long-term stable injection locking technique for amplification of the light needed for optical cooling was developed and successfully implemented in the experimental routine. To spatially overlap the two ultracold clouds, highly efficient optical transport over $1\,\mathrm{m}$ distance is demonstrated. As the final results, thermalization of $^6$Li and $^{166}$Er is presented and sympathetic cooling of $^6$Li to quantum degeneracy by $^{166}$Er is demonstrated.
This thesis is structured as follows:

> In Chapter 2, the basic theoretical concepts of optical dipole traps, fermionic and bosonic dilute gases at ultra-low temperatures and cooling limits for the production of these ultracold gases are introduced.
>
> In Chapter 3, physical properties of $^6$Li, $^{166}$Er and of an $^6$Li$^{166}$Er mixture relevant for laser cooling and reaching ultra-low temperatures are discussed and compared.
>
> In Chapter 4, the vacuum system of the ErLi experiment is presented and basic optical cooling steps for $^6$Li are characterized.
>
> In Chapter 5, the laser systems to provide the light for laser cooling of $^6$Li, optical dipole traps and optical transport of $^6$Li and $^{166}$Er are described.
>
> In Chapter 6, the experimental cooling steps and optical transport to provide the ultracold cloud of $^6$Li in a glass cell of high optical access is characterized.
>
> In Chapter 7, thermalization and lifetime properties of an $^6$Li$^{166}$Er mixture is presented and sympathetic cooling of $^6$Li to quantum degeneracy by $^{166}$Er is demonstrated, next to the realization of a BEC of $^{166}$Er.
>
> In Chapter 8, the presented work is briefly summarized and an outlook on recent and future work is given.

## Publications

The following articles have been published in the context of this thesis:

> ***Long-term stable laser injection locking for quasi-CW applications***
> Florian Kiesel*, Kirill Karpov*, Alexandre De Martino, Jonas Auch, and Christian Groß
> EPJ tech. instrum. 12.1, (2025)
> Patent application number EP24209446.4, 29 October 2024.
>
> ***Dissipationless tune-out trapping for a lanthanide–alkali-metal quantum gas mixture***
> Florian Kiesel*, Alexandre De Martino*, Jonas Auch, Kirill Karpov, and Christian Groß
> Phys. Rev. A 112, L051304 (2025)

* Equal contributors

# Chapter 2

# Theory

## 2.1 Polarizability and optical dipole traps

When atoms are placed in a light field, an electric dipole moment is induced. As it oscillates with the same frequency as the light field, the in-phase and out-of-phase components result in two phenomena: refraction and absorption. Both originate from coupling of the light field to the atom and thus represent two sides of the same coin.

For now, the atom is considered a simple oscillator placed in a classical monochromatic light field [52]

$$\boldsymbol{E}(\boldsymbol{r},t) = \hat{\boldsymbol{e}}\tilde{E}(\boldsymbol{r})\text{exp}(-i\omega t) + \hat{\boldsymbol{e}}^*\tilde{E}^*(\boldsymbol{r})\text{exp}(+i\omega t),$$

with the unit polarization vector $\hat{\boldsymbol{e}}$, the electric field amplitude $\tilde{E}$ and the driving frequency $\omega$. The induced polarization vector of the atom is given by

$$\boldsymbol{p}(\boldsymbol{r},t) = \hat{\boldsymbol{e}}\tilde{p}(\boldsymbol{r})\text{exp}(-i\omega t) + \hat{\boldsymbol{e}}^*\tilde{p}^*(\boldsymbol{r})\text{exp}(+i\omega t).$$

The amplitude $\tilde{p}$ of the polarization vector is related to that of the driving electric field via the *complex* polarizability $\tilde{\alpha}$:

$$\tilde{p} = \tilde{\alpha}\tilde{E}.$$

From this complex polarizability, the interaction potential

$$U_{\text{dip}}(\boldsymbol{r}) = -\frac{1}{2}\langle\boldsymbol{pE}\rangle = -\frac{1}{2\epsilon_0 c}\mathfrak{Re}(\tilde{\alpha})I(\boldsymbol{r}) \tag{2.1}$$

and the scattering rate

$$\Gamma_{\text{sc}}(\boldsymbol{r}) = \frac{\langle\dot{\boldsymbol{p}}\boldsymbol{E}\rangle}{\hbar\omega} = +\frac{1}{\hbar\epsilon_0 c}\mathfrak{Im}(\tilde{\alpha})I(\boldsymbol{r}) \tag{2.2}$$

are derived[1]. The interaction potential originates from the real part and the absorptive scattering from the imaginary part of the complex polarizability. Time average of the rapid oscillation is represented with $\langle ... \rangle$. The field intensity is $I = 2\epsilon_0 c|\tilde{E}|^2$, with $\epsilon_0$ the vacuum permittivity, $c$ the speed of light and $\hbar$ the reduced Planck constant. The above equations generally apply to any polarizable neutral particle. The dipole force is derived from the gradient of the interaction potential

$$\boldsymbol{F}_{dip}(\boldsymbol{r}) = -\nabla U_{\text{dip}}(\boldsymbol{r}) = -\frac{1}{2\epsilon_0 c}\mathfrak{Re}(\tilde{\alpha})\cdot\nabla I(\boldsymbol{r}). \tag{2.3}$$

---

[1] Here the quantized nature of the light field is treated as a stream of photons of $\hbar\omega$.

It is a conservative force emerging from the intensity gradient of the driving light field. High field gradients are provided by tightly focused laser beams capable of containing polarizable particles. This was first successfully demonstrated in 1986 by later Nobel Prize laureate Arthur Ashkin for a dielectric particle [75], and one year later even for bacteria and viruses [76].

Sticking to the more familiar atom, the complex polarizability can be calculated in the Lorentz's model of a classical oscillator. In this simple picture an electron of charge $e$ and mass $m_e$ is bound elastically to the core with an eigenfrequency $\omega_0$. Damping of the oscillation by dipole radiation, represented by

$$\Gamma_\omega = \frac{e^2\omega^2}{6\pi\epsilon_0 m_e c^3}, \tag{2.4}$$

is introduced through Larmor's formula for a radiating charged particle. With the equation of motion for a driven oscillator $\ddot{x} + \Gamma_\omega \dot{x} + \omega_0^2 x = -eE(t)/m_e$ a first explicit expression for the complex polarizability

$$\tilde{\alpha} = \frac{e^2}{m_e}\frac{1}{w_0^2 - \omega^2 - i\omega\Gamma_w} \tag{2.5}$$

is obtained. By substituting $e^2/m_e = 6\pi\epsilon_0 m_e c^3 \Gamma_\omega/\omega^2$ (Eq. (2.4)) and the definition of the on resonance damping rate $\Gamma \equiv \Gamma_{\omega_0} = (\omega/\omega_0)^2\Gamma_\omega$, Eq. (2.5) is rewritten in its well known form:

$$\tilde{\alpha} = 6\pi\epsilon_0 c^3 \frac{\Gamma/\omega_0^2}{\omega_0^2 - \omega^2 - i\Gamma(\omega/\omega_0)^3}. \tag{2.6}$$

The above classical considerations already allow giving expressions for the dipole potential and scattering of an atom placed in a light field:

$$U_{\text{dip}}(\boldsymbol{r}) = -\frac{3\pi c^2}{2\omega_0^3}\left(\frac{\Gamma}{\omega_0-\omega} + \frac{\Gamma}{\omega_0+\omega}\right) I(\boldsymbol{r}), \tag{2.7}$$

$$\Gamma_{\text{sc}}(\boldsymbol{r}) = \frac{3\pi c^2}{2\hbar\omega_0^3}\left(\frac{\omega}{\omega_0}\right)^3\left(\frac{\Gamma}{\omega_0-\omega} + \frac{\Gamma}{\omega_0+\omega}\right)^2 I(\boldsymbol{r}). \tag{2.8}$$

Here $\Gamma$ reveals to be the natural scaling factor of the two phenomena. Both descriptions are limited to large detunings and a weakly excited oscillating electron. For dipole trapping of atoms, these conditions are usually fulfilled. In Eqs. (2.7) and (2.8) there are two resonant contributions. The resonance for $\omega = \omega_0$ of the so-called *co-rotating* part of the light commonly is the only relevant contribution. Even though the light field is typically far detuned from resonance, the detuning $\Delta \equiv \omega - \omega_0$ still satisfies the condition of $|\Delta| \ll \omega_0$. By that, contribution from the *counter-rotating* resonance[2] at $\omega = -\omega_0$ can be neglected. In the *rotating wave approximation* the counter-rotating term is dropped and $\omega/\omega_0 \approx 1$ is assumed. This reduces the expressions of Eqs. (2.7) and (2.8) to

$$U_{\text{dip}}(\boldsymbol{r}) = \frac{3\pi c^2}{2\omega_0^3}\frac{\Gamma}{\Delta} I(\boldsymbol{r}) \quad \text{and} \tag{2.9}$$

---

[2] It is often referred to as a *resonance*, even though the strictly positive definition of a frequency prohibits the *resonance condition* to be met.

$$\Gamma_{\text{sc}}(\boldsymbol{r}) = \frac{3\pi c^2}{2\hbar\omega_0^3}\left(\frac{\Gamma}{\Delta}\right)^2 I(\boldsymbol{r}). \tag{2.10}$$

These two equations contain the essential physics to understand trapping in far-detuned light fields. Besides of constants, the dipole potential and the scattering rate differ only in their scaling with detuning:

$$U_{\text{dip}} \propto \frac{I}{\Delta} \text{ and } \Gamma_{\text{sc}} \propto \frac{I}{\Delta^2}.$$

While the scattering rate is symmetric in the detuning, the sign of the dipole potential changes with detuning. For *red-detuned* light ($\Delta < 0$) an attractive potential is provided. The force on the atoms moves them towards higher intensity. In an experimental setup, they would gather around the focus of a high power laser beam providing a trapping potential. For *blue-detuned* light ($\Delta > 0$) the interaction is repulsive. Here, the atoms would be pushed out of the light field of the laser beam. Superimposing laser beams with a local intensity minimum, atoms can still be trapped. In both scenarios, these configurations are referred to as Optical Dipole Traps (ODTs).
While the atoms are held in a conservative dipole trap, scattering heats them up until they eventually overcome the potential and are lost. The ratio of the scattering rate per trap depth governs the timescale for this process:

$$\hbar\frac{\Gamma_{\text{sc}}}{U_{\text{dip}}} = \frac{\Gamma}{\Delta}. \tag{2.11}$$

Ideally, the detuning is chosen to be as large as possible to minimize heating from scattering. At the same time, the laser source has to be powerful enough to still achieve the trap depth needed. This compromise is frequently found in lasers outputting $\sim 100\,\mathrm{W}$ at $1064\,\mathrm{nm}$. They are far detuned to the $D$-lines of alkalis and cost-efficient with a wavelength, that is experimentally easy to handle.

In a semiclassical approach to the quantum problem, where the atom is described as a two-level system and the light as a classical wave, the above findings from a purely classical system remain valid to a great extent. To gain an understanding on the generalization on a (real-world) multi-level atom, it is best to examine the two-level case first. The following derivations are done under the same approximations (rotating wave, low saturation and high detuning) as for the classical system. Here, the light field is treated as a perturbation coupling the ground state $|g\rangle$ to the excited state $|e\rangle$ with the interaction Hamiltonian

$$\hat{V}_I = e\hat{\boldsymbol{r}} \cdot \boldsymbol{E} = -\hat{\boldsymbol{\mu}} \cdot \boldsymbol{E}, \tag{2.12}$$

with the dipole operator $\hat{\boldsymbol{\mu}} = -e\hat{\boldsymbol{r}}$. The calculation of the perturbation has to be carried out in a combined base of the atom and the light field. In the so-called *dressed-state* picture, the bare atomic states are combined with the states of the light field of $n$ photons [77]:

$$|g\rangle \rightarrow |g'\rangle = |g\rangle|n\rangle \text{ and } |e\rangle \rightarrow |e'\rangle = |e\rangle|n-1\rangle. \tag{2.13}$$

In $|g'\rangle$, the atom is in the ground state with $n$ photons in the mode of the light field. The energy of the light field is $n\hbar\omega$. In $|e'\rangle$, the atom is in the excited state, and, having absorbed one photon, the photon number is reduced. The shift of the ground state energy $\Delta E_g$ is calculated in second-order perturbation theory, as the correction in first order vanishes owing the absence of a permanent dipole moment[3]:

$$\Delta E_g = \frac{|\langle e'|\hat{V}_I|g'\rangle|^2}{E_{g'} - E_{e'}} = \frac{|\langle e|\hat{V}_I|g\rangle|^2}{\hbar(\omega - \omega_0)} = \frac{|\langle e|\hat{V}_I|g\rangle|^2}{\hbar\Delta} = \frac{|\langle e|\hat{\boldsymbol{\mu}} \cdot \hat{\boldsymbol{e}}|g\rangle|^2}{\hbar\Delta}|E|^2. \tag{2.14}$$

In the dressed-state picture, the ground state of the atom is essentially given by the unperturbed atomic ground state with only a small admixture of the excited state. With this, the dipole potential arises from the ground state energy shift caused by the perturbation of the light field.

At this point, most textbooks proceed by relating the (absolute square) of the dipole matrix element to the spontaneous decay rate [78]:

$$\Gamma = \Gamma_{e,g} = \frac{\omega_0^3}{3\pi\epsilon_0\hbar c^3}|\langle g|\hat{\boldsymbol{\mu}}|e\rangle|^2. \tag{2.15}$$

With this, Eq. (2.9) is recovered, now containing an explicit expression of the spontaneous decay rate[4]. With the Rabi frequency[5]

$$\Omega = -\frac{\langle e|\hat{\boldsymbol{\mu}} \cdot \hat{\boldsymbol{e}}|g\rangle}{\hbar}|E|, \tag{2.16}$$

the dipole potential and the scattering rate are given by:

$$U_{\text{dip}} = \frac{\hbar\Omega^2}{4\Delta} \quad \text{and} \tag{2.17}$$

$$\Gamma_{\text{sc}} = \frac{\Omega^2}{4\Delta^2}\frac{1}{\tau}, \tag{2.18}$$

with the lifetime $\tau$ of the excited state.

In multi-level atoms with many excited states $|e_i\rangle$ the total dipole potential $U_{\text{dip},\Sigma}$ and the total scattering rate $\Gamma_{\text{sc},\Sigma}$ are given by the sum of the individual contributions:

$$U_{\text{dip},\Sigma} = \sum_i U_{\text{dip,i}} = \sum_i \frac{\hbar\Omega_i^2}{4\Delta_i} \quad \text{and} \quad \Gamma_{\text{sc},\Sigma} = \sum_i \Gamma_{\text{sc,i}} = \sum_i \frac{\Omega_i^2}{4\Delta_i^2}\frac{1}{\tau_i}. \tag{2.19}$$

Depending on the detuning (blue or red), the individual $U_{\text{dip,i}}$ contribute to either an increase or a decrease in energy. For certain so-called *tune-out* wavelengths, the potential even vanishes: $U_{\text{dip},\Sigma}(\omega_T) = 0$. For a three-level atom with two excited states of equal strength, the tune-out frequency $\omega_T$ lies midway between the two levels. Between any two excited states (no matter their linestrenghts), there is always one tune-out wavelength at which all red-detuned contributions balance all blue-detuned contributions. Even though the potential vanishes, scattering still persists. Optical traps operated at the tune-out wavelength

---

[3] First order correction in the ground state energy: $\Delta E_g^1 = \langle g|\hat{V}_I|g\rangle = 0$

[4] This holds for the two-level system, but potentially leads to confusion, when the above considerations are extended to multi-level atoms. With the **spontaneous decay** rate $\Gamma$ the coupling strength of $|g\rangle$ to $|e\rangle$ is expressed. When talking about **scattering** rates of a ground state atom (in context of e.g. optical cooling) more channels of spontaneous decay other than the one to the ground state has to be considered. For alkali atoms most of the decay rates (couplings) to other levels than the ground state are negligible. For more complicated atoms such as Er or Sr, decay channels other than to the ground state become relevant.

[5] We switched to the electric field definition of $\boldsymbol{E}(\boldsymbol{r},t) = \frac{1}{2}(\hat{\boldsymbol{e}}\tilde{E}(\boldsymbol{r})\text{exp}(-i\omega t) + \hat{\boldsymbol{e}}^*\tilde{E}^*(\boldsymbol{r})\text{exp}(+i\omega t))$ to match the standard notation.

can be of great use in dual-species experiments. Here, one species is trapped while the other one remains unaffected, enabling differential control between the two. Such a tune-out wavelength exists near a narrow $841\,\mathrm{nm}$ line in Er, which is far red detuned to the Li lines [64].
Besides the tune-out wavelengths, another special wavelength deserves to be mentioned at this point. At the so-called *magic* wavelength, the differential shift of the ground state and an exited state vanishes. This effect is exploited in experiments with e.g. optical clocks, where narrow transitions in optically trapped atoms are precisely measured [79].

### Gaussian beam

Optical dipole traps are commonly provided by a focused Gaussian beam [80]. The intensity is radially symmetric about the axis of propagation $z$:

$$I(r,z) = \frac{2P}{\pi w^2(z)} \exp\left(-2\frac{r^2}{w^2(z)}\right). \tag{2.20}$$

A beam of power $P$ is focused to a $1/e^2$-radius of $w_0$ at $z = 0$ and expands according to

$$w(z) = w_0\sqrt{1+\left(\frac{z}{z_r}\right)^2}. \tag{2.21}$$

The Rayleigh length $z_R = \pi w_0^2 \lambda$ gives the distance from the focus at which the intensity decreases to $1/e^2$ along the axial direction. The optical potential is proportional to the intensity: $U_{\text{dip}}(r,z) \propto I(r,z)$ and the trap depth is defined as $U_0 = U_{\text{dip}}(0,0)$. The oscillation frequencies of atoms trapped at the beam focus in the radial and axial direction are given by:

$$\omega_r = \sqrt{\frac{4U_0}{m w_0^2}} \text{ and } \omega_z = \sqrt{\frac{2U_0}{m z_R^2}}, \tag{2.22}$$

with the mass of an atom $m$. They are obtained by Taylor expansion of the potential along respective directions $(x = z, r)$: $U_x = U_0 + \frac{1}{2} m \omega_x^2 x^2 + \mathcal{O}(x^4)$.

## 2.2 Fermions and Bosons - statistics is everything

Every massive particle in the universe is classified as either a fermion or a boson. This also holds for composite particles in our 3D world. At first glance, this classification seems to be only relevant for physicists and the difference between the two only significant on a microscopic level. However, recognizing that the electron is a fermion obeying the Pauli exclusion principle allows us to understand the entire periodic table and, with it, everything that surrounds us in our daily life.
The classification into fermions and bosons is straightforward. Particles with a half-integer spin are referred to as fermions, whereas particles of integer spin are referred to as bosons. All components that make up an atom—electrons in the shell and protons and neutrons in the nucleus—are fermions. A special property of fermions is that when several of them form a composite particle, it can be of fermionic *or* bosonic nature. This, in turn, depends on the total spin of the resulting composite particle. With an even number of constituents, the composite particle's total spin is an integer; it is therefore a (composite) boson. With an odd number, a fermionic particle is formed. In the quantum regime, the statistical properties of these particles are diametrically opposed. In neutral atoms, by definition the sum of the electron and proton number is even. For this reason, the quantum statistics of an atom is governed by the parity of the number of neutrons in the core.
The considerations that led to that classification and triggered the investigation of other fundamental properties were based on a simple permutation of two indistinguishable particles [81]. Consider the wave function $\Psi(1,2)$ of two *indistinguishable* particles $1$ and $2$. Interchanging the particles to $\Psi(2,1)$ must not change any observable quantity:

$$|\Psi(1,2)|^2 = |\Psi(2,1)|^2 \quad \text{and thus} \tag{2.23}$$

$$\Psi(1,2) = \pm\Psi(2,1). \tag{2.24}$$

The permutation of the two particles either leaves the wave function unchanged or adds a minus sign to it. In the unaltered case, the wave function is referred to as *symmetric*; with the minus sign added, it is referred to as *antisymmetric*. Suppose now that the particles occupy the *single*-particle states $a$ and $b$, represented by the wave functions $\phi_a$ and $\phi_b$. There are two wave functions constructed from the single particle states, that obey Eq. (2.24):

$$\Psi_{\text{sym}} \propto \phi_a(1)\phi_b(2) + \phi_a(2)\phi_b(1) \quad \text{and} \tag{2.25}$$

$$\Psi_{\text{asym}} \propto \phi_a(1)\phi_b(2) - \phi_a(2)\phi_b(1). \tag{2.26}$$

For identical bosons the wave function is symmetric: $\Psi_{\text{sym}}$. For identical fermions the antisymmetric wave function $\Psi_{\text{asym}}$ applies. Here, a striking peculiarity arises: If the two fermions were in the same state ($\phi_a = \phi_b$) the two particles wave function vanishes. In other words: Two identical fermions cannot occupy the same quantum state. This is the famous Pauli exclusion principle.

The symmetrization and antisymmetrization can be generalized to an $N$-particle quantum state. These states are used in thermodynamic considerations to obtain the mean occupation $\langle n_i \rangle$ of a single-particle state of energy $\epsilon_i$. With this the famous *Bose-Einstein statistics* $\langle n_i \rangle_B$

for bosons ($-$) and the *Fermi-Dirac statistics* $\langle n_i \rangle_F$ for fermions ($+$):

$$\langle n_i \rangle = \frac{1}{e^{(\epsilon_i - \mu)/k_B T} \mp 1} \tag{2.27}$$

for non-interacting gases are derived. The Boltzmann constant is denoted $k_B$. The chemical potential $\mu$ at temperature $T$ is fixed by the atom number $N$ of the system

$$N = \sum_i \langle n_i \rangle. \tag{2.28}$$

In the high-temperature regime, the exponential term in the denominator becomes dominant over the "$\pm 1$" for both quantum statistics, yielding the *Maxwell-Boltzmann distribution*:

$$\langle n_i \rangle = e^{-(\epsilon_i - \mu)/k_B T}.$$

At low temperatures, the ground-state occupation for bosons is enhanced. It can even reach macroscopic values and form a so-called Bose–Einstein condensate (BEC). For fermions the mean occupation is limited to $\langle n_i \rangle_F \leq 1$, because the *Pauli blocking* prevents double occupation of individual states. In a temperature regime, where $\langle n_i \rangle_F$ strongly deviates from the classical Maxwell-Boltzmann distribution, it is referred to as a Degenerate Fermi Gas (DFG). A useful illustration to understand at which point the quantum nature influences the statistics of the system is provided when the *de Broglie* wavelength

$$\lambda_{\mathrm{dB}} = \sqrt{\frac{2\pi\hbar^2}{m k_B T}} \tag{2.29}$$

is considered. It represents the coherence length of an atom of mass $m$ at temperature $T$. The reduced Planck constant is denoted with $\hbar$. When the average interatomic distance in a gas of density $n$ is comparable to the de Broglie wavelength, wave functions start overlapping and exhibit collective phenomena. The value is expressed as the Phase-Space Density (PSD) $\rho = n\lambda_{\mathrm{dB}}^3$. As the PSD approaches unity, the quantum nature of the atoms becomes apparent.

### 2.2.1 Fermions and Bosons in a harmonic potential

In experimental setups, the atomic gases are often confined in a 3D harmonic potential:

$$V(\boldsymbol{r}) = \frac{1}{2} m(\omega_x^2 x^2 + \omega_y^2 y^2 + \omega_z^2 z^2), \tag{2.30}$$

with trap frequencies $\omega_{x,y,z}$. If the level spacing of the harmonic oscillator is much smaller than the thermal energy $k_B T \equiv 1/\beta$, the distribution is given by [82]

$$f(\boldsymbol{r}, \boldsymbol{p}) = \frac{1}{e^{\beta(\boldsymbol{p}^2/2m + V(\boldsymbol{r}) - \mu)} \mp 1} \tag{2.31}$$

in the semiclassical approximation. Here, the picture of discrete levels is changed to be continuous. The distribution $f(\boldsymbol{r}, \boldsymbol{p})$ gives the occupation of $\{\boldsymbol{r}, \boldsymbol{p}\}$ in phase space with a unit cell of volume $h^3$. The density distribution is obtained by integration over the momentum space:

$$\begin{aligned} n(\boldsymbol{r}) &= \int \frac{d^3\boldsymbol{p}}{h^3} f(\boldsymbol{r},\boldsymbol{p}) \qquad &(2.32)\\ &= \pm\frac{1}{\lambda_{\mathrm{dB}}^3}\mathrm{Li}_{3/2}\left(\pm\, e^{\beta(\mu-V(\boldsymbol{r}))}\right). &(2.33)\end{aligned}$$

$\mathrm{Li}_n$ is the $n$-th order polylogarithm, which provides a compact representation of the integral[6]. Equation (2.33) is valid for any potential. Sticking to the 3D harmonic potential, the atom number $N$ is given by

$$\begin{aligned} N &= \int d^3\boldsymbol{r}\, n(\boldsymbol{r}) \\ &= \pm\left(\frac{k_BT}{\hbar\bar{\omega}}\right)^3 \mathrm{Li}_3(\pm e^{\beta\mu}), \end{aligned} \tag{2.34}$$

with the geometric mean of the trapping frequencies $\bar{\omega} = (\omega_x\omega_y\omega_z)^{1/3}$. For high temperatures, the *classical* Maxwell-Boltzmann distribution results in a Gaussian shape density profile

$$n_{\mathrm{cl}}(\boldsymbol{r}) = \frac{N}{\pi^{3/2}\sigma_x\sigma_y\sigma_z} e^{-\left(x^2/\sigma_x^2+y^2/\sigma_y^2+z^2/\sigma_z^2\right)}, \tag{2.35}$$

with the waists $\sigma_i^2 = \frac{2k_BT}{m\omega_i^2}$ for each direction $i = x, y, z$.
For $T = 0$, the difference in quantum statistics for bosons and fermions dominates the density distributions.
In the case of non-interacting *bosons*, the distribution is condensed to all atoms ($N = N_0$) populating the 3D harmonic oscillator ground state

$$n_c(\boldsymbol{r}) = \frac{N_0}{\pi^{3/2}d_xd_yd_z} e^{-\left(x^2/d_x^2+y^2/d_y^2+z^2/d_z^2\right)}. \tag{2.36}$$

As for the high-temperature classical gas, a Gaussian profile is obtained. The shape is now governed by the harmonic oscillator lengths $d_i^2 = \hbar/(m\omega_i)$. When the ground state starts to be macroscopically populated, the chemical potential $\mu \approx k_BT/N_0$ is close to the ground state energy and can be set to $\mu = 0$. In this limit, the density of the non-condensed thermal fraction is

$$n_{th,b}(\boldsymbol{r}) = +\frac{1}{\lambda_{\mathrm{dB}}^3}\mathrm{Li}_{3/2}\left(+\,e^{-\beta V(\boldsymbol{r})}\right). \tag{2.37}$$

Below the critical temperature

$$T_c = \tfrac{\hbar\bar{\omega}}{k_B}(N/\mathrm{Li}_3(1))^{1/3} \approx 0.94\tfrac{\hbar\bar{\omega}}{k_B}N^{1/3} \tag{2.38}$$

the condensed fraction grows rapidly as

$$N_0/N = 1 - (T/T_c)^3. \tag{2.39}$$

---

[6] $\mathrm{Li}_n(z) \equiv \frac{1}{\pi^n}\int d^{2n}r \frac{1}{e^{r^2}/z-1}$, $r$ is the radius vector in $2n$ dimensions. For more mathematical details see [83].

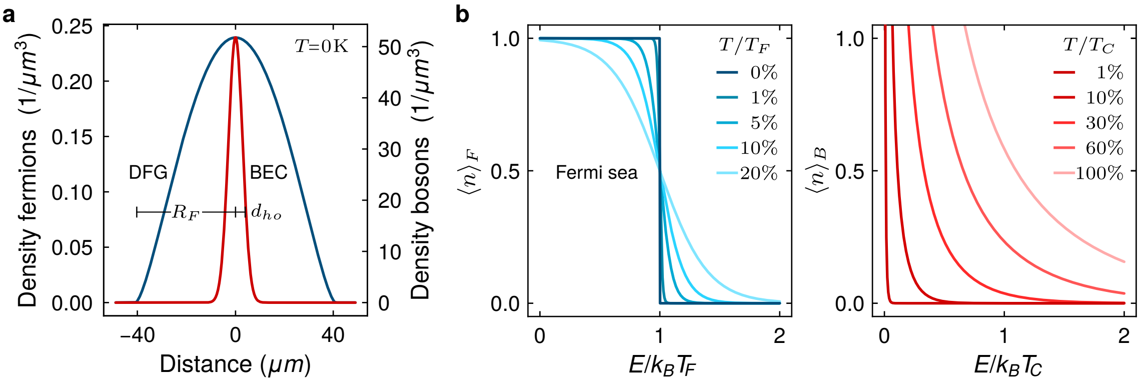

**Figure 2.1** **Fermi-Dirac and Bose-Einstein distributions. a.** Density distributions of a fermionic (blue, Eq. (2.43)) and a non-interacting bosonic (red, Eq. (2.36)) atom cloud of $N = 2 \cdot 10^4$ atoms in harmonic potential of $\omega_{x,y,z} = 2\pi \cdot 100\,\mathrm{Hz}$. The Fermi radius of $R_F = 41\,\mu\mathrm{m}$ and the harmonic oscillator length of $d_{ho} = 4.1\,\mu\mathrm{m}$ differ by one order of magnitude. **b.** Visualization of Eq. (2.27): *Fermi-Dirac* distribution (left) at low temperatures with $\mu = E_F$. For $T = 0$ it is a step function with all levels up to the Fermi energy occupied with one fermion. *Bose–Einstein* distribution (right) for temperatures $T$ smaller than an initial temperature $T_C$ and $\mu = 0$. The decreasing temperatures push the population towards the ground state.

For *fermions*, the occupation of states below the chemical potential approaches one for zero temperature, whereas above the chemical potential the states are empty. The shape of the zero temperature Fermi gas is not Gaussian anymore:

$$n_F(\boldsymbol{r}) = \frac{1}{6\pi^2}\left(\frac{2m}{\hbar^2}\right)^{3/2}[\mu - V(\boldsymbol{r})]^{3/2}. \tag{2.40}$$

The energy of the highest occupied state is referred to as the Fermi energy $E_F = \mu$. The associated Fermi momentum is $p_F \equiv \hbar k_F \equiv \sqrt{2mE_F}$. For the harmonic potential the total atom number sets the Fermi energy to

$$N = \int d^3\boldsymbol{r}\, n_F(\boldsymbol{r}) = \frac{1}{6}\left(\frac{E_F}{\hbar\omega}\right) \tag{2.41}$$

$$\Rightarrow E_F = \hbar\omega(6N)^{1/3}. \tag{2.42}$$

At zero temperature, the density distribution of the DFG in the harmonic trap is

$$n_F(\boldsymbol{r}) = \frac{8}{\pi^2}\frac{N}{R_{Fx}R_{Fy}R_{Fz}}\left[\max\left(1 - [x^2/R_{Fx}^2 + y^2/R_{Fy}^2 + z^2/R_{Fz}^2]\,, 0\right)\right]^{3/2}. \tag{2.43}$$

The Fermi radius $R_{Fi}^2 = \frac{2E_F}{m\omega_i^2}$ gives the size of the degenerate cloud.

The density distributions of a DFG and a BEC in a harmonic potential with atoms of identical properties but opposing quantum statistics are shown in Fig. 2.1. The Fermi pressure keeps the DFG at comparably large size with a fully filled Fermi sea[7]. The size of the non-interacting BEC is given by the harmonic oscillator length of the trap, which is much smaller than the Fermi radius[8]. As all atoms are in the ground state, the central density of the

---

[7] For DFGs, the (occupied) states below the Fermi energy are commonly referred to as the Fermi sea.

[8] With interactions present, the size of the BEC is altered significantly. See Section 2.3.3 for a detailed discussion.

BEC towers above the one of the DFG. For visualization, the Fermi-Dirac and Bose-Einstein distributions for a typical low temperature case are also shown.

### 2.2.2 Thermometry of Fermions with ToF

The temperature of the ultracold gases trapped in harmonic potentials are usually not obtained from *in situ* density measurements. High optical densities often hinder precise measurements in this case. Furthermore, fitting the in-trap density distributions to obtain the temperature of the gas requires precise knowledge of the potential. Especially for evaporative cooling schemes in Optical Dipole Traps (ODTs), where the trap depth is lowered gradually, the harmonic approximation in the wings of the cloud eventually fails.

In Time-of-Flight (ToF) measurements, the (column) density of the atomic cloud is measured after some time of ballistic expansion after a sudden switch-off of the trapping potential. An atom initially at position $\boldsymbol{r}_0$ and momentum $\boldsymbol{p}_0$ is found at $\boldsymbol{r} = \boldsymbol{r}_0 + \frac{\boldsymbol{p}_0}{m}t$ after a time $t$ of free flight. The ToF density distribution $n(\boldsymbol{r}, t)$ incorporates all atoms at places $\boldsymbol{r}_0$ that made it to $\boldsymbol{r}$ with their momentum $\boldsymbol{p}_0$ in time $t$. The probability for an atom with these initial conditions is $f(\boldsymbol{r}_0, \boldsymbol{p}_0)$ (see Eq. (2.31)). In the semiclassical approximation for a gas released from a harmonic potential, it is given by [82]:

$$\begin{aligned} n(\boldsymbol{r}, t) &= \int d^3\boldsymbol{r}_0 \int \frac{d^3\boldsymbol{p}_0}{h^3} f(\boldsymbol{r}_0, \boldsymbol{p}_0)\, \delta\left(\boldsymbol{r} - \boldsymbol{r}_0 - \frac{\boldsymbol{p}_0}{m}t\right) \\ &= \pm\frac{1}{\lambda_{\text{dB}}^3} \prod_j \frac{1}{\sqrt{1+\omega_j^2 t^2}} \mathrm{Li}_{3/2}\left[\pm \exp\left(\beta\mu - \beta \sum_i \frac{1}{2} m \frac{\omega_i^2 x_i^2}{1+\omega_i^2 t^2}\right)\right]. \end{aligned} \tag{2.44}$$

For a sufficiently long ToF with respect to the (lowest) trap frequency ($\omega_i^2 t^2 \gg 1$), the density distribution simplifies to

$$n(\boldsymbol{r}, t) = \pm\frac{1}{\lambda_{\text{dB}}^3} \frac{1}{(\bar{\omega} t)^3} \mathrm{Li}_{3/2}\left[\pm \exp\left(\beta\mu - \beta \frac{1}{2} m \frac{\boldsymbol{r}^2}{t^2}\right)\right]. \tag{2.45}$$

After the long expansion time, the initially anisotropic density distribution has become radially symmetric, reflecting the initial isotropic momentum distribution of the atoms before the release. The potential, the atoms were trapped in, is not contributing to the cloud shape anymore.
As discussed before, the cloud size in the thermal limit is given by the Gaussian radius $\sigma_i^2 = \frac{2k_B T}{m\omega_i^2}$ and by the Fermi radius $R_{Fi}^2 = \frac{2E_F}{m\omega_i^2}$ for a fully degenerate cloud. For the experimental analysis of the atomic cloud, it is therefore convenient to define a parameter, that interpolates the two limits:

$$R_i^2 = \frac{2k_B T}{m\omega_i^2} f(e^{\mu\beta}) \to \begin{cases} \sigma_i^2, & T \gg T_F \\ R_{Fi}^2, & T \ll T_F \end{cases} \tag{2.46}$$

$$\text{where } f(x) = \frac{1+x}{x} \ln(1+x). \tag{2.47}$$

It reflects the cloud size for all $T$.

For *fitting* a measured column density, it is made use of together with Eq. (2.45) integrated along the direction of imaging $z$. The 2D fitting function for a measured density profile for fermions is

$$n_{\mathrm{2D}}(x,y) = n_{\mathrm{2D},0}\frac{\mathrm{Li}_2\left(-\exp\left[q-\left(\frac{x^2}{R_x^2}+\frac{y^2}{R_y^2}\right)f(e^q)\right]\right)}{\mathrm{Li}_2(-e^q)}. \tag{2.48}$$

The shape of the cloud is governed by the logarithm of the fugacity $q=\mu\beta$. In Eq. (2.48), the number of parameters has reduced to a manageable amount and does not require precise knowledge of the trapping potential. The representation of the fit function directly relates $\mu$ to $T$ in $q$. The degeneracy of the cloud is derived from

$$\frac{T}{T_F} = [-6\mathrm{Li}_3(-e^q)]^{-1/3}. \tag{2.49}$$

Exact knowledge on the potential is therefore not necessary to obtain the degeneracy. To extract the temperature from the fitted parameters knowledge of the expansion time and the trap parameters are required again:

$$k_B T = \frac{1}{2}m\omega_i^2\frac{R_i^2}{1+\omega_i^2t^2}\frac{1}{f(e^q)}. \tag{2.50}$$

At zero temperature, the 2D density distribution is of shape:

$$n_{\mathrm{2D}}(x,y,T=0) = n_{\mathrm{2D},0}\left(1-\left[\frac{x^2}{R_{Fx}^2}+\frac{y^2}{R_{Fy}^2}\right]\right)^2. \tag{2.51}$$

For completeness at this point, also the 1D fit function for the 2D density distribution summed up along one direction is given:

$$n_{\mathrm{1D}}(x) = n_{\mathrm{1D},0}\frac{\mathrm{Li}_{5/2}\left(-\exp\left[q-\frac{x^2}{R_x^2}f(e^q)\right]\right)}{\mathrm{Li}_{5/2}(-e^q)}. \tag{2.52}$$

In general, relying on the 2D fit yields more accurate results. It is more sensitive to the relatively small deviations from the high temperature Gaussian profile. For the 1D fit, points with locally high and low $T_F$ are mixed, resulting in a washed-out profile.

In practice, extracting $T/T_F$ with the ToF method is quite challenging in the deeply degenerate regime. The density distribution of Eq. (2.51) does not change significantly anymore below $\sim T/T_F = 20\%$. Small deviations from a fully degenerate cloud emerge only in the wings (see Fig. 2.2). Precise thermometry is therefore limited and prone to aberrations, noise, and other systematic errors. In order to determine $T/T_F$ for highly degenerate Fermi gases, one has to apply different techniques. Many of them rely on the atoms being loaded to an optical lattice, which brings considerable experimental effort [84]. For Bose gases, the temperature can still be determined precisely even for highly degenerate clouds from the thermal fraction in the wings of the distribution. In a system of a thermalized Fermi and Bose gas, this can be made use of to determine the temperature of the fermions via the bosons [85].

Before closing this section, the behavior for some parameters in the quantum degenerate regime is worth mentioning. At low temperatures, the chemical potential $\mu$ (Eq. (2.34))

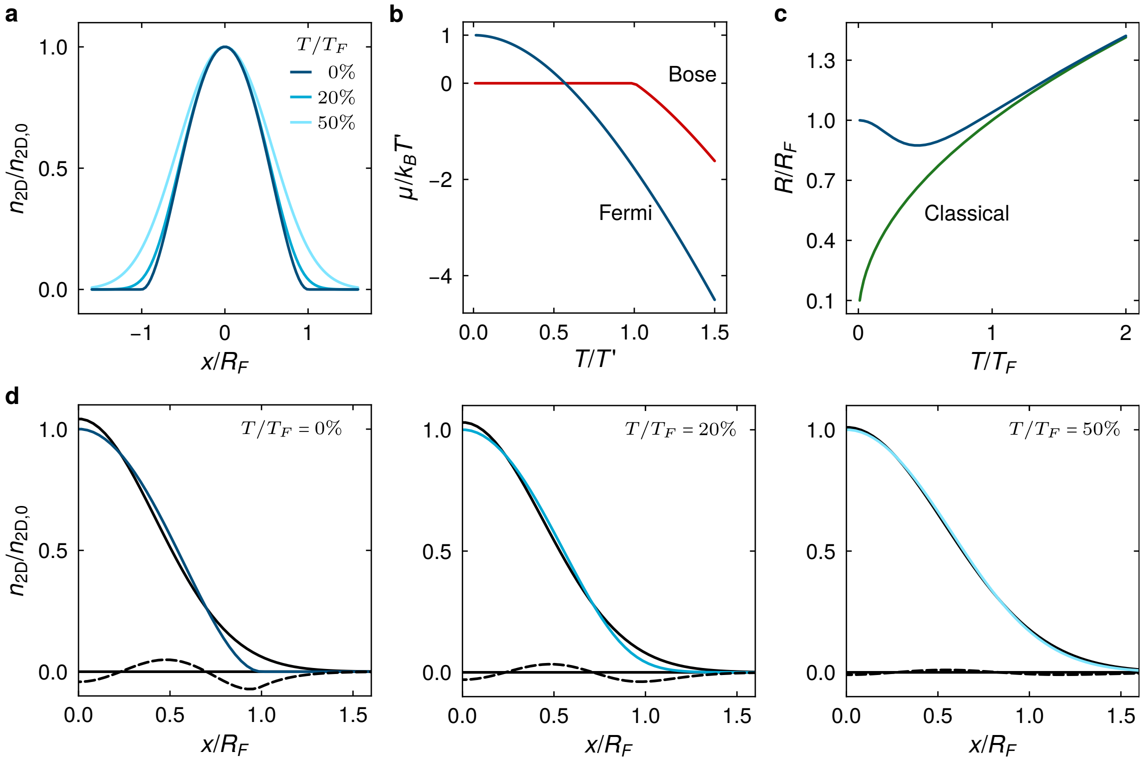

**Figure 2.2 ToF distributions and cloud parameters near degeneracy. a.** 2D column density distribution $n_{2D}(x, y = 0)$ from Eq. (2.48) for $T/T_F = 0\%, 20\%, 50\%$. **b.** Chemical potential for fermions (blue) and bosons (red) at low temperatures. For fermions $T' = T_F$ and for bosons $T' = T_C$. **c.** Radius $R$ (blue) from Eq. (2.46) and the Gaussian waist of a classical gas (green). **d.** Density distributions from a. (blue) with Gaussian fit (black) together with the residuum (black dashed).

behaves quite differently for ideal Bose and Fermi gases (see Fig. 2.2). For bosons, $\mu = 0$ for temperatures below $T_C$, marking the phase transition to the BEC. For the fermions, the chemical potential varies strongly for $T < T_F$ and even crosses zero at $T/T_F \approx 0.57$. Here, no phase transition occurs. Assuming $\mu \approx E_F$ is valid only for very deeply degenerate systems and therefore must be applied with care. For fitting the long ToF density distribution (Eq. (2.48)), the parameter $R$ was introduced. It is not to be confused with a root-mean-square radius of the cloud. Physically, $R$ only has a clear interpretation in the limit of $T = 0$ and $T \gg T_F$, because it does not grow monotonically (see Eq. (2.48)). Finally, the “smoking gun” signature of a degenerate fermi gas is worth a brief discussion. For $T \gg T_F$, the temperature is usually determined via the expansion of Gaussian cloud waist over time (see Section 6.1). A Gaussian fit still manages to capture the shape of the expanded cloud quite well for $T/T_F > 0.5$. For more degenerate clouds, however, the Gaussian fit tends to overshoot in the center and the edge of the wings (see Fig. 2.2).

## 2.3 Cooling limits

### 2.3.1 Fermi-Fermi

In modern ultracold gas experiments the final cooling step towards quantum degeneracy usually is performed by forced evaporative cooling [51]. An exception to this norm was demonstrated for bosonic Sr [86], which was brought to quantum degeneracy by laser cooling on a narrow transition in specially tailored ODTs. Unfortunately, those clever methods are not applicable to Li and other alkalis. For Li, Phase-Space Densitys (PSDs) of $\approx 10^{-4}$ are the best achieved so far through laser cooling alone [87, 88]. After the laser cooling stage, the atoms are commonly loaded to ODTs. This allows trapping atoms independent of their magnetic substate and also allows applying magnetic fields for tuning of the scattering length by means of magnetic Feshbach resonances [28][9].

In ODTs, the temperature of the atoms can be reduced by (forced) evaporative cooling. By removing the high-energy atoms, the remaining ensemble rethermalizes to a lower temperature than before. While this technique has proven to be very successful on the path to the BEC [89, 90], its application to fermions is limited. In a spin-polarized Fermi gas, the quantum numbers of all atoms are the same. Evaporative cooling relies on (fast) thermalization of the cloud via elastic collisions of the atoms. At low temperatures only s-wave collisions are energetically accessible. However, due to Pauli blocking of the symmetric total wave function for an s-wave collision, thermalization is suppressed [82]. To overcome this so-called *centrifugal barrier* to the antisymmetric p-wave channel, kinetic energy corresponding to a temperature of $\approx 6\,\mathrm{mK}$ is required for Li. This is well above the temperature of the MOT. For fermionic atoms with large magnetic dipole moments elastic scattering prevails down to zero temperature. The long-range Dipole-Dipole Interaction (DDI) is not suppressed in the same way as the short-range contact interaction, enabling thermalization in a single component gas. This has been demonstrated for the highly magnetic fermionic isotopes of Dy and Er, cooling down to $T/T_F = 0.2$ [91, 92].

Because Li is not among the magnetic atomic species, other measures have to be taken to achieve thermalization at low temperatures. A common technique is preparing half of the atoms in another Hyperfine (HF) state. In a system of two sets of indistinguishable particles cross thermalization of the Fermi gases is achievable. In some aspects this dual evaporation approach even exhibits advantages over evaporative cooling of bosons. Enhancing the scattering length with Feshbach resonances also inelastic processes such as three-body recombination are enhanced. However, the Pauli exclusion principle suppresses this unwanted effect for fermions [54].

The timescale $\tau_{\text{rel}}$, that governs the rethermalization is the elastic collision rate $\gamma_{\text{col}}$. It takes on average about $2.5$ collisions per particle for a classical gas trapped in a harmonic potential to relax to thermal equilibrium ($\tau_{\text{rel}} = 2.5\,\gamma_{\text{col,c}}^{-1}$) [53]. In this classical case, the collision rate is given by

$$\gamma_{\text{col,c}} = \bar{n}\sigma v, \tag{2.53}$$

with the spatially averaged density-weighted density $\bar{n}$, the cross-section of the collision $\sigma$ and the root-mean-square velocity $v$ of the colliding species [93]. For evaporative cooling of atoms in a harmonic trap, an increase in density $\bar{n}$ can dominate over the reduction in

---

[9] These are only two of the reasons why the once popular and successfully applied magnetic trap has basically vanished in modern experiments. The other are the limited trap geometry and the comparably slow switching times compared to ODTs.

velocity $v$, making the evaporation speed up as the cloud cools down. This so-called *runaway evaporation* lead the way of the cooling trajectory to quantum degeneracy for bosons.
For fermions the Pauli pressure is expected to limit the growth of $\bar{n}$. As the Fermi gas approaches the quantum degenerate regime, already occupied states below the Fermi energy start to be relevant. Consider an elastic scattering event of two atoms 1 and 2 with initial energies $\epsilon_{\mathrm{i},1}$ and $\epsilon_{\mathrm{i},2}$. The probability of those states being occupied is $f(\epsilon_{\mathrm{i},1})$ and $f(\epsilon_{\mathrm{i},2})$ (see Eq. (2.27)). After scattering the energy of the atoms changed to $\epsilon_{\mathrm{o},1}$ and $\epsilon_{\mathrm{o},2}$. For a scattering event to be elastic $\epsilon_{\mathrm{i},1} + \epsilon_{\mathrm{i},2} = \epsilon_{\mathrm{o},1} + \epsilon_{\mathrm{o},2}$ is fulfilled. According to Pauli, for this process to have happened the states must have been previously unoccupied. This is encoded in the probabilities $[1 - f(\epsilon_{\mathrm{o},1})]$ and $[1 - f(\epsilon_{\mathrm{o},2})]$. The collision rate is obtained form integration over all possible scattering channels:

$$\begin{aligned}\gamma_{col,F} = \frac{m\sigma}{2N\pi^2\hbar^3} \int & d\epsilon_{\mathrm{i},1} d\epsilon_{\mathrm{i},2} d\epsilon_{\mathrm{o},1} d\epsilon_{\mathrm{o},2}\, \delta(\epsilon_{\mathrm{i},1} + \epsilon_{\mathrm{i},2} - [\epsilon_{\mathrm{o},1} + \epsilon_{\mathrm{o},2}]) \rho(\epsilon_{\mathrm{min}}) \\ & \times f(\epsilon_{\mathrm{i},1}) f(\epsilon_{\mathrm{i},2}) [1 - f(\epsilon_{\mathrm{o},1})][1 - f(\epsilon_{\mathrm{o},2})].\end{aligned} \tag{2.54}$$

With $\rho(\epsilon_{\mathrm{min}})$ is the density of states[10] of the smallest energy involved in the collision [93]. As the fermions cool down all available states below the Fermi energy are being filled up gradually:

$$f(\epsilon \leq E_F) \xrightarrow{T/T_F \to 0} 1 \text{ and with this } [1 - f(\epsilon \leq E_F)] \xrightarrow{T/T_F \to 0} 0.$$

The Fermi sea fills up and the scattering channels below the Fermi energy deplete. The effect of the closing Fermi sea on the collision and thermalization time was studied by [93, 94] to optimize cooling trajectories for dual evaporation. In a similar approach in [53] these times were simulated for reasonable experimental parameters in a K spin-mixture. Here it was found, that in the quantum regime on average less collisions than in the classical case are required for thermalization: $\tau_{\mathrm{rel}}/\tau_{\mathrm{col,F}} < 2.5$. Down to $T/T_F \approx 0.3$ the thermalization time gets shorter as the cloud cools down and gets more dense. For higher degeneracy the depletion of unoccupied states slows the thermalization down. For $T/T_F < 0.15$ the thermalization time grows rapidly. In this deeply degenerate regime the collision rate scales quadratically $\gamma_{col,F} \propto (T/T_F)^2$ [95, 96]. Below this limit one has to wait longer and longer for the cloud to rethermalize to a lower temperature during evaporation. The final temperature is always reached at the equilibrium of cooling and heating rates. As the cooling is slowing down when the deeply degenerate regime is approached, heating persists. This limits the degeneracy reachable to $T/T_F \gtrsim 0.1$.
Even though the system just discussed is quite specific, the point of $T/T_F \approx 0.1$, where quantum statistics strongly suppresses thermalization also applies to other systems relying on cross thermalization of two Fermi seas. More generally, it applies to all ultracold gas systems, where thermalization is achieved by elastic collisions between two fermions. This includes elastic collisions of two indistinguishable fermions with long-range interactions (e.g. DDI) and two distinguishable fermions (different spin state, isotope or element) with short range interaction. For some setups more favorable experimental parameters may lead to higher collision rates in the classical limit (prefactor in Eq. (2.54)), but due to the quantum statistics of the fermions the "quadratic" wall around $T/T_F = 0.15$ persists.
In a dual-evaporation experiment for a spin-mixture of Li, cooling stopped at $T/T_F = 0.16$ [88]. In other spin-mixture experiments similar maximum achievable degeneracies

---

[10] It is not changing much and is therefore not considered in the following qualitative argumentation.

were reported: Yb: $T/T_F = 0.37$ in mixture of 6 spin states [97], Sr: $T/T_F = 0.27$ in a mixture of 10 spin states [98], K: $T/T_F = 0.3$ in a mixture of 2 spin states [99]. Often inefficient evaporation or slowed down cooling at $T/T_F = 0.5$ were reported. The first degenerate Fermi gas was observed in 1999 by evaporative cooling in a spin-mixture of K reaching $T/T_F = 0.5$ [100]. Since then great technical progress to reduce heating by noise and progress in understanding heating by inelastic processes has been made. This pushed the best degeneracy achievable in systems where fermions are cooled with fermions closer to, but not over the wall around $T/T_F = 0.1$.

### 2.3.2 Fermi-Bose

An alternative approach is to cool fermions in thermal contact with bosons. Bosons do not suffer from depleting scattering channels due to Pauli blocking. By evaporating only the bosons or the fermions together with the bosons the thermalization time improves. In principle, with this sympathetic cooling approach higher degeneracy of the Fermi gas is achievable, but with the quantum statistics of the coolant a new obstacle arises.

*Heat capacity mismatch* When the bosons are being evaporatively cooled below the critical temperature $T_C$, the fraction of the non-condensed atoms drops as $({}^{T}\!/\!{}_{T_C})^3$ (Eq. (2.39)). With the vanishing classical fraction the heat capacity of the Bose gas is reduced as well. The heat capacity $C = {}^{\partial E}\!/\!{}_{\partial T}$ relates a change of internal energy $E$ to the change in temperature for a constant atom number. Below the critical temperature $T_C$ for bosons and respective the Fermi temperature $T_F$ for fermions, it is approximated by [57]

$$C_B \approx 10.8\, k_B N_B \left({}^{T}\!/\!{}_{T_C}\right)^3 \text{ and } C_F \approx \pi k_B N_F \left({}^{T}\!/\!{}_{T_F}\right), \tag{2.55}$$

with the atom numbers $N_B$ for the bosons and $N_F$ for the fermions. In a mixture of fermions and bosons, that share the same properties but the quantum statistics, the critical temperature and the Fermi temperature are almost equal: $T_C \approx {}^{1}\!/\!{}_{2} T_F$. Consequently, efficient sympathetic cooling stops already for high $T_0/T_F$, when the heat capacities cross: $C_B(T_0) = C_F(T_0)$.

To obtain the heat capacities for the entire span over the degenerate and non-degenerate regimes, numerical calculations are employed. Assuming a spherical symmetric potential ($\bar{\omega} = \omega_x = \omega_y = \omega_z$), the total energy is given by the sum of the quantum statistics weighted individual level energies $E_j$:

$$E = \sum_j E_j \frac{g_j}{e^{(E_j - \mu(T))/k_B T} \mp 1}, \tag{2.56}$$

with $E_j = \hbar\bar{\omega}(j + 3/2)$ and the degeneracy factor $g_j = \frac{(j+1)(j+2)}{2}$ [57]. The chemical potential $\mu(T, N = \text{const})$ is found by numerically solving

$$N = \sum_j \frac{g_j}{e^{(E_j - \mu(T))/k_B T} \mp 1}. \tag{2.57}$$

In Fig. 2.3 the obtained heat capacities for fermions and bosons are shown. For the fermions the heat capacity per particle smoothly blends over from the linear scaling to the classical

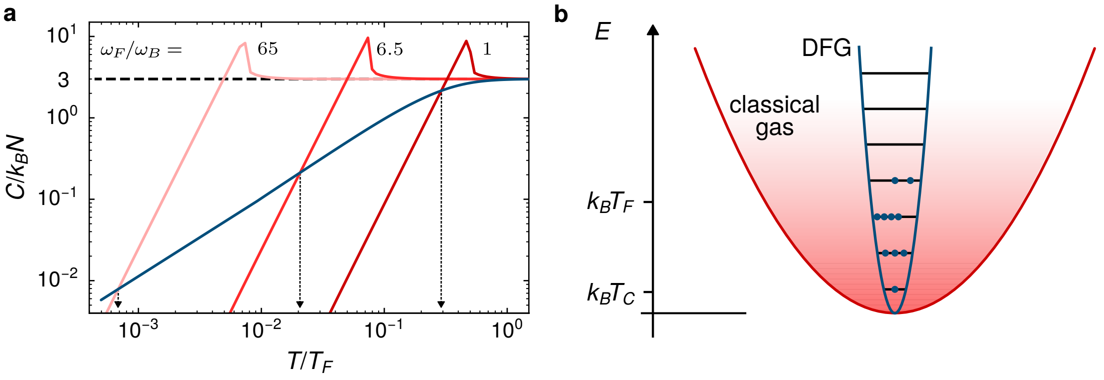

**Figure 2.3 Heat capacities in a Fermi-Bose mixture. a.** Heat capacity per particle for fermions (blue) and bosons (red) in a 3D harmonic potential for various trap frequency ratios $\omega_F/\omega_B$. The limit for a classical gas is indicated by the black dashed line. As the ratio increases, the point of efficient cooling $T_0$ from $C_F(T_0) = C_B(T_0)$ shifts down to higher degeneracies of the fermions. Adapted from [58]. **b.** Visualization of a Fermi-Bose mixture with high $\omega_F/\omega_B$. The difference in energy scale, where the quantum regime is reached is marked on the energy axis.

limit of $3k_B$ around the Fermi temperature[11]. As expected for $T \gg T_C$, the heat capacity of the bosons is well represented by the classical value. As the temperature passes the critical temperature, a sharp increase due to the phase transition to the BEC occurs. For even lower temperatures it drops much faster, than for the fermions.

Both the Fermi temperature and the critical temperature are proportional to $\bar{\omega}$. For the case discussed above, the trapping frequencies $\omega_B$ for the bosons and $\omega_F$ for the fermions are the same: $\omega_F/\omega_B = 1$. The heat capacity of the two cross at $T_0/T_F \approx 0.3$. A $^6$Li-$^7$Li mixture confined in an ODT well realizes this scenario. Indeed, in such a mixture $T_0/T_F \approx 0.25$ was achieved [101, 102]. More than 10 years later the degeneracy of the same mixture was improved by one order of magnitude to $T/T_F \approx 0.03$ [56]. In this experiment the $^6$Li-$^7$Li were evaporated together. With the $^6$Li spin-mixture outnumbering $^7$Li, the bosons were used as a kind of thermalization catalyst between the Fermi seas.

If only ODTs of one wavelength are forming the optical potential, the trap frequency ratio is altered with the mass ratio $m_F/m_B$ and polarizability $\alpha_F/\alpha_B$ of the fermionic and bosonic constituents:

$$\omega_F/\omega_B = \sqrt{\frac{\alpha_F}{\alpha_B}\frac{m_B}{m_F}}. \tag{2.58}$$

For our $^6$Li-$^{166}$Er mixture in a $1064\,\mathrm{nm}$ ODT a ratio of $\omega_F/\omega_B = 6.5$ is obtained [103, 104]. In this light-heavy mixture the heat capacities crossing point is pushed by more than one order of magnitude to $T_0/T_F \approx 0.02$. In a similar $^6$Li-$^{174}$Yb mixture $T/T_F = 0.08$ was achieved [105]. For a $^6$Li-$^{23}$Na mixture with only $\omega_F/\omega_B = 2$ a degeneracy of $T/T_F = 0.05$ was reached without a significant loss of Li in the evaporation stage [55]. The reduction in heat capacity of the bosons was compensated for by a large ratio of $N_B/N_F = 10^2$ in atom numbers. Another reason this temperature record was accomplished is the favorably low inelastic scattering rate in the $^6$Li-$^{23}$Na mixture. For a new mixture it is a priori not known and has to be experimentally measured.

---

[11] Simulation for $N = 3 \cdot 10^4$. Linear extrapolation for the fermions at high degeneracy $T/T_F < 4 \cdot 10^{-3}$, because of too long computing time.

Another approach to further tune the trap frequency ratio is by species selective trapping [59]. This can be realized with bichromatic ODTs or magnetic trapping of atoms with very different magnetic moments. By employing an ODT for one of the species at a tune-out wavelength of the other, the ratio can be further increased almost arbitrarily. A still experimentally meaningful increase by $\times 10$ is achievable for our $^6$Li-$^{166}$Er mixture by adding a tightly focused $841\,\mathrm{nm}$ ODT to the before mentioned $1064\,\mathrm{nm}$ ODT. Tuned to the Er tune-out wavelength, the trap is still far red detuned for Li [64]. For this configuration the trap ratio is pushed further to $\omega_F/\omega_B = 65$. The crossing of the heat capacities shifts to $T_0/T_F < 10^{-3}$. By detaching the energy scales of the Fermi and Bose gases the former is already deeply degenerate, while the other still behaves like a classical gas.

### 2.3.3 Spatial overlap

*Size of a BEC* Having a large ratio of the respective trap frequencies also helps to achieve spatial overlap when both clouds are degenerate. The characteristic sizes of a DFG and a non-interacting BEC are quite different for equal trap frequencies (see again Fig. 2.1). At zero temperature, the size of the DFG is simply given by the Fermi radius, because all contact interactions are Pauli blocked. For the non-interacting BEC, the characteristic size is given by the harmonic oscillator length. It is quite intuitive to imagine that contact interactions alter the size of this high density state a lot. The ground state of the many-body system is described by the complex order-parameter $\Psi(\boldsymbol{r})$ [51]. It is obtained by solving the effective single particle Gross-Pitaevskii equation

$$i\hbar\frac{d\Psi}{dt} = -\frac{\hbar^2}{2m}\nabla^2\Psi + U(\boldsymbol{r})\Psi + \tilde{U}|\Psi|^2\Psi. \tag{2.59}$$

The interaction parameter $\tilde{U} = 4\pi\hbar^2 a/m$ represents the effect of the two-body collisions with the s-wave scattering length $a$ and the mass $m$. If the contact interaction is much stronger than the harmonic oscillator energy ($n\tilde{U} \gg \hbar\omega_i$), the kinetic energy term can be neglected. In this so-called *Thomas-Fermi* approximation the shape of the density distribution is governed by the shape of the potential only:

$$n_c(\boldsymbol{r}) = \max\left(\frac{\mu - U(\boldsymbol{r})}{\tilde{U}}, 0\right). \tag{2.60}$$

The bosons fill up the potential up to the chemical potential $\mu$. It is non-zero due to the interactions and depends on the atom number $N$ of the condensate:

$$\mu = \left[\frac{15\hbar^2 m^{1/2}}{2^{5/2}} N\bar{\omega}^3 a\right]^{2/5}. \tag{2.61}$$

By plugging the harmonic potential for $U(\boldsymbol{r})$ in Eq. (2.60) and normalizing to the atom number an explicit expression for the denisty is obtained:

$$n_c(\boldsymbol{r}) = \frac{15}{8\pi}\frac{N}{\sigma_{x,c,0}\,\sigma_{y,c,0}\,\sigma_{z,c,0}}\max\left(1 - \left[\frac{x^2}{\sigma_{x,c,0}} + \frac{y^2}{\sigma_{y,c,0}} + \frac{z^2}{\sigma_{z,c,0}}\right], 0\right), \tag{2.62}$$

with the half lengths $\sigma_{i,c,0} = \sqrt{2\mu/m\omega_i^2}$. While the BEC shape is changed dramatically by introducing interactions, the critical temperature $T_c$ remains essentially unaffected. The change $\delta T_c^{\text{int}}$ is given by [106]:

$$\frac{\delta T_c^{\text{int}}}{T_c} \approx -1.33 \frac{a}{d_{\text{ho}}} N^{1/6}. \tag{2.63}$$

For typical experimental values of $a = 100\,\mathrm{a}_0$, $d_{\text{ho}} = 1\,\mu\mathrm{m}$ and $N = 10^5$, the correction to the critical temperature of the non-interacting Bose gas is only $-3\%$.
For simplicity, let us assume a spherical symmetric potential. The half-length scales only weakly with the parameters: $\sigma_{c,0} \propto (Na/m^2\omega^2)^{1/5}$. Changing the condensate size to match the size of the DFG is best achieved by a combination of trap frequency adjustment and tuning of the s-wave scattering length. Increasing $a$ is limited to the onset of higher order density heating effects. In the experiment, lowering the trap frequency also slows down thermalization. Here it is advisable to lower the trap frequencies of the bosons and increase the trap frequencies for the fermions. One must also ensure that the trap does not open in the vertical direction due to gravity, which acts very differently on Er and Li due to the mass difference.
In Fig. 2.4a density profiles for the large trap ratio of $\omega_F/\omega_B = 65$ are shown. With a geometric mean trap frequency of $\bar{\omega}_B = 2\pi \cdot 30\,\mathrm{Hz}$ and atom numbers for the fermions and bosons of $N_F = 10^4$ and $N_B = 10^5$ an experimentally realistic scenario for our ErLi-mixture is covered. The scattering length of the bosons is chosen to be $100\,\mathrm{a}_0$, with $a_0$ representing the Bohr radius. The sizes of the Fermi and Bose gases match well with the chosen parameter sets.

*Mean-field demixing* Up to this point the bosonic and fermionic density distributions were treated as independent. Interactions between the two can alter the shape of the clouds a lot. Here, the relative strength among the bosons and between the bosons and the fermions are important [107]. In a system, where the bosons outnumber the fermions strong repulsive Fermi-Bose interaction pushes the fermions out of the BEC forming a shell (see Fig. 2.4b). For attractive interactions, the bosons are providing an effective potential, that pulls the fermions inside. Under certain conditions it can be so strong, that the Fermi gas collapses: fermions rush in, causing three-body collisions that lead to losses and heating [82, 108].

*Gravitational sag* When placed in an ODT, atoms are held against gravity ($F_G = -mg$) by the trap's vertical confinement ($F_{ho} = m\omega_v^2 z$), where $g$ is the gravitational acceleration of the earth. Gravity displaces the center of the atomic cloud by $\Delta z = g/\omega_v^2$. For two species $1$ and $2$ in the same ODT, the difference in trap frequencies results in a displacement of the two relative to each other by

$$\Delta z_{1,2} = g(1/\omega_{1,v}^2 - 1/\omega_{2,v}^2). \tag{2.64}$$

If $\Delta z_{1,2}$ is on the order of the cloud sizes overlap is lost. The above considerations are true for harmonic potentials, that extend to infinity resulting in a trap of infinite depth. For a real ODT the harmonic approximation of the potential provided by the Gaussian beam(s) is only of finite extend. When the trap depth is gradually lowered, the maximum displacement of one species is given by half of the waist of the (Gaussian) beam. Here, the force of the ODT

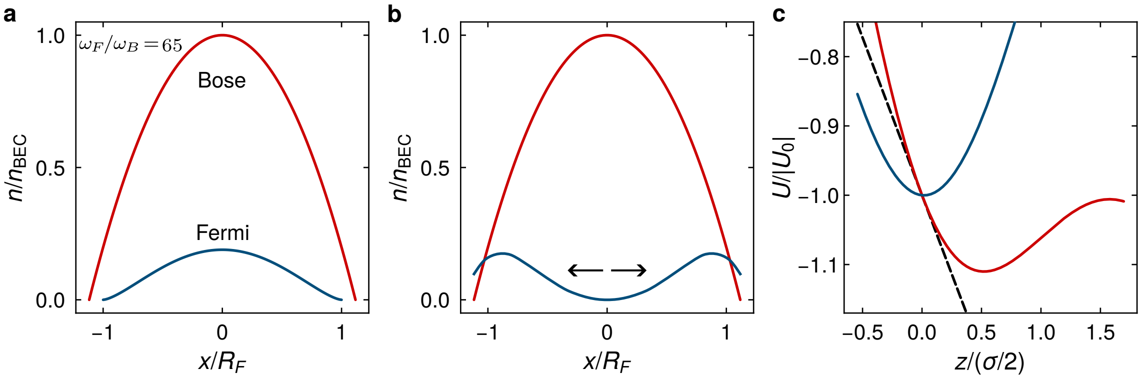

**Figure 2.4 Spatial overlap of DFG and BEC. a.** Density distribution of a DFG (blue) and BEC (red) both in Thomas-Fermi approximation. The atom number of the fermions is $\times 10$ smaller and the trap frequencies $\times 65$ larger than for the bosons. For the bosons an s-wave scattering length of $100\,\mathrm{a}_0$ and a mass of $166\,\mathrm{u}$ is assumed. **b.** Sketch for demixing by repulsive interaction between the fermions and the bosons of a. **c.** Optical potential of a Gaussian beam and gravity for a light (blue) and heavy (red) atomic species. The mass ratio is the one of $^{6}$Li$^{166}$Er. The curvature of the trap is chosen such that the maximum force of the ODT is $25\%$ stronger than gravity for the heavy atom (black dashed). Both traps are normalized to the trap depth for absent gravity.

onto the atoms is largest. For even lower trap depths the ODT no longer confines the atoms. It gets clear, that the harmonic approximation quickly fails to predict the displacement $\Delta z$ for shallow traps. Instead, the entire Gaussian beam has to be taken into account.
An example for the gravitational sag between the light Li and heavy Er is shown in Fig. 2.4c. Here, the optical potential from a Gaussian beam is chosen such, that it is significantly modified by gravity for Er. Meanwhile, the same potential is not notably altered through gravity for the much lighter Li atoms. The difference results in a strong displacement of the two trap centers by one quarter of the waist of the Gaussian beam. Here again species selective trapping can be employed to compensate the gravitational sag by independent tuning of the trap centers.

### 2.3.4 Heating sources

In the following, selected heating sources on the atoms are presented: Hole heating, heating by vacuum collisions, heating by dipolar relaxation, heating by off-resonant scattering and heating by intensity noise. They are of physically varying origin and heat-up the system by distinctive effects. Typical heating rates are discussed and the dominating one is examined in the end.

*Hole heating* Consider a highly degenerate Fermi gas with $T \ll T_F$. The energy levels in the Fermi sea are almost perfectly filled up to the Fermi energy $E_F$. If one fermion is removed randomly, the total energy $E(N, T)$ is reduced by the average energy per particle in the system. In 3D the average energy per fermion is $\frac{3}{5}E_F$ [109]. The total energy after the removal writes as [110]

$$\begin{aligned} E' &= E(N,T) - \tfrac{3}{5}E_F \\ &\approx [E(N-1,T) + E_F] - \tfrac{3}{5}E_F \\ &= E(N-1,T) + \tfrac{2}{5}E_F. \end{aligned} \tag{2.65}$$

For $T \ll T_F$ the energy change per particle is well approximated by

$$E(N,T) - E(N-1,T) = \mu \approx E_F$$

(see again Fig. 2.2). Creation of a hole in the Fermi sea leads to a subsequent rethermalization with an excess energy of

$$E_{h,F} = \tfrac{2}{5}E_F. \tag{2.66}$$

This idealized removal of a particle is a best-case scenario, in which no additional collisions heat other particles during the loss process.

Similar considerations for the Bose gas, where an atom form the BEC of average energy $\frac{5}{7}\mu$ [77] is removed, provides an excess energy $E' = E(N-1,T) + \frac{2}{7}\mu_{\text{Bose}}$. In contrast to the fermions, where $\mu_{\text{Fermi}} = T_F k_B$, the chemical potential is independent of the critical temperature $T_c$. Therefore, a general statement about an equivalent hole heating effect for bosons with respect to the critical energy scale is not reasonable. Typically, the chemical potential for the bosons is much lower than the critical temperature.

*Vacuum collisions* While the atoms are held in the ODT, background gas particles collide with them. For high vacuum, the remaining pressure basically consists of He and $H_2$ only. In the following, the considerations from [111] are considered to obtain the expected heating rates for the conditions of the ErLi-experiment. Since the reference only considers alkali-metal atoms, the values obtained for $^{133}$Cs are used as a good approximation for $^{166}$Er. Compared to the background vacuum particles with a thermal velocity of $\sim 1000\,\mathrm{m/s}$ at room temperature, the atoms in the trap are basically at rest: $v = 0\,\mathrm{m/s}$. When a trapped atom of mass $m$ is hit, the natural scale of energy change is

$$\epsilon_d = \tfrac{1}{2}m\Delta v^2 = \frac{4\pi\hbar^2}{m\sigma}, \tag{2.67}$$

with the cross-section $\sigma$ of the collision. The energy transfer depends on the two atoms involved in the collision and the temperature. For the light Li atoms they are $\epsilon_d = 624\,\mathrm{mK}$ (LiHe) and $\epsilon_d = 423\,\mathrm{mK}$ ($\mathrm{LiH_2}$). For the heavy Cs atoms they are $\epsilon_d = 21\,\mathrm{mK}$ (CsHe) and $\epsilon_d = 14.3\,\mathrm{mK}$ ($\mathrm{LiH_2}$). Even for Cs, $\epsilon_d$ is about four orders of magnitude higher, than common ODT depths of typically $U = 1\,\mu\mathrm{K}$. At room temperature the collision rate per vacuum particle density $\gamma_c/n_p$ is already provided by[12] [111]. With the ideal gas law the particle density ($n_p = p/Tk_B$) is obtained for a pressure of $p = 10^{-11}\,\mathrm{mbar}$, which is well reached in the later experiment. For the different cases, the rate $\gamma_c$ at which an atom is removed

---

[12] Generalization to obtain $\gamma_c$ for other temperatures are also provided, but not needed here.

from the trap by a collision are:

$$\begin{aligned}\text{Li}: \gamma_c &= 0.5\,\text{mHz (He)} \;\;\&\;\; \gamma_c = 1.0\,\text{mHz } (\text{H}_2)\\ \text{Cs}: \gamma_c &= 0.6\,\text{mHz (He)} \;\;\&\;\; \gamma_c = 1.3\,\text{mHz } (\text{H}_2).\end{aligned}$$

For a DFG, a particle removal accompanied by the energy excess through hole heating of $\frac{2}{5}E_F$ leads to a heating rate of

$$\dot{q}_r = \tfrac{2}{5}E_F\gamma_c. \tag{2.68}$$

For collisions under a small angle the atom remains trapped, but is heated. The heating rate by this process is

$$\dot{q}_t = 0.37\gamma_c U\frac{U}{\epsilon_d}. \tag{2.69}$$

For typically conditions of $U = 10^{-4}\epsilon_d$ and $U = 10E_F$ this additional heating rate is found to be negligible:

$$\dot{q}_t = 0.37\gamma_c E_F 10^{-3} \approx \dot{q}_r 10^{-3}. \tag{2.70}$$

Due to the diluteness of the quantum gases, a consecutive collision of the before trapped atom or the background gas particle with another trapped atom is also negligible.

*Dipolar relaxation* In dipolar relaxation processes internal angular momentum from e.g. the spin of the electrons or the nucleus are transformed to relative motion of the atoms [82]. In contrast to spin-exchange collisions, the total spin is not conserved. Dipolar relaxations are known to introduce significant heating for non-spin polarized Bose gases of dipolar atoms such as Er [112]. The magnetic moment of Er is $\mu_{\text{ER}} \approx 7\mu_B$ and for Li $\mu_{\text{Li}} \approx 1\mu_B$, with $\mu_B$ the Bohr magneton (see also Section 3.2.2). This leads to additional relaxation processes in our Fermi-Bose mixture, if both species are not in their ground states. As for Er all atoms anyway need to be in the absolute ground state to avoid dipolar relaxation among them, we only consider Li occupying states other than the absolute ground state $|1\rangle$. The cross-section of the process is proportional to the square of the magnetic moments of the two [113]

$$\sigma_{\text{DD,F}} \propto (\mu_{\text{Li}}\mu_{\text{Er}})^2 = 49\mu_B^4. \tag{2.71}$$

This holds for the Zeeman regime, where the nuclear spin $I$ and electron spin $S$ are still coupled. For increasing magnetic fields the Paschen-Back regime is reached, where $I$ and $S$ decouple. There, the electron spin of the three lowest substates of Li ($|1\rangle$, $|2\rangle$ and $|3\rangle$) have the same orientation ($m_S = -1/2$). Remaining admixtures of $m_s = +1/2$ to the states are more and more fading for higher fields. This reduces the dipolar interaction coupling to the small nuclear magnetic moment of $\mu_I = 0.45\cdot 10^{-3}\mu_B$. Thereby the cross-section is reduced to

$$\sigma_{\text{DD,I}} \propto (\mu_{\text{I}}\mu_{\text{Er}})^2 = 10^{-5}\mu_B^4. \tag{2.72}$$

Therefore, heating due to dipolar relaxation of state $|2\rangle$ and $|3\rangle$ is expected to be suppressed in high fields.

*Off-resonant scattering* Atoms placed in ODTs scatter photons from the far off-resonant light field. In the following heating effects for the standard $1064\,\text{nm}$ wavelength and the $841\,\text{nm}$ tune-out wavelength of Er are considered [64]. For experiments described in this thesis only ODTs at $1064\,\mathrm{nm}$ for Er and Li were employed. Since the tune-out wavelength at $841\,\mathrm{nm}$ is a key aspect of the ErLi-mixture, heating due to off-resonant scattering is discussed as well.

The recoil energy $E_{\text{rec}} = \hbar^2 k^2/2m$ due to absorption or emission of a photon of wavelength $\lambda = 2\pi/k$ is of inverse scaling with the mass $m$ of the atom. When an atom absorbs and spontaneously re-emits a photon its thermal energy increases by $T_{\text{rec}} = 2E_{\text{rec}}/k_B$ [52]. The recoil temperatures for Li and Er differ significantly due to their unequal masses:

$$\text{Li}: \quad T_{\text{rec}} = 2.8\,\mu\text{K} \quad (1064\,\text{nm}) \quad \& \quad T_{\text{rec}} = 4.5\,\mu\text{K} \quad (841\,\text{nm}) \tag{2.73}$$

$$\text{Er}: \quad T_{\text{rec}} = 0.1\,\mu\text{K} \quad (1064\,\text{nm}) \quad \& \quad T_{\text{rec}} = 0.16\,\mu\text{K} \quad (841\,\text{nm}) \tag{2.74}$$

If the trap depth is smaller than $2E_{\text{rec}}$, the atom is lost from the trap by a single scattering event. For Li this is commonly fulfilled. When the atoms are deeply degenerate, the energy due to hole heating (Eq. (2.66)) has to be taken into account instead to calculate heating of the atomic cloud. With the scattering rate $\Gamma_{sc}$, the heating rate calculates as $\dot{P} = 2E_{\text{rec}}\Gamma_{\text{sc}} = k_B T_{\text{rec}}\Gamma_{\text{sc}}$ [52]. For Li it is sufficient to take only scattering from the lines at $671\,\mathrm{nm}$ into account. With Eq. (2.11) the scattering rate is obtained as $\Gamma_{sc} = \frac{\Gamma}{\Delta}\frac{U}{\hbar}$. For a standard dipole trap depth of $U/k_B = 1\,\mu\mathrm{K}$ the scattering rates are

$$\text{Li}: \quad \Gamma_{sc} = 4.6\,\text{mHz} \quad (1064\,\text{nm}) \quad \& \quad \Gamma_{sc} = 8.4\,\text{mHz} \quad (841\,\text{nm}). \tag{2.75}$$

For Er a two level approximation does not hold. The complex polarizability at $1064\,\mathrm{nm}$ is taken from [114] to calculate the scattering rate with Eqs. (2.1) and (2.2) for a $U/k_B = 1\,\mu\mathrm{K}$ trap for Er. For scattering at the tune-out wavelength, the intensity for a $U/k_B = 1\,\mu\mathrm{K}$ trap for Li is taken into account [64]:

$$\text{Er}: \quad \Gamma_{sc} = 3.7\,\text{mHz} \quad (1064\,\text{nm}) \quad \& \quad \Gamma_{sc} = 8\,\text{mHz} \quad (841\,\text{nm}). \tag{2.76}$$

The scattering rates for Er and Li are roughly equal for each wavelength, but due to the lower mass the heating rate is about $\times 28$ higher for Li:

$$\text{Li}: \quad \dot{P}_{\text{sc}} = 13\,\text{mHz}\,\mu\text{K} \quad (1064\,\text{nm}) \quad \& \quad \dot{P}_{\text{sc}} = 38\,\text{mHz}\,\mu\text{K} \quad (841\,\text{nm}) \tag{2.77}$$

$$\text{Er}: \quad \dot{P}_{\text{sc}} = 0.4\,\text{mHz}\,\mu\text{K} \quad (1064\,\text{nm}) \quad \& \quad \dot{P}_{\text{sc}} = 1.4\,\text{mHz}\,\mu\text{K} \quad (841\,\text{nm}). \tag{2.78}$$

In the limit, where the energy increase is given by hole heating for Li, the heating rate is reduced a lot since the Fermi energy is typically orders of magnitude lower than the trap depth.

*Intensity noise* When an atom is placed in an ODT, the potential depth fluctuates with the Relative Intensity Noise (RIN) of the laser source. These perturbations cause the atom to heat-up over time [115]. The system describing Hamiltonian in 1D is given by

$$H = \frac{p^2}{2m} + \frac{1}{2}m\omega_x^2[1+\epsilon(t)]x^2 = H_{ho} + H'(t), \tag{2.79}$$

with the perturbation Hamiltonian $H' = \frac{1}{2}m\omega_x^2\epsilon(t)x^2$. Here, the modulation of the potential is described by $\epsilon(t) \propto \Delta I(t)$.

Before considering the general case of $\epsilon(t)$ representing noise, a specific example of a single frequency perturbation $\epsilon(t) \propto \sin(\omega_{\text{mod}})$ is examined briefly. For this sinusoidal modulation, a parametric resonance at $\omega_{\text{mod}} = 2\omega_x$ is found to cause exponential heat-up. The parametric heating technique is commonly used to determine trap frequencies of ODTs by atom loss spectroscopy.

Back to the general case, the time evolution in the basis of the static Hamiltonian $H_{ho}$ is derived by perturbation theory. Here, findings complementary to single frequency parametric heating are obtained. An exponential increase of the mean energy per particle $\langle E_x \rangle$ is found:

$$\langle \dot{E}_x \rangle = \Gamma_x \langle E_x \rangle \quad \text{with} \quad \Gamma_x = \frac{\pi}{2} \omega_x^2 S(2\omega_x). \tag{2.80}$$

Here $S(\omega)$ represents the (one-sided[13]) RIN defined as

$$S(\omega) = \frac{2}{\pi} \int_0^\infty d\tau \cos(\omega\tau) \langle \epsilon(t)\epsilon(t+\tau) \rangle. \tag{2.81}$$

Heating depends only on the frequency component in the noise spectrum, that matches double the trap frequency. Therefore, it can be regarded as unvoluntary parametric heating due to intensity noise of the laser source.

The results of the 1D considerations are used to derive the evolution for a 3D system. The total energy $E_{\text{tot}}$ is given by the sum of the energies of the three axes. It is reasonable to assume, that the axes are not decoupled, and therefore the total energy is distributed equally among them: $\langle E_x \rangle = \langle E_y \rangle = \langle E_z \rangle = E_{\text{tot}}/3$. The individual heating rates add up to the total heating rate $\Gamma_{\text{tot}} = \Gamma_x + \Gamma_y + \Gamma_z$. Similar to Eq. (2.80) an exponential increase of the total energy is obtained:

$$\dot{E}_{\text{tot}} = \Gamma_{\text{tot}} E_{\text{tot}} = \frac{\pi^2}{3} \left[ \nu_x^2 S(2\nu_x) + \nu_y^2 S(2\nu_y) + \nu_z^2 S(2\nu_z) \right] E_{\text{tot}}. \tag{2.82}$$

For short times ($t \ll \Gamma$) the (linear) heating rate is given by $\Gamma_{\text{tot}}$ with the oscillation frequencies $\omega_i = 2\pi\nu_i$.

At low trap frequencies of $< 3\,\text{kHz}$ the heating rate $\Gamma_{\text{tot}}$ is typically extremely small. In this regime our standard analog intensity PI-controller has a RIN, which is smaller than $10^{-12}\,/\text{Hz}$ [116]. This results in a negligible heating rate of $\Gamma_{\text{tot}} \ll 1\,\text{mHz}$. For optical lattices, trap frequencies are typically around $\sim 100\,\text{kHz}$ [22]. At these high frequencies intensity noise can become the major heating source of the atoms. Derived from a Ti:Sa laser with a RIN of $\approx 10^{-12}\,/\text{Hz}$ at $200\,\text{kHz}$ [117], a heating rate of $100\,\text{mHz}$ is obtained.

*Conclusion* The heating sources presented are of distinct origins. Nevertheless, they can be divided into two categories: technical heating sources and physically inherent heating sources. Heating by intensity noise and collisions with background vacuum particles belong to technical heating sources.

Advances in vacuum technologies has helped to provide a low enough pressure environment for our experiment to consider the associated heating as negligible. The effect of intensity noise on the atoms heavily depends on the natural oscillation frequencies in the system. For the reduction of intensity noise there is no standard equipment to ensure low enough RIN at the desired frequencies. Active intensity stabilization to provide low RIN therefore still is under investigation [118, 119].

---

[13] The one-sided RIN is half of the usually measured two-sided RIN.

Heating due to dipolar relaxation, hole-heating and off-resonant scattering are of physically inherent origin. Their effect on the system cannot be reduced by technical advances, but changing the system itself. Heating by dipolar relaxation in a spin-mixture of Li in contact with Er still has to be experimentally investigated. The excess energy of hole-heating by particle loss is fundamental. Here only the rate of the process can be reduced, but not the effect itself. Heating by off-resonant scattering in ODTs depend on the level structure and mass of the atom. It can be reduced by changing the wavelength of the ODT providing laser. Here, with the availability of a suitable alternative laser source a technical issue arises again. Since the presented heating sources depend on very different parameters of the system, it is difficult to make a general statement about the dominating one. Providing a good vacuum environment definitely is a must-have. For achieving the lowest temperatures for Li in a $1064\,\mathrm{nm}$ 3D harmonic trap of modest trap frequencies heating by off-resonant scattering of $5\,\frac{E_F}{1000\,\mathrm{s}}$ is expected to be dominating.

# Chapter 3

# ErLi

The following chapter presents the various properties of Er, Li, and an ErLi mixture that are relevant to our experiment. It primarily focuses on Li. The Er properties are shown in a reduced fashion and presented together with Li to highlight their similarities and differences. More information about Er is given in the complementary thesis concentrating on the Er part [74].

## 3.1 Li properties

Lithium is the 3rd lightest atom in the periodic table and has two stable isotopes: $^{6}$Li and $^{7}$Li. As for all neutral atoms, the quantum statistical nature of the isotopes is determined by the parity of the neutron number of the core. With three (odd) neutrons $^{6}$Li is a fermion and with four (even) neutrons $^{7}$Li is a boson [120]. Away from quantum degeneracy, the physical properties of both isotopes are very similar. Only $^{6}$Li is discussed in the following, as exclusively this isotope is experimentally considered in this thesis.

The optical properties of the alkali-metal atom $^{6}$Li is governed by its single valence electron. From the $2^2S_{1/2}$ ground state[1] the $D_1$- and $D_2$-lines at $671\,\mathrm{nm}$ [121] are commonly used for laser cooling (see Fig. 3.1a). The two lines are separated by about $10\,\mathrm{GHz}$ only. The Hyperfine (HF) splitting of the excited states are small and comparable to their natural linewidths of $\Gamma = 2\pi \cdot 5.87\,\mathrm{MHz}$ [122].
Compared to other alkalis, the ground state's HF splitting of $228.2\,\mathrm{MHz}$ is small as well. Because of this, the magnetic sublevels swiftly leave the linear Zeeman and enter the Paschen-Back regime, when exposed to an increasing magnetic field. The magnetic field dependent energy shift was calculated with the Breit-Rabi formula (see Fig. 3.1b). In high fields the electron and nuclear spin decouple. Here, the two orientations of the $S = 1/2$ spin dictate the high- or low-field seeking nature of the state. The reason for this is the dominating ($\approx \times 4500$ larger) g-factor of the electron spin compared to the one of the nucleus. In high fields the orientation of the $I = 1$ nuclear spin only contributes to an almost equal splitting between the states. Because it is field dependent, if the coupled or non-coupled quantum number set is best for describing the states, numerating them $|1\rangle$ to $|6\rangle$ with rising energy is commonly used.
By applying a magnetic field also the scattering lengths of the state mixtures are tunable. All three low field seeking mixtures: $|1\rangle{+}|2\rangle$, $|1\rangle{+}|3\rangle$, $|2\rangle{+}|3\rangle$ posses broad Feshbach resonances at around $800\,\mathrm{G}$ [123]. For intermediate fields of $300\,\mathrm{G}$ - $400\,\mathrm{G}$ they all show maxima in the absolute scattering length of varying magnitude. At zero field the scattering lengths for

---

[1] Standard notation: $n^{(2S+1)}L_J$

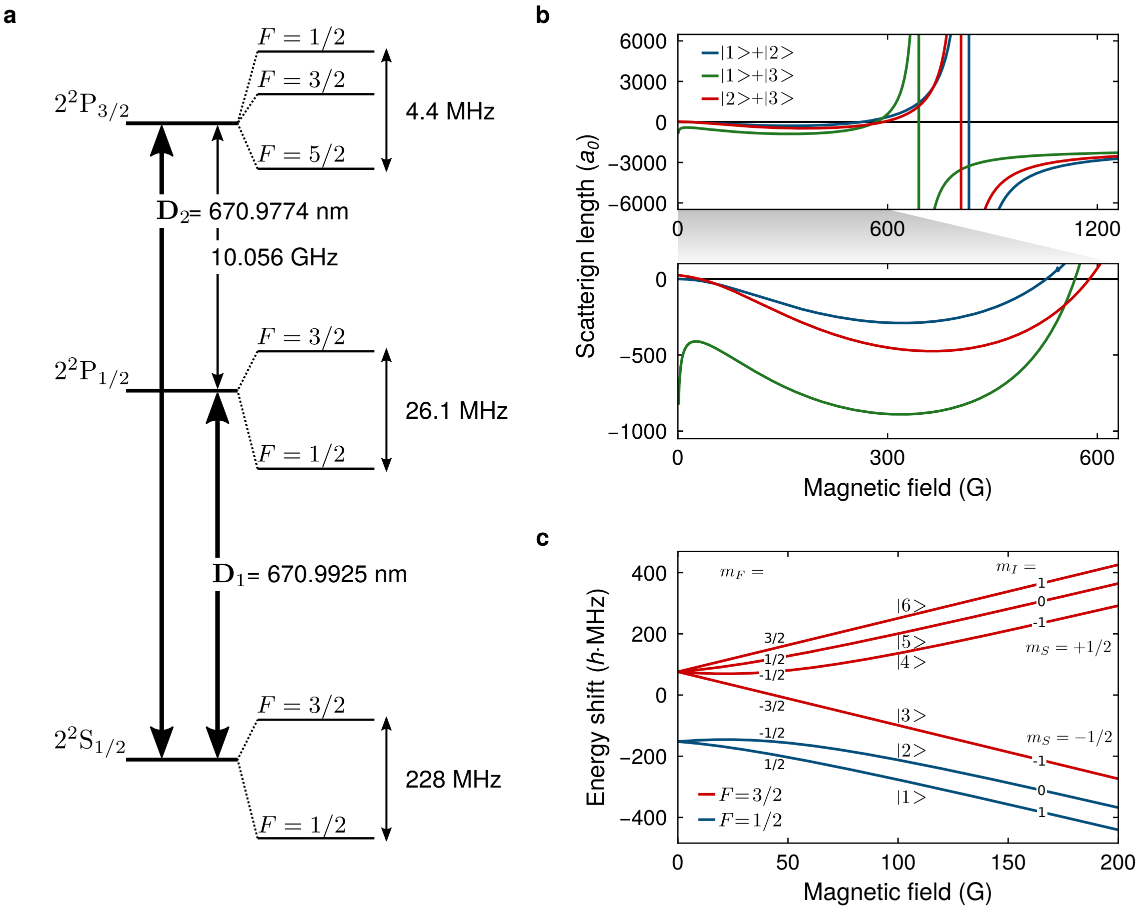

**Figure 3.1** **$^6$Li spectroscopic and B-field properties. a.** Fine- and hyperfine structure within the $^6$Li $D_1$- and $D_2$-lines. **b.** Feshbach spectrum of the three high-field seeking state mixtures taken from [123]. Zoomed view to the experimentally accessed interval. Here, the $|1\rangle + |3\rangle$ mixture shows a nonnegligible scattering length in the low field regime. **c.** Energy shift of the six magnetic substates of the $2^2S_{1/2}$ manifold. For low fields $m_F$ is still a good quantum number. As the field rises to the Paschen-Back regime, the nuclear and electronic spin decouple. The states $|1\rangle$ - $|6\rangle$ are used for field independent labeling.

$|1\rangle$+$|2\rangle$ and $|2\rangle$+$|3\rangle$ are basically vanishing, while for $|1\rangle$+$|3\rangle$ it exceeds $-500\,a_0$. The Bohr radius is denoted with $a_0$.

## 3.2 ErLi properites

The following sections provide a comprehensive overview of the properties of Er, Li, and an ErLi mixture. The aim is to identify both the differences and the similarities between the two elements, which are important for the experimental approach. Electron configurations of their respective ground states, their behavior in magnetic fields, and optical transitions commonly used for laser cooling are examined.

Erbium and lithium are elements of very different properties (see Table 3.1). With a mass of $166\,\mathrm{u}$, the lanthanide atom $^{166}$Er is approx. 28 times heavier than $^{6}$Li, whose mass is only $6\,\mathrm{u}$. To have sufficient vapor pressure for later experiments, different temperatures are required. This directly affects the technical design of their respective ovens.

### 3.2.1 Ground state configurations

The atomic properties of $^{6}$Li are well described by a single valence electron. The electron configuration of $^{166}$Er is much more complex [124]. The ground state configuration is given by $[\mathrm{Xe}]4\mathrm{f}^{12}6\mathrm{s}^{2}$. It is referred to as a *submerged-shell* configuration. $[\mathrm{Xe}]$ represents a filled shell xenon core. The 6s-orbital is filled up with two electrons. The 4f-orbital has the capacity to hold 14 electrons, but is only filled with 12, leaving two "missing".
The angular momentum coupling is more difficult than for $^{6}$Li, due to the high number of electrons. The total electronic angular momentum $J$ is given by the coupling of the two outer s-shell electrons and the others. In the ground state the orbital angular momentum quantum number is $L = 5$ (H-state), due to the LS-coupling of all electrons. With $S$ being the total electron spin, the (ground state) is given by

$$^{166}\mathrm{Er}: \quad {}^{3}\mathbf{H}_{6}, \text{ with}^{2}$$

$$L = 5, \quad S = 1, \quad J = 6.$$

Like all other bosonic erbium isotopes, $^{166}$Er has a vanishing total nuclear spin ($I = 0$) and therefore does not exhibit HF splitting. Compared to alkali and alkaline-earth atoms, $^{166}$Er has a very large angular momentum.
As for all other alkalis, the angular momentum of the ground state of Li vanishes ($L = 0$). However, the coupling of the valence electron spin with the non-vanishing nuclear spin $I$ leads to HF splitting of the ground state:

$$^{6}\mathrm{Li}: \quad 2^{2}S_{1/2}, \text{ with}$$

$$L = 0, \quad S = 1/2, \quad J = 1/2, \quad I = 1, \quad F = 1/2, 3/2.$$

### 3.2.2 Linear Zeeman shifts

The difference in total angular momentum between the $^{166}$ Er and $^{6}$Li ground state directly affects their respective sensitivity to magnetic fields. For low fields, in general the atomic magnetic moment is given by

$$\mu = m_i g_i \mu_B, \tag{3.1}$$

with the magnetic substate quantum number $m_i$, its associated Landé g-factor $g_i$ and the Bohr magneton $\mu_B \approx h \cdot 1.4\,\mathrm{MHz/G}$[3] [80]. The index $i$ represents the relevant angular momentum coupling ($^{6}$Li: $i = F$; $^{166}$Er: $i = J$).

---

[2] Notation: $^{(2S+1)}L_J$

[3] $\mu_B = e\hbar/2m_e$, with $e$: electron charge and $m_e$: electron mass

| Property | Symbol | $^{6}$Li | | $^{166}$Er | Ref |
|---|---|---|---|---|---|
| Melting point | $T_\mathrm{M}$ | 454 K | | 1802 K | [128], [129] |
| Boiling point | $T_\mathrm{B}$ | 1615 K | | 3173 K | [128], [130] |
| Mass | $m$ | 6.015 u | | 165.9 u | [131], [131] |
| Angular momentum | $L$ | 0 | | 5 | |
| Tot. electron spin | $S$ | $1/2$ | | 1 | |
| Tot. electronic ang. mom. | $J$ | $1/2$ | | 6 | |
| Tot. nuclear spin | $I$ | 1 | | 0 | [131], [131] |
| Tot. atomic ang. mom. | $F$ | $1/2$ | $3/2$ | - | |
| Spin g-factor | $g_S$ | 2 | | 2 | [132], [132] |
| Total electronic g-factor | $g_J$ | 2 | | 1.16 | [126] |
| Nuclear g-factor | $g_I$ | $-0.448\cdot10^{-3}$ | | 0 | [132] |
| | **Substate** | $m_F = \pm1/2$ | $m_F = -3/2$ | $m_J = -6$ | Unit |
| Total atomic g-factor | $g_F$ ; $g_J$ | $-2/3$ | $+2/3$ | $+1.16$ | |
| Magnetic moment | $\mu$ | $\mp1/3$ | $-1$ | $-7$ | $\mu_\mathrm{B}$ |
| Lin. Zeeman shift | $\Delta E/B$ | $\mp0.47$ | $-1.4$ | $-9.77$ | $h$·MHz/G |
| Levitation gradient | $dB/dx$ | $\mp3.16$ | $-1.05$ | $-4.17$ | G/cm |

**Table 3.1** Ground state properties of $^{6}$Li and $^{166}$Er.

The standard angular momentum coupling techniques apply very well to the ground state of $^{6}$Li [125]. For $F = 1/2$ the magnetic substates g-factor is $-2/3$. The magnetic moment of its $m_F = \pm1/2$ magnetic substates is $\mp1/3\mu_\mathrm{B}$. For $F = 3/2$ the magnetic substates g-factor is of opposite sign: $+2/3$ and for the stretched state with $m_F = -3/2$ the magnetic moment is $-1\mu_\mathrm{B}$.

It is harder to obtain the exact g-factor of Er due to the many contributions of its electrons to the total angular momentum and its high mass[4] [126]. Experimentally it was found that $g_J = 1.16$ [127]. This results in a large magnetic moment of $-7\mu_\mathrm{B}$ for the energetically lowest magnetic substate $m_J = -6$. Due to the high energy associated with the fine structure of $^{166}$Er, the Zeeman shift remains linear up to fields of several hundred Gauss [126].

The high mass of $^{166}$Er makes it difficult to hold against gravity in optical dipole traps. This places unwanted constraints on the geometry of these traps. However, magnetic levitation using a magnetic gradient field acting in opposite direction overcomes this restriction. This is achieved already for a moderate (vertical) gradient of $dB/dx = \frac{mg}{\mu} \approx -4.2\,\mathrm{G/cm}$, due to its large magnetic moment. Here, $m$ is the mass of the atom and $g$ the gravitational acceleration[5].

Applying the same formula to Li, one finds for the $m_F = \pm1/2$ ground state a magnetic gradient field of similar magnitude: $\mp3.2\,\mathrm{G/cm}$. For the $m_F = -3/2$ ground state a gradient of only $-1.1\,\mathrm{G/cm}$ is sufficient.

---

[4] The correction to the standard coupling approach is about $1\%$.

[5] Used: $g = 9.81\,\mathrm{m/s^2}$

### 3.2.3 Laser cooling properties

In Fig. 3.2 the level systems of $^{166}$Er and $^{6}$Li are presented. It shows a striking difference in the number of optical transitions of the two. In the following, selected transitions and their properties for laser cooling are discussed.

The final temperatures achieved through laser cooling on these transitions are determined by the wavelength $\lambda$ and, in particular, the linewidth $\Gamma$, respectively the lifetime $\tau = {}^{1}\!/\Gamma$ of the excited state. The Doppler temperature $T_\mathrm{D} = \frac{\hbar\Gamma}{2k_\mathrm{B}}$ and the associated Doppler velocity $v_D = \sqrt{2k_\mathrm{B}T_\mathrm{D}/m}$ are usually the limits of molasses cooling, which often are employed in the first steps of a cooling process. It is reached, when Doppler cooling and heating due to spontaneous emission balance. This temperature limit is solely determined by the width of the transition. The recoil temperature $T_r = \frac{h^2}{mk_\mathrm{B}\lambda^2}$ is associated to the momentum transfer of a single spontaneous emission process. In this case, only the mass of the atom and the energy of the photon are relevant. The associated recoil velocity is given by $v_r = h/m\lambda$. For sub-Doppler cooling techniques such as Sisyphus cooling, the recoil temperature provides the lower bound of temperatures achievable [80]. The heavier the atom and the lower the transition energy, the smaller the heating effect of a single recoil kick [80].

*Erbium:* Erbium's complex electron configuration results in many optical transitions. Some of them exhibit closed cycling transitions, that are well-suited for Magneto-Optical Traps (MOTs) and optical cooling in general. The various transitions vary widely in strength and can be exploited to achieve efficient optical cooling from different initial temperatures.

Of the many optical transitions, three are particularly well-suited for laser cooling of $^{166}$Er (see Table 3.2). A broad transition of about $30\,\mathrm{MHz}$ at $401\,\mathrm{nm}$ (blue) is ideal to cool the atoms down from initially high temperatures. The maximum scattering rate on a transition can never exceed $\Gamma/2$. Therefore, wide transitions are ideal for cooling atoms quickly. Transitions in the blue spectral range are also advantageous here, because the energy transferred per scattering event is higher than in the red. On the other hand, a disadvantage of cooling with wide transitions is the inherent increase in the heating rate due to spontaneous emission and the resulting minimum temperature to be reached. Therefore, cooling on this blue transition is commonly used for the first cooling steps like Zeeman Slowing, transversal cooling [124, 133] and angled slowing [134].

Having the atoms already slowed down by cooling on the blue transition, the cooling process can be continued on a more narrow line. The transition of Er with a linewidth of $186\,\mathrm{kHz}$ at $583\,\mathrm{nm}$ in the yellow spectral range is well suited for this. It is about $\times 150$ more narrow than the blue transition and has therefore a $\times 150$ lower Doppler temperature of only $4.6\,\mu\mathrm{K}$. In our ErLi experiment, Zeeman slowing and angled slowing is performed on the blue, and the MOT is employed on the yellow transition [74].

From this point onwards its seems straightforward, that cooling further on smaller and smaller transitions is favorable to achieve lower and lower temperatures. In fact, for narrow-line[6] MOTs [135], the recoil temperature sets a hard limit on the minimum temperature achievable. Therefore, cooling on transitions with a linewidth, that falls below this threshold is not beneficial. Also, the influence of gravity gets relevant for increasingly narrow transitions. If the maximum scattering force does not overcome the gravitational force, a

---

[6] The term *narrow-line* refers to the linewidth of a transition being similar to the associated single recoil frequency: $\Gamma/\omega_r \sim 1$ [135].

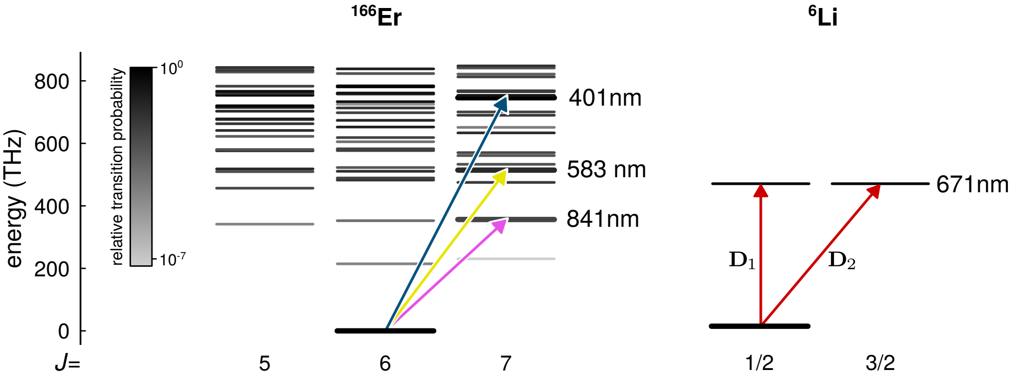

**Figure 3.2 Er and Li level system** Energy level system of $^{166}$Er [103] and $^{6}$Li. Higher energy levels and the HF splitting for Li are omitted. Transitions used for laser cooling are highlighted. Their properties are listed in Table 3.2. For $^{166}$Er the gray level represents the relative transition probability with respect to the strongest line at $401\,\mathrm{nm}$.

MOT can not be employed on that line.
In the end, the next experimental step after the MOT, is to transfer the atoms to an Optical Dipole Trap (ODT). Here, spatially varying light shifts generally influence the efficiency of this loading process. For these reasons, it was a priori not clear whether further cooling on the $8\,\mathrm{kHz}$ line of $^{166}$Er at $841\,\mathrm{nm}$ and the subsequent loading of an optical dipole trap is advantageous for our system. A test implementation has shown that it has no advantage over the yellow MOT for our dipole trap setup [136].

*Lithium:* Laser cooling of $^{6}$Li is performed on the $D_1$- and $D_2$-lines at $671\,\mathrm{nm}$. The MOT operates on the $D_2$: $2^2S_{1/2}$ $F = 3/2$ $m_F = 3/2$ to $2^2P_{3/2}$ $F = 5/2$ $m_F = 5/2$ transition, called the cooling transition. During the cooling process on this line, the atoms would eventually end up in the ground state $F = 1/2$ manifold and are therefore lost. For this reason a repumper beam exciting from those states is needed to keep the atoms in the cooling process. In fact, for $^{6}$Li its contribution to the optical power required to maintain efficient cooling is in the range of 1/3.
For many alkali atoms including Na, Rb, and Cs operating a MOT on the $D_2$-line finds even lower (sub-Doppler) temperatures [48]. The multi-level character of these atoms allows the implementation of polarization gradient cooling, also known as Sisyphus cooling. Here, temperatures close to the recoil limit $\sim 10\,\mu\mathrm{K}$ are achieved. This cooling effect requires the linewidth of the transition to be smaller than the HF splitting. For $^{6}$Li this condition is not met. With a linewidth of $\Gamma = 2\pi \cdot 5.87\,\mathrm{MHz}$, the $2^2P_{3/2}$ HF splitting is only $4.4\,\mathrm{MHz}$. This restricts the minimum temperature, that is typically reached to around $300\,\mu\mathrm{K}$. For $^{6}$Li there is also a more narrow transition, for which compressed Magneto-Optical Trap (cMOT) temperatures of $59\,\mu\mathrm{K}$ have been demonstrated [87]. The $2^2S_{1/2} \to 3^2P_{3/2}$ transition with a natural lifetime of $\Gamma_{3\mathrm{P}} = 2\pi \cdot 754\,\mathrm{kHz}$ is at $323\,\mathrm{nm}$. Generating and handling the required laser light in the UV is technically challenging [137]. For this reason, the Gray Molasses (GM) technique employed on the $D_1$-line is a popular for cooling for $^{6}$Li. It reaches temperatures of $\sim 50\,\mu\mathrm{K}$ and below. It is demonstrated and discussed in more detail in Section 6.2.

| Property | Symbol | Unit | $^{6}$Li | $^{166}$Er | | |
|---|---|---|---|---|---|---|
| Wavelength | $\lambda$ | nm | 671 | 401 | 583 | 841 |
| Linewidth | $\Gamma$ | $2\pi\cdot$ | 5.87 MHz | 29.7 MHz | 186 kHz | 8.0 kHz |
| Lifetime | $\tau$ | ns | 27.1 | 5.35 | 857 | $19,894$ |
| Doppler temperature | $T_{\mathrm{D}}$ | $\mu$K | 138 | 714 | 4.6 | 0.19 |
| Doppler velocity | $v_{\mathrm{D}}$ | $\mu$m/ms | 625 | 267 | 21 | 4.4 |
| Recoil temperature | $T_{\mathrm{r}}$ | nK | $3,536$ | 717 | 339 | 163 |
| Recoil velocity | $v_{\mathrm{r}}$ | $\mu$m/ms | 99 | 6.0 | 4.1 | 2.9 |

**Table 3.2** Laser cooling properties of various transition for $^{6}$Li [121] and $^{166}$Er [124, 138, 139].

### 3.2.4 Feshbach resonances

For a stable mixture of $^{166}$Er and $^{6}$Li the intra- and interspecies elastic and inelastic scattering properties have to be considered. The elastic scattering properties can be tuned by means of magnetic Feshbach resonances. However, three-body loss channels are also addressed through the same means.

For Er, a spin-polarized system with atoms in the energetically lowest substate $m_J = -6$ is considered only, since other mixtures suffer from dipolar losses [112]. Compared to alkalis, the Feshbach spectrum of Er is very rich in resonances [140]. Er already exhibits more than ten resonances below $10\,\mathrm{G}$, but not all resonances are suitable to tune interactions for efficient evaporative cooling to quantum degeneracy. In BECs the atomic density is very high, making it prone to three-body losses and accompanied heating [141]. Three-body losses are parametrized by the loss coefficient $L_3$ in $\dot{n}(r) = -L_3 n^3(r)$. In [62] three-body losses below $4.1\,\mathrm{G}$ were investigated. In this interval there are three Feshbach resonances at $0.02\,\mathrm{G}$, $3.04\,\mathrm{G}$ and $4.08\,\mathrm{G}$ [142]. Here six additional narrow three-body loss features were reported. This restricts the fields for which condensation is achievable to around two values: $B_1 = 1.4\,\mathrm{G}$ with a scattering length of $a_1 = 73\,\mathrm{a}_0$ and $B_2 \approx 2\,\mathrm{G}$ (also found in [143]) with $a_2 = 80\,\mathrm{a}_0$. For these two fields $L_3 = 4 \cdot 10^{-12}\,\mu\mathrm{m}^6/\mathrm{s}$ were found. For a typical density of $500\,\mu\mathrm{m}^{-3}$ a $1\,\mathrm{s}$ lifetime with $\tau = n^2/L_3$ is obtained.

The Feshbach spectrum for a two component spin-mixture of Li was already presented in Fig. 3.1. In a gas of spin-polarized Li, interactions among the atoms are Pauli blocked. In a mixture of spin-polarized Li in $|1\rangle$ or $|2\rangle$ and Er, Feshbach resonances have been theoretically and experimentally investigated. For Li in $|1\rangle$ two broad ($> 1\,\mathrm{G}$) Feshbach resonances at $\approx 20\,\mathrm{G}$ and $\approx 80\,\mathrm{G}$ have been predicted [144]. These resonances were experimentally not observed in a mixture in the thermal regime [145]. Here, no Feshbach resonance[7] below $19\,\mathrm{G}$ and 32 narrow ones ($< 300\,\mathrm{mG}$) for fields up to $660\,\mathrm{G}$ were reported. For Li in $|2\rangle$ no Feshbach resonances below $13\,\mathrm{G}$ were observed. In contrast to the mixture, where the two species are in their absolute ground state—among many narrow ones—three broad resonances were found at: $57\,\mathrm{G}$ with $1.7\,\Delta\mathrm{G}$, $247\,\mathrm{G}$ with $4.2\,\Delta\mathrm{G}$ and $259\,\mathrm{G}$ with $3.2\,\Delta\mathrm{G}$. S-wave scattering length between Er and Li have not been measured yet. In [144] about $25\,\mathrm{a}_0$ for Li in $|1\rangle$ and Er in $m_J = -6$ is predicted for low fields. In a mixture experiment of bosonic $^{7}$Li and $^{166}$Er a scattering length of $103 \pm 13 a_0$ was reported at an offset field of $1.3\,\mathrm{G}$ [146].

---

[7] Resolution of $\leq 60\,\mathrm{mG}$

### 3.2.5 Heavy-light mixture

The extreme mass imbalance of factro $28$ leads to a different response of Er and Li for the same experimental conditions. In a thermalized system, the mean thermal velocity of Li is about five times larger than for Er. The same is true for the trap frequencies of the two for equal polarizabilities. Thermalization is affected by the mass imbalance as well. For two gases of temperature $T_1$ and $T_2$ and mass $m_1$ and $m_2$ the average energy transfer per collision is given by [147]

$$\Delta E_{1\to 2} = \xi k_B (T_1 - T_2) \quad \text{with} \quad \xi = \frac{4 m_1 m_2}{(m_1 + m_2)^2}. \tag{3.2}$$

The “penalty” factor $\xi$ represents the reduction in energy transfer compared to a mass balanced mixture. For ErLi, the transfer is reduced by almost one order of magnitude: $\xi = 0.135$. In free space $1/\xi \approx 7.4$ also gives the increase factor in collisions and time needed to achieve thermalization.

Luckily, in a harmonic trap environment the reduced mass of Li positively influences the trap frequency and with this speeds up the thermalization process. While on average still $1/\xi$ more collisions are needed for thermalization, the thermalization time only scales as $1/\sqrt{\xi}$. Therefore, the thermalization time increases by $1/\sqrt{\xi} \approx 2.7$ only, for Er and Li in a harmonic potential.

To conclude, Er and Li show a separation of scale in many properties: mass, widths and number of Feshbach resonances, variation in line strengths, number of optical transitions and magnetic moments. In a mixture of Er and Li, these differences can be made use of for differential control of the two species.

# Chapter 4

# Vacuum system

## 4.1 General outline

The general design of the vacuum system consists of two independent and connected single-species machines equipped with a glass cell for high optical access. During the planning phase, we found that the magnetic properties of Er and Li were too different to use the same Zeeman slowing and MOT gradient fields for efficient loading at the same time. For this reason, the two MOT regions are separated by half a meter, which allows for independent operation with minor magnetic crosstalk. As shown in Fig. 4.1, both single species sections contain the same stages. They are adapted to the respective needs for efficient cooling of the element. The two sections are now coarsely presented to get an initial overview of the complex system.

The Li and Er sections both start with an oven stage. Er requires a commercial oven, reaching temperatures up to $1450\,^{\circ}\mathrm{C}$. It consists of an effusion cell and a hot lip. For a sufficiently high atom flux, the Li oven only runs on temperatures of about $350\,^{\circ}\mathrm{C}$. Therefore, a homebuilt design was possible. Both ovens are mounted on port-aligners allowing to set their orientations after the vacuum is already closed.

A pre-cooling stage follows up each oven stage. Here, CF40 vacuum cubes allow for optical access to the atomic beams emerging from the ovens. Additionally, the Li part possesses coils to control the magnetic fields in all three directions at that point.

The next stage used for vacuum pumping and isolation from the main experiment is identical for the two. It consists of another CF40 vacuum cube holding a large $55\,\mathrm{L/s}$ ion pump and a titanium sublimation tower. It also possesses an angle valve for connecting turbo pumps and a gate valve to isolate the oven regions from the main chamber.

The Zeeman slower and MOT stage starts with a long vacuum tube sticking through the main Zeeman slower coils, providing a differential pumping stage. The MOT chambers of the two elements are almost alike again. They are part of a single piece custom-made vacuum chamber. Both MOT chambers are equipped with the same set of coils. Additionally, the Li MOT chamber possesses a bigger pair of MOT coils required for a combined Zeeman Slowing (ZS) and MOT field. The main chamber is equipped with two vacuum pumps, that provide pressure in the low UHV regime.

Opposite to the entrance direction of the atoms to the main chamber, a small tube leads the way out of it again. It connects to a vacuum cross piece, which hosts a viewport and a mirror to reflect the light for ZS into the vacuum tube. On top of the so called Zee. cross a small $20\,\mathrm{L/s}$ ion pump is placed.

The final experiments are performed in the vacuum part of the science chamber consisting of a glass cell. Its center, together with the centers of the MOT chambers, define the transport

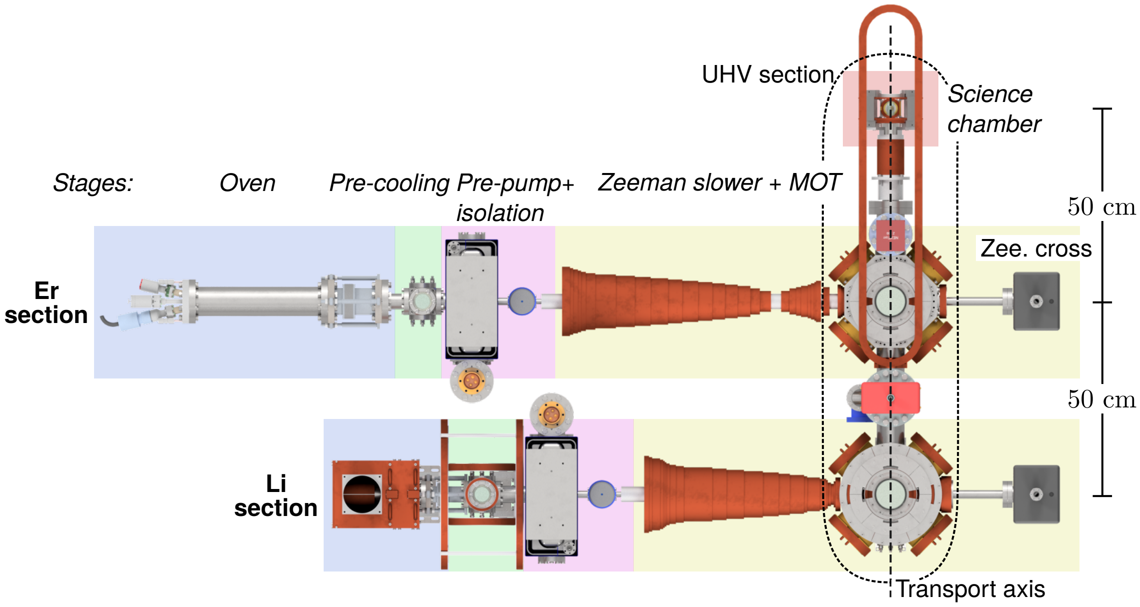

**Figure 4.1** **Top view of the ErLi machine.** Render of the vacuum system with coils attached to it. The Er and Li sections are split into different stages indicated by color. These stages are very similar, but adapted to the specific requirements needed to cool each species. The center of the MOT chambers are aligned to the glass cell by the transport axis.

axis of the atoms. On the Li chamber side, the transport axis is optically accessed through the transport viewport. The science chamber is equipped with offset coils, a pair of Feshbach coils and a pair of gradient coils. Beneath the glass cell a high NA objective is already installed for future experiments.

## 4.2 Lithium section

In the following, the different stages of the Li vacuum section of the apparatus are presented. Here, all ingredients needed, to provide an initial cold cloud of Li are described. This then marks the starting point of all further experimental steps. The order of presentation follows the atoms' path from the oven to the MOT.
The design of the stages are based on their intended purpose to provide a good vacuum environment and to in the end provide the Li cloud. For this reason, the two are described hand-in-hand and together with the physics to understand the working principles of their laser cooling steps. The experimental parameters for the initial generation of the cold Li cloud are static, but the large number of fine-tuned parameters result in a complex system. The basic cooling steps are therefore presented here, separated from the various following experimental steps presented in Chapter 6. The generation of the laser beams needed is described in the following Chapter 5.
The presentation of every stage starts with the description and motivation of its vacuum setup design and its general role in the system. Subsequently, its properties regarding optical cooling are explained, and its performance is characterized.

### 4.2.1 Li oven

The Li oven is a new design for the ErLi experiment (see Fig. 4.2). It is made out of stainless steel and follows the typical reservoir + nozzle architecture. The reservoir is filled with $13\,\mathrm{g}$ of enriched $(95\%)$ $^6$Li [1]. A copper cap encloses the reservoir from the outside. It is used for efficient heat transfer from an enclosing commercial heat clamp and the reservoir body. The reservoir operating temperature typically is $T = 350\,^\circ\mathrm{C}$ and not actively stabilized.
At that temperature Li is liquid and accumulates initially at the bottom of the reservoir. The gas pressure of Li is $p \approx 10^{-5}\,\mathrm{mbar}$ here [125]. Applying the ideal gas law $p = nk_\mathrm{B}T$, the number density of $n \approx 10^{11}\,\mathrm{cm}^{-3}$ is obtained. With an atomic diameter of $d_0 \approx 300\,\mathrm{pm}$ [148], the mean free path between two successive collisions of Li atoms is $l = (\sqrt{2}\pi n d_0^2)^{-1} \approx 50\,\mathrm{m}$ [149]. Therefore, atomic motion of Li in the gas phase is dominated by ballistic motion and collision with the inner vacuum surfaces. For a $50\,\mathrm{K}$ higher reservoir temperature, the number density and with this the atomic flux increases by about one order of magnitude.
Inside the reservoir the velocity $(v)$ distribution of the Li atoms is given by the 3D Boltzmann distribution:

$$p(v) = \sqrt{\frac{2}{\pi}} \left(\frac{m}{k_\mathrm{B}T}\right)^{3/2} v^2 e^{\frac{-mv^2}{2k_\mathrm{B}T}}, \tag{4.1}$$

with $m$ being the mass. Inside the reservoir the most probable velocity is $v_{mp} = \sqrt{2k_\mathrm{B}T/m} \approx 1310\,\mathrm{m/s}$.
The atoms leave the reservoir through a tungsten nozzle with an inner diameter of $10\,\mathrm{mm}$ and a length of $140\,\mathrm{mm}$. It provides collimation of the atomic beam with a geometric opening angle of $\sim 8\,^\circ$. A heat clamp with an efficient heat transfer by a copper ring is employed to keep the nozzle temperature on $400\,^\circ\mathrm{C}$. The most probable velocity of the atoms, that are re-emitted from the inner nozzle surface is $\sim 1360\,\mathrm{m/s}$, which is still similar to the one of the reservoir. Clogging of the nozzle is intended to be prohibited by the temperature difference to the reservoir. The thermal conductivity of tungsten is about one order of magnitude higher than that of the other stainless steel parts [150]. The high thermal conductivity material was chosen to ensure a minimal temperature drop towards the end of the nozzle, preventing cold spots, where Li accumulates.
It is well known, that copper gaskets get leaky due to chemical reactions when in contact with even small amounts of Li. For this reason CF gaskets made out nickel[2] were employed for the flange connection to the oven and all other flange connections the atoms pass on their way to the chamber. As an additional safety measure, the nozzle of the oven sticks out further than the connecting flange, to have no line of sight to the inside of it.
For thermal stability of the final experimental setup, the oven is wrapped in isolation material and placed inside a water cooled housing. In day-to-day operation the oven has proven to be a reliable source. No sign of an emptying reservoir has been observed for an operation time of $4$ years. We observed only minor heat transfer between the reservoir and nozzle, which provides almost independent temperature control of the two. Keeping the nozzle temperature $50\,\mathrm{K}$ above the one of the reservoir has proven to keep an open nozzle and provide an unaltered atom flux. The refilling procedure of the Li oven and pictures of the final setup are detailed in Section A.1

---

[1] Sigma-Aldrich, 340421-10G

[2] MDC Vacuum Ltd NG16 and NG40

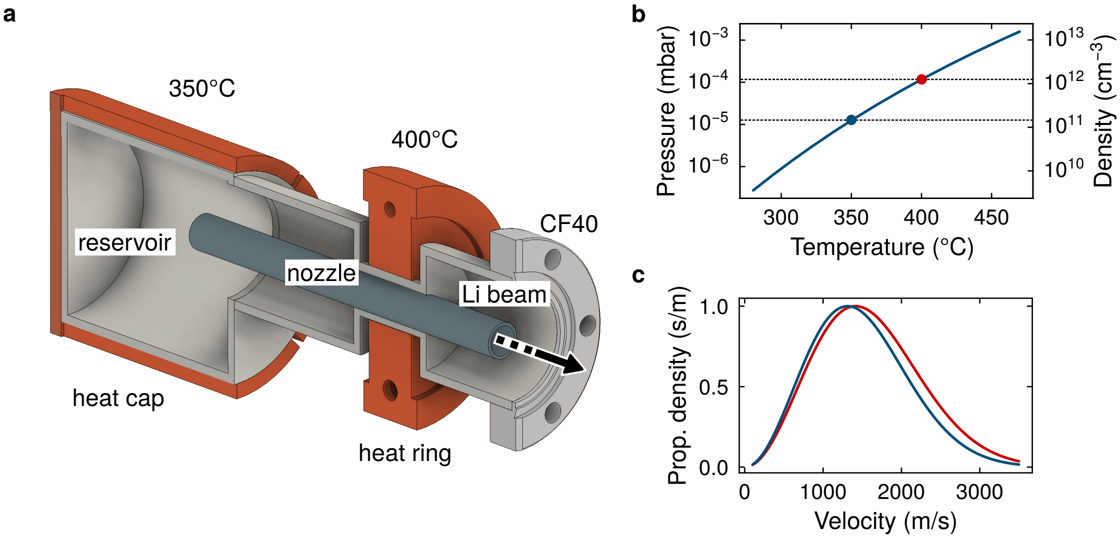

**Figure 4.2 Li oven properties. a.** Cut view of the Li oven. It is divided into two temperature zones, which are heated by individual heat clamps. The reservoir zone filled with Li is heated to $350\,°\mathrm{C}$. The atoms leave the reservoir through a tungsten nozzle, which is heated to $400\,°\mathrm{C}$ to prevent clogging. The rest of the vacuum parts are made out of stainless steel. Heat clamps, heat shields housing and isolation material are not shown here. **b.** Gas pressure and density of Li with respect to the temperature. The two curves basically overlap. The working points of reservoir (blue) and the nozzle (red) are marked with dots. **c.** Boltzmann velocity distribution for a gas of Li at $350\,°\mathrm{C}$ (blue) and $400\,°\mathrm{C}$ (red). For convenience the probability density distributions are normalized.

### 4.2.2 Optical pumping / transversal cooling stage

Refilling an empty oven is a time-consuming event, that hinders the continuous operation of the experiment for days. Furthermore, obtaining precise knowledge of the current filling level requires considerable effort. Efficient usage of the atomic source is therefore advisable. Common MOT loading rates of $10^7\,\mathrm{s}^{-1}$ to $10^9\,\mathrm{s}^{-1}$ are multiple orders of magnitude lower, than a constant effusion rate of $\sim 10^{15}\,\mathrm{s}^{-1}$ for a $1\mathrm{mol}$ sample over a $10$ years run time. Even though, catching each and every atom is far from being realistic and not even needed, there is plenty of room for improvement. In the following a technique, which consists of optical pumping and transversal cooling of the atomic beam near the oven is presented. Applying it, an increase of the usable flux of the oven by one order of magnitude is demonstrated. For Li, this is a promising non-standard approach for an efficient usage of the atomic source. The technique lends its name to the pre-cooling stage in which it is used.

The Optical Pumping / Transversal Cooling (OP/TC) stage connects directly to the oven via a CF40 port aligner[3] (see Fig. 4.3a). The stage itself consists of a CF40 vacuum cube[4] with viewports[5] coated for $671\,\mathrm{nm}$ light. It allows for optical access to the atomic beam in vertical and horizontal direction. An in-vacuum aperture with a central opening of $10\,\mathrm{mm}$ mounted on groove grabbers[6] reduces coating of the vacuum system with Li.

A large pair of coils in Helmholtz configuration with a radius of $178\,\mathrm{mm}$ is centered to the

---

[3] Pfeiffer 420MPA040

[4] Kimball MCF275-SphCube-C6

[5] Hositrad HOVPZ38Q

[6] Kimball MCF275-GrvGrb-C02

vacuum cube and aligned to the longitudinal direction of the atomic beam. With individual current control of the two coils, it allows for precise compensation of the Zeeman slower field (both offset and gradient), that extends into this area with several Gauss. Magnetic offset fields in the vertical and horizontal direction are compensated by two pairs of smaller coils. The vertical / horizontal coils have a radius of $37\,\mathrm{mm}$ / $85\,\mathrm{mm}$ and are offset by $133\,\mathrm{mm}$ / $144\,\mathrm{mm}$ from each other. Due to lack of space they do not obey the Helmholtz condition.

The initial consideration, that lead to the planning of the stage presented here was the fact, that only one of the six equally populated sublevels of the $^2S_{1/2}$ ground state is addressed in the Zeeman slowing process. Optical pumping the ground state population to the only addressable state therefore holds the chance of increasing the usable flux by a factor of up to six. Exposing the atoms with $\sigma^+$-light on the cooling and repumping transitions of the $D_1$-line in principle transfers the atoms to the $|F = 3/2, m_F = 3/2\rangle$ dark state, which is used for slowing (see Fig. 4.3b). To achieve this, only a couple of scattering events are needed. Addressing the atoms perpendicular to their much faster longitudinal direction of motion requires adiabatic turning of the magnetic field in the transversal direction. The need for precise field control was the reason for the installation of the 3 three coil pairs in this section.

The initial attempt was to increase the usable flux by pumping the atoms with a single pass beam in the horizontal direction. As a measure for this the MOT loading rate was considered. The beam used was enlarged to a waist of $7.5\,\mathrm{mm}$ in the longitudinal (horizontal) direction to have a long interaction distance and to a vertical waist of $3.25\,\mathrm{mm}$ to cover the radial spread of the atomic beam. For optimized beam power, detuning, polarization and magnetic fields a maximum increase in the MOT loading rate of only factor $1.3$ was found. Adding and aligning a retro reflection mirror to the single pass beam setup helped to increase the MOT loading rate by a factor of $2.5$. The idea was to balance the recoil kicks from optical pumping to minimize deflection of the beam.

At the same time, it was found that having the beams slightly red detuned brings the best results, meaning that there is also an optical molasses effect which cools the transversal velocity component. This motivated the installation of the same setup on the vertical direction as well.

Collimating the atomic beam by cooling the transversal velocity component decreases the cross-section and therefore enhances the usable flux of it in the following stages [151]. Considering the geometry of the setup (see Fig. 4.3c), the ratio of the cross-section $A_0$ of the uncollimated atomic beam at the start of the Zeeman slowing stage to the cross-section of the collimated beam $A_1$ is:

$$\frac{A_0}{A_1} = \left(\frac{l_0}{l_1}\right)^2 \approx 10.8. \tag{4.2}$$

This ratio marks an upper bound for the maximum achievable increase of the flux by transversal cooling. Here $l_0$ / $l_1$ represent the distance of the nozzle center to the beginning of the Zeeman slower / the center of the OP/TC stage. After careful optimization, an increase of the MOT loading rate by a factor of $10.8$ was achieved. Crucial for this one order of magnitude enhancement was the precise control of the magnetic field in that region. The enhancement is less than half for an uncompensated ambient field condition, which is dominated by the nearby Zeeman slower coils.

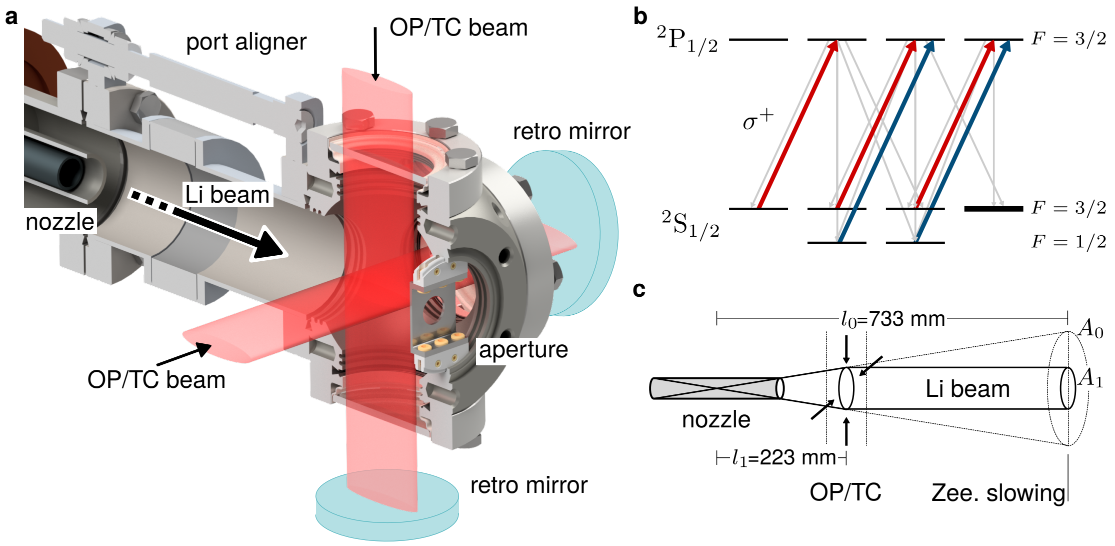

**Figure 4.3** **Optical pumping stage.** **a.** Render of the vacuum parts and laser beams of the OP/TC stage. The preceding oven stage is cut away for visibility. **b.** Optical pumping into the $|F = 3/2, m_F = 3/2\rangle$ (bold) ground state by $\sigma^+$-light on the $D_1$-line. The red and blue arrows indicate the pumping light and the gray arrows the channels of spontaneous decay of the excited states. **c.** Sketch of the geometry relevant to estimate the reduction of the atomic beam cross-sections $A_1$ and $A_2$ at the start of the Zeeman slower stage by collimating it in the OP/TC stage.

The best enhancement factor of 10.8 was found for a detuning $\Delta \approx -\Gamma/2$ from the $^2P_{1/2}$, $F = 3/2$ line (see Fig. 4.4a). A reduced enhancement of factor 5.7 was obtained for a similar detuning from the other $^2P_{1/2}$, $F = 1/2$ line. Going blue detuned, the MOT loading rate is strongly reduced and shows a reduction by almost one order of magnitude for $\Delta \approx +\Gamma/2$. This is due to a further spread of the atomic beam by transversal heating. For further blue detuning this effect vanishes. In between the enhancement maxima the competition of a red and blue detuned molasses from the two $D_1$-line transitions result in strong fluctuations of the enhancement factor. Testing individual detunings for cooler and repumper beam lead to a reduction in the enhancement factor only.

Even though, the laser beams were expanded a lot (see Fig. 4.4b) a central intensity of $\approx 3 \cdot I_{\mathrm{sat}}^{\mathrm{D1}}$ with $I_{\mathrm{sat}}^{\mathrm{D1}} = 7.59\,\mathrm{mW/cm^2}$ for cooler and repumper was provided per axis. Characterization of the enhancement factor for different intensities shows saturation for both cooler and repumper for our maximally available power (see Fig. 4.4c).

A final conclusion on the individual contributions of optical pumping and transversal cooling on the enhancement is hard to give. Precise analysis as done for a Dy [152] machine is beyond the scope of this work. Nevertheless, it is reasonable to attribute the main effect to the contribution of the transversal cooling. Here, the typical result of the best performance for e.g. $\approx \Gamma/2$ red detuned laser beams as for Er [124, 133], Cs [153], Sr [154] were obtained. As the initial attempt of optical pumping alone only lead to a small increase in the loading rate, its contribution in the final two axis configuration is expected to be small as well.

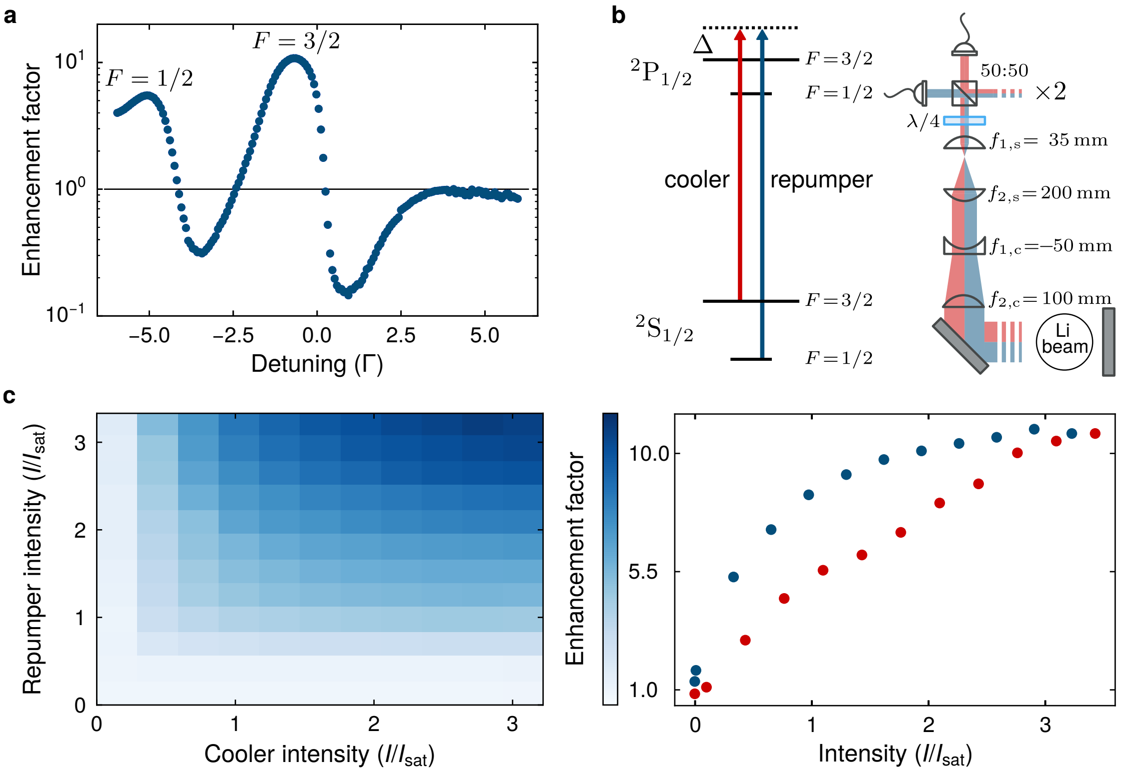

**Figure 4.4** **OP/TC performance. a.** Enhancement factor of the MOT loading rate with respect to the detuning from the $^2P_{1/2}$, $F = 3/2$ line. The two maxima are separated by the HF splitting of the excited $^2P_{1/2}$ state. **b.** Energy level system of the $D_1$-line and schematic of the optical setup used to provide the OP/TC beams on the experimental table. **c.** Left: Enhancement factor with respect to the central intensity of the cooler and repumper beam. Right: Enhancement factor for varying cooler (red) or repumper (blue) intensities with the other set to the maximum value.

As listed in the paragraph before, transversal cooling is often associated with high mass atoms such as Er and Sr. They exhibit broad $30\,\mathrm{MHz}$ lines, which are ideal for cooling from high initial velocities in a short amount of time. The maximum scattering is about $5$ times faster than for Li. On the other hand, cooling of Li benefits from the low mass with a higher recoil velocity ($\propto (m\lambda)^{-1}$). Compared to Er, Li requires $17$ times less scattering events for the same reduction in velocity. In the end, many more factors such as the geometry of the apparatus and initial collimation of the atomic beam determine the efficiency of a transversal cooling stage. With the short considerations done before, and the measurements presented, applying the transversal cooling technique to increase the usable atomic flux is beneficial also for light atoms.

### 4.2.3 Prepumping and isolation stage

The prepumping and isolation stage presented in Fig. 4.5 marks the end of the high vacuum pressure zone ($< 10^{-8}\,\mathrm{mbar}$) dominated by the out gassing of the hot oven. A gate valve[7] allows isolating it from the UHV zone ($\lesssim 10^{-11}\,\mathrm{mbar}$) of the MOT and science chamber.

---

[7] VAT 48124-CE01-0001

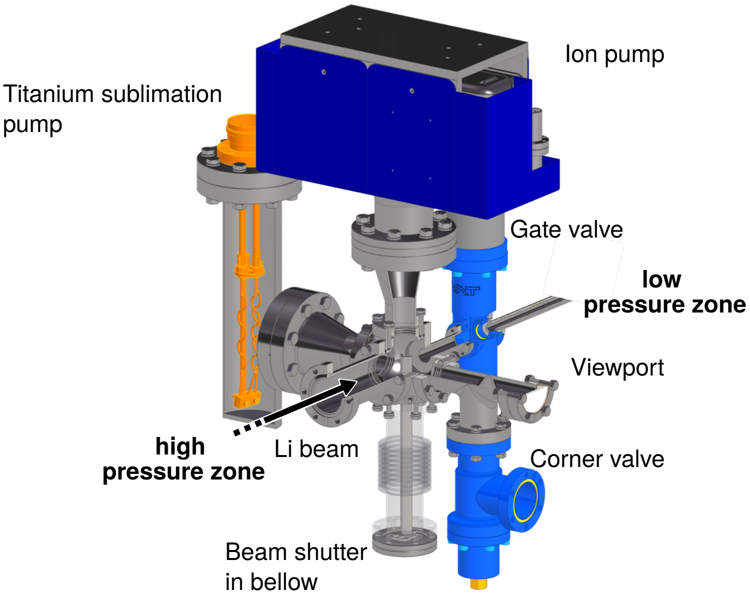

**Figure 4.5 Prepumping and isolation stage.** See Section 4.2.3 for detailed description.

Dividing the vacuum apparatus in subsystems allows for breaking the vacuum in one part without affecting the other. This is particular useful for e.g. refilling the oven. The other (angle) valve[8] connects the vacuum system to the outside world. Here, the turbo pump is connected for e.g. the bake-out procedure.

The stage possesses two vacuum pumping units: a $55\,\mathrm{l/s}$ ion pump[9] and a Titanium Sublimation Pump (TSP)[10]. The large ion pump has a high pumping speed and a high total capacity, which is required here. The information about the pressure of the stage is obtained from its controller[11]. The conically shaped vacuum tube ensures a good connection to the rest of the vacuum system.

The TSP is connected with a conical element for the same reason. It consists of three titanium filaments. Once activated and purged during the bake-out, one of the filaments is heated up when the pressure rises into the $10^{-8}\,\mathrm{mbar}$ regime. The heat-up of a filament is done by applying $47\,\mathrm{A}$ for $2\,\mathrm{min}$, which makes titanium sputter on the wall of the vacuum tube around. The film created is a very good getter material [155]. Components of the residual gas chemically react with the titanium and are held in place, which effectively reduces the ambient pressure. Once the film is saturated, a new one can be applied as described above.

The stage is designed to shutter the atomic beam with a shutter stick mounted in a bellow[12]. A piston pushing against the bottom flange moves the flexible bellow enough to let the atoms pass. We found, that shuttering the atomic beam is not needed in normal operation of the system. For this reason, it is set to be permanently open.

---

[8] VAT 54124-GE02-0001

[9] Agilent VacIon 55 9191340 VACION PLUS 55 STARCELL

[10] Agilent 9160050 TSP filament cartridge

[11] Agilent X3602-64010

[12] Pfeiffer 420SFK040-160

### 4.2.4 Zeeman slower / MOT stage

The Zeeman slower / MOT stage is the most complex stage of the Li section. It combines many different components, needed for the first steps of creating an ultracold gas of Li. A vertical cut view of the section is presented in Fig. 4.6a.
The atomic beam enters the section through a vacuum tube of length $L = 608\,\mathrm{mm}$ and an inner diameter of $r = 10\,\mathrm{mm}$. It provides a differential pumping stage with a suppression of more than $10^{-3}$ towards the preceding section. The vacuum tube is enclosed by a stainless steel tube, that hosts the large main and small connection coils for generating the high field part of the Zeeman slowing field.
The following stainless steel MOT chamber (Fig. 4.6b) allows for good optical access to the atoms with CF64 viewports[13] in the horizontal and a pair of reentrant viewports in the vertical direction. They are anti-reflection coated for $671\,\mathrm{nm}$ and $1064\,\mathrm{nm}$ light (see Table A.1 for detailed information). Inside the reentrant viewports three pairs of coils are located for generating an offset, Feshbach and jump field (see Fig. 4.6c for layout and Section 4.2.5 for field details). Their mounts are designed to be close to the atoms without touching the reentrant viewport.
The gradient field for the MOT is provided by a pair of vertical oriented coils with a diameter of $230\,\mathrm{mm}$ in anti-Helmholtz configuration. On the other side of the chamber a compensation coil with the same orientation as the main Zeeman slowing coil is designated to cancel its offset field in the center of the chamber. A detailed description is given in Fig. 4.7.
Opposing the atoms' entrance side of the MOT chamber a vacuum tube leads the way out of it again. It is intended to collect and guide gas particles exiting the Zeeman slower tube to the ion pump[14] of the vacuum 4-way-cross-piece (Zeeman cross). The vacuum tube as well provides differential pumping of more than $10^{-2}$. The Zeeman cross hosts a $1\,\mathrm{inch}$ in-vacuum mirror[15] with protected aluminum coating. Its reflectivity is $\sim 90\%$ for $671\,\mathrm{nm}$ light. The Zeeman slowing light is guided to the mirror through a CF40 viewport and reflected under an angle of $45\,^{\circ}$ towards the atomic beam. The in-vacuum mirror allows the laser light to enter the Zeeman cross through a viewport that is not directly exposed to the atomic beam, preventing its occlusion and corrosion [156].

#### Zeeman slower

For slowing the atomic beam emerging from the oven, we follow the well established Zeeman slowing technique pioneered by William D. Phillips and Harold Metcalf in 1982 [157]. A counterpropagating laser beam is kept resonant to an atomic transition by cancelling the speed dependent Doppler shifts with a spatially varying magnetic field. Persistent momentum kicks opposite to the direction of motion due to the absorption of the photons result in a constant deceleration of the atoms. The atoms leave the oven with high velocities around $1300\,\mathrm{m/s}$ (see Fig. 4.2). Slowing the atoms before the consecutive MOT stage is crucial. Only a small fraction of the atoms leaving the oven is below the capture velocity of the MOT, which is typically $v_{\mathrm{cap}}^{\mathrm{MOT}} = 50\,\mathrm{m/s}$.
Slowing is performed on the transition from the $|J = 1/2, m_J = -1/2\rangle$ of the ground state

---

[13] Hositrad HOVPZ64Q-NM

[14] Agilent VacIon 20 9191145 PLUS 20 STARCELL

[15] Edmund 47-113

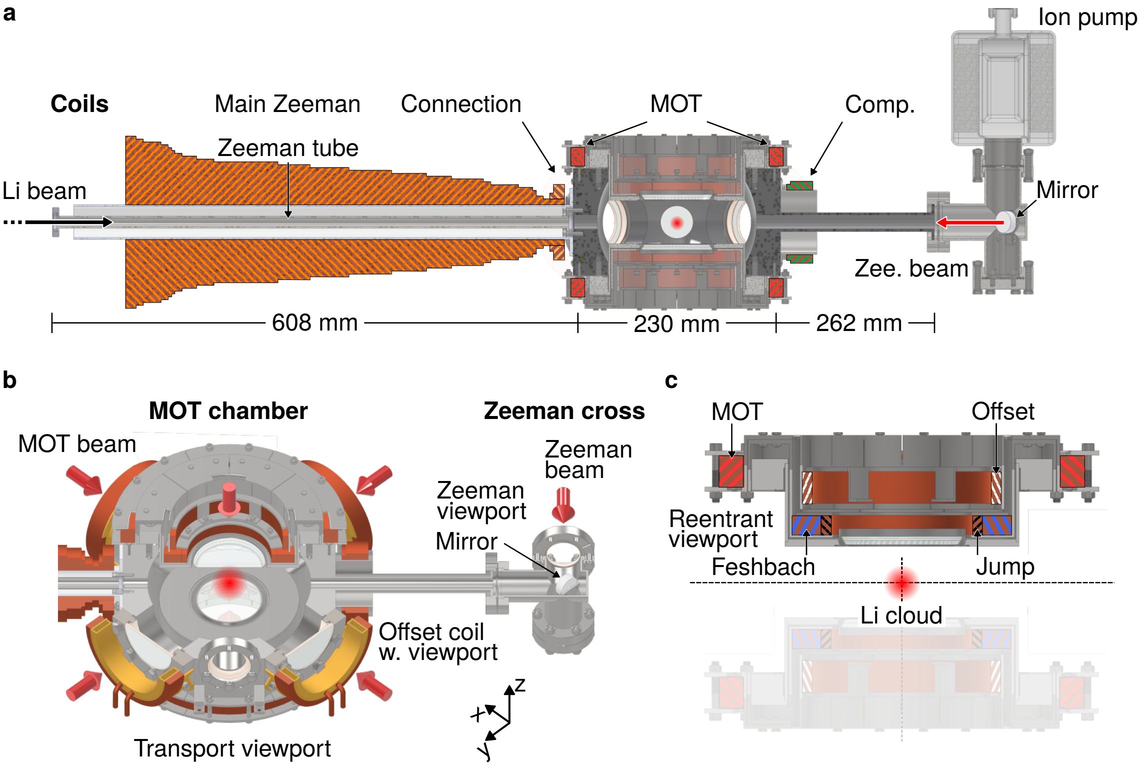

**Figure 4.6 Vacuum system and coils of the Zeeman slowing and MOT stage. a.** Vertical cut view of the Zeeman slower / MOT stage of the Li section. For better visualization, the coils to provide the magnetic field for Zeeman slowing and the MOT are highlighted with color. **b.** More detailed presentation of the Li MOT chamber and Zeeman cross. The MOT beams and Zeeman slowing beam are sketched. **c.** More detailed presentation of the reentrant viewport and the three coils mounted inside. The cross-sections are also colored here. A Li cloud is artificially placed in all three subfigures to mark the center of the MOT chamber.

to the $|J' = 3/2, m_{J'} = -3/2\rangle$ excited state of the $D_2$-line, which is closed for high magnetic fields. The total detuning $\Delta$ from the transition consists of three contributions:

$$\Delta = \Delta_L - \boldsymbol{k}\boldsymbol{v} - \gamma B/\hbar. \tag{4.3}$$

$\Delta_L$ is the detuning of the laser to the transition in zero field. The Doppler shift is $-\boldsymbol{k}\boldsymbol{v}$, with the velocity $\boldsymbol{v}$ of the atom and the wavenumber $\boldsymbol{k}$ of the laser beam. The Zeeman shift $-\gamma B/\hbar$ is given by the differential magnetic moment $\gamma = (g_{J'}m_{J'} - g_J m_J)\mu_\mathrm{B} \approx -1\mu_\mathrm{B}$ of the two states [125].

For the resonance condition of vanishing $\Delta$ and the laser beam propagating against the direction of motion of the atoms, the magnetic field is obtained as

$$B(x) = \frac{\hbar}{\gamma}\left(\Delta_L + kv(x)\right) = \frac{\hbar}{\gamma}\left(\Delta_L + k\sqrt{v_0^2 - 2ax}\right). \tag{4.4}$$

It is of a square-root-shape and its offset is governed by the chosen detuning of the laser beam. It was used, that during the slowing process with a constant deceleration $a$ of an atom with initial velocity $v_0$, the local velocity is: $v(x) = \sqrt{v_0^2 - 2ax}$. The deceleration on

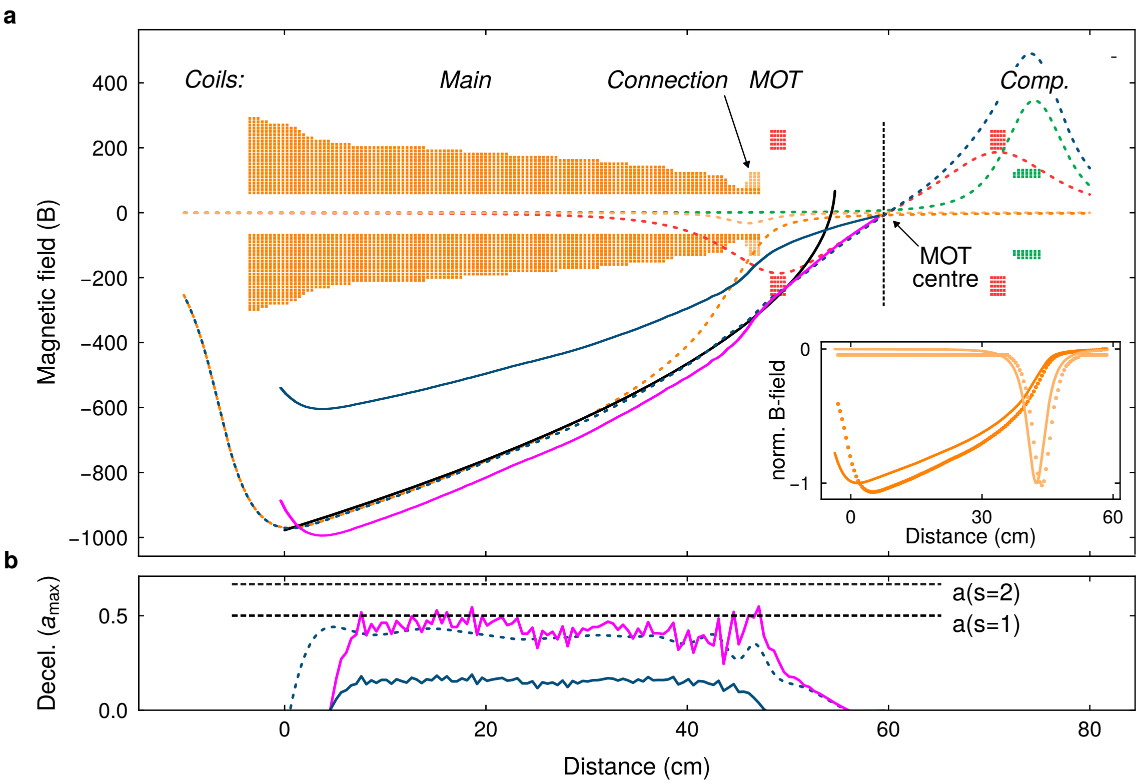

**Figure 4.7 Zeeman and MOT field. a.** The coil configuration for generating the Zeeman slowing and MOT field is shown as a vertical cut view. The rectangles represent the cross-sections of the wires. The ideal magnetic field from Eq. (4.4) for a laser detuning $\Delta_L = -2\pi \cdot 120\,\mathrm{MHz}$, capture velocity $v_0 = 1000\,\mathrm{m/s}$ and deceleration $a(s=1)$ given by Eq. (4.5) is represented by the solid black line. The (planned) total magnetic field (dashed blue) consists of the contributions of the main, connection, MOT and compensation coils. The colors of their respective simulated fields match the one of their cut view representation. The simulated field curve follows the ideal Zeeman slowing field almost to the end. There it smoothly merges with the gradient field of the MOT coils. The field consisting of the measured main and connection coil values together with the simulated field for the MOT and compensation coil is shown in pink. Here the currents obtained from the simulation was used. Finally, the field using the currents obtained from experimental optimization is given by the solid blue line. The inset shows the normalized simulated and measured magnetic fields of the main and connection coils expressing moderate agreement. **b.** Required (absolute) deceleration (Eq. (4.7)) for the magnetic fields (same color and line style) shown in a. to maintain the Zeeman slowing process. Deceleration achieved by resonant scattering for saturation parameters $s = 1, 2$ are represented by the black dotted lines.

resonance due to scattering is given by

$$a = \frac{F_{\text{scat}}}{m} = \underbrace{\frac{\hbar k \Gamma}{2m}}_{a_{\max}} \underbrace{\frac{s}{1+s}}_{\eta} . \tag{4.5}$$

The saturation parameter $s = I/I_{\text{sat}}$ gives the intensity in units of the saturation intensity $I_{\text{sat}}$. The deceleration is limited by the excited state lifetime $1/\Gamma$, because only spontaneous emission can alter the momentum of the atom. Due to limited laser power, the maximum deceleration $a_{\max}$ is not reached in experiments. The intensity $I = I_{\text{sat}}^{\text{D2}} \cdot s$ with

$s = 1$ and $I_{\text{sat}}^{\text{D2}} = 2.54\,\mathrm{mW/cm^2}$ is used in the following considerations. We target to slow atoms with initial velocity $v_0 = v_{\text{cap}}^{\text{ZS}} \leq 1000\,\mathrm{m/s}$. The detuning of the laser is set to $\Delta_{\text{L}} = -2\pi \cdot 120\,\mathrm{MHz} \approx -20\,\Gamma$. This large detuning ensures negligible radiation pressure from the ZS laser beam on the atoms captured in the MOT.

As the atoms are slowed down in the longitudinal direction, the transversal direction is heated [158]. Due to the isotropic nature of the spontaneous emission, the mean transversal velocity of the atoms on average stays the same. However, the root-mean-square velocity increases as $v_\perp = \sqrt{\frac{v_{\text{rec}}}{3}(v_{\text{cap}}^{\text{ZS}} - v_{\text{cap}}^{\text{MOT}})} \approx 1.3\,\mathrm{m/s}$. Even though, this velocity is small compared to the capture velocity of the MOT, it is best to keep the travel distance between the end of the Zeeman Slowing stage and the subsequent MOT stage as short as possible to minimize atom loss due to the transversal spread of the atomic beam.

For the Zeeman slowing field of Li, it is possible to provide the end of it here by the gradient field of the MOT stage [159]. This design reduces the transversal spread to a bare minimum by a smooth and gapless handover from one stage to the other. The coil configuration and simulated fields to achieve such a ZS to MOT gradient handover is presented in Fig. 4.7. Here, the field of the big main Zeeman coil is smoothly handed over to the MOT coil with the help of a small connection coil located in the transition region. A compensation coil on the other side counteracts the offset from the main and connection coil in the center of the MOT coils. A MOT gradient field of $18\,\mathrm{G/cm}$ (weak axis) was chosen, which was expected to be in the common parameter regime of operation.

The simulation was done by individual loop representations of the coils with the Biot-Savart law. Comparison of the simulated and measured field of main and connection coil show small deviations. For the simulation an effective wire spacing of $0.3\,\mathrm{mm}$[16] was added to the hollow ($4\,\mathrm{mm} \times 3\,\mathrm{mm}$) core ($\varnothing\ 2\,\mathrm{mm}$) copper wire. Not considering any extra spacing results in a better matching of the simulation to the measured value.

Starting from the values simulated, the currents used for driving the coils were optimized experimentally for best MOT loading rates (see Fig. 4.8). Here, for all coils substantially lower values and with this lower fields were found. The main / connection coils were planned to run on $20.8\,\mathrm{A}$ / $10.5\,\mathrm{A}$, but $12\,\mathrm{A}$ / $8\,\mathrm{A}$ lead to the best performance. Due to the now lower field of the main coil, the capture velocity is decreased from $v_{\text{cap}}^{\text{ZS}} = 1000\,\mathrm{m/s} \to 600\,\mathrm{m/s}$. Looking back to the Boltzmann distribution of the atoms in *Fig. 4.2*, the decrease in the number of addressed atoms is expected to be quadratic in this velocity regime. This results in a reduction by a factor of $2.8$. Together with the main and connection coil currents, also the MOT gradient field was optimized for best loading rates. Here, a substantially lower value of $6\,\mathrm{G/cm}$ compared to a planned value of $18\,\mathrm{G/cm}$ was found as well. With the lowered MOT gradient field the volume of the MOT increases. This positive effect appears to be dominating over the reduction in addressed atoms.

At this point, it as well has to be made sure, that the strong deviation from the expected and experimentally found values for the magnetic field is not due to defects in the realized magnetic field. In order for an atom to stay in the slowing process, local field changes must not exceed the change in velocity at any point [159]:

$$\frac{dv(x)}{dx} = \frac{a(x)}{v(x)} \leq \frac{\gamma}{k} B'(x). \tag{4.6}$$

---

[16] This value was considered to be a good estimated by other people using the same wire and simulation script before.

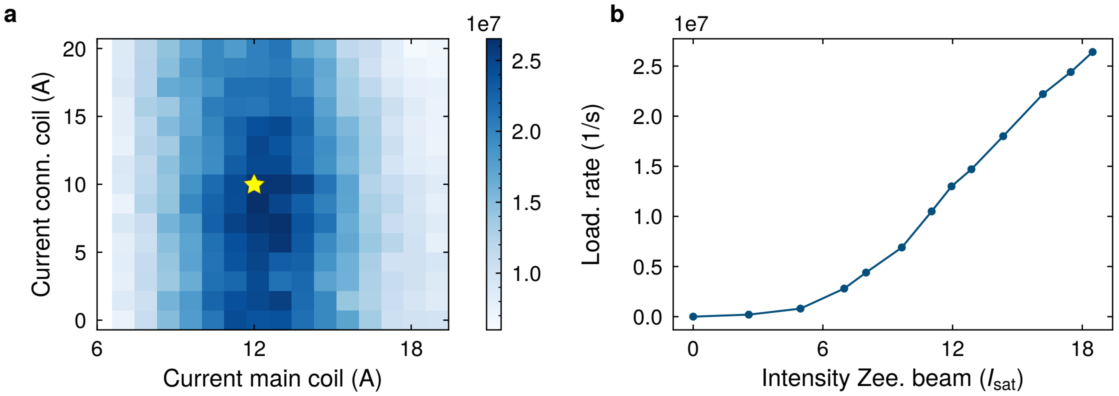

**Figure 4.8 Zeeman slower performance. a.** MOT loading rate for varying currents of the main and connection coil providing the Zeeman slower field. The influence of the main coil current on the loading rate is much more pronounced, than for the connection coil. The best performing currents are indicated with an asterisk. **b.** MOT loading rate for varying central intensities of the Zeeman slower beam. Even though multiple $I_{\text{sat}}$ are provided no saturation is observed yet.

Expressing the velocity with the resonance condition from Eq. (4.3), the locally required deceleration is given by

$$a_{\text{req}}(x) = \frac{\gamma^2}{k^2} B'(x) \left( B(x) + \frac{|\Delta_L|}{\gamma} \right) . \tag{4.7}$$

From this expression it can be well understood, that strong local gradients pose a threat to loosing atoms in the continuous slowing process. For this reason, the required deceleration is calculated for the combined field of the measured main and connection coil together with the simulated field of the MOT and compensation coils (see Fig. 4.7b). This is done for the planned and experimentally determined currents. Here it is shown, that in principle providing resonant scattering with a saturation parameter of $s = 2$ fulfills the continuous slowing condition of Eq. (4.6) for both settings.

The total available optical power for the Zeeman slower beam at the experimental table is $\sim 60\,\mathrm{mW}$. It is expanded to a beam size of $8.5\,\mathrm{mm}$ before being sent onto the atoms via the in-vacuum mirror. This provides a beam with a saturation parameter of $s \geq 9$ over the entire cross-section of the Zeeman slower vacuum tube ($\varnothing 10\,\mathrm{mm}$) with a peak saturation parameter of $s = 18.3$. Even though enough optical power is in principle provided, no saturation on the MOT loading rate was found experimentally. Moving the Injection-Lock providing the optical power to the experimental table would provide about double the power. This option for reconstruction was not pursued to maintain the modular structure of the system. In addition to this, the achieved MOT loading rate of about $2 \cdot 10^7\,\mathrm{s}^{-1}$ was not limiting further experimental steps.

### MOT

After Zeeman Slowing, the atoms have reached low enough velocities to be capture by the subsequent Magneto-Optical Trap (MOT) stage. The MOT surely was and still is one of the key techniques in modern AMO experimental physics. It was proposed by Jean

Dalibard [160]. Only a little later, the first experimental realization was demonstrated for Na at the Bell Laboratories in 1987 [161]. The MOT was the first trap with a combined restoring and friction force. Thereby atoms approaching the trap are cooled and spatially confined. To realize a MOT a light field and a magnetic gradient field are needed. Three pairs of counterpropagating laser beams intersect at the center of a quadrupole magnetic field. Trapping is only provided by the radiation force of the light field onto the atoms. The beams of each pair are circular polarized and of opposite helicity. An atom moving along either direction is Zeeman and Doppler shifted into resonance with the laser beam such that the radiation force accelerates it towards the center. Spatial confinement originates from the locally varying Zeeman shift. Cooling is provided with the friction of the optical molasses, which relies on the Doppler effect.
The principles of the MOT operation are explained best in a 1D system for an atom of a $J = 0$ ground and a $J = 1$ excited state. It is illustrated in Fig. 4.9a. This simple picture covers the core features and was initially conceived this way [161]. Being in the center region, the excited state Zeeman levels ($m_J = -1, +1$) shift linearly in position due to the gradient field. The laser beams' frequency is slightly red detuned to the unshifted transition. An atom moving away from the $0\,\mathrm{G}$ field center gets Zeeman shifted. The circularity of the beams is chosen in such a way, that the atom gets closer/further detuned to the beam, that pushes the atom towards/away from the center. The imbalance of radiation forces effectively provides a restoring force. The principles also apply to a 3D system and an atom with a higher orbital momentum $J \to J + 1$ transition. Here, the atoms are pumped from one stretched state to the other, when crossing the $0\,\mathrm{G}$ region. A more detailed description of the MOT's working principle and derivation of the trapping force is found in basically every textbook, that deals with the fundamental concepts of optical cooling [80, 162].

The Li MOT is operated on the $D_2$-line. It consists of three retro reflected beam pairs (MOT beams), that intersect in the center of the chamber (see again Fig. 4.6b). They are red-detuned to the $F = 3/2 \to F' = 5/2$ transition. For historic reasons it is also referred to as the *cooler* transition as it fulfills the $F \to F + 1$ condition. As for all other alkalis, Li possesses two ground state levels, but only the $F = 3/2$ would be addressed here. In order not to lose atoms, that decay to the $F = 1/2$ ground state, an additional frequency component is added to the MOT beams. This so called *repumper* addresses the $F = 1/2$ state, to keep the atoms in the cooling cycle.

In the experiment all three MOT beams' waists are $8.5\,\mathrm{mm}$, which is the same as for the Zeeman Slowing beam. The horizontal beam pairs consist of up to $13\,\mathrm{mW} \hat{=} 4.5 \cdot I_{\mathrm{sat}}^{\mathrm{D2}}$ cooler power and up to $10\,\mathrm{mW} \hat{=} 3.5 \cdot I_{\mathrm{sat}}^{\mathrm{D2}}$ repumper power. In the vertical direction the maximum available power is about double, with $25\,\mathrm{mW} \hat{=} 8.7 \cdot I_{\mathrm{sat}}^{\mathrm{D2}}$ cooler power and $21\,\mathrm{mW} \hat{=} 7.3 \cdot I_{\mathrm{sat}}^{\mathrm{D2}}$ repumper power.
The cooler and repumper light is overlapped before being fibered to experimental table. This guarantees spatial overlap of the two. Li MOTs require a significant admixture of repumper light in every axis. Heavier and with this slower alkalis, such as Rb, typical require only little admixture of repumper light.
For optimized parameters a loading rate of about $2.5 \cdot 10^{7}\,\mathrm{s}^{-1}$ is achieved (see Fig. 4.9). The temperature of the reservoir is $350\,^{\circ}\mathrm{C}$ and the nozzle temperature is $400\,^{\circ}\mathrm{C}$. Under static loading conditions, the atom number rises to half its maximum of $N_{\mathrm{max}} = 1.35 \cdot 10^{8}$ in $\tau_{1/2} = 5\,\mathrm{s}$[17]. The best loading rate was found for a MOT gradient field of $6\,\mathrm{G/cm}$ and

---

[17] Atom number fitted to: $N(t) = a \cdot 2^{-t/\tau_{1/2}} + N_{\mathrm{max}}$

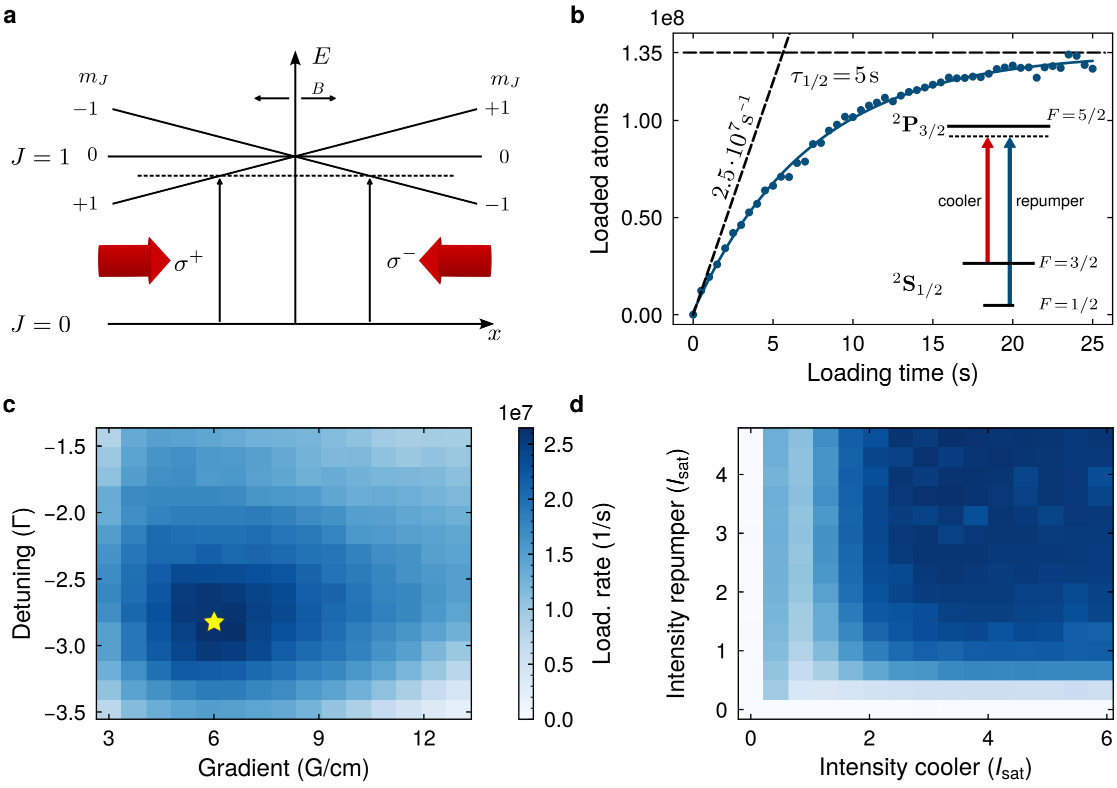

**Figure 4.9** **MOT characterization. a.** Sketch of the working principle of the MOT for a $J=0 \rightarrow J=1$ atom in 1D. The excited state Zeeman levels are shifted in resonance with the light field (dotted) line as they move away from the center. The handedness of the beams are chosen such that scattering from the one pushing the atoms back towards the center is dominating. **b.** Loading curve of the MOT. An exponential curve (line) is fitted to the data (dots). With this the initial loading rate of $2.5\cdot10^7\,\mathrm{s}^{-1}$, the half load time $\tau_{1/2}=5\,\mathrm{s}$ and the steady state atom number of $N_{\mathrm{max}}=1.35\cdot10^8$ are extracted. The inset shows the transitions of Li used for the MOT. **c.** Loading rate for varying MOT gradient fields and detuning from the cooler transition. The best parameter set is indicated with an asterisk. **d.** Loading rate for varying average cooler and repumper intensities. For both saturation is observed.

a detuning of $-2.8\,\Gamma$ of the cooler beam. Meanwhile, the best loading is found for the repumper beam almost on resonance ($\sim 0\,\Gamma$). Varying the optical power of the cooler and repumper light, a clear saturation of the loading rate is observed. Intensities of more than $3\,\mathrm{I}_{\mathrm{sat}}$ for both are sufficient to achieve good loading. In default operation the intensities are set to their maximum values.

### 4.2.5 Coils of the Li chamber

The Li chamber is equipped with a variety of coil pairs, presented in Fig. 4.6. They provide precise control of the magnetic field offset and gradient field needed for the experiment. Their geometric, electric and magnetic properties are listed in Table 4.1. The numbers presented here were obtained from the same simulation program as for the fields for Zeeman Slowing of the previous section. As the coils considered here are of much fewer windings, errors due to wrongly estimated effective wire spacings are expected not to be relevant. In the following, the fields in the Li chamber and the accompanied crosstalk to the Er chamber are presented. For a dual-species experiment with one of the elements being highly magnetic, field changes in the experimental sequence of the other one have to be taken into account.

### Fields in the Li chamber

The Li chamber hosts two pairs of horizontal and one pair of vertical offset coils, a coil pair to provide the MOT gradient field, a coil pair to realize high Feshbach fields and a multipurpose jump coil pair. Except for the horizontal offset coils, they were all wound from the same hollow core copper wire as the Zeeman slower coils. The hollow core allows for efficient water cooling without the need of additional cooling elements. The space saved as a result allows mounting the vertical offset, Feshbach and jump coil pairs inside the reentrant viewport without reducing the optical access to the atoms.
The horizontal offset coils however were wound from a $2 \times 1\,\mathrm{mm}$ "flat" copper wire[18]. Their water-cooled brass mounts are oriented on axis with the horizontal CF63 view ports. The reason for this different choice of wire was the maximum available output current of the bipolar current supplies[19] employed to drive all three offset coil pairs. With a maximum supplied current of $\pm 15\,\mathrm{A}$, a desired range of $\pm 10\,\mathrm{G}$ was planned to be covered. The geometry of the chamber requires about $60$ windings to do so, which would have resulted in too bulky coils, if wound from the hollow core wire.
In the vertical direction, the offset coils are placed much closer to the atoms in the reentrant viewports. Here a field range of $\pm 10\,\mathrm{G}$ is conveniently covered with $10$ windings of the hollow core wire only. This range of magnetic field is sufficient to control the position of the MOT and to compensate for external magnetic offset fields.
To tune the scattering length of Li with the Feshbach resonances (see again Fig. 3.1), fields in the regime of hundreds of Gauss are needed. For the field supplying pair of coils, it was taken special care to closely fulfill the Helmholtz condition in order to minimize magnetic gradients. For a maximum available current of $400\,\mathrm{A}$ a maximum field of $889\,\mathrm{G}$ is in principle reached. This comes along with a gradient of $-1.76\,\mathrm{G/cm}$ in axial direction and a gradient of $0.88\,\mathrm{G/cm}$ in radial direction. The current supply[20] provides a maximum voltage of $15\,\mathrm{V}$. Cables connecting the current supply to the coils and the heat-up of the coils increase the total resistance during operation. The increased resistance requires a higher voltage, than the current supply is capable to provide. This is limiting the maximum current reachable to $330\,\mathrm{A}$, respective $733\,\mathrm{G}$ for a steady-state operation of the Feshbach coils.

The MOT and the jump coil pairs are operated in gradient configuration. They are oriented along the vertical ($z$-axis) direction. The MOT coil pair is the biggest set of coils at the Li chamber. In principle, it provides a gradient field of up to $43\,\mathrm{G/cm}$ in the axial and $21.5\,\mathrm{G/cm}$ in the radial direction for a maximum current of $220\,\mathrm{A}$. As for the Feshbach coils, additional resistance in the system limits the maximum reachable current of the current supply[21] under steady operation to $160\,\mathrm{A}$. This reduces the actual reachable gradients to

---

[18] Synflex Elektro GmbH: Typ W200 2L IEC 60317-29

[19] SERVOWATT Leistungselektronik GmbH: DCP 390 ($\pm 15\,\mathrm{A}$ at $25\,\mathrm{V}$)

[20] Delta Elektronika B.V. SM 15-400-P166

[21] Delta Elektronika B.V. SM18-220

$31\,\mathrm{G/cm}$ (axial) and $15.5\,\mathrm{G/cm}$ (radial). As presented in Fig. 4.7, the large size of the MOT coils is needed for a smooth handover of the Zeeman slowing into the MOT field. This on the other hand reduces the speed of dynamic operation and especially a fast switch-off. For this reason, the jump coil is operated in gradient configuration. It allows taking over the generation of the gradient field from the MOT coils after the loading stage. Its small size and close distance to the atoms allows for a fast switch-off in about $200\,\mu\mathrm{s}$. This is achieved with an electric circuit, that quickly transfers the energy of the coils' magnetic field to the electric field of a high voltage capacitor. See Section A.4 for detailed information. The jump coils provide a gradient of up to $25.5\,\mathrm{G/cm}$ (axial) and $12.8\,\mathrm{G/cm}$ (radial) for a maximum current of $120\,\mathrm{A}$ of the current supply[22].

### Crosstalk to the Er chamber

Applying magnetic fields in the Li chamber in principle affect the field in the Er chamber, even though they are separated by a distance of half a meter. This crosstalk is considered in the following, since Er is prone to magnetic (gradient-) fields. If significant, those later have to be accounted for, in order to provide simultaneous operation of the Li and Er part of the system.

First, the vertically orientated coils of the Li chamber are considered. Here, the direction of the stray field at the center of the Er chamber is given by the configuration of the coils. For coil pairs of parallel (field) configuration, the stray field is oriented along the same (vertical) direction as in the Li chamber. For coils in anti-parallel (gradient) configuration, the stray field is oriented along a connecting line of the two chamber centers. The vertical offset coil pair and the jump coil pair have the least influence on the field in the Er chamber. Their stray fields are only in the low $\mathrm{mG}$ regime, which is not significantly influencing the operation of the Er part.

In contrast to them, the Feshbach and MOT coils of the Li system cause stray fields of up to $\sim 1.5\,\mathrm{G}$ in the Er chamber. In the later experimental operation the actually applied fields cause stray fields of $\sim 0.5\,\mathrm{G}$.

Similar strengths in stray fields, but different orientations are caused by the horizontal offset coils of the Li system. Even though, they are of rather low maximum field range in the Li chamber, their comparably large separation yields strong stray fields in the Er chamber. Here typically, stray fields of $0.5\,\mathrm{G}$ in the Er chamber occur for the operation of the Li system.

The operation of the experiment showed, that changes of the static magnetic field for the MOT loading of Li influences the MOT loading of Er. Here, adaptation of the magnetic offset fields of the Er system to maintain optimized MOT loading is needed. Loading of the Er MOT proved to be only minorly influenced by dynamic magnetic field changes in the half a meter away Li chamber. Field ramps in the Li chamber for the cMOT and evaporation at $330\,\mathrm{G}$ do not affect it. In contrast, the cMOT stage of Er and especially loading to tightly focused Optical Dipole Traps (ODTs) are strongly influenced by changed ambient offset field conditions. At the same time Er also is prone to magnetic gradient fields when already loaded to an ODT. In a combined sequence, for this reason all coils of the Li system are turned off before the start of the Er cMOT stage. The reciprocal influence of the coils of

---

[22] TDK-Lambda GEN12.5-120

the Er system to the performance of the Li part has shown to be negligible, as Li is less sensitive to offset fields. At the same time Er does not require high fields for evaporation as it possesses a rich Feshbach spectrum already for low fields.

| Coil name: | Hor. offsets | Vert. offset | Feshbach | Jump | MOT |
|---|---|---|---|---|---|
| Orientation | $x$ / $y$ | $z$ | $z$ | $z$ | $z$ |
| Configuration | parallel | | | anti-parallel | |
| Field ($\parallel$) | 0.70 G/A | 0.71 G/A | 2.22 G/A | +0.21 $\frac{\text{G}}{\text{cm A}}$ | +0.19 $\frac{\text{G}}{\text{cm A}}$ |
| Max. field ($\parallel$) | ±10.5 G | ±10.6 G | 889 G | +25.5 G/cm | +42.6 G/cm |
| Field ($\perp$) | - | - | - | -0.11 $\frac{\text{G}}{\text{cm A}}$ | -0.10 $\frac{\text{G}}{\text{cm A}}$ |
| Max. field ($\perp$) | - | - | - | -12.8 G/cm | -21.3 G/cm |
| Windings | $6 \times 10 = 60$ | $2 \times 5 = 10$ | $6 \times 3 = 18$ | $3 \times 3 = 9$ | $5 \times 5 = 25$ |
| Wire type | flat | hollow | hollow | hollow | hollow |
| Diameter | 119 mm | 110 mm | 108 mm | 95 mm | 212 mm |
| Distance | 278 mm | 108 mm | 66 mm | 66 mm | 130 mm |
| Resistance | 112 mΩ | 17 mΩ | 31 mΩ | 8 mΩ | 77 mΩ |
| Max. current | ±15 A | ±15 A | $^{*}$400 A | 120 A | $^{**}$220 A |
| Need. voltage | ±1.7 V | ±0.26 V | 12.5 V | 1.0 V | 17 V |
| Max. power | 25.2 W | 3.9 W | 4988 W | 119 W | 3735 W |
| Field in Er chamber *(crosstalk)* | | | | | |
| Max. field ($\parallel$) | $^{***}$2.7 G | -29 mG | -1.5 G | - | - |
| Max. field ($\perp$) | - | - | - | -22 mG | -1.7 G |

**Table 4.1 Coils of the Li chamber and their fields.** Real maximum achievable currents: $^{*}$330 A, $^{**}$160 A. $^{***}$Actual field direction $-2.4\,\mathrm{G_x}$;$-1.2\,\mathrm{G_y}$

## 4.3 UHV section

The Ultra-High Vacuum (UHV) section of the ErLi experiment consists of the main chamber and the glass cell. The pressure range of $10^{-7}\,\mathrm{mbar}$ to $10^{-12}\,\mathrm{mbar}$ is referred to as UHV. In this regime the pressure can still be accessed via the ion pump's control units[23].

Providing an ultra-low pressure environment is a basic requirement for all ultracold atoms experiments. Achieving optimal pressure conditions was a maxim of the section's design. By deciding for a one piece welded main chamber, leakages due flange connections are reduced. The main chamber corpus hosts both the Li and the Er MOT chambers. It is self designed and manufactured by PINK GmbH Vakuumtechnik. Not relying on standard commercial vacuum pieces also allowed to add extra features for convenient mounting of the chamber to the table and other objects to it.
For the selection of stainless steel, it was also taken care, that only material of low magnetic permeability ($\mu_r < 1.01$) was used. As Er is prone to magnetic fields, magnetization of the chamber must be kept to a bare minimum. To satisfy this, the raw material of the chamber blocks and flanges are 316LN(1.4429esu) and 316L(1.4404) for the tubes.

The main chamber is equipped with two vacuum pumps that contain a Non-Evaporative Getter (NEG) and Sputter Ion Pump (SIP). Both vacuum pumps reach quite far into the chamber with a distance of $\sim 10\,\mathrm{mm}$ to the transport axis, that connects the MOT centers to the glass cell. This enhances the capture of residual gas particles. The larger of the two vacuum pumps[24] is located between the Li and Er MOT chambers. Here, a pressure of about $3 \cdot 10^{-11}\,\mathrm{mbar}$ is reached. The smaller one[25] is located in between the Er MOT chamber and the glass cell. Both are advanced UHV vacuum pumps, that next to high pumping speed for the standard gases ($H_2$, $H_2O$, ...) also provide enhanced performance in pumping of noble gases and methane.
An in-vacuum aperture between the Er MOT chamber and the smaller vacuum pump reduces the flux of gas particles into the glass cell. Here, a pressure below the pump controller's detection limit of $2.1 \cdot 10^{-11}\,\mathrm{mbar}$ is realized. Choosing a comparably large inner diameter ($\varnothing 43\,\mathrm{mm}$) of the glass cell's transition piece provides good vacuum connectivity between it and the vacuum pump. For this reason, the local pressure in the glass cell is assumed to be well below $2.1 \cdot 10^{-11}\,\mathrm{mbar}$.

### Air baking

For UHV systems the ultimately reached pressure is usually limited by outgasing of the stainless steel surfaces of the vacuum system. Trapped hydrogen in the material moves through the lattice, eventually reaches the surface, recombines and is released into the gas phase. This process is effectively suppressed by three orders of magnitude by baking the stainless steel parts in normal air [163]. During the baking process an oxide layer is formed, that strongly reduces the transit of hydrogen and with this outgasing into the vacuum.
The main chamber and the attached stainless steel components (Zeeman tubes and Zeeman

---

[23] The ion pump's control unit infers to the pressure by the measured current of ionized gas particles between its anode and cathode.

[24] SAES Getters S.p.A. NEXTorr D1000-StarCell

[25] SAES Getters S.p.A. NEXTorr Z300-StarCell

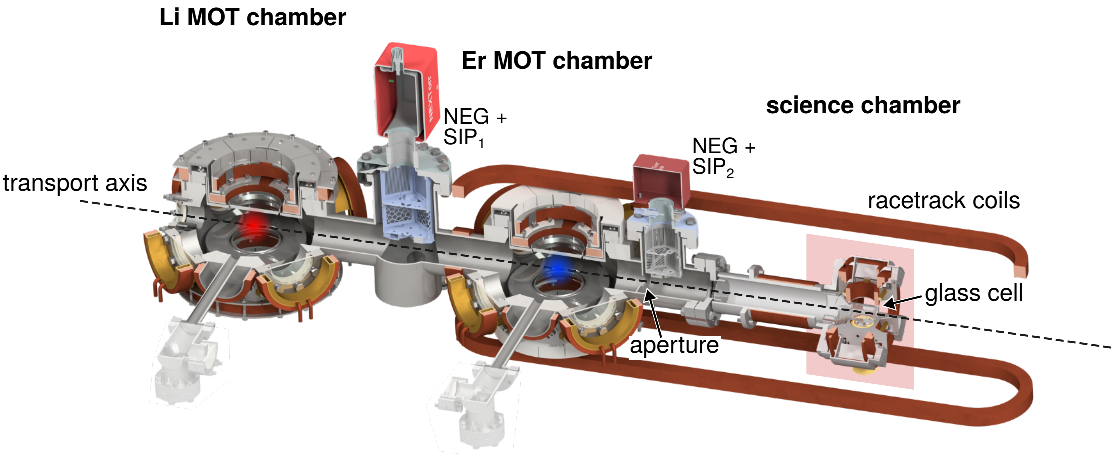

**Figure 4.10** **UHV section.** Quarter cut view of the UHV section of the ErLi experiment. It consists of the main chamber and the glass cell of the science chamber section. The center of the Li and Er chambers are indicated by red/blue MOT clouds. An in-vacuum aperture ($\varnothing 20\,\mathrm{mm}$) helps to isolate the glass cell's vacuum from the main chamber. Two vacuum pumps (NEXTorr D1000-StarCell$_1$, NEXTorr Z300-StarCell$_2$) with combined NEG and SIP systems provide ultra low pressure. The prominent racetrack shaped coils provide a magnetic gradient field to levitate Er during transport (details in [74]). For better orientation, the two Zeeman crosses are transparently displayed.

crosses) were baked in air at $400\,°\mathrm{C}$ for $24\,\mathrm{h}$. In order to protect the knife edges from oxidation, all CF connections were closed with blind flanges and annealed copper gaskets. For every component, at least one blind flange had a hole drilled in to allow for ventilation. Due to the oxidation layer, the chamber's appearance changed from the typical shiny silver to a flat copper like shade (see Section A.5).

## 4.4 Science chamber

The science chamber is the heart of the experiment, consisting of a glass cell and five pairs of coils. It provides high optical access, a clean vacuum environment and highly controllable magnetic fields (see Fig. 4.11). These ingredients are prerequisites for state-of-the-art ultracold gasses experiments.

The coils' mount consists of an aluminum tube screwed to a heavy stainless steel foot and coils' clamps of slim design. The clamps are arranged in such a way, that they do not reduce the optical access further than the coils they held in place. Magnetization of the material, when ramping close to the $800\,\mathrm{G}$ Feshbach resonances of Li would likely disturb the highly magnetic Er atoms. It was taken care to use only material of low magnetic permeability in the vicinity of the glass cell. The usage of stainless steel parts was avoided. Aluminum and brass, both with $\mu_r \approx 1$ were applied instead. Three pairs of offset coils allow applying defined fields up to $16\,\mathrm{G}$ along the transport direction and up to $6.3\,\mathrm{G}$ perpendicular to it. A pair of Feshbach coils oriented along the transport direction provide highly homogenous fields up to $842\,\mathrm{G}$. A vertical oriented spin-separation coil pair in anti-Helmholtz configuration allows generating gradients up to $348\,\mathrm{G/cm}$. In between the lower spin-separation coil a high NA

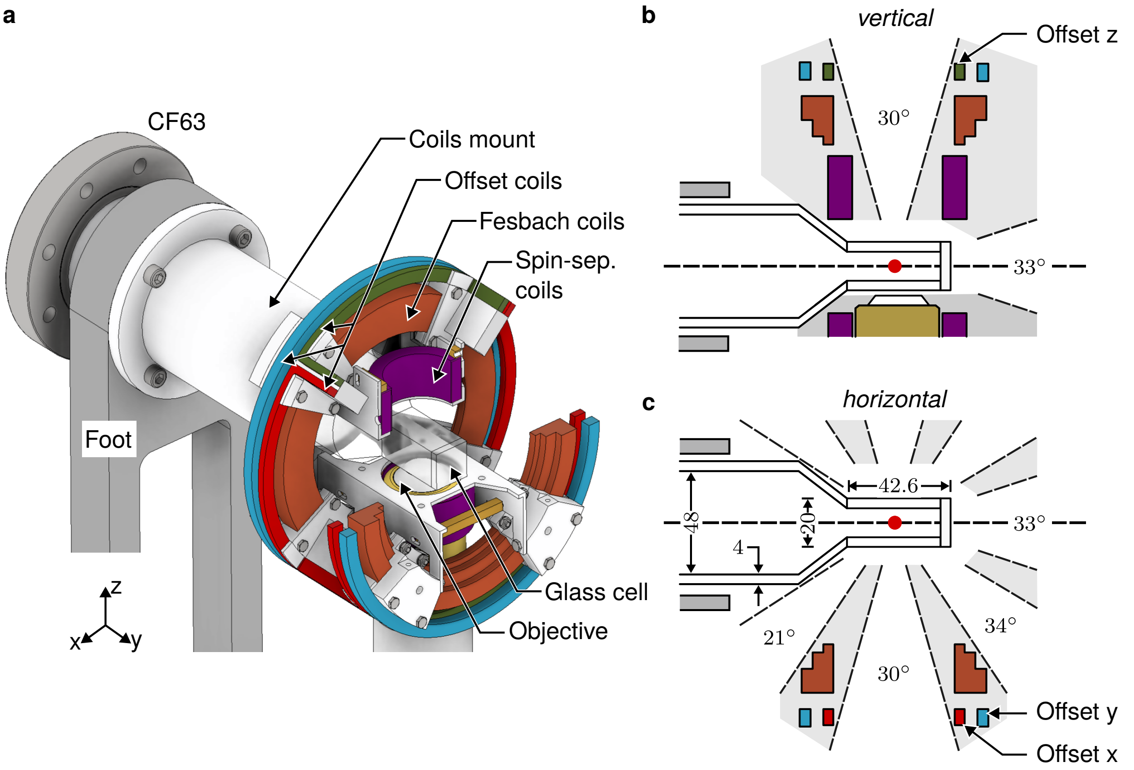

**Figure 4.11 Science chamber coils and optical access. a.** Coils layout around the glass cell. Five pairs of coils: Three offsets, the Feshbach and the spin-separation coil are placed around the glass cell center. Slim coil clamps are held by a massive aluminum tube, that surrounds the glass. A high NA objective is already set in place for future experiments. **b.** Optical access in the vertical direction. The spin-separation coils and the objective restrict the access to the top. The center of the glass cell is marked with a red dot. **c.** The optical access in the horizontal direction is only limited by the Feshbach coils.

objective[26] for future experiments is already installed. It is placed just 1.5 mm below the glass cell.

## Glass cell

Large optical access is provided by a vacuum glass cell[27]. The cuboid shaped cell is made out of 4 mm thick optically bond glass plates. It is $20 \times 20$ mm wide and 42.6 mm long. Here, the final experimental steps take place. The glass cell is made out of fused silica to avoid thermal lensing of high power laser beams. A drawback of this choice is, that due to high bonding temperatures optical coating on the inside is not possible. Optimized coatings for certain wavelengths usually come with enhanced reflectivities for others, which limits the future flexibility of the apparatus. Bare fused silica shows high transmission of more than 94% for the entire spectral range of 401 nm to 1064 nm employed at the glass cell at the moment. Er has a very rich optical spectrum reaching in the IR. An interesting 1 Hz line at 1299 nm is still well within the transmission spectrum of fused silica [164]. For these

---

[26] Special Optics Inc., NA= 0.65, design wavelengths: 401 nm, 671 nm, 1064 nm

[27] Japan Cell Co., Ltd

reasons, we decided to leave the glass cell uncoated on the outside as well.

The small glass cell at the front has a tapered connection to a glass tube of $48\,\mathrm{mm}$ inner diameter. The large diameter allows for good vacuum conductance from the glass cell to the SIP/NEG vacuum pump. The glass tube blends over to a non-magnetic CF63 stainless steel flange in a glass metal transition. The center of the glass cell and the flange connection is $\sim 25\,\mathrm{cm}$ apart. With this, it is well separated from the magnets of the SIP.

### Coils

For the design of the Feshbach coils, it was taken great care to obtain a highly homogenous field. This was done by following the Helmholtz condition for as closely as possible, which results in a 'staircase' shape of the coil's cross-section. During the winding process heat-resistant two component glue was applied between individual windings and layers. With this, stiff and self-supporting coils were obtained. The hollow wire does not require additional cooling elements, enabling a slim design of the coils' clamps.

The Feshbach coils are oriented along the transport direction. The geometry of the coils was found by a balance of size, homogeneity and number of windings. The coil has to provide a field of $\sim 800\,\mathrm{G}$ to reach the Feshbach resonances of Li with a current of $400\,\mathrm{A}$. The provided field needs to be homogenous, which is limited by the radius of the coils. At the same time employing many windings and a very large radius leads to a bulky and slow coil with high self-inductance.

The installed Feshbach coils have an inner diameter of $100.5\,\mathrm{mm}$ and are separated by $50\,\mathrm{mm}$. Each coil is wound in three layers with one, two and three windings. With a maximum of $400\,\mathrm{A}$ it reaches a central field of $824\,\mathrm{G}$. Simulations of the magnetic field show adequate homogeneity (see Fig. 4.12). For a displacement of $2\,\mathrm{mm}$ it changes by $-1.5 \cdot 10^{-4}$ $(+0.6 \cdot 10^{-4})$ in the longitudinal (radial) direction. This corresponds to an

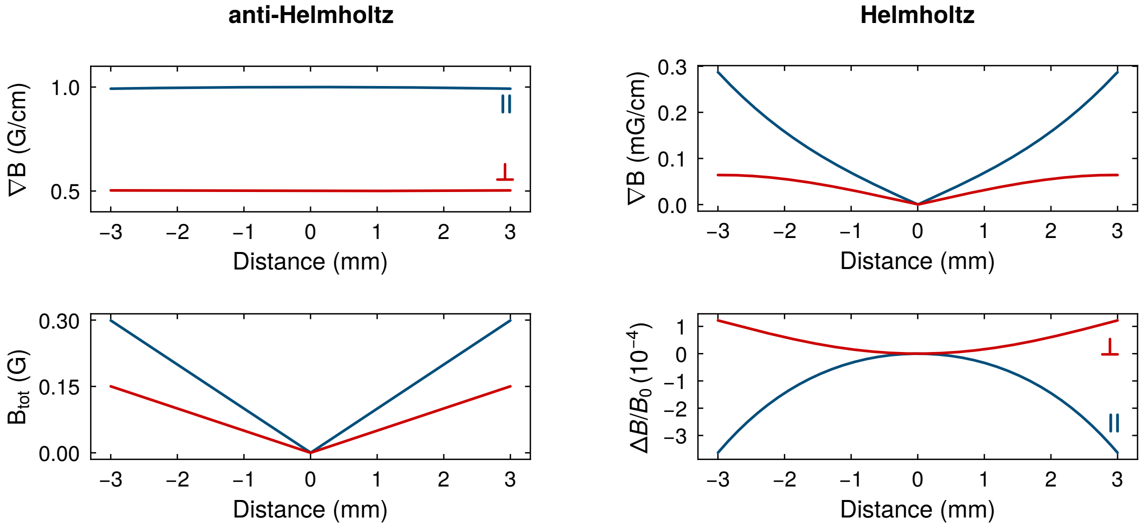

**Figure 4.12** **Magnetic field of the Feshbach coils.** Magnetic (gradient-)field of the Feshbach coil pair in (anti-)Helmholtz configuration along their radial ($\perp$) and axial ($\|$) axes. In Helmholtz configuration the deviation from the central field ($\Delta B/B_0$) is in the order of $10^{-4}$ on the relevant scale. Simulations are done for central fields of $1\,\mathrm{G}$, respective $1\,\mathrm{G/cm}$. They provide a (gradient-)field of ($0.4\,\mathrm{G/cm/A}$) and $2.06\,\mathrm{G/A}$ in (anti-)Helmholtz configuration.

absolute maximum deviation by $-120\,\mathrm{mG}$ ($+50\,\mathrm{mG}$) from the $824\,\mathrm{G}$ at the center. Being displaced also is accompanied by a magnetic field gradient. Here, a maximum of $130\,\mathrm{mG/cm}$ ($47\,\mathrm{mG/cm}$) at $824\,\mathrm{G}$ is calculated.

The spin-separation coils are designed to provide a gradient field in the vertical direction to spatially separate the spin states of Li at the end of an experimental cycle. To do so, strong gradients of typically $\sim 95\,\mathrm{G/cm}$ are required for the Stern-Gerlach separation of Li [165]. Together with single site resolved imaging it is the state-of-the-art imaging technique to obtain full information in 1D and 2D (fermionic) lattice systems [166–168]. The spin-separation coils were added to the coil system, when it was already fully assembled. For this reason, its geometry does not follow the (anti-)Helmholtz condition. In order to fit around the objective, the two times four layer coils have an inner diameter of $40\,\mathrm{mm}$. The coils are separated by $34\,\mathrm{mm}$. For this geometry $384\,\mathrm{G/cm}$ at $400\,\mathrm{A}$ are in principle reached.
Using the spin-separation coils in Helmholtz configuration, fields up to $550\,\mathrm{G}$ are in range. Because of its smaller size and violation of the Helmholtz conditions, displacement from the coils center results in almost two orders of magnitude stronger deviations, than for the Feshbach coil. For a displacement of $2\,\mathrm{mm}$ it changes by $-0.4 \cdot 10^{-2}$ ($+0.8 \cdot 10^{-4}$) in the longitudinal (radial) direction.

The offset coils were wound directly on the Feshbach coil mount. For reasons of restricted space, for all three coil pairs the non-hollow flat rectangular wire ($2\,\mathrm{mm} \times 1\,\mathrm{mm}$) was employed. In order not to block additional optical access, they were placed in the dead angles of the Feshbach coils and the $\pm 45°$ vertically tilted axes. Here, the optical glass bonding permits shining (high power) laser beams, for it could permanently damage the bonding. The offset coils in x- and z-direction are of rectangular ($100\,\mathrm{mm} \times 50\,\mathrm{mm}$) shape

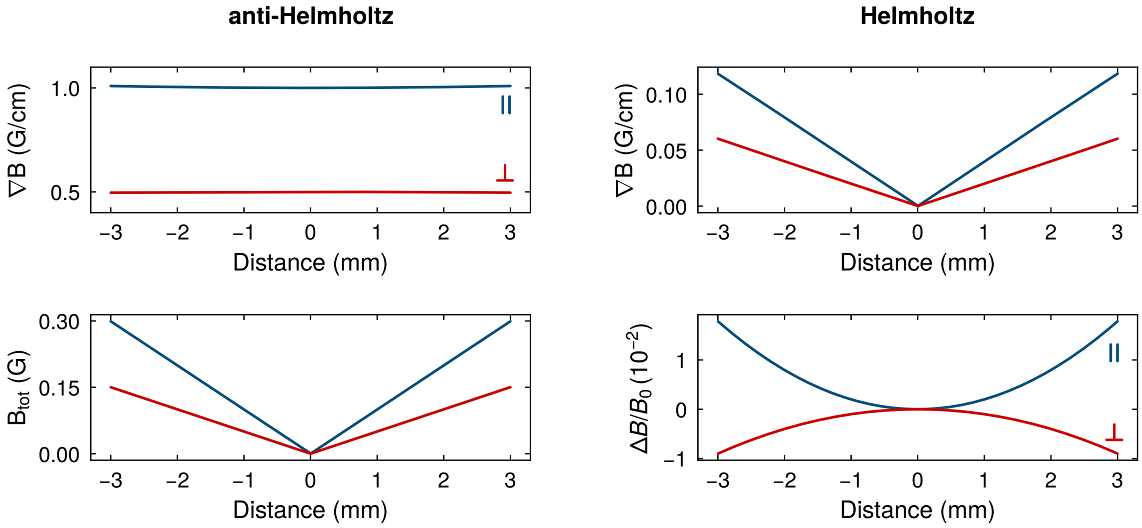

**Figure 4.13 Magnetic field of the spin-separation coils.** Magnetic (gradient-)field of the Feshbach coil pair in (anti-)Helmholtz configuration along their radial (⊥) and axial (∥) axes. In Helmholtz configuration the deviation from the central field ($\Delta B/B_0$) is in the order of $10^{-2}$ on the relevant scale. Simulations are done for central fields of $1\,\mathrm{G}$, respective $1\,\mathrm{G/cm}$. They provide a (gradient-)field of ($0.87\,\mathrm{G/cm/A}$) and $1.38\,\mathrm{G/A}$ in (anti-)Helmholtz configuration.

and bent along the curvature of the mount. With a spacing of $120\,\mathrm{mm}$ and three layers of three windings, $\pm 6.3\,\mathrm{G}$ are reached with $\pm 15\,\mathrm{A}$. The offset coils in y-direction is of round shape and wound around the Feshbach coils. They were wound with three layers of three windings as well. With an inner diameter of $153\,\mathrm{mm}$ with a spacing of $68\,\mathrm{mm}$ a field of $\pm 16\,\mathrm{G}$ for $\pm 15\,\mathrm{A}$ is reached. Using high current relays, the bipolar current supplies employed for the Li chamber's offset coils are used to drive the science chambers offset coils as well.

# Chapter 5

# Laser system

In the following chapter the laser systems employed for imaging, cooling and trapping are presented. The chapter is divided into two parts: the generation of resonant and far-offresonant light. The resonant light is employed to address the $D_1$- and $D_2$-line of Li at $671\,\mathrm{nm}$. The generated light is used in many different cooling stages: Optical Pumping / Transversal Cooling (OP/TC), Zeeman Slowing (ZS), Magneto-Optical Trap (MOT) and Gray Molasses (GM). Each stage requires frequency stabilized cooler and repumper light of sufficient power, exposed to the atoms from different axes. At the same time, dynamical tunability of the frequencies and powers are necessary. It is presented in Section 5.1 how these requirements are met in our system's architecture.

Generating and providing off-resonant light for Optical Dipole Traps face different challenges. High optical powers, accurate beam shaping and alignment together with precise power control are the main drivers for the laser system's design. In our dual-species experiment, the light for the ODTs at $1064\,\mathrm{nm}$ and $1070\,\mathrm{nm}$ can be shared between Er and Li. This can be either sequentially, when the optical power is dynamically switched between the Er and Li chamber, or when the atoms are exposed to the same laser beams at different positions in the chamber at the same time. For this reason, the setups in Section 5.2 are not restricted to Li only, but also incorporate the application for Er as well.

## 5.1 Generating resonant light - $671\,\mathrm{nm}$

In the following section the generation of the $671\,\mathrm{nm}$ light for optical cooling and absorption imaging of Li is presented. The general layout of the laser system is shown in Fig. 5.1. Here, only the system's major building blocks are displayed. The system is structured in three stages, which are well separated. An initial light generating stage hosting three External Cavity Diode Lasers (ECDLs) is followed by a stage for diagnostics, fiber couplings to frequency locking stages and the $1^{\mathrm{st}}$ amplification stage with Injection-Locks (ILs). In the following stage, the light is amplified again by $2^{\mathrm{nd}}$ stage ILs, split, frequency shifted, recombined and finally fibred to the experiment. More detailed descriptions of the individual blocks are given in the following sections.

Generally, the laser system is designed to be modular by employing many optical fibers, that separate the different blocks of the system. Additionally, the system relies on self-built lasers and amplifiers exclusively. Those two design choices help to have a system, that is easily serviceable. Drifts of the system are recovered by local optimization within the concerning building block only. Broken lasers are quickly exchanged with prebuild replacements, which keeps the downtime of the system to a minimum. At the same time, the self-built system proves to be a good low-cost alternative to commercial laser systems, that often only provide limited access to core components for the end-user.

The laser system is located on an optical table different from the one of the main experiment. The light is prepared well isolated from any sources of noise, and it is then fibred to the experiment. This separation allows the laser system to stay undisturbed and maintain a well thermalized and stable state for days.

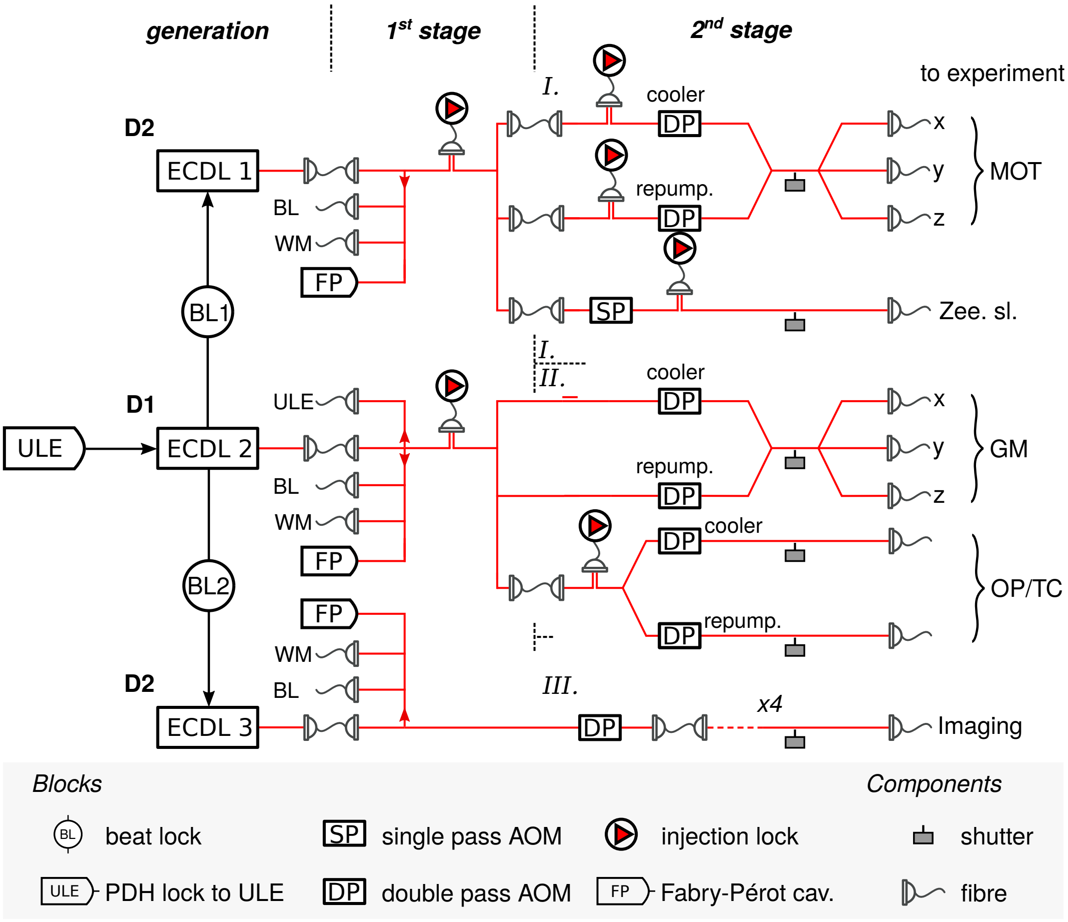

**Figure 5.1 General layout of the Li laser system.** Three ECDLs provide $D_1$ and $D_2$ light for optical cooling and absorption imaging. They make up the initial light generation stage of the system. After being fibred to the following stage, they all have a FP cavity and WM fiber port for diagnostics. They as well have fiber ports for the ULE and BL, and a $1^{\text{st}}$ stage IL amplification if needed. The $D_1$ ECDL is locked to the ULE-cavity and the two others are beat locked ($\sim 10\,\mathrm{GHz}$) to it. In the following stage, the light of ECDL1 & 2 is amplified again with four ILs for the MOT, ZS and OP/TC. The (double pass) AOMs control the frequency and intensity of the light. Mechanical shutters additionally provide full extinction of the resonant light before it is fibred towards the experimental table. The second $D_2$ ECDL provides independent light for imaging in four axes. The $2^{\text{nd}}$ stage is described in more detail in Fig. 5.2.

### General layout

The layout of the laser system presented in Fig. 5.1. Three External Cavity Diode Lasers (ECDLs) generate light for addressing the $D_1$- and $D_2$-line of Li. They form the basis of the laser system and present the initial light generation stage of the setup. See Section 5.1.1 for a detailed description.

ECDL 2 running on $D_1$ is frequency stabilized (locked) to an Ultra Low Expansion (ULE)-cavity with the Pound–Drever–Hall (PDH) technique. The ULE-cavity setup and the locking technique are described in more detail in Section 5.1.2. ECDL 2 provides the source light for optical cooling of the Gray Molasses (GM) and Optical Pumping / Transversal Cooling (OP/TC) stages operating on the $D_1$-line. This ECDL is the master laser of the system, as it provides the frequency reference for the other two ECDLs running on the $D_2$-line. They themselves are frequency stabilized to the $D_1$ ECDL by an offset beat of about $10\,\mathrm{GHz}$. This technique together with the optical and electronic setup is presented in more detail in Section 5.1.3.

ECDL 1 running on $D_2$ provides the source light for optical cooling of the Magneto-Optical Trap (MOT) and the Zeeman Slowing (ZS) stages. ECDL 3, also running on $D_2$, is exclusively utilized to provide light for absorption imaging. As it is used for this purpose only, its frequency is freely tunable without affecting any other stages of the system.

All ECDLs together with the required optics, are placed on individual breadboards. Two of them are laid on shock absorbing and vibration damping sorbothane. The mechanical isolation was needed to stop cross-talk of the ECDLs' piezos, when activating the lock of one of the lasers.

After being fibred, the output light of the ECDLs are monitored by two diagnostics tools. One of them is a Wave-Meter (WM)[1], which allows to coarsely set the laser to the desired output frequency by $600\,\mathrm{MHz}$. This is precise enough to initially set the laser frequency close to the locking point. The other diagnostics tool is a Fabry-Pérot (FP) cavity. The transmission signal of a scanning FP cavity allows detecting undesired multi-mode lasing of the ECDL (see Section A.6 for more information).

As ECDL 1 & 2 provide too little output power for reasonable optical cooling performances, a 1st stage amplification for each one is employed. This is done with high power Laser Diodes (LDs), that are injection locked to the low power seed light of the ECDLs (see Section 5.1.4). For convenience these systems are called Injection-Lock (IL) from now on.

In the following 2nd stage, the light of the ECDLs is split in many paths, amplified, frequency shifted and recombined to provide the light for the MOT, ZS and imaging operating on the $D_2$-line and the GM and OP/TC operating on the $D_1$-line. Its optical setup is quite complex and presented in detail in Fig. 5.2. Here, a 2nd stage of ILs is employed to generate enough optical power. The ILs are designed as modular stand-alone devices, that are easily placed and exchanged by a single fibre coupling only. The locking technique, typical performance and a detailed optical and electronic setup is presented in Section 5.1.4. Here, a focus to our new locking technique, that leads to a well-thermalized state is set.

The Hyperfine splitting of the ground state of Li often requires having both cooler and repumper overlapped in one beam. As the splitting is only $228\,\mathrm{MHz}$ (see again Fig. 3.1), the frequency gap is easily bridged with standard Acousto-Optic Modulators (AOMs). The setup relies on three types of AOMs with central frequencies of $80\,\mathrm{MHz}$, $100\,\mathrm{MHz}$ and

---

[1] HighFinesse Laser and Electronic Systems GmbH WS6-600.

200 MHz[2]. They achieve a first order diffraction efficiency of 90% for single-pass and 80% for double-pass configuration. The AOMs in double-pass configuration are used for fast dynamical control of the frequency and the intensity of the light being sent to the atoms. As the AOMs are not capable to fully extinguish the laser light, mechanical shutters are employed. They fully block the resonant light, to avoid its heating effect on the atoms when they are ultracold already.

The 2**nd** stage of the ECDL 1 path provides the light for the MOT and ZS. For the MOT the light for cooler and repumper was already split and fibred in the previous stage. Both are again amplified with an IL, that delivers $\sim 100\,\mathrm{mW}$ of power for each. Then the cooler and repumper light pass AOMs in double-pass configuration, before being overlapped on a Polarizing BeamSplitter (PBS) cube. The overlapped cooler and repumper light is of orthogonal linear polarization. A subsequent $\lambda/2$-waveplate turns the polarization angle by $45\,^\circ$ to have an equal amount of light being transmitted and reflected by the next PBS[3]. The transmitted light is coupled to the z-axis fiber. The reflected light is split equally again and then coupled to the x- and y-axis fibers.

Fiber couplings were optimized with the mirror pairs in front of each fiber for the cooler light only. Here, coupling efficiencies of $\sim 64\%$ are achieved for all of them. The coupling of the repumper light was optimized with the mirror pair in front of the overlap PBS cube. Due to differences in the optical path to the fibers, it is not possible to have fully optimized couplings to all of them at the same time. The repumper coupling efficiencies spread over an interval of 47% to 60%.

For Zeeman Slowing, the light coming for the 1st stage is the same as for the MOT. The light is first frequency shifted by a single pass AOM and then amplified by an IL. Here, it is possible to invert the order of amplification and frequency shifting, because there is no need for dynamical frequency tuning and power control of the ZS beam. A mechanical shutter to open or block the optical path provides sufficient control. This setup allows retaining more of the 85 mW optical power provided by the IL, of which in the end 65 mW is fibre coupled towards the experiment.

The 2**nd** stage of the ECDL 2 path provides the light for the GM and OP/TC stages. Initially, it was planned to *reuse* the MOT setup for the GM, by switching the light coming from the 1st stage from ECDL 1 to ECDL 2 as in [169]. This would have been an efficient approach, because the MOT and GM work with the same optics at the experimental table and are never needed simultaneously. Unfortunately, seed switching unlocked the 2nd ILs for intermediate to high output powers[4]. For this reason, the GM stage was built separately. It does not have a 2nd satge IL, but receives 32 mW of input light free space from the stage before. The light is split in a cooler (80%) and repumper (20%) path, frequency shifted, recombined and fibered analog to the one of the MOT. Because of differences in the optical paths, the optical powers coupled to the different fibers vary as well.

The light for OP/TC coming from the 1st stage is amplified by an IL to 78 mW and equally split for cooler and repumper. After frequency shifting with an AOM in double-pass configuration, the two beams are coupled to individual fibers. For both about 18 mW of optical power is guided to the experimental table.

---

[2] Gooch & Housego AOMO 3080-125 / 3100-125 / 3200-125

[3] The polarization of the repumper light has a non-negligible component of circular polarization after being reflected by the overlap PBS. This leads to a non-equal cooler and repumper power splitting ratio at the following PBS.

[4] In [169] the $D_1$ to $D_2$ switching was demonstrated for rather low currents and output powers only, because additional amplification with a consecutive TA was provided as well.

ECDL3, which is used for absorbing imaging exclusively, provides sufficient output power and therefore no amplification of its output light is needed. Moreover, amplification of the light is not desired. Non-perfect amplification by the IL results in parasitic frequency modes admixture, which are non-resonant and therefore bias the detected optical depth. Here, an AOM in double-pass configuration is used to send the fast imaging pulses. A subsequent fiber guides the light to a distribution bread board laying on sorbothane. The light is split and coupled to four individual fibers allowing to have two absorption imaging axes at the MOT- and science chamber. Only little power of 150 $\mu$W is needed to be fiber coupled to the experiment here.

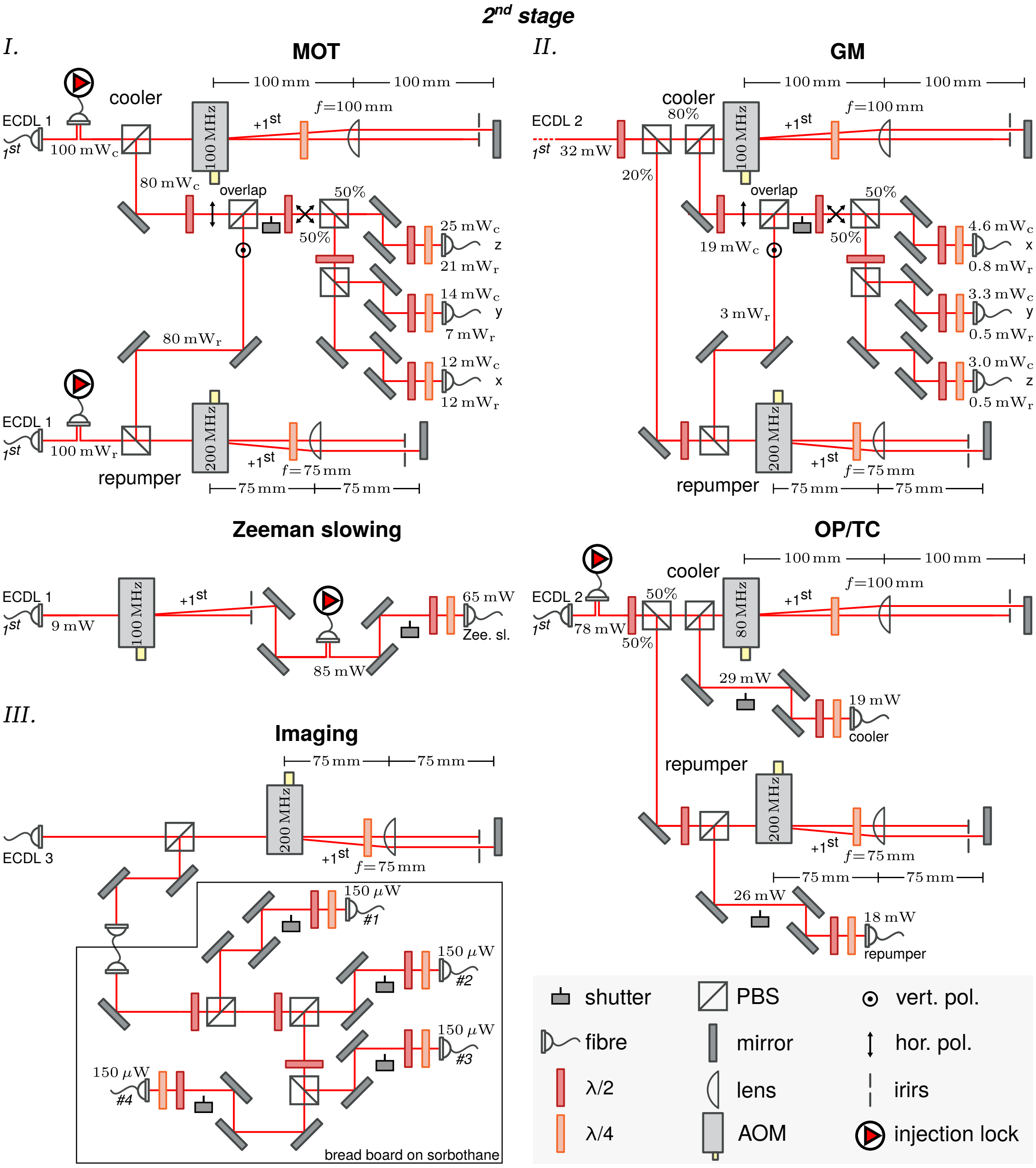

**Figure 5.2 Laser system 2nd stage.** Detailed layout plan of the 2nd of the laser system presented in Fig. 5.1. Assignment of *I.*, *II.* and *III.* as in there. See text for detailed description.

### Frequency scheme

A detailed frequency scheme of the Li laser system is presented in Fig. 5.3. Here, the laser light frequencies are given as *detunings* from to the cooler/repumper transition of the $D_1$- and $D_2$-lines. With this the $10.056\,\mathrm{GHz}$ fine splitting of the lines is removed and the readability of the scheme is increased. The Hyperfine splitting of the $D_2$-line's excited state $2^2P_{3/2}$ is small compared to the linewidth and is therefore omitted (see again Fig. 3.1). For the $D_1$-line, the HF splitting of the excited state $2^2P_{1/2}$ is non-negligible. Here, the frequencies are given with respect to the $2^2P_{1/2}$ $F = 3/2$ state transition.
The bare output frequencies of the ECDLs are all red detuned to the transitions. After being split into the different paths, the light is frequency shifted to the final detunings with AOMs mostly in double-pass configuration. The denoted AOM driving frequencies for MOT, ZS, GM and OP/TC are the values for optimal static operation of the respective cooling stage.
As already explained earlier, the $D_1$ ECDL 2 is the main frequency reference of the system as it is locked to the ULE-cavity. Its detuning to the $D_1$-line is denoted with $\Delta f_{\mathrm{E2,\,D1}}$. The other two $D_2$ ECDLs 1 & 3 are locked relative to it by a frequency offset. Their detunings to the $D_2$-line are denoted with $\Delta f_{\mathrm{E1,\,D2}}$ and $\Delta f_{\mathrm{E3,\,D2}}$.
The locks of the three ECDLs require stable reference frequencies. They are provided by a Direct digital synthesizer (DDS)[5] system with a $10\,\mathrm{MHz}$ reference clock[6]. Tuning the DDS output frequencies, the detunings of the ECDLs are tuned as well. For ECDL 2 the detuning from the $D_1$-line is given by

$$\Delta f_{\mathrm{E2,\,D1}} = +2 \cdot (f_{\mathrm{PDH,DDS}} - f_0). \tag{5.1}$$

The frequency $f_{\mathrm{PDH,DDS}}$ is provided by the DDS and is fed into the locking electronics of the PDH lock. The offset frequency $f_0$ is given by the length of the ULE cavity. It is the only frequency, that has to be determined experimentally. The offset frequency was found to be $f_0 = 224.15\,\mathrm{MHz}$. With this the DDS frequency for our system is $f_{\mathrm{PDH,DDS}} = 301\,\mathrm{MHz}$.
Knowing the detuning of ECDL 2 to the $D_1$-line, the detunings of the ECDLs 1 & 2 to the $D_2$-line can be determined as well:

$$\begin{aligned}\Delta f_{\mathrm{E1,D2}} &= \Delta f_{\mathrm{E2,\,D1}} - 10 \cdot (f_{\mathrm{BL1,DDS}} - 16.8\,\mathrm{MHz}),\\ \Delta f_{\mathrm{E3,D2}} &= \Delta f_{\mathrm{E2,\,D1}} - 10 \cdot (f_{\mathrm{BL2,DDS}} - 16.8\,\mathrm{MHz}).\end{aligned}$$

The frequencies $f_{\mathrm{BL1,DDS}}$ and $f_{\mathrm{BL2,DDS}}$ are provided by the DDS and are fed into the BL1 system for ECDL 1 and into the BL2 system for ECDL 3 respectively. The $-16.8\,\mathrm{MHz}$ offset originates from the chosen layout of the BL system and is not of deeper physical origin. The DDS frequencies for the presented setup are $f_{\mathrm{BL1,DDS}} = 22.13\,\mathrm{MHz}$ and $f_{\mathrm{BL2,DDS}} = 41.43\,\mathrm{MHz}$. More details of the frequency locking schemes are presented in Section 5.1.2 and Section 5.1.3.

---

[5] Analog Devices AD9910

[6] Stanford Research Systems FS725 10 MHz Rb Frequency Standard

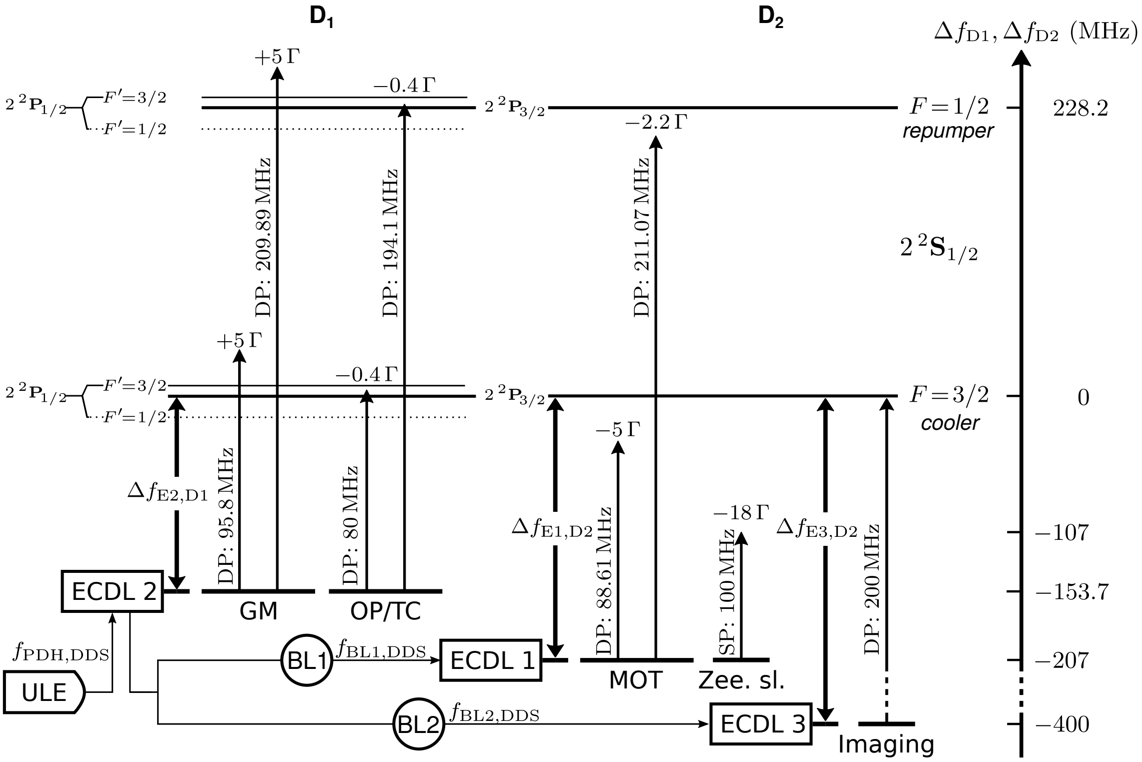

**Figure 5.3 Frequency scheme of the Li laser system.** The frequency anchor of the laser system is ECDL 2 ($D_1$), which is locked to the ULE-cavity and tunable with $f_{\mathrm{PDH,DDS}}$. ECDL1 / 3 ($D_2$) are frequency stabilized to it by an offset frequency, which is tunable with $f_{\mathrm{BL1,DDS}}$ / $f_{\mathrm{BL2,DDS}}$ fed to the BL1 / 2 systems. The output frequencies of the ECDLs and the AOM shifted frequencies of the cooler and repumper beams from the different optical cooling stages are given with respect to the $D$-line they are closely detuned to. The transitions from the $F = 1/2$ and $F = 3/2$ of the $2^2S_{1/2}$ ground state are called cooler and repumper. In contrast to the HF splitting of the $2^2P_{3/2}$ excited state of the $D_2$-line, the $2^2P_{1/2}$ splitting of $D_1$ is non-negligible and therefore displayed.

### 5.1.1 ECDL

An External Cavity Diode Laser (ECDL) consists of a Laser Diode (LD), which is placed in an external optical cavity. The ECDL presented in the following is a design, that was further developed in the group in the last years [170, 171]. Its schematics, characteristic output and final implementation into the laser system are presented in Fig. 5.4.

The LD[7] is placed inside a collimation tube[8] with a strongly focusing aspherical lens. The collimated beam is again focused onto a back reflecting mirror[9] with a reflectivity of 30%. The mirror being placed in the focal plane of the lens is commonly referred to as *cat-eye configuration*. Some part of the light is back reflected into the LD and thus an optical cavity is formed. In principle, this cavity supports equally spaced optical modes, which are amplified chaotically by the lasing medium. For this reason an additional interference filter[10]—which basically is a cavity itself—is placed in the optical path, to select a single mode.

---

[7] Toptica Eagleyard EYP-RWE-0670'

[8] Thorlabs LT230-B

[9] Laseroptik L-17265

[10] Laseroptik L-10813-01

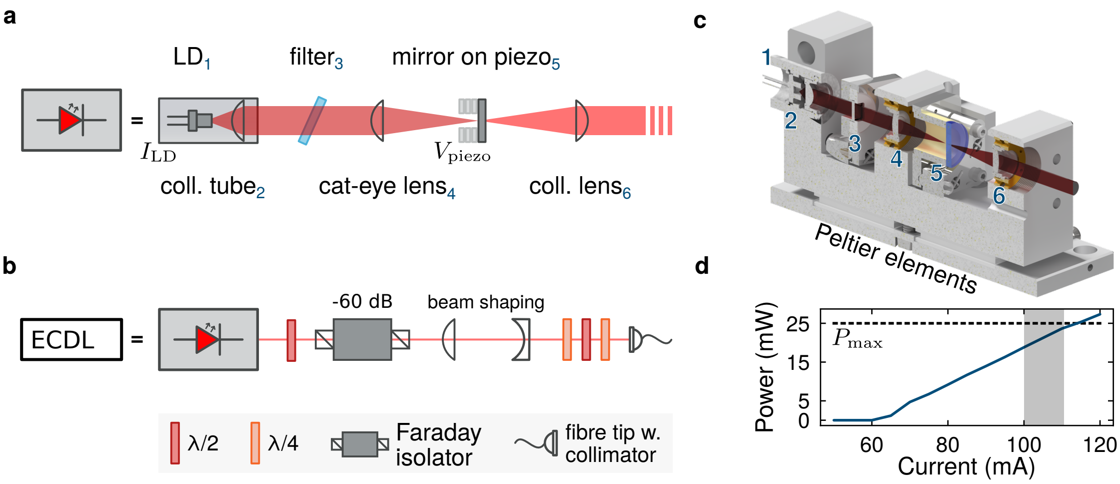

**Figure 5.4** **ECDL setup and characterization.** **a.** Schematic structure of an ECDL: A cavity is formed with a collimated LD together with a lens and a back reflecting mirror in cat-eye configuration. Single mode selection is done with an optical filter. The out coupled light is collimated by a second lens. **b.** The generated output light passes a FI and the optical mode is shaped with a combination of a cylindric and spherical telescope. These elements make up the ECDL building block from Fig. 5.1. **c.** A render (cut view) of the laser body. The elements are numbered as in a. Active temperature control of the laser body is provided with two Peltier elements. A fully closed plexiglass housing and the electric circuit protecting the LD is omitted for simplicity. **d.** A typical output power curve of an ECDL is shown. The maximum rated power $P_{\mathrm{max}}$ is represented by a dotted line and the typical operation interval with a shaded area.

The optical path of the cavity and consequently the emitted wavelength have two tuning knobs in our setup. The cat-eye mirror is mounted on a ring piezo stack. Modulation of the applied voltage $V_{\mathrm{piezo}}$ actuates the mirror changing the length of the cavity. This provides a slow, but high tuning range control of the wavelength. Altering the current $I_{\mathrm{LD}}$ provides a fast, but low tuning range control. Here, a modulation of the current changes the charge carrier density in the lasing material altering the optical path length of the resonator. The LD is driven by a laser diode controller[11] with an electric protection circuit employed before the LD. This protection circuit also allows modulating $I_{\mathrm{LD}}$ proportional to an applied voltage. The two laser frequency tuning knobs are later used for active stabilization of the output frequency.

A rendered representation of the final setup is shown in Fig. 5.4c. Passive temperature stabilization of the laser body itself is provided by a plexiglass housing (not shown), that blocks air flow and turbulences inside the resonator. To be fully closed, the laser beam exits the system through an anti-reflection coated window glued to the housing. Thermal stabilization and temperature tuning of the laser body is assured by two Peltier elements driven by a temperature controller[12].

A Faraday Isolator (FI)[13] is placed at the output of the ECDL. It acts as an optical diode, that blocks light from being back reflected from following optics into the laser, disturbing the system. As the beam profile of the LD is strongly elliptic, beam shaping with a cylindric next to a spherical telescope is needed to achieve $\sim 50\%$ coupling efficiency.

---

[11] Toptica DCC-110

[12] Toptica DTC-110

[13] Thorlabs IOT-5-670-VLP (-57 dB), Qioptic FI-670/5TVC (-60 dB)

The output power performance and point of operation is similar for all three ECDLs. Running on $100 - 110\,\mathrm{mA}$ results in an output power of $\sim 22\,\mathrm{mW}$, which is well below the rated maximum. A typical power curve is shown in Fig. 5.4d. Power loss due to the FI reduces the available power and ultimately $\sim 7.5\,\mathrm{mW}$ is coupled to the fiber and sent to the next stage.

### 5.1.2 PDH lock to a ULE cavity

Stable frequency reference sources are needed for locking the many lasers of the ErLi experiment. Stabilizing lasers to optical modes of Ultra Low Expansion (ULE) cavities is a standard approach in modern AMO experiments. The Pound–Drever–Hall technique is usually employed to actively stabilize lasers to the cavity modes. It gains more and more in popularity over 'traditional' spectroscopy locks [172]. It is especially suitable to lock lasers used for addressing narrow transitions [173, 174].

#### ULE cavity

Stable optical modes to lock to require a stable optical resonator. A combination of different measures are needed to achieve this: vacuum environment, precise temperature control and vibrational isolation.
The ULE cavity[14] of the ErLi experiment consists of a cylindric body cavity spacer with four bores. Each bore is equipped with a set of plane and curved mirrors attached to it, forming the optical resonator. They are separated by $L = 10\,\mathrm{cm}$ providing a free spectral range of $\nu_{\mathrm{FSR}} = c/2L \approx 1.5\,\mathrm{GHz}$ [175]. The mirrors' substrate is of the same ULE material as the cavity spacer and optically bond to it. The mirror pairs come in two different sets of coatings[15], to cover the relevant wavelengths needed. The finesse of the cavity $\mathcal{F} = \nu_{\mathrm{FSR}}/\Delta\nu_{\mathrm{FWHM}}$ is the ratio of the free spectral range and the linewidth $\Delta\nu_{\mathrm{FWHM}}$ of the cavity. It also is obtained as $\mathcal{F} = \pi\sqrt{R}/(1-R)$ with the reflectivity $R$ of the mirrors. With the specified reflectivity for $671\,\mathrm{nm}$ by the manufacturer, a finesse of $\mathcal{F}_{671} \approx 16,500$ is calculated. Therefore, a linewidth of $\Delta_{\mathrm{FWHM,671}} \approx 91\,\mathrm{kHz}$ of the ULE cavity is expected. For three other wavelengths the finesse of the ULE cavity was measured: $\mathcal{F}_{770} \approx 10,000$ (for $\lambda = 770\,\mathrm{nm}$) [176], $\mathcal{F}_{841} \approx 15,000$ (for $\lambda = 841\,\mathrm{nm}$) [136] and $\mathcal{F}_{1166} \approx 13,000$ (for $\lambda = 1166\,\mathrm{nm}$) [177]. Here, always reasonable matching to the finesse obtained from the specified reflectivities were found.
The ULE cavity is placed in a vacuum environment (see Fig. 5.5a). With the employed ion pump[16] a pressure of $\sim 10^{-7}\,\mathrm{mbar}$ is reached. Low ambient gas pressure is needed for a stable optical path length of the cavity. The setup is an in-group design for a one-bore ULE cavity [178] and was adapted to our four-bore one [176]. The main body rests on Viton damped PEEK wedges. Two thermally well isolated copper shields surround the cavity. Thermalization of the two and the ULE cavity is mainly due to black-body radiation creating a homogenous temperature distribution over the ULE material. Here, thermal stability also benefits from the vacuum environment. The outer copper shield rests on a Peltier element, that is thermally well coupled to the vacuum housing, allowing for temperature

---

[14] Stable Laser Systems SLS-6010-1-4bore

[15] Coating 1: $671\,\mathrm{nm}$, $770\,\mathrm{nm}$-$802\,\mathrm{nm}$, $1166\,\mathrm{nm}$. Coating 2: $770\,\mathrm{nm}$-$841\,\mathrm{nm}$, $1030\,\mathrm{nm}$-$1070\,\mathrm{nm}$

[16] Gamma Vacuum Titan 3S

stabilization[17] of the cavity and its enclosure. The vacuum housing together with the optical elements needed are placed on a vibration isolation stage[18], to decouple from acoustic noise of the optical table.

For best frequency stability, the ULE material is operated at the zero expansion point temperature $T_c$. Here, the coefficient of thermal expansion possesses a zero crossing, resulting in a first order insensitivity of the cavity length to temperature deviations [179]. It is dependent on the material batch and therefore has to be determined experimentally. To do so, a laser running on $770\,\mathrm{nm}$ was frequency stabilized to an optical mode of the ULE cavity. The employed locking technique is described in the subsequent section. The beat-node frequency $f_{\text{beat}}$ to another stable laser source[19] was recorded for different temperatures $T$ of the ULE material, displayed in Fig. 5.5b. Here, the long thermalization time of the thermally well shielded system has to be taken into account. An exponential fit to the beat-node for a time interval of at least $12\,\mathrm{h}$ after setting a new temperature was employed to extract the thermalized state value. With this, a $1/e$-thermalization time of $\sim 8\,\mathrm{h}$ was found as well. This means, that the thermalized state is approached by $95\%$ after a settle time of $24\,\mathrm{h}$. A quadratic fit [180] to the data with

$$\Delta f_{\text{beat}}(T) = a(T - T_c)^2 + b$$

determined the zero expansion temperature point of our cavity to be $T_c = (35.10 \pm 0.07)\,^\circ\mathrm{C}$.

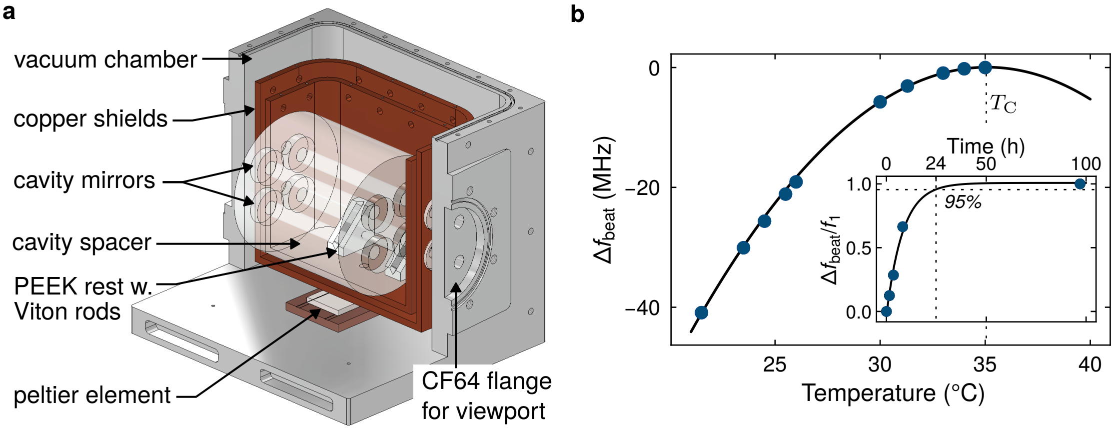

**Figure 5.5 ULE vacuum setup. a.** Rendered (cut-) view of the ULE cavity and vacuum setup. Lids, windows, and the ion pump are not shown here. The four-bore ULE cavity is laying on PEEK rests with Viton rods padding. It is placed well thermally isolated inside two copper shields. A Peltier element allows controlling the temperature of the cavity via the outer copper shield. The four cavities are optically accessible with holes drilled in the shields and vacuum housing. Having wedged surface flanges for the vacuum housings viewports prevents the formation of an extra cavity. **b.** Beat frequency of a laser locked to the ULE cavity with a stable laser source for different temperatures. The zero expansion temperature point $T_c = (35.10 \pm 0.07)\,^\circ\mathrm{C}$ is determined with a quadratic fit to the data. Thermalization of the system is visualized in the inset. Here, the change in beat frequency was recorded after a new temperature was set.

---

[17] Meerstetter TEC-1092

[18] Accurion AC810038

[19] Spectroscopy lock to potassium line of the neighboring lab

### PDH locking technique

Having the ULE cavity as a stable frequency reference, the Pound–Drever–Hall (PDH)-technique is employed to generate a usable error signal for locking [181, 182]. The bare peak-like transmission or reflection signals of the ULE cavity cannot be made used of. Proportional–Integral–Derivative (PID)-controllers require an error signal, that ideally is a flank crossing zero (or any desired stable offset). Therefore, stabilizing to the peak of a transmission/reflection signal is not possible. A side-of-fringe lock, where the frequency is stabilized to a point in the flank of the signal is prone to power drifts and therefore not suitable for precise locking [183].
The PDH-technique represents a clever approach, that with the help of some optical and electronic components, derives an error signal to lock spot on the cavity resonance. Its working principle is discussed in great detail in [184]. In the following, only the essential points of the PDH-technique are explained. The presented setup is for locking ECDL 2 running on $671\,\mathrm{nm}$ (see Fig. 5.6), but its principles are generally valid.
On the optics side a fibre Electro–Optic Modulator (EOM)[20] modulates the phase of the electric field by $8\,\mathrm{MHz}$, creating sidebands. Demodulating the reflection signal of the light coupled to the ULE cavity with the same frequency provides the characteristic PDH-signal with a steep zero crossing flank at the resonance position (see Fig. 5.6b). As this would only allow for locking the laser to the bare cavity resonances (carriers), the EOM is modulated with an additional frequency component. The additional "large" sidebands create PDH-signals, which are offsetted to the carriers by their modulation frequency. This allows to lock the laser at any point between neighboring cavity modes. To cover the full free spectral range $\nu_{FSR} \approx 1.5\,\mathrm{GHz}$, modulation frequencies for the large sideband up to $\nu_{FSR}/2 \approx 750\,\mathrm{MHz}$ are needed. As our DDS has an output range limited to $f_{\mathrm{PDH,DDS}} \leq 400\,\mathrm{MHz}$ a frequency doubler is employed. The electronic components[21] used for generating the signal are presented in Fig. 5.6.
The PDH-signal is fed to PID-controllers, to provide feedback. A "slow" in-house built controller acts on the piezo mirror of the ECDL and accounts for drifts in the laser frequency. High frequency feedback is provided by a fast analog controller (FALC[22]) modulating the current of the LD. The PDH-lock of ECDL 2 proves to be robust against perturbations. In the locked state, the laser shows frequency excursions over the entire locking flank of the PDH-signal. This still limits the frequency deviation to roughly the cavity linewidth of $90\,\mathrm{kHz}$, which is well below the $2\pi \cdot 6\,\mathrm{MHz}$ linewidth of the addressing line.

## 5.1.3 Beat lock

Having ECDL 2 ($D_1$) locked to the ULE cavity as a stable frequency reference, its output light is now made use of as a stable frequency reference for locking the other two ECDLs ($D_2$). The locking technique, which from now on is simply referred to as Beat Lock (BL), stabilizes the beat frequency of ECDL 1 with ECDL 2 (BL1) and ECDL 3 with ECDL 2 (BL2)

---

[20] JENOPTIK PM600

[21] Components used for EOM modulation and PDH-signal derivation (see Fig. 5.6a)
DDS path: Trafo: FTB-1-1+, Amp$_1$: ZFL-500HLN+, Doubler: MK-2, Filter: SLP-800, Amp$_2$: ZFL-1000H+, Combiner: ZFSC-2-2-S. Generator: Rigol DG1022Z
PD path: Amp3: ZFL-1000LN+, Mixer: ZFM-3-S, Filter: BLP-2.5

[22] Toptica FALC 110

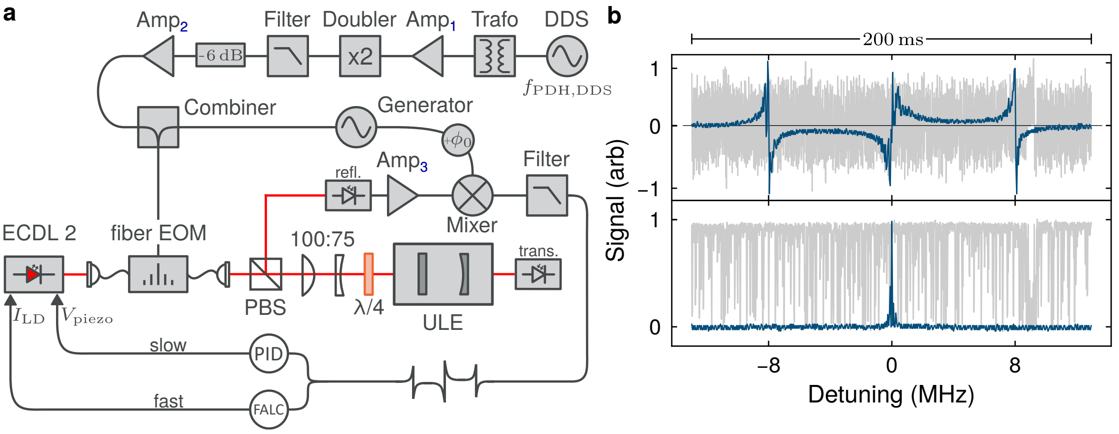

**Figure 5.6 PDH setup and signals. a.** Schematics of the optical and electronic setup to derive the PDH-signal and to lock the ECDL 2 to the ULE cavity. Sidebands are generated by modulating with an EOM. Sidebands of $8\,\mathrm{MHz}$ to provide an initial PDH-signal is combined with a frequency from the DDS to create PDH-signals with a variable offset from the carrier. The PDH-signal obtained from demodulating the reflection PD signal is fed to PID-controllers, providing feedback to the laser. **b.** PDH-signals (top) for a frequency scan over the cavity resonance (blue) and in the locked state (gray) for $200\,\mathrm{ms}$. The simultaneously recorded transmission signals are shown below. Frequency excursions in the locked state of about $90\,\mathrm{kHz}$ proved not to influence the stability of system.

to an externally set value [185]. The optical and electronic setup is shown in Fig. 5.7. The setups for BL1 and BL2 only differ in the beat frequency set in the end. This allows to share components between the two.

As a first step, the beat signals between ECDL 1 with ECDL 2 ($f_{\mathrm{E1,E2}}$) and ECDL 3 with ECDL 2 ($f_{\mathrm{E3,E2}}$) are generated. To do so, the optical modes of the laser beams are overlapped by coupling them to the same fibres. Here, it has to be taken care, that the laser beams' polarization is the same before being coupled. The overlapped modes are outcoupled and focused on PDs[23] with a bandwidth of $12.5\,\mathrm{GHz}$. Little power of $\sim 100\,\mu\mathrm{W}$ per beam is sufficient here. High detection speeds are needed, as the beat frequencies are of the order of the $^2P$ excited state fine splitting ($\sim 10\,\mathrm{GHz}$). In this frequency regime the wavelength of the signals are comparable to standard length coax cables, causing deterioration by internal reflections. For this reason, the two beat signals are fed to an in-house built mixer box located right next to the PDs. In the box, the beat signals are amplified[24] and then mixed[25] with a stable $10.224\,\mathrm{GHz}$ local oscillator[26]. The local oscillator's output frequency is split[27] to have it in both BL paths. Mixing the fast beat signals with the local oscillator, effectively leaves one with the frequency difference of the two: $\tilde{f}_{\mathrm{E1,E2}} = |f_{\mathrm{E1,E2}} - 10.224\,\mathrm{GHz}|$ and $\tilde{f}_{\mathrm{E3,E2}} = |f_{\mathrm{E3,E2}} - 10.224\,\mathrm{GHz}|$.

The down mixed signals are now slow enough to be fed to the phase lock boxes with standard coax cables. Here, the signal frequencies are pre-scaled by a factor $^1/_{10}$ with a

---

[23] EOT ET-4000
[24] ZX60-123LN-S+
[25] ZX05-153-S+
[26] MKU LO 8-13 PLL
[27] ZX10-2-126-S+

frequency divider[28]. A phase detector chip[29] provides an error signal, that represents the phase difference between the pre-scaled beat signal and the reference frequency signal $f_{\mathrm{BL1,DDS}}$, $f_{\mathrm{BL2,DDS}}$ (see Fig. 5.7b). The steep locking flank is given by a phase difference of $2\pi$. For further phase differences the error signal stays on the flanks extreme value, providing a high locking range.
The error signal is fed to an internal PID-controller circuit to provide fast feedback to the ECDL via modulation of the LD's current. An external slow PID-controller (same as for the PDH lock) provides feedback by modulating the ECDL's piezo. As the lock actively minimizes the phase difference, the beat frequency is stabilized as well. Monitoring the frequency spectrum of the locked beat signal shows a main non-resolvable peak ($< 10\,\mathrm{kHz}$). Servo bumps at $0.5\,\mathrm{MHz}$ are due to the locking feedback.

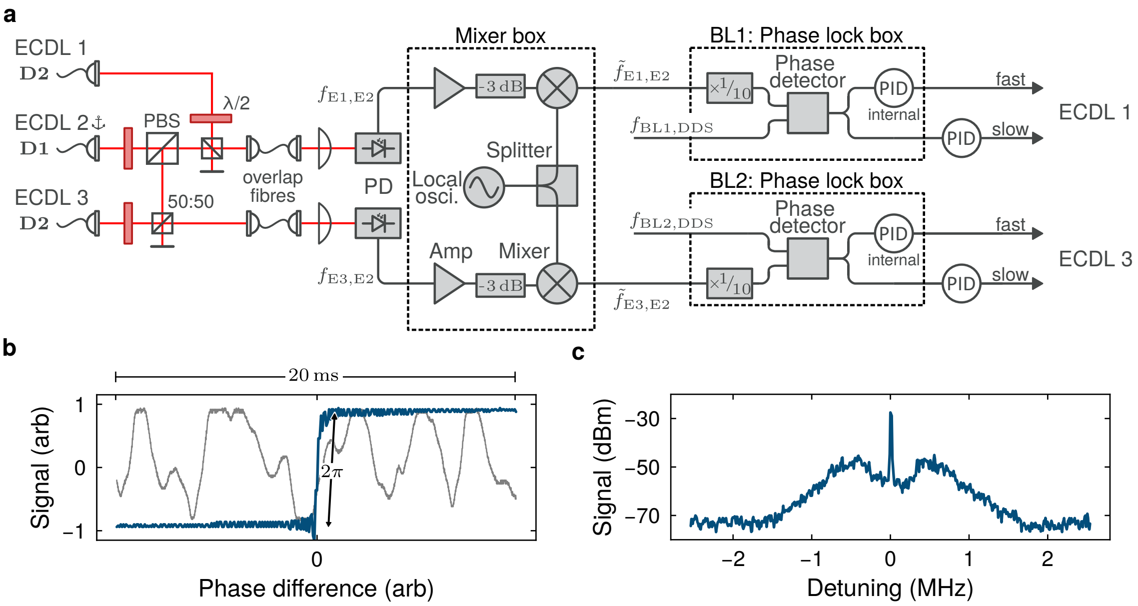

**Figure 5.7 Beatlock setup. a.** Electric and optical setup for beat locking ECDL 1 to ECDL 2 (BL1) and ECDL 3 to ECDL 2 (BL2). The beat signals are generated by focusing the overlapped modes to PDs. The fast ($\sim 10\,\mathrm{GHz}$) beat signals are mixed down with a local oscillator of similar frequency. The down mixed beat signals are fed to the phase lock box. Here, the signals are divided by factor 10. A phase detector generates an error signal, that represents the phase difference between the beat signal and a reference frequency. To provide feedback to the laser, the error signal is passed to an internal fast PID-controller and an external slow PID-controller circuit. **b.** Error signal (blue) sweep of the beat signal frequency over the reference frequency. The fast jump represents a phase change of $2\pi$. The error signal for the locked state is displayed in gray. The lock parameters were optimized to obtain a single narrow beat frequency peak. **c.** Frequency spectrum of the locked state beat signal given as detuning from the reference frequency.

---

[28] Onsemi MC12080D

[29] Analog Devices AD9901

### 5.1.4 Injection locking

Injection locking generally refers to the synchronization phenomena of a free running oscillator to a second oscillator, when disturbed by it [186, 187]. Its principle is applicable to e.g. electrical oscillators for synchronization to a common reference clock frequency [188]. The concept of injection locking also applies to optical oscillators. By injecting seed light into a free running laser, its output is forced to run on the seed's frequency [189]. In fact, the laser is phase- and frequency locked to the seed light. The beforehand free running laser usually is referred to as the *slave* laser. Amplification of weak seed light by forcing a powerful slave laser onto its output mode has become a common tool in telecommunication technologies [190].

The injection locking technique as well is made great use of in AMO experiments. Generating narrow-line and precisely frequency stabilized light for optical cooling, typically performs best for lasers of modest output power. Amplifying the light with the injection locking technique poses an effective approach to deliver sufficient optical power. Injection locked single-frequency lasing with output powers of $220\,\mathrm{W}$ have been demonstrated for a high-power ring oscillator [191]. A technically less challenging approach is injection locking of high power Laser Diodes (LDs), that typically output $0.1\,\mathrm{W}$ to $2\,\mathrm{W}$. Similar power levels are reached by amplification with Tapered Amplifiers (TAs), which is also widespread in AMO. Technical advances in the last years made high power LDs commercially available, that cover almost the entire visual spectrum, reaching from the IR to the UV regime. The optical spectrum covered by TAs however does not reach in the blue. It starts in the red and extends into the IR regime[30].

With rising popularity of alkaline-earth and alkaline-earth like atoms, the need for light amplification in the blue spectrum rises [61, 192, 193]. Many of these atoms feature brought ($\sim 2\pi \cdot 30\,\mathrm{MHz}$) transitions suitable for optical cooling: ytterbium at $399\,\mathrm{nm}$ [194], erbium at $401\,\mathrm{nm}$ [139] and strontium at $461\,\mathrm{nm}$ [195]. Here, amplification with injection locked high-power LDs can be made use of, as it is done for optical cooling of erbium in our experiment [74].

A major drawback of amplification with high-power LDs however is, that a stable and optically pure injection locked state is only achieved for narrow windows of the slave LD's current $I_{LD}$. The position of these windows strongly depend on the LD's state of thermalization. At the same time, the injection locked state is easily lost due to external disturbances. The loss of a stable injection locked state changes the state of thermalization. There is a great variety of active locking techniques to maintain the injection locked state [196–198]. They all come with a nonnegligible amount of overhead equipment, which hinders their scalable employment. At the same time, these different techniques often rely on specific properties of the LD they had been demonstrated on.

In the course of building the Li laser system, we developed a passive locking technique to achieve and maintain a well thermalized state of the slave LD [199]. This new technique relies on periodic re-optimization of the injection locking point. It is presented in the following sections for amplifying $671\,\mathrm{nm}$ light. Its principles are applicable independent of the specific slave LD and have been successfully employed for $401\,\mathrm{nm}$ [74], $461\,\mathrm{nm}$ and $489\,\mathrm{nm}$ in our group. On the 29 October 2024, a patent for our new technique was applied for under the application number EP24209446.4.

---

[30] Spectral range (with some gaps) of commercially available TAs: $632\,\mathrm{nm}$ to $1590\,\mathrm{nm}$.

### Injection locking for $671\,\mathrm{nm}$

Initially, for the laser system of Li, amplification of the light provided by the ECDLs was planned to be done with TAs. Amplifying the $671\,\mathrm{nm}$ light with TAs is common and reliable in ultracold atoms experiments with Li atoms [137, 200]. A shortage in commercially available TA chips at the beginning of the built-up stage (2020/21) of the laser system required switching to an alternative amplification resource. This alternative was found in a LD[31] providing up to $210\,\mathrm{mW}$ at $670\,\mathrm{nm} - 680\,\mathrm{nm}$.

The employed configuration of the injection lock setup is the so-called reflection type [190]. The optical setup together with the electronics used for our locking technique are depicted in Fig. 5.8a. A FI[32] is used as an optical circulator to overlap the seed and slave light. The seed light is reflected on the output side PBS of the FI and sent through it opposite to the usual transmission direction. It is then coupled to an optical fibre and injected into the slave LD. Coupling the slave LD's output light to the same fiber[33] then provides the spatial overlap of the optical modes needed. Typically, coupling efficiencies of $62\,\%$ to $76\,\%$ are achieved without the need of additional beam shaping optics. Matching polarization of the two beams is provided with a $\lambda/2$-plate. Being outcoupled from the overlap fibre, the slave light passes the FI. From this point it can be made use of in further stages. If the injection locked slave light is used as a seed for a subsequent IL, an optical filter[34] is added to the path. It is in principle not needed for optimized system parameters and was put in after a while of successful operation. Filtering the free running modes of the slave LD keeps a spectrally pure seed for the next stage, even if the system has drifted.

The fiber coupling for overlapping the beams also allows having a modular system design. The optical setup of the slave laser up to the fiber port is mounted on its own breadboard. It is easily exchangeable with another pre-built setup in case of a broken slave LD.

The slave laser is of very compact design. It consists of an aluminum block holding the collimation tube[35] of the LD. The aluminum block is resting on a Peltier element used for temperature stabilization[36]. An enclosing plexiglass housing with an optical window protects the laser from dust and air fluctuations.

The LD package comes with a built-in PD. It is located opposite to the output direction of the small LD cavity. Its photo current is converted to a voltage signal $V_{\mathrm{PD}}$ with a standard transimpedance amplifier circuit[37]. The PD signal is monitored with a microcontroller[38]. It controls the slave LD's current $I_{\mathrm{LD}}$ via its true analog 32-bit output channel plugged to the current controllers[39] modulation input. Scanning $I_{\mathrm{LD}}$ without the seed light being present shows a typical linear dependence of $V_{\mathrm{PD}}$ after the lasing threshold is passed (see Fig. 5.8b). The presence of the seed light leads to a significant change of this signal. On top of the linear slope repetitive features emerge. Every $\approx 11\,\mathrm{mA}$ a sharp increase of the signal followed by a decay to the baseline appears. They are characteristic injection locking signals. An increase in the signal is observed, when the slave LD's cavity gets in resonance with the seed light, and a spectrally pure injection locked state is achieved. For increasing seed power, injection

---

[31] USHIO HL67001DG

[32] LINOS FI-680-5SV ($-30\,\mathrm{dB}$)

[33] Fiber: OZ Optics PMJ-3A3A-633-4/125-3-2-1 with coupler: Thorlabs F240APC-B

[34] Laseroptik L-10813-01 (same as in the ECDL)

[35] LT230P-B

[36] Meerstetter Engineering GmbH TEC-1091 or TEC-1161-4A

[37] $V_{\mathrm{PD}} < 3.3\,\mathrm{V}$ to stay within the accepted input voltage range of the Arduino Due

[38] Arduino Due

[39] Thorlabs LDC205C

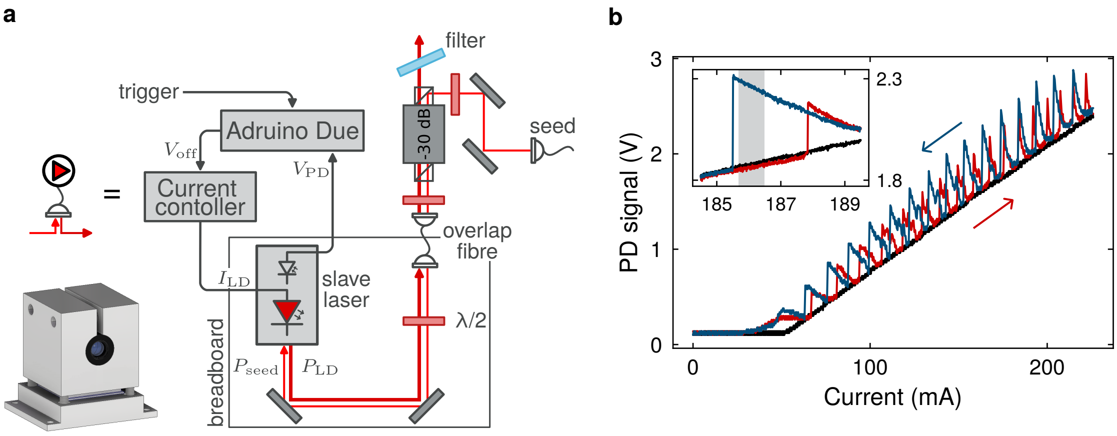

**Figure 5.8 Injection lock setup and signals. a.** Optical and electric setup sketch of the injection lock system. The seed light is injected into the slave laser diode through the side port of the FI. Spatial overlap of the seed and slave laser modes are provided by coupling both to the same (overlap) fibre. The slave laser light passes the FI through its intended direction. If the injection locked light is used to seed a second stage injection lock, an optical filter is placed to purify the spectrum. The slave LD package is equipped with a PD. Its signal is fed to a microcontroller (*Arduino Due*), which controls the slave LD current. These elements are made use of in the Injection Lock Algorithm (ILA). In the left lower corner a render of the compact slave laser is shown. **b.** Signal of the integrated PD for varying slave laser current ($I_{\mathrm{LD}}$). With the seed light blocked (black) a typical linear power dependence is observed. For the seed light being present the linear slope shows regular asymmetric features, which are typical injection lock signals. Hysteresis of the system for sweep up (red) and sweep down (blue) PD signals is observed. The injection lock feature is more pronounced and shifted to lower currents for a decreasing current. A more detailed view of a single feature is presented in the inset. The gray area marks a region, where a pure injection lock is achievable.

locking is realized for an increased current range. This interval is located close to the signal jump and typically $\gtrsim 1\,\mathrm{mA}$ wide for stable operation. For a changing current, the cavity length and with it the free spectral range is tuned by Joule heating. The cavity is shifted out of resonance until a neighboring longitudinal mode matches the seed light's frequency. The strong asymmetric shape originates from a combination of Joule heating and heating from the seed light resonance [196].

When sweeping the current, a hysteresis effect on the injection lock signal is observed. For decreasing current the features are more pronounced and the jump point is shifted to lower current values compared to the increasing current scan. Approaching the injection lock point with a decreasing current leads to a more stable and spectrally purer injection locked state. Also, the current range for a stable injection lock is increased.

## Injection lock algorithm

The injection locked state of the slave LD is easily lost, when disturbed. External disruptions are unavoidable under normal working conditions in the laboratory. Manually re-optimizing $I_{\mathrm{LD}}$ after the injection locked state is lost, is not a reasonable modus operandi, especially when ILs are employed at multiple locations in the laser system. Even if the injection locked state is restored manually, thermalization of the system is lost. Re-thermalization then shifts

the optimum operation point away from the previously set value.
These challenges are mastered with the implementation of a three-steps Injection Lock Algorithm (ILA) via the microcontroller:

I Sweep up $I_{\mathrm{LD}}$ with the resonance jump in the middle of the ramp.

II Sweep down $I_{\mathrm{LD}}$ over the same interval while recording the PD signal and take the numerical derivative to identify the jump point in the resonance feature.

III Sweep up again and then sweep down to the optimal current, which is offset from the previously detected jump point and has to be fine-tuned for every diode and working point separately.

A typical PD signal for a single run of the ILA is shown in Fig. 5.9. Executing it takes a bit more than half a second. It is applied every cycle of the experiment, started by an external trigger. The sweep time has to be adjusted for different slave LDs. Typically, longer sweep times are required for LDs in the blue. Applying the ILA sequentially to chained ILs also proves to be reliable in daily operation. The ILA of the second stage is applied after a short settle time of the first stage ILA. The total time required is about $1.5\,\mathrm{s}$. The start of the first stage ILA unlocks the second stage IL. The change of the injection locked state during this time period shows not to alter the thermalization significantly. The ILA can be applied while no resonant light is needed in the experiment, e.g. during evaporation. This way the cycle time remains unaffected.
If the system is already thermalized, a single execution of the ILA is sufficient to maintain the injection locked state in a quasi-CW manner. Starting form a non-thermalized state, continuous application of the ILA is required. After about $15$ executions the system has thermalized. During the thermalization process the jump point moves by almost $20\,\mathrm{mA}$ to the lower current side.

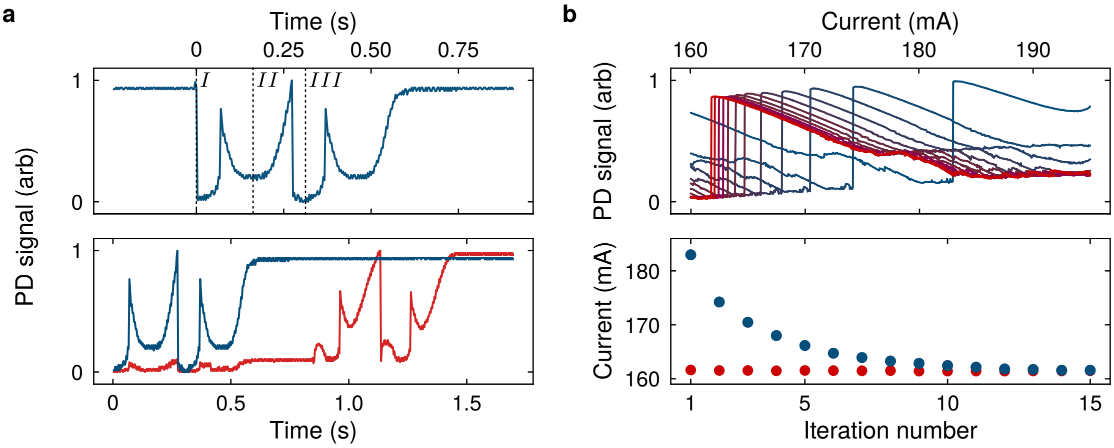

**Figure 5.9 Injection locking algorithm and thermalization. a.** Top: PD signal of a single run of the ILA. The three steps of the algorithm are marked with Roman numerals (see text). Before the start of the algorithm, the slave LD was in an injection locked state already. A sweep up (*I*) is followed by a sweep down (*II*) of the current over the same interval. After another sweep up, the current is ramped up offset to the jump position of *II*. Bottom: PD signals of ILA runs executed in chained injection lock systems. Here, the seed light for the second stage (red) is provided by the first stage (blue) injection locked slave LD. **b.** Top: Thermalization of the jump point in *II* for repeated (blue to red) execution of the ILA. The convergence of the recorded jump points for repeated executions (blue) are displayed together with the jump points of a well thermalized injection locked system (red).

### ILA performance and characterization

To find the optimum working point, the slave LD's light is monitored with an Optical Spectrum Analyzer (OSA)[40]. The spectrum of the free running slave LD is about $2\,\mathrm{nm}$ wide and centered at a wavelength of $674\,\mathrm{nm}$ at a temperature of $22\,^{\circ}\mathrm{C}$ (see Fig. 5.10). The seed light and the spectrum of the free running slave LD do not overlap. Here, the multimode lasing characteristic of the free running LD results in a large detuning for best operation. In standard injection locking theory of single-frequency lasing slave lasers, injection locking occurs only in a narrow detuning range from the seed light [186, 201]. No stable injection locking was observed for the free spectrum of the slave LD tuned in resonance with the seed light.

To quantify the spectral purity of the injection locked slave light, the integrated optical power in the seed mode $P_{\text{lock}}$ and free running modes $P_{\text{free}}$ are extracted with the OSA. With this the spectral purity is defined as $S = (P_{\text{lock}} - P_{\text{free}})/(P_{\text{lock}} + P_{\text{free}})$ and similarly the spectral impurity as $\bar{S} = 1 - S$. For $\bar{S} = 0$ the injection lock is referred to as spectrally pure. The slave LD then lases on the seed mode exclusively.

The performance of the ILA was tested for a current driver setpoint of $204\,\mathrm{mA}$, which provides $180\,\mathrm{mW}$ output power. After making sure the system is in a well thermalized state, the algorithm was applied and the spectral purity was recorded. For a seed power of $3.2\,\mathrm{mW}$ a spectrally pure and stable locking interval was found for an offset current to the jump feature of $1.9\,\mathrm{mA}$ to $3.6\,\mathrm{mA}$. The interval shrinks non-linearly from the high current side for reduced seed power. Below $2\,\mathrm{mW}$ of seed light no stable injection locking was observed anymore. The threshold in seed power for a spectrally pure injection lock was the reason for the two stages IL amplification scheme of the Li laser system.

For characterizing the long term reliability of the ILA, the offset current was chosen to be $2.7\,\mathrm{mA}$, which is well within the injection lock interval. The ILA was periodically applied every minute for a total time span of $6\,\mathrm{h}$. For each execution the spectral purity and the setpoint determined by the algorithm were recorded (see Fig. 5.10b). During the entire time the ILA maintained on average a spectral impurity of $1.18\,‰$. None of the $360$ repetitions resulted in impurities of more than $6\,‰$. The deviation of the setpoint stayed basically unchanged during the first $3\,\mathrm{h}$ of the characterization time. It then drifted a bit to $0.18\,\mathrm{mA}$ at the end. Meanwhile, the spectral purity stayed unaffected by this drift.

---

[40] HighFinesse Laser Spectrum Analyzer

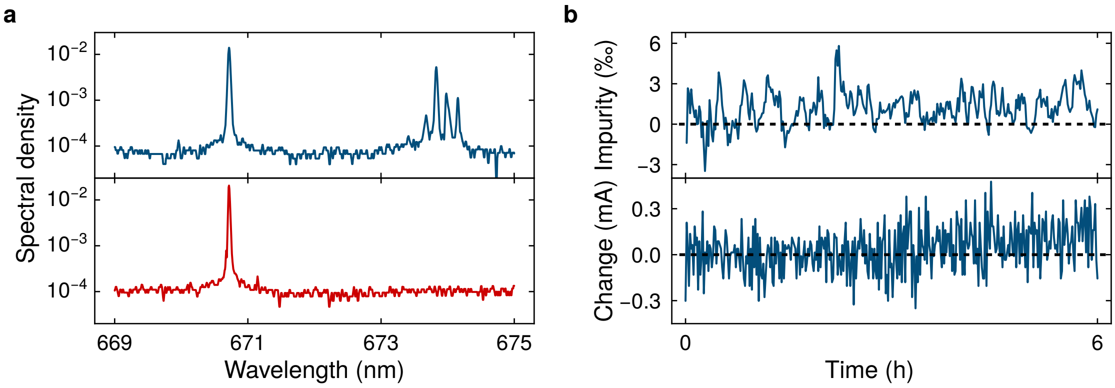

**Figure 5.10** **Injection lock purity and long-term stability. a.** Optical spectra of a non injection locked (top) and spectrally pure injection locked slave LD (bottom). The seed light at $\sim 671\,\mathrm{nm}$ is well separated form the $2\,\mathrm{nm}$ wide spectrum of the free running diode with a central wavelength of $\sim 674\,\mathrm{nm}$. **b.** Spectral impurity (top) for periodic ($T = 1\,\mathrm{min}$) ILA executions over a time span of $6\,\mathrm{h}$. The change in the detected jump positions (bottom) shows a minor drift starting after $\sim 3\,\mathrm{h}$, which does not affect the spectral purity achieved.

## 5.2 Far off-resonant light - optical dipole traps

### 5.2.1 Crossed beam optical dipole trap (CBODT)

The light for the Crossed Beam Optical Dipole Trap (CBODT) is provided by a high-power multi-mode ytterbium fibre laser (IPG[41]). It is capable of outputting optical powers of up to $214\,\mathrm{W}$ at rather low cost. Its spectrum is about $3\,\mathrm{nm}$ wide at a central wavelength of $1070\,\mathrm{nm}$. In many Li experiments, it has proven to be a reliable laser source for optical dipole traps [137, 202–204]. Typically, it is made use of in first stage dipole traps, when the atoms are still rather hot. In our setup, the optical power of the IPG can be made use of for Er as well. In a combined sequence of Er and Li the light is not required in both chambers at the same time. The IPG light is either guided towards the Li or Er chamber by a combination of a motorized $\lambda/2$ plate and a PBS. The sequential usage of the IPG light allows using a single AOM for intensity stabilization for both paths.
The optical setup to provide the crossed dipole trap beams with waists of $65\,\mu\mathrm{m}$ is presented in Fig. 5.11. Passive stability of the setup is crucial to keep the beams overlapped. In the planning and built-up phase, it was taken great care to place critical elements such as the outcoupler and the AOM in the focal plane of the lenses to minimize the effect of drifts. To avoid thermal lensing only lenses made out of fused silica were built in.
The IPG's output mode of waist of $2.45\,\mathrm{mm}$ is demagnified by a telescope to fit the aperture of the low drift AOM[42]. The first diffraction order of the AOM with a maximum optical power of $145\,\mathrm{W}$ is sent towards the atoms, while the zero order is dumped. A subsequent

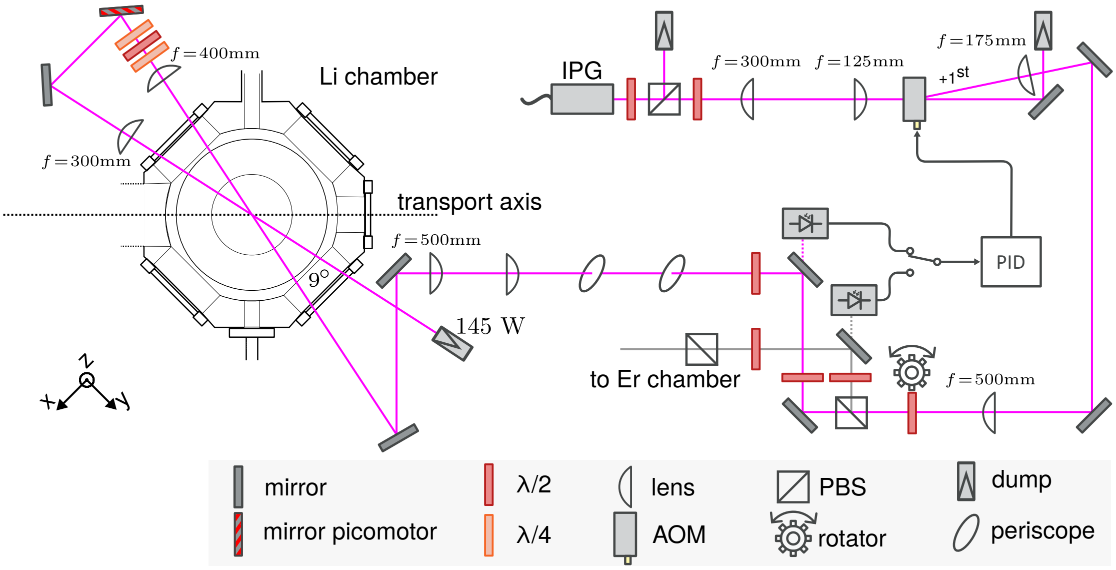

**Figure 5.11** **CBODT optical setup.** The IPG output mode is demagnified and sent through a low drift AOM for intensity stabilization. The first order is demagnified again and sent towards the atoms. A rotating $\lambda/2$ in front of a PBS guides the power either to Li or Er. Feedback to the intensity PID controller is provided by the PDs in the respective paths. Following the Li path, the beam is focused onto the atoms ($w = 65\,\mu\mathrm{m}$), collimated and focused onto the atoms again ($w = 60\,\mu\mathrm{m}$).

---

[41] IPG YLR-200-LP-WC
[42] Gooch & Housego 3080-1990

optical telescope magnifies the beam to a waist of $2.9\,\mathrm{mm}$. The beam passes a $\lambda/2$ plate mounted on a stepper motor[43] controlled by a microcontroller[44]. The controller rotates the $\lambda/2$ to have full reflection or full transmission on a subsequent PBS depending on a TTL signal. The transmission (reflection) is sent towards the Li (Er) chamber. The rotation takes about $400\,\mathrm{ms}$ to guide the light to Er instead of Li. Feedback for the intensity stabilization is provided with PDs picking up mirror transmissions in the respective paths. A relay connects the intensity stabilization PID controller to the PD signal to the path in use.

Following the path to the Li chamber, the laser beam is brought from the table ground to the level of the atoms by a periscope. Then the beam is focused down by a lens with a focal length of $500\,\mathrm{mm}$ and sent to the atoms. Having crossed the Li chamber, the beam is re-collimated. With a $\lambda/4$, $\lambda/2$, $\lambda/4$ combination, it is made sure to have perfect orthogonal linear polarization of the crossed beams. Here, an extinction ratio of more than $1:10{,}000$ is achieved on a test PBS. Non-perfect orthogonality in polarization leads to heating and an accompanied reduced lifetime of the atoms in the multimode dipole trap. The collimated laser beam is focused onto the atoms again with a lens of $300\,\mathrm{mm}$ focal length under an angle of $9\,°$. The stronger lens provides a tighter focused beam with a waist of $60\,\mu\mathrm{m}$. The short coherence length of the broad multimode laser prevents interference of the crossing beams. One of the back reflecting mirrors is motorized[45], to precisely overlap the beams.

The optical path was built with the IPG running on the power level, later used in the experiment. Collimation and output beam size are varying for high and intermediate power levels. During operation, we saw movement of the IPG beam at the Er chamber. This was caused by air fluctuations due to the heated up stepper motor. An alternative rotation mechanism is under investigation. Its implementation has not been urgent so far, since the Er CBODT has shown not to be advantageous over the cMOT in the dual-species sequence [74].

### 5.2.2 Optical transport

The transport of the atoms from their respective MOT chambers to the science chamber is provided by a running 1D-lattice at $1064\,\mathrm{nm}$. From the Li MOT chamber to the center of the science chamber a distance of $1\,\mathrm{m}$ has to be overcome. For Er, it is half of that, which still is on the upper end of commonly realized optical transport distances. The optical transport relies on precise frequency control of two high-power interfering laser beams forming the lattice. The high-power beams are derived from two fiber amplifiers[46] ("ALS 1" and "ALS 2"), which are externally seeded. In order to limit the complexity of the laser system, it is divided into a low-power part for frequency tuning of the seed light and a high-power part on the experimental table (see Fig. 5.12).

The seed light is prepared in the low-power part. It is derived from a low-noise, single-frequency laser[47] ("Mephisto") providing up to $2\,\mathrm{W}$. The output of the Mephisto is split into multiple paths for seeding different laser amplifiers. The seed light for ALS 2 is frequency shifted by two AOMs[48] in double-pass configuration. In the first double-pass the $+1^{\text{st}}$ order and in the second the $-1^{\text{st}}$ order is used. The light is freely tunable in a range of

---

[43] Pololu SY20STH30-0604A with A4988 driver

[44] Arduino Due

[45] Newport New Focus 8821

[46] ALS 1: ALS-1064-130-E-CC-SF-ANRS, ALS 2: ALS-IR-1064-50-A-CC-SF

[47] Coherent, Mephisto 2000

[48] Gooch & Housego, 3110-197

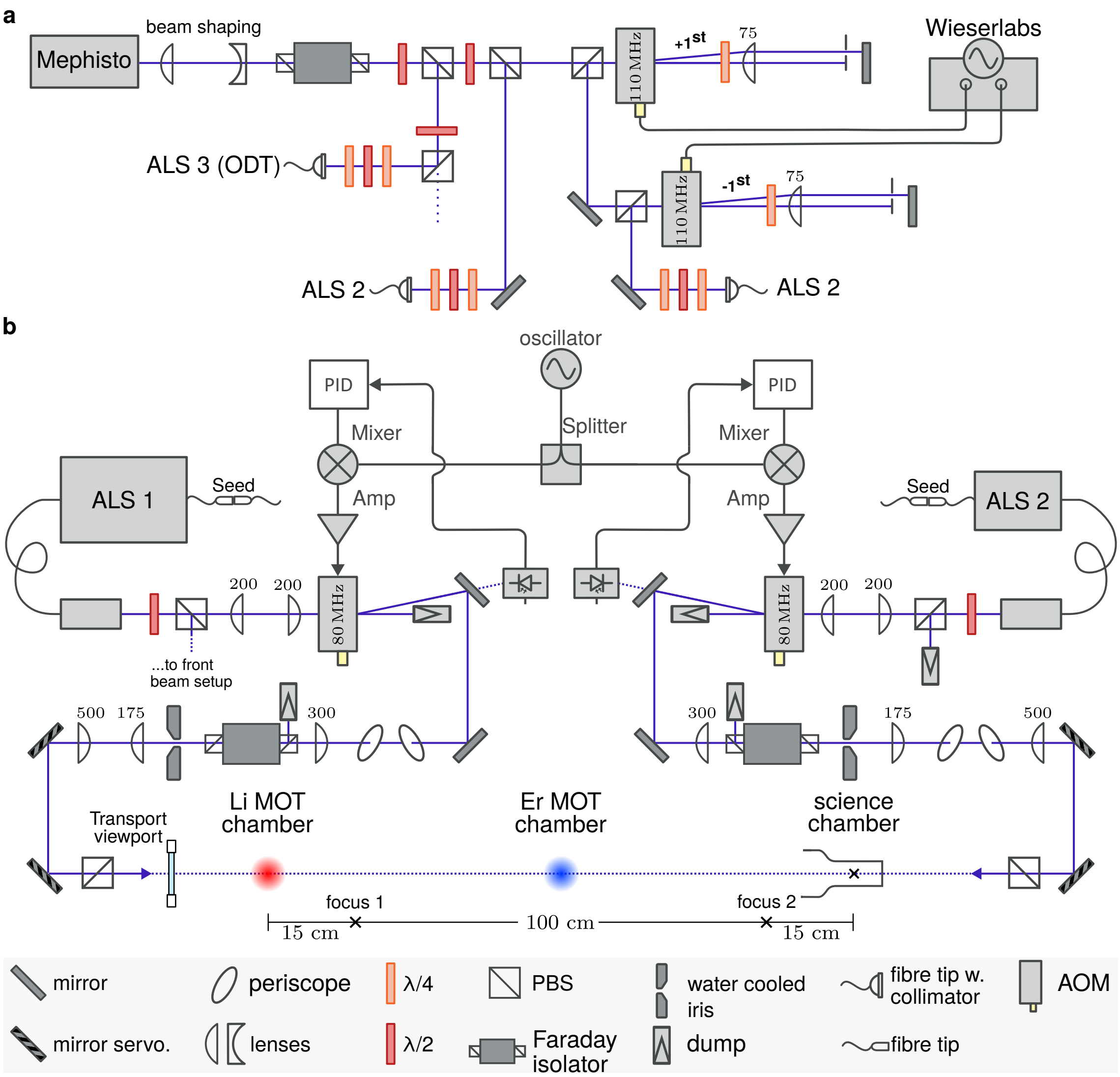

**Figure 5.12 Optical transport laser setups. a.** The $1064\,\mathrm{nm}$ light, provided by the Mephisto, is split in different paths to seed the two transport ALS 1 and ALS 2, and another ALS 3 amplifiers. The seed light for ALS 1 is frequency shifted by two AOMs in double-pass configuration. Precise control of the driving frequencies is provided by a DDS ("Wieserlabs") **b.** High-power setup at the experimental table. The output of the ALS 1 $(100\,\mathrm{W})$ and ALS 2 $(50\,\mathrm{W})$ amplifiers is power controlled by AOMs and focused $15\,\mathrm{cm}$ next to the start / stop of transport track. Having passed the vacuum chamber, the optical power is mostly dumped by a water-cooled iris.

$\pm 20\,\mathrm{MHz}$, by applying different AOM driving frequencies in the two double-pass AOMs. Since the ALS fiber amplifiers require a minimum seed power, the tunability is limited by the frequency dependent diffraction efficiency of the AOMs. Precise frequency control of the ALS 2 seed light is provided by a DDS[49] ("Wieserlabs"). The ALS amplifiers are very sensitive to underseeding. For this reason, we restrict the frequency tuning to only one of them. The ALS 1 amplifier is seeded with the unshifted Mephisto light. In the end both fiber amplifiers receive about $100\,\mathrm{mW}$ of seed light, which is well above the amplifiers' threshold of $15\,\mathrm{mW}$.

---

[49] Wieserlabs, WL-FlexDDS-NG

Another safety measure is having the seed controlling AOMs run on a Voltage-Controlled Oscillator (VCO) by default and only switch to the Wieserlabs source when needed.
The ALS 1 and ALS 2 fiber amplifiers are located on opposite ends of the experimental table, receiving the fibred seed light from the Mephisto setup from the laser table. With up to $100\,\mathrm{W}$, the ALS 1 laser output power is about double of ALS 2. As for the IPG setup from Section 5.2.1, it was taken great care for both beam paths to position lenses in the stability providing *4f-configuration*. The laser heads are mounted on the bottom level of the optical table. The power of the laser beams is controlled with AOMs[50] in single-pass configuration. Feedback to the power stabilizing PI-contoller is provided by PDs, that pick-up the light from mirror transmissions. The frequency source to drive the intensity stabilization AOMs proved to be crucial. Here, a low-noise, fixed-frequency oscillator[51] is employed to provide the rf-frequency source for both.
The optics required for the two beam paths are very similar. They differ only due to the space available on each side of the table. The light is brought to the atomic level bread boards with periscopes and passes FIs and water cooled irises. After that, the beams are focused to a waist of $300\,\mu\mathrm{m}$ at a distance of $15\,\mathrm{cm}$ from the start / end of the transport track. Overlap of the two beams is controlled with two pairs of servomotor controlled mirrors on each side of the chamber. The difference in focal position helps to dump most of the power of the counter propagating beam in the water cooled iris before the FI is reached. With this the FIs are protected, and the power is dumped in a controlled way.

### Setup at the MOT chamber

The optical setup at the Li chamber is presented in Fig. 5.13. It includes all beams of resonant light for ZS, MOT, GM and absorption imaging that are exposed to the Li atoms. The generation, amplification, and distribution to the individual optical fibers was presented in Section 5.1 and is shown in great detail in Fig. 5.2. The optical setup for the GM is not used anymore, since it did not bring any advantage over loading the CBODT with a compressed MOT only. Nevertheless, interesting experiments described in Section 6.2, where achieved with this setup. Next to the resonant light beams, also the CBODT and the optical transport beams are shown. The figure highlights the variety of beams and elements needed to prepare an ultracold cloud of Li atoms and transport it to science chamber, where the final experimental steps are executed.

---

[50] Gooch & Housego 3080-1990

[51] QuanticWenzel Premium 80MHz Sprinter Crystal Oscillator, 501-10295

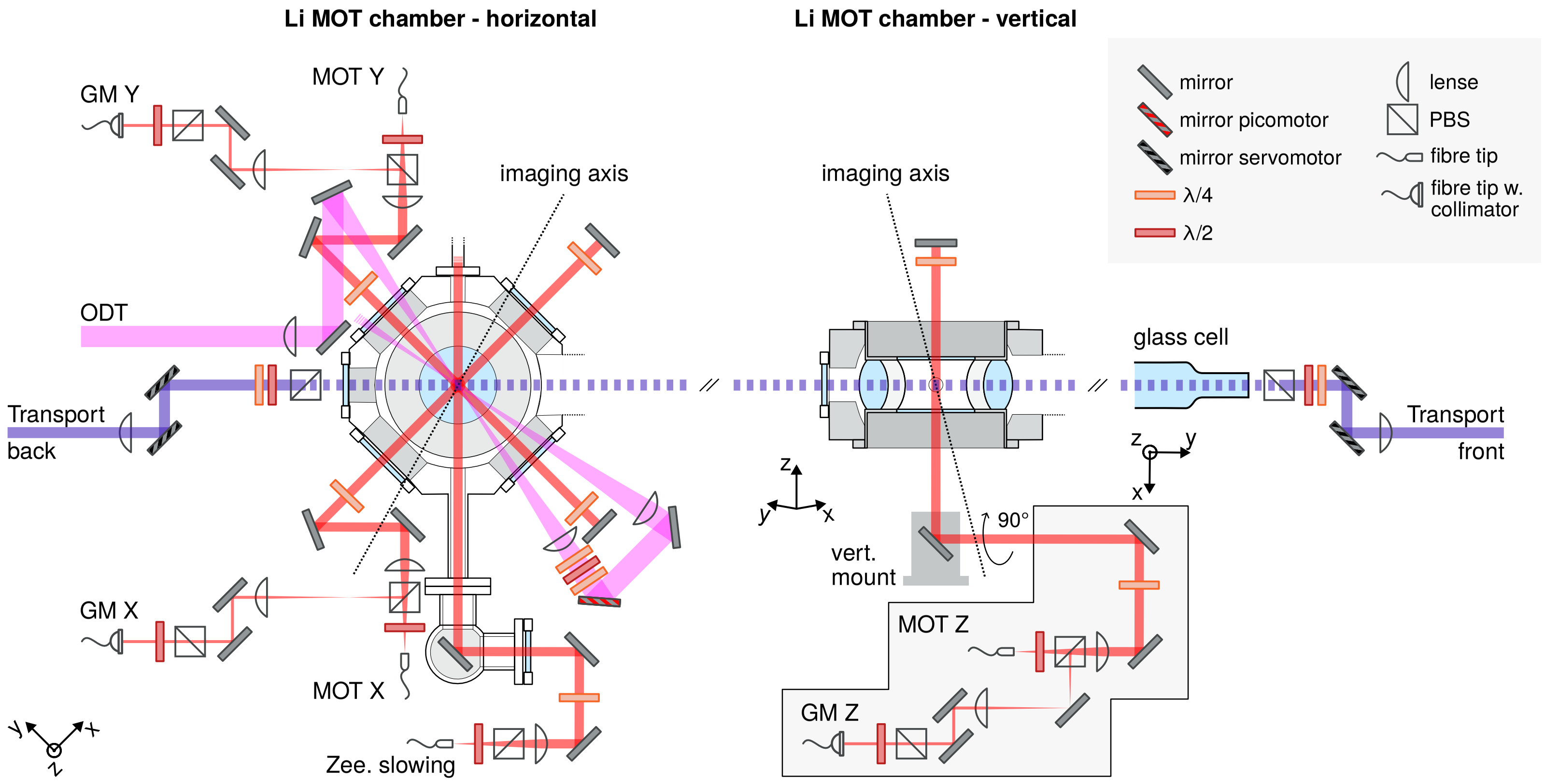

Figure 5.13 **Optical setup at the Li MOT chamber.** See end of Section 5.2.2 for descriptions.

### 5.2.3 Setup at the science chamber

After the atoms have been transported to the science chamber, they are loaded to other Optical Dipole Traps (ODTs). In total there are three 1064 nm ODTs, provided by the so-called "sheet beam", "cross beam" and "front beam". They are all horizontally oriented. Schematics of the optical setups, to provide the traps is given in Fig. 5.14.
The optical power for the sheet and cross beam is provided by a 50 W ALS fiber amplifier[52] (ALS 3) seeded by the unshifted Mephisto. As for the two ALS amplifiers of the optical transport, the ALS 3 laser head is directly mounted on the experimental table. The output of ALS 3 passes an AOM[53] in the non-diffracted order. The first order of the AOM is guided to the Er chamber, since the optical power of ALS 3 is never required at the Er chamber and the science chamber at the same time. The light for the sheet and cross beams is split with a PBS and pass two shear mode AOMs[54] for active power control. The sheet beam is shifted

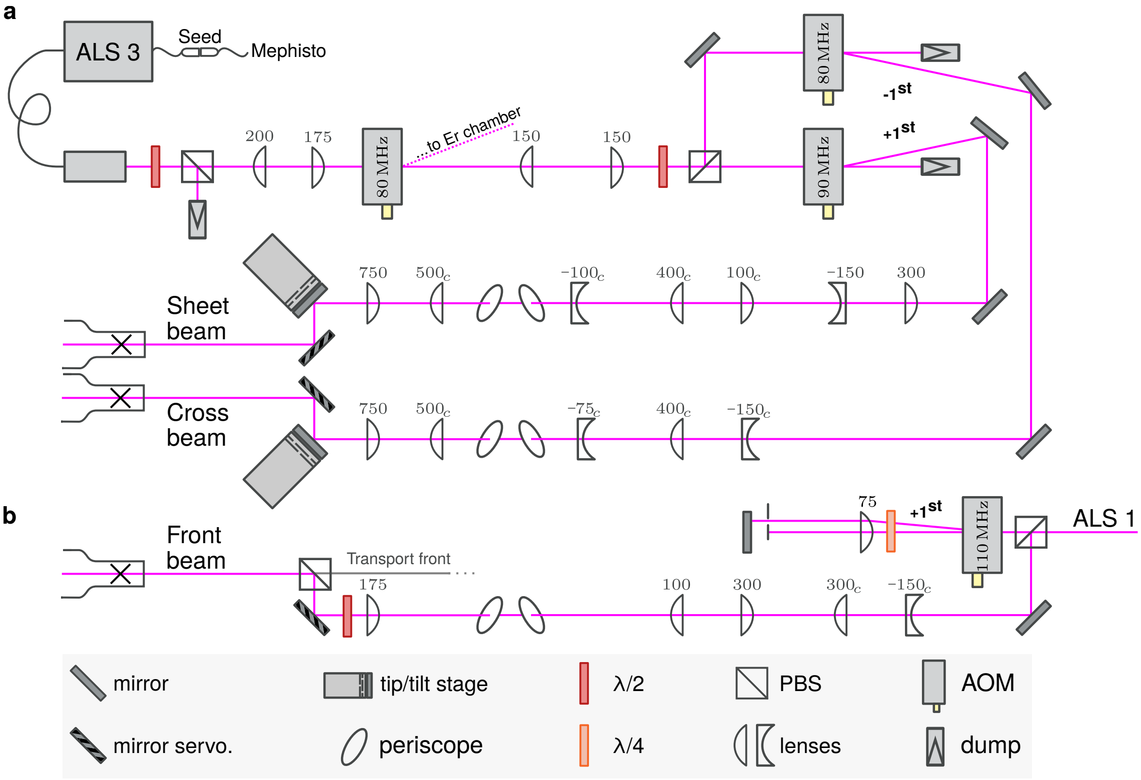

**Figure 5.14 Schematics for providing ODTs at the science chamber. a.** The light for the sheet and cross beams are derived from a $50\,\mathrm{W}$ fiber amplifier (ALS 3). The ALS 3 output passes an AOM to guide the light to the Er chamber, when needed. After being split in separate paths, the laser beams pass AOMs for power control and telescopes for beam shaping. Cylindrical lenses are indicated with the index "$c$" in the focal length. After the focusing lenses, mirrors controlled by tip-tilt stages and servomotors allow for precise control of the focus position. **b.** The light for the front beam is split from ALS 1 and passes a double-pass AOM for power control. After beam shaping, it is brought to the atom level by a periscope. A servomotor controlled mirror allows aligning the beam focused onto the atoms.

---

[52] ALS 3: ALS-IR-1064-50-A-CC-SF
[53] Gooch & Housego 3080-1990
[54] Gooch & Housego I-M080-2S2G-3-LV11

by $+90\,\mathrm{MHz}$ and the cross beam by $-80\,\mathrm{MHz}$ by their respective power control AOM. From this point on, the optical paths for the two traps differ only by the lenses used for beam shaping. The beams are brought to the atom plane by periscopes. There they are focused by lenses with focal lengths of $750\,\mathrm{mm}$. Right after the lenses, the beams are reflected by mirrors mounted on tip-tilt stages[55]. They provide precise dynamical control of the atomic beam position. With a maximum tilt angle of $2\,\mathrm{mrad}$ the focal point is displaced by $1.5\,\mathrm{mm}$. Drifts of the overlap of the ODTs in the glass cell is compensated with servomotor controlled mirrors, which are placed after the tip-tilt stages. At the atoms, the sheet beam is focused to horizontal / vertical waist of $730\,\mu\mathrm{m}$ / $41\,\mu\mathrm{m}$ and the cross beam to $360\,\mu\mathrm{m}$ / $43\,\mu\mathrm{m}$.
For the front beam, about $3\,\mathrm{W}$ of optical power is split from the ALS 1 path (see again Fig. 5.12). For power control, it passes a standard AOM[56] in double pass configuration, to avoid thermal drifts. After passing a cylindrical and spherical telescope for beam shaping, it is brought to the atom level by a periscope. There the beam is focused with a lens of $175\,\mathrm{mm}$ focal length. It is overlapped with the transport beams by reflecting it from a PBS employed to purify the polarization of the front transport beam. As for the sheet and cross beam, a servomotor controlled mirror is placed at the end of the optical path, to compensate for drifts in overlap. At the center of the glass cell, the beam is focused to a horizontal / vertical waist of $30\,\mu\mathrm{m}$ / $48\,\mu\mathrm{m}$.
The AOM driving frequencies were chosen to avoid heating of the atoms by running lattices and beating of the beams. With respect to Mephisto output, the transport beams are detuned by $+80\,\mathrm{MHz}$, the sheet beam by $+90\,\mathrm{MHz}$, the cross beam by $-80\,\mathrm{MHz}$ and the front beam by $+220\,\mathrm{MHz}$. A detailed sketch of the optical system at the science chamber is presented in Fig. 5.15. The sheet / cross beam is sent under an angle of $45\,^\circ$ / $-80\,^\circ$ towards the atoms with respect to the transport axis. The front beam is sent onto the atoms along the transport direction. Imaging light for Li ($671\,\mathrm{nm}$) and Er ($401\,\mathrm{nm}$) is overlapped on a dichroic mirror before being sent towards the atoms. Repumper light, needed for imaging Li in the $F = 1/2$ ground state manifold is overlapped with the absorption beam on a beam sampler with low reflectivity for $671\,\mathrm{nm}$ and $401\,\mathrm{nm}$. The atomic clouds are imaged by the same lens pair with a magnification of $\times 2.5$. The light is split by another dichroic mirror, to image Li and Er on independent cameras. For Li a scientific camera[57] ("Zyla") is employed, to obtain low noise images, needed for precise Fermi profile temperature fits. For Er our standard camera[58] ("Manta") proved to provide sufficient imaging quality.

---

[55] Physik Instrumente S-330.2SH
[56] Gooch & Housego, 3110-197
[57] Andor ZYLA-4.2P-USB3-W
[58] Alvium 1800 U-501m NIR

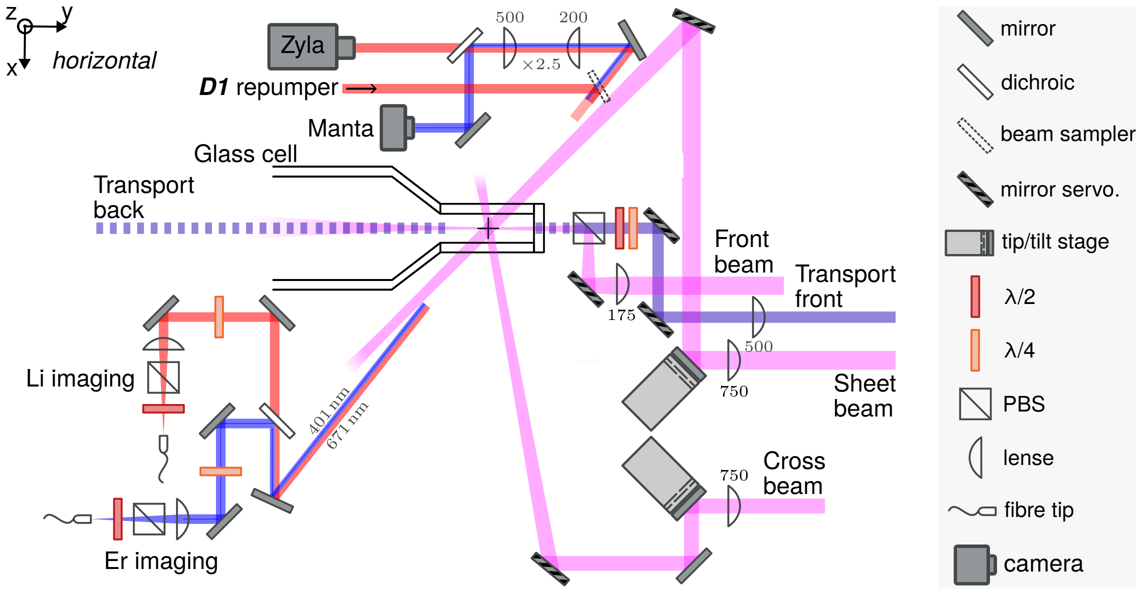

**Figure 5.15 Optical setup at the science chamber.** See text for detailed descriptions.

# Chapter 6

# Preparation of ultracold Li

This chapter reports on the preparation of a cloud of ultracold Li. In the first section (Section 6.1), the standard absorption imaging technique and standard ToF temperature measurement is introduced. Event though, these two techniques are standard procedures in experiments with ultracold gases, they deserve to be mentioned briefly, because our analysis relies heavily on them. In the following section (Section 6.2) an improved non-standard Gray Molasses for cooling Li to $13\,\mu$K is demonstrated, characterized and compared to the standard approach, which provides only $50\,\mu$K. The GM technique is not used in the final sequence, in which Li is overlapped with Er, because it did not lead to an enhanced loading performance of the Crossed Beam Optical Dipole Trap compared to the cMOT stage alone. Finally, in Section 6.3 and Section 6.4 loading the CBODT, evaporation into the transport lattice and subsequent transport the glass cell is characterized.

## 6.1 Absorption imaging and standard ToF thermometry

Throughout this thesis, information about the atomic cloud is received by means of absorption imaging. In the absorption imaging technique, a collimated resonant light beam is exposed to the atomic cloud and then imaged on a camera chip [51]. The magnification $m = f_2/f_1$ of the image is set by the focal lengths $f_1$ and $f_2$ of the imaging system (see Fig. 6.1). The atoms scatter the resonant light and with this reduce the count which is proportional to $I_{\text{abs}}(x, y)$ locally on the camera. The received image is compared to a reference image $I_0(x, y)$, without atoms being present. With the Beer-Lambert law, the reduction in optical transmission by the atoms relates to the optical density $\text{OD}(x, y)$, respectively the column density $n(x, y) = \int n(x, y, z)dz$ as [205]:

$$\frac{I_{\text{abs}}(x,y)}{I_0(x,y)} = e^{-\text{OD}(x,y)} = e^{-\sigma_{\text{abs}} n(x,y)}. \tag{6.1}$$

The absorption cross-section of the atoms is given by

$$\sigma_{\text{abs}} = \frac{\sigma_{\text{abs},0}}{1 + I_0/I_{\text{sat}}} \quad \text{with} \quad \sigma_{\text{abs},0} = \frac{\hbar\omega\Gamma}{2I_{\text{sat}}}. \tag{6.2}$$

Typically, the sensitivity of the camera and the width of the transition allow sending low intensity light to the atoms ($I_0 \ll I_{\text{sat}}$). In this limit, the cross-section $\sigma_{\text{abs}} = \sigma_{\text{abs},0}$ is intensity independent and a calibration of the system is therefore not required[1]. Imaging

---

[1] Clean circular polarization is needed, as non-circular components of the imaging light result in an underestimation of the atomic density.

light for Li drives the transition from $F = 3/2, m_F = 3/2$ to $F' = 5/2, m_{F'} = 5/2$ on the $D_2$-line. During the imaging light pulse, the atoms are also exposed to repumper light of very little power, to pump the atoms back to the $F = 3/2, m_F = 3/2$ state, if lost from the cycling transition. The obtained column density $n(x, y) = \mathrm{OD}/\sigma_{\mathrm{abs}}$ is the basis of the analysis for every experimental run. An absorption image of Li released from the cMOT is shown in Fig. 6.1b. The atom number $N$ is derived by integrating $n(x, y)$ over the spatial extent of the cloud. By fitting density distributions to $n(x, y, t_{\mathrm{tof}})$ for various expansion times $t_{\mathrm{tof}}$ in ToF measurements, more parameters can be extracted.

The spatial shape of a thermal cloud follows a Gaussian distribution, obtained from the classical Maxwell-Boltzmann equation. In ToF, the Gaussian waist of the cloud expands as

$$\sigma(t_{\mathrm{tof}}) = \sqrt{\sigma_0^2 + \frac{k_B T}{m} t_{\mathrm{tof}}^2}, \tag{6.3}$$

from the initial waist $\sigma_0$, governed by the temperature $T$, with the Boltzmann constant $k_B$ and the mass $m$ of an atom. The parameters $\sigma_0$ and $T$ are obtained from a fit of Eq. (6.3) to the Gaussian waists of different ToFs.

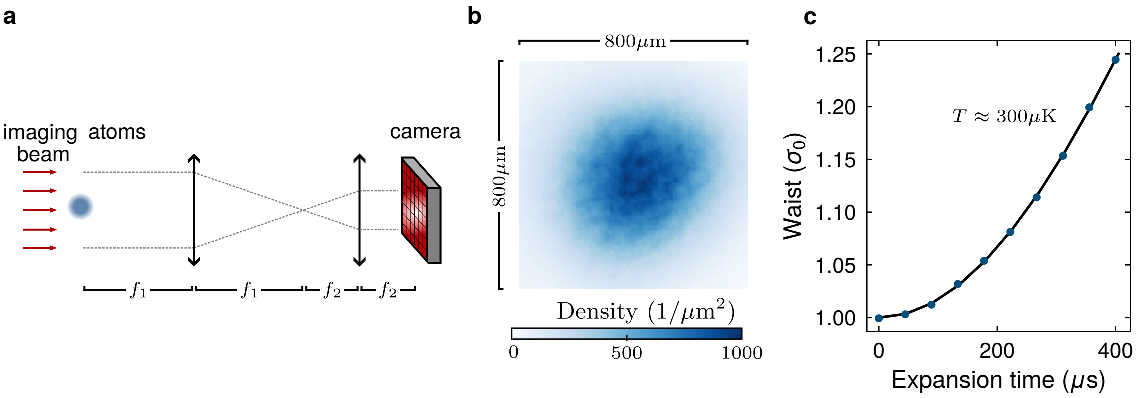

**Figure 6.1 Absorption imaging and standard thermometry. a.** Optical setup for absorption imaging. **b.** Recorded column density of $N = 6 \cdot 10^6$ Li atoms released from the cMOT after $400\,\mu$s of ToF. **c.** Standard thermometry by fitting Eq. (6.3) to the Gaussian waist of the atomic cloud for varying ToF.

## 6.2 Gray Molasses cooling

While the standard $D_2$ MOT for Li is well suited to caputre atoms from a slowed atomic beam, it usually does not provide low enough temperatures ($\sim 300\,\mu\mathrm{K}$) for the final experimental stage. In contrast to other alkali atoms, Li as well as K lack a well resolved $D_2$-line. This prevents standard sub-Doppler cooling techniques like polarization gradient cooling to work efficiently [206–208]. Non-standard MOTs in the near-UV e.g. for $^6$Li at $323\,\mathrm{nm}$ [87] or $^{40}$K at $405\,\mathrm{nm}$ [209] provide $\sim 60\,\mu\mathrm{K}$. They work on an about seven times more narrow transition, than the $D_2$-transition in the red, thus proving a lower Doppler temperature. Using those MOTs consecutively to a standard $D_2$ MOT stage helps to improve the Phase-Space Density (PSD) by one order of magnitude. However, generating near-UV light generally is technically challenging and therefore possibly leads to experimental difficulties in the setup of the system itself and its day-to-day maintenance.

Another optical cooling technique for Li is provided by the so-called GM, operating on the $D_1$-line. Since its theoretical proposal in 1994 [210] and experimental realization in the following year for Cs [211], it has been and still is widely used, especially for atoms with an unresolved $D_2$-line. It relies on the emergence of an almost dark (gray) state $|\Psi_D\rangle$ in the ground state manifold for $F \to F$ or $F \to F-1$ transitions [212].

In a classical picture, the GM-technique provides a friction force, thus it does not yield spatial confinement. Its working principle is similar to Sisyphus cooling, where the atom looses kinetic energy by "climbing" a spatially varying potential and scatter into a lower lying state, where the process immediately starts again. In contrary for the GM scheme, after climbing the potential hill, the atom is scattered into a state, that does not couple to the light field. To participate in the cooling process again, it first has to transit to the coupling state. This process slows down as the atoms are further cooled. Therefore, GM cooling can be understood as a combination of Velocity-Selective Coherent Population Trapping (VSCPT) and Sisyphus cooling [213]. However, a major difference from GM to Sisyphus cooling is its VSCPT feature: the fact, that the cooled atoms accumulate in a non-coupling state. Theoretically, this allows the GM technique to reach temperatures below the recoil limit, which Sisyphus cooling is restricted to.

### 6.2.1 Principles

We follow the standard theoretical description of GM cooling, by considering a simple $\Lambda$-three-level system. It consists of two almost degenerate ground states $|1\rangle$ and $|2\rangle$ and an excited state $|3\rangle$. States $|1\rangle$ and $|2\rangle$ couple to $|3\rangle$ with the Rabi frequency $\Omega_{1/2} = \Gamma\sqrt{I_{1/2}/2I_{\mathrm{sat}}}$, where $I_{1/2}$ are the intensities of the light field and $I_{\mathrm{sat}}$ the saturation intensity of the transition. Their detuning to $|3\rangle$ is given by $\delta_{1/2}$ and their relative detuning by $\delta = \delta_1 - \delta_2$, see Fig. 6.2. Further investigation focuses on the case of Raman condition $\delta = 0$, which in the end also provides the lowest temperatures.

Sending the light fields to the system yields to mixing of the states similar to the dressed state picture without taking the quantization of the light field into account. The Hamiltonian in the rotating frame

$$H = H_0 + V = \frac{\hbar}{2}\begin{pmatrix} 0 & 0 & \Omega_1 \\ 0 & 0 & \Omega_2 \\ \Omega_1 & \Omega_2 & -2\delta_{1/2} \end{pmatrix} \tag{6.4}$$

is divided into $H_0 = -\hbar\delta_{1/2}|3\rangle\langle 3|$, that shifts the exited state energy by $-\hbar\delta_{1/2}$. The coupling term $V$ of the Hamiltonian drives the two ground states to the excited state as

$$V = \frac{\hbar\Omega_1}{2}|1\rangle\langle 3| + \frac{\hbar\Omega_2}{2}|2\rangle\langle 3| + c.c.. \tag{6.5}$$

By diagonalizing of $H$, the following eigenstates are derived:

$$\begin{aligned} |\Psi_D\rangle &= \frac{1}{\sqrt{\Omega_1^2 + \Omega_2^2}}(\Omega_1|1\rangle - \Omega_2|2\rangle), \\ |\Psi_B\rangle &= \frac{1}{\sqrt{\Omega_1^2 + \Omega_2^2}}(\Omega_1|1\rangle + \Omega_2|2\rangle). \end{aligned} \tag{6.6}$$

Applying the coupling term $V$ on the eigenstates reveals:

$$\langle 3|V|\Psi_D\rangle = 0. \tag{6.7}$$

Therefore, state $|\Psi_D\rangle$ is dark to the light field. While $|\Psi_D\rangle$ does not couple to the excited state anymore, the matrix element for $|\Psi_B\rangle$ does not vanish:

$$\langle 3|V|\Psi_B\rangle = \frac{\hbar}{2}\sqrt{\Omega_1^2 + \Omega_2^2}. \tag{6.8}$$

Following these findings, $|\Psi_D\rangle$ is commonly referred to as the *dark state* and $|\Psi_B\rangle$ as the *bright state*. The energy of the bright state is shifted by $E_B = \hbar\frac{\Omega_1^2+\Omega_2^2}{\delta_{1/2}}$. For a red detuned light field it shifts down and for a blue detuned light field up. Meanwhile, the energy of the dark state is not affected $E_D = 0$.

If $H$ was the true Hamiltonian of a real world (atomic) system, its dynamics were rather simple. The atoms would adiabatically follow the imposed light field to a bright or dark state. Eventually, all atoms in the bright state would scatter into the dark state, in which they are decoupled from the light field. Transitions from the dark to the bright state are not possible due to their orthogonality in $H$.

When the momentum of the atom is taken into consideration as well, a channel for transitions from the dark to the bright state opens [215]. With the kinetic energy term added, finally the full Hamiltonian describing the GM technique is obtained: $\mathcal{H} = \frac{\hat{p}^2}{2m} + H$. The motional coupling of the dark to the bright state for the full Hamiltonian is

$$\langle\Psi_B|\mathcal{H}|\Psi_D\rangle = \langle\Psi_B|\frac{\hat{p}^2}{2m}|\Psi_D\rangle = -\hbar\frac{2\Omega_1\Omega_2}{\Omega_1^2 + \Omega_2^2}\frac{kp}{m}, \tag{6.9}$$

where $p$ is the momentum of the atom and $k$ is the wave number of the transition.
For vanishing momentum, $|\Psi_D(p = 0)\rangle$ is a perfectly decoupled state. Neither the atom-light field nor the kinetic energy coupling affect it. This process is a Velocity-Selective Coherent Population Trapping mechanism. The transition probability due to the atomic motion is

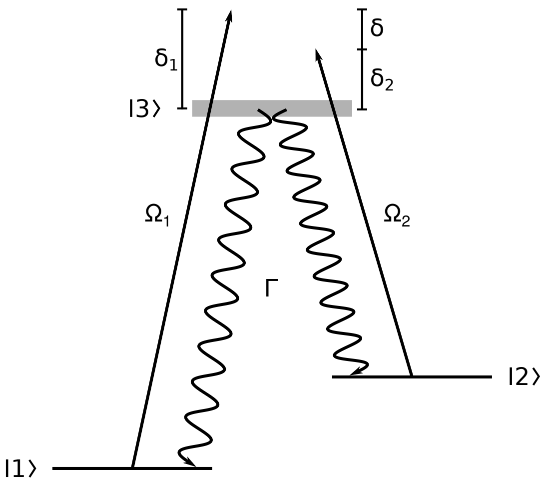

**Figure 6.2** **$\Lambda$-three-level system** The gray molasses' underlying level scheme consists of two ground states $|1\rangle$ and $|2\rangle$, that couple to the excited state $|3\rangle$ with their respective Rabi frequencies $\Omega_1$ and $\Omega_2$. The light fields are detuned by $\delta_1$ and $\delta_2$, with the relative detuning $\delta$. The natural linewidth of $|3\rangle$ is given by $\Gamma$. Adapted from [214]

obtained in the limit of weak atom light field coupling ($\Omega \ll |\Gamma/2 - \delta|$) and small velocities ($\frac{pk}{m} \ll 1$) :

$$P_{D\to B} = \left(\frac{\langle\Psi_B|\frac{\hat{p}^2}{2m}|\Psi_D\rangle}{E_B - E_D}\right)^2 = \left(2\frac{\Omega_1\Omega_2}{(\Omega_1^2+\Omega_2^2)^2}\frac{pk}{m}\delta_{1/2}\right)^2 . \tag{6.10}$$

This formula directly reveals, that the non-adiabatic transition probability is highest when the energy difference between the bright and dark state is lowest. Furthermore, the probability decreases for slower atoms $P_{D\to B} \propto v^2 \propto E_{kin}$ ($v = p/m$). Consequently, an atom that is in the process of being cooled down under static light field conditions takes more and more time to transit from the dark to the bright state. An increase in the detuning $\delta_{1/2}$ is expected to counteract the slowed down cooling process. Also decreasing the light intensities $I_1$ and $I_2$ prevent a reduction of $P_{D\to B}$.

The final ingredient for GM cooling is a spatially varying polarization field. It is commonly provided by the interference of counterpropagating beams with lin⊥lin or $\sigma^+$-$\sigma^-$ polarization (see Fig. 6.3). The latter is especially popular because it allows to reuse the optical path of the MOT beams. Yet, as for Sisyphus cooling, the theoretical description in the $\sigma^+$-$\sigma^-$ polarization field is conceptually more difficult to understand [216]. The lin⊥lin configuration consists of two counter propagating beams of linearly polarized light, which are rotated by 90° with respect to each other. While the intensity remains constant, the polarization locally changes from $\sigma^-$, to linear, to $\sigma^+$ with a period of half of the wavelength. The coupling strength and therefore the Rabi frequencies $\Omega_1$ and $\Omega_2$ are polarization dependent. Hence, the energy of the bright state ($E_B \propto \Omega_1^2 + \Omega_2^2$) is modulated as the polarization changes spatially.

In the full picture, a well-founded qualitative understanding of the GM cooling process is obtained. A graphical representation of the following description is provided in Fig. 6.3:

A $\Lambda$-three-level system atom (as in Fig. 6.2) being in the dark state $|\Psi_D\rangle$ propagates freely along the $z$ axis with initial velocity $v_{\text{init}}$. Since it does not couple to the light field it stays unaffected by it. The atomic momentum leads to a non-adiabatic transit to the bright

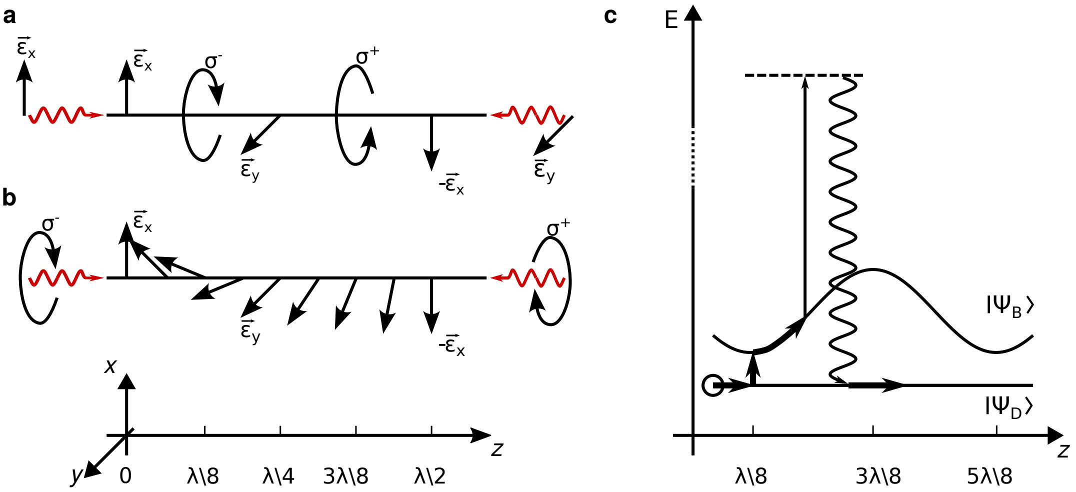

**Figure 6.3** **Polarization gradients and GM cooling scheme.** Polarization gradients in one dimension for counterpropagating beams of lin⊥lin and $\sigma^+$-$\sigma^-$ polarization. While for both configurations the intensity is constant along $z$, two distinct polarization patterns form. **a.** For lin⊥lin the polarization smoothly changes from linear-vertical, to $\sigma^-$, to linear-horizontal, to $\sigma^+$ and to linear vertical again with a period of $\lambda/2$. **b.** For $\sigma^+$-$\sigma^-$ the polarization pattern stays linear and turns around the $z$ axis with a period of $\lambda/2$. **c.** An atom with a $\Lambda$-three-level system (see Fig. 6.2) is placed in a GM light field with a polarization gradient as in b. Initially, the atom starts in the dark state $|\Psi_D\rangle$ and moves along $z$. It is non-adiabatically transferred to the bright state $|\Psi_B\rangle$, where the energy splitting of the two is smallest. The atom now experiences a spatially varying light shift due to the spatially varying polarization. By that kinetic energy is transferred to potential energy. While climbing up the potential hill, the atom is pumped into the dark state $|\Psi_D\rangle$. The atom propagates along $z$ with a now reduced velocity. It again undergoes cooling cycles until it is motionally decoupled from $|\Psi_B\rangle$ at $v = 0$.

state $|\Psi_B\rangle$, where the energy of the bright state $E_B$ is lowest. Here—as obtained from Eq. (6.10)—the transition probability is highest. The atom being now in the bright state $|\Psi_B\rangle$, moves in the potential generated by the polarization gradient. As the atom climbs the potential hill, kinetic energy is transferred to potential energy. Eventually the atom in the bright state gets excited and decays to the lower lying dark state. Now the cooling cycle starts again.

### 6.2.2 An improved non-standard GM of $^6$Li

In this section, the implementation of a non-standard GM sequence for $^6$Li is presented. Applying a linear ramp to zero power of cooler and repumper after a preceding standard pulse allows cooling the atoms further than the usually obtained $40\,\mu$K to $50\,\mu$K. The modified sequence provides temperatures of $13\,\mu$K, which is a factor four improvement to the conventional approach. To the best knowledge of the author, the $13\,\mu$K GM is the coldest, that has been reported so far for $^6$Li. In [217] also a ramped GM was applied to cool $^6$Li. There a temperature of $40\,\mu$K was demonstrated with a comparably high temperature for the pulsed GM of $115\,\mu$K. Similar improvements to the one found in this work, was obtained in [218] for $^{23}$Na. There a pulsed GM temperature of $45\,\mu$K was further reduced to $9\,\mu$K by a consecutive intensity ramp. For bosonic $^7$Li, $25\,\mu$K was achieved with the GM

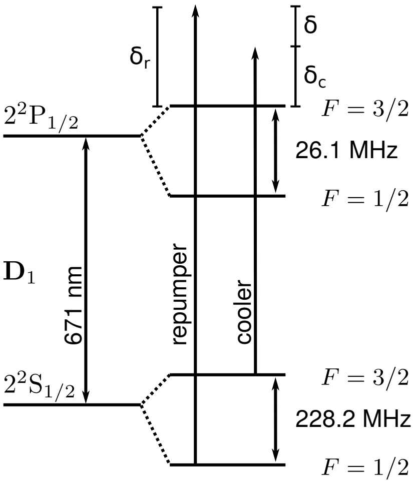

**Figure 6.4** **GM light fields in the $^6$Li level system.** The experimental realization of the Λ-three-level scheme is implemented on the $D_1$-line. The cooler and repumper are detuned from the excited state by $\delta_c$ and $\delta_r$ respectively. Their relative detuning is given by $\delta = \delta_c - \delta_r$.

technique [219]. The HF splitting of the $^2P_{1/2}$ state in $^7$Li is three times larger than for $^6$Li. In the latter, the performance of the ramped technique is characterized and compared to the standard constant pulse approach.

### GM implementation for $^6$Li

As for the standard approach, the GM technique is employed on the well isolated $D_1$-line (see Fig. 6.4). Here, the transition condition $F \to F$ needed for the formation of a dark state is satisfied. The two ground states of the Λ-three-level system are given by the states $|F = 1/2\rangle$ and $|F = 3/2\rangle$ of the ground state $2^2S_{1/2}$ manifold. With respect to the $671\,\mathrm{nm}$ $D_1$ transition, the ground state splitting of $228\,\mathrm{MHz}$ is negligible, which makes the two states effectively degenerate in this picture. The excited state in the scheme of the Λ-three-level system is given by the $|F = 3/2\rangle$ state of the $2^2P_{1/2}$ manifold. It is separated by about $4.4\Gamma$ to its lower lying $|F = 1/2\rangle$ neighboring state.

Taking into account the $(2F + 1)$ Zeeman sub-levels of each participating state, the simple theoretical Λ-three-level system picture does not hold anymore. To analyze this larger Hilbert space, techniques of numerical diagonalization of the 6x6 ground state Hamiltonian as in [220] or semiclassical Monte Carlo simulation of the atom light system as in [217] can be applied. There, still the formation of almost flat and weakly coupling states and higher lying bright states with a modulated energy landscape are found. They show, that the simple Λ-three-level system GM cooling principles still apply in a reduced way to more complicated multi-level atoms.

Sticking to the convention and naming introduced for the MOT (see Section 4.2.4), the light field exciting the $|F = 3/2\rangle$ state is referred to as the *cooler transition* and from the $|F = 1/2\rangle$ state is referred to as the *repumper transition*. For convenience—as for the MOT—from now on the abbreviations *cooler* and *repumper* are used. Their detunings are denoted by $\delta_c$ and $\delta_r$ respectively. Their relative detuning $\delta$ is defined as $\delta = \delta_c - \delta_r$.

The GM beams are overlapped with the MOT beams on a PBS for every axis (see Fig. 5.13), resulting in three retro-reflected beam pairs of $\sigma^+$-$\sigma^-$ polarization[2]. Each beam pair has a waist of $1.7\,\mathrm{mm}$ and a maximum power of $P_c = 3.6\,\mathrm{mW}$ for the cooler and $P_r = 0.58\,\mathrm{mW}$ for the repumper, resulting in central intensities of $I_c = 10I_{sat}$ and $I_r = 1.6I_{sat}$. Before the GM stage, the atoms are being compressed in the MOT and quickly released by a sudden switch-off of the gradient jump coil and MOT light fields. At the same point in time also the magnetic offset field is tuned to compensate the ambient magnetic field. After $250\,\mu\mathrm{s}$ the magnetic field has settled enough to be able to switch on the GM beams. Coming from the compressed MOT, the $320\mu\mathrm{K}$ cloud consists of about $N_0 = 2 \cdot 10^7$ atoms.

### GM pulse vs ramp

Using the standard pulsed GM a temperature of $50\,\mu\mathrm{K}$ was achieved. The optimum pulse length was found to be $2000\,\mu\mathrm{s}$. At the end of the pulse, the cooler is switched off $5\,\mu\mathrm{s}$ prior to the repumper, to ensure the atoms to be in the $2^2S_{1/2}|F = 1/2\rangle$ ground state. On Raman condition ($\delta = 0$) a common (rather insensitive) detuning of cooler and repumper of about $6.6\Gamma$ maximizes the capture efficiency from the cMOT to about $80\%$. To achieve the $50\,\mu\mathrm{K}$, the maximum available cooler and repumper was employed.
Working with a consecutive power ramp after a pulse of constant GM light helped to reduce the achieved temperature to $13\,\mu\mathrm{K}$. A pulse of $1550\,\mu\mathrm{s}$ is followed by a simultaneous $650\,\mu\mathrm{s}$ linear power ramp of cooler and repumper to zero powers. Performing absorption imaging without repumper light showed no population in the $2^2S_{1/2}|F = 3/2\rangle$ manifold, indicating, that pumping into $2^2S_{1/2}|F = 1/2\rangle$ is provided. On Raman condition, the common detuning of cooler and repumper is also rather insensitive and provides the best performance for $5\Gamma$. The highest captured fraction for the ramped GM is $80\%$ as well, found for cooler and repumper intensities of $I_c = 10.6I_{\mathrm{sat}}$ and $I_r = 0.75I_{\mathrm{sat}}$.
The final power ramp contributes to a reduced temperature in three ways:

- Cooling stays efficient longer as $P_{D\rightarrow B}$ increases.
- Heating due to off-resonant scattering is reduced.
- Heating by a pumping pulse after the GM is removed.

The achieved PSD of the pulsed GM is about $6 \cdot 10^{-6}$. With about $4.5 \cdot 10^{-5}$, the PSD is improved by a factor $7.5$ with the final intensity ramp added.

| **GM type** | $T$ | $N/N_{cMOT}$ | $\delta_{c,r}$ | $I_c$ | $I_r$ | $I_c : I_r$ | $dt_{pulse}$ | $dt_{ramp}$ | $dt_{tot}$ |
|---|---|---|---|---|---|---|---|---|---|
| **Pulsed** | $50\,\mu\mathrm{K}$ | $80\%$ | $6.6\,\Gamma$ | $10.6I_{\mathrm{sat}}$ | $1.67I_{\mathrm{sat}}$ | $6.3:1$ | $2000\,\mu\mathrm{s}$ | - | $2000\,\mu\mathrm{s}$ |
| **Ramped** | $13\,\mu\mathrm{K}$ | $80\%$ | $5.0\,\Gamma$ | $10.6I_{\mathrm{sat}}$ | $1.50I_{\mathrm{sat}}$ | $7.1:1$ | $1550\,\mu\mathrm{s}$ | $650\,\mu\mathrm{s}$ | $2200\,\mu\mathrm{s}$ |

**Table 6.1 Optimized GM parameters and performance**

---

[2] Due to the overlap on the PBS the actual configuration is $\sigma^-$-$\sigma^+$ polarization with respect to the MOT field. However, GM operates at $B = 0$. Therefore, it only requires opposite handedness for the polarization gradient to build up, which both $\sigma^+$-$\sigma^-$ and $\sigma^-$-$\sigma^+$ fulfill.

### GM pulse vs ramp: Detuning

After the parameters of the pulsed and ramped GM were carefully tuned (see Table 6.1 for optimized values), the dependence of the relative detuning $\delta$ on the cloud temperatures and cooled fraction was recorded (see Fig. 6.5). For both, the cooler frequency was kept on the optimized detuning and the repumper frequency was scanned, because of the larger frequency tuning range of the repumper controlling AOM. For the pulsed GM, the lowest temperature of $50\,\mu\text{K}$ with a cooled fraction of $80\%$ is observed for $\delta = 0$, the maximum cooled fraction ($100\%$ of cMOT atoms) is found for $\delta \approx -2500\,\text{kHz}$ with a temperature of about $90\,\mu\text{K}$.

For the ramped GM, both maximum capture efficiency and lowest temperature were observed on Raman condition. Here, deviations from Raman condition are much more critical, than for the pulsed GM. Violating the Raman condition by $\pm 250\,\text{kHz}$ already doubles the minimum temperature of $13\,\mu\text{K}$. Further detuning induces strong heating to the atoms, that quickly

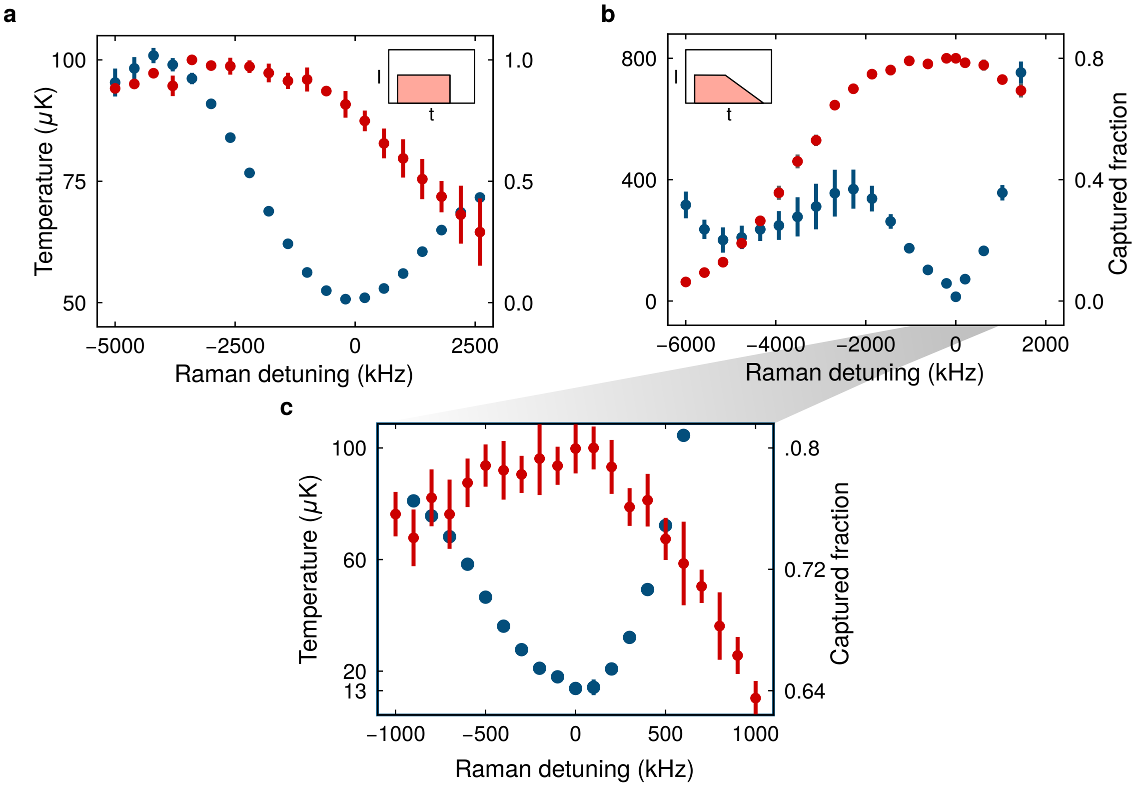

**Figure 6.5 Relative detuning $\delta$ dependence for pulsed and ramped GM around Raman condition.** **a.** Scan of relative detuning $\delta$ for a GM pulse of $2000\,\mu\text{s}$ on optimized conditions. The repumper frequency was scanned while the cooler frequency was kept on a constant detuning of $\delta_c = 6.6\Gamma$. The resulting temperature (blue) and the captured atom fraction (red) were recorded. A minimum temperature of $50\,\mu\text{K}$ was found on Raman condition ($\delta = 0$), while the maximum captured fraction occurs at $\delta \approx -2500\,\text{kHz}$. **b.** Scan of relative detuning for a GM pulse of $1550\,\mu\text{s}$ followed by a $650\,\mu\text{s}$ linear power ramp to zero power for optimized conditions. The repumper frequency was scanned for a constant cooler detuning of $\delta_c = 5\Gamma$. Both the minimum temperature of $13\,\mu\text{K}$ and maximum captured fraction of $80\%$ were found, when the Raman condition is met. **c.** Fine scan of the relative detuning of b. The temperature dependence on the detuning is more narrow, than for the pulsed GM in a. It doubles for $|\delta| \approx 250\,\text{kHz}$.

surpasses the cMOT temperature of $300\,\mu\mathrm{K}$. Increased red detunings heat the cloud much stronger and induces higher atom loss, than going in the blue direction. Precise offset field control below $50\,\mathrm{mG}$ is required, to achieve the GM temperature of $13\,\mu\mathrm{K}$.

### GM pulse vs ramp: Intensity

Keeping all other experimental parameters on their optimized values, the GM performance with respect to the cooler and repumper intensities was investigated (see Fig. 6.6). First, the impact of the repumper intensity was scanned, while the cooler intensity was kept at its maximum of $I_c = 10.6 I_{\text{sat}}$. For increasing repumper intensity the temperatures for the pulsed and ramped GM both decrease and saturate at around $I_r \approx 1 I_{\text{sat}}$ to $50\,\mu\mathrm{K}$ and $13\,\mu\mathrm{K}$ respectively. While the captured fraction for the ramped GM stayed constant, it grew for higher repumper intensities in the pulsed GM. The best repumper intensities are found to be: $I_r = 1.67 I_{\text{sat}}$ for the pulsed and $I_r = 1.5 I_{\text{sat}}$ for the ramped GM. With this, the ratio of cooler and repumper was fixed to: Pulsed $6.3 : 1$ and Ramped $7.1 : 1$.

Then the two types of GM were applied for varying cooler intensities with the repumper intensity changing accordingly by the ratio just set. Here, for both pulsed and ramped GM the captured fraction and temperature rose for increased intensities. For the maximally available cooler intensity the captured fraction was found to be $80\%$ on $50\,\mu\mathrm{K}$. Due to a lack of optical power, saturation in the captured fraction was not observed. In contrast, for the ramped GM, saturation in the captured fraction can be achieved for $I_c > 10 I_{\text{sat}}$. For both, applying less optical power leads to slightly lower achievable temperatures, which is at the same time accompanied by a strong decrease in the captured fraction.

### GM pulse vs ramp: Atom number

Working with the optimized parameters for the two types of GM, the initial atom number $N_0$ was varied by varying the MOT loading time. For the pulsed GM, a linear increase in temperature for atom numbers up to $\approx 1.5 \cdot 10^8$ was observed. In this interval, the temperature rises from $\approx 48\,\mu\mathrm{K}$ to $\approx 53\,\mu\mathrm{K}$ and then saturates. A linear fit to the data finds a slope of: $(2.84 \pm 0.39)\,\mu\mathrm{K}/10^8$ atoms.

The ramped GM temperature as well shows a linear temperature dependence for rising atom numbers. Starting at $\approx 12\,\mu\mathrm{K}$ it linearly rises to $\approx 18\,\mu\mathrm{K}$ for $\approx 2 \cdot 10^8$ atoms and then settles at this value for even higher atom numbers. A linear fit shows a slightly stronger rise in temperature of $(3.51 \pm 0.21)\,\mu\mathrm{K}/10^8$ atoms. The reason for rising temperatures likely results from heating due to radiation trapping in the atomic cloud. This effect is more pronounced for denser clouds, which explains the steeper slope for the ramped GM.

Using GM cooling for enhanced loading into an ODT was tried in different attempts, but failed to demonstrate a superior performance compared to loading with the $300\,\mu\mathrm{K}$ cMOT alone. The efforts were motivated by [221], that demonstrated enhanced loading of a multi-mode single beam ODT. By applying a GM pulse during the loading process, they showed a reduction in temperature of the atoms to $135\,\mu\mathrm{K}$ and with a consecutive GM cooling pulse they reduced the temperature further to $80\,\mu\mathrm{K}$. In our multi-mode Crossed Beam Optical Dipole Trap setup, we observed reduced loading efficiencies and heating when applying GM cooling during the loading stage and in trap. When scanning the detuning of the GM beams, periodic resonances of $\sim 6\,\mathrm{MHz}$ spacing corresponding to the multi-mode spacing of the laser were observed. Recreating the results of [221] in a single beam configuration was not attempted, since the reduced trap frequency slows down the subsequent evaporation stage.

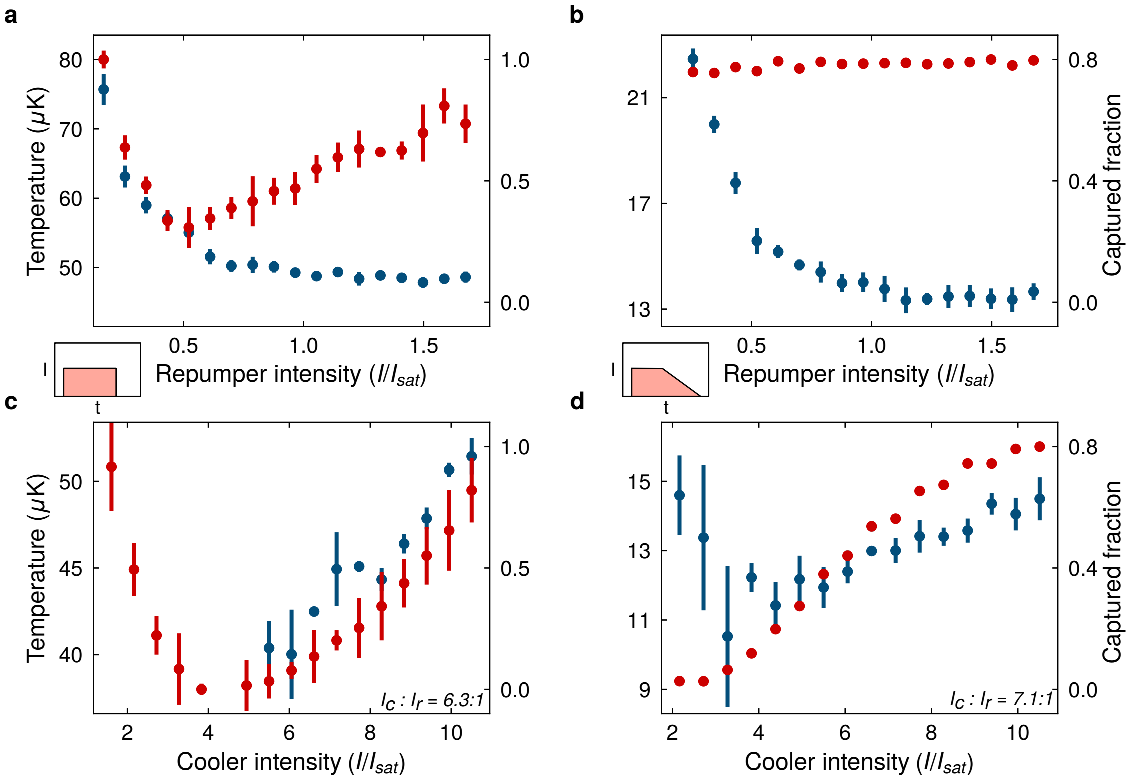

**Figure 6.6 Pulsed and ramped GM performance with cooler and repumper intensities.** Achieved temperatures (blue) and captured fraction (red) for varying repumper intensities for pulsed (**a**) and ramped (**b**) GM for constant cooler intensity $I_c = 10.6 I_{\text{sat}}$. Dependence of the cooler intensity for constant relative repumper intensities (see insets) for pulsed (**c**) and ramped (**d**) GM. In (**c**) temperatures for $I_c < 5 I_{\text{sat}}$ are not displayed due to too little atom numbers or too high values.

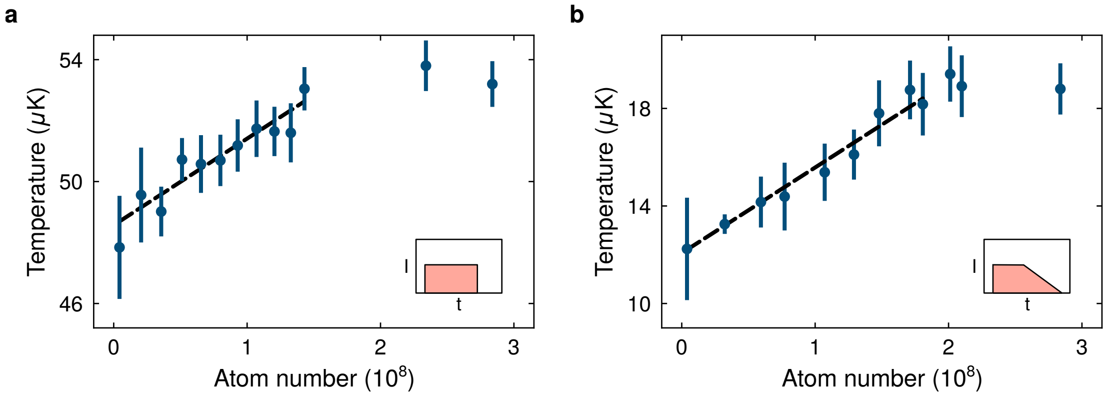

**Figure 6.7 Atom number dependence on GM temperatures.** Temperature for pulsed (**a**) and ramped (**b**) GM for varying initial cMOT atom number. In the linear regime, the temperature dependence is fitted (dashed black) and found to be: Pulsed $(2.84 \pm 0.39)\,\mu\mathrm{K}/10^8$ atoms, ramped $(3.51 \pm 0.21)\,\mu\mathrm{K}/10^8$ atoms.

## 6.3 Loading the Crossed Beam Optical Dipole Trap (CBODT)

The light for the Crossed Beam Optical Dipole Trap (CBODT) is derived from a multi-mode ytterbium fiber laser and sent horizontally onto the atoms (see again Fig. 5.11). The two beams with waists[3] of $60\,\mu\mathrm{m}$ and $65\,\mu\mathrm{m}$ cross under a shallow angle of $\sim 9°$. With a maximum power of $145\,\mathrm{W}$, a central trap depth of $2.45\,\mathrm{mK}$ for Li is provided. At this power, trap frequencies of $2\pi \cdot 5.8\,\mathrm{kHz}$ in the radial direction and $2\pi \cdot 454\,\mathrm{Hz}$ along the symmetry axis are achieved. In order to have a fast and efficient evaporation, high trap frequencies are needed. The single beam longitudinal trap frequency of $2\pi \cdot 20\,\mathrm{Hz}$ is not sufficient here. A simulation of the trap depth in the horizontal plane is presented in Fig. 6.8. High trap depth regions of $\sim 1\,\mathrm{mK}$ extend far into the single beam arms. The CBODT is the transition stage between the MOT and the optical transport. With $300\,\mu\mathrm{K}$, the cMOT temperature is well above the $35\,\mu\mathrm{K}$ trap depth of the transport beams. The CBODT is designed to bridge this temperature gap by loading the hot atoms and evaporate them into the transport lattice. In a past setup, the laser beams were oriented vertically. This resulted in a more than factor two worse capture and handover efficiency. As the power is lowered during evaporation, hot atoms in the wings are lost from the vertically aligned trap due to gravity. A comparison of the two scenarios is given in Fig. 6.8.

Before the atoms of the MOT are loaded, the fields and laser beam for Zeeman Slowing are switched off. For the magnetic fields of these large coils to settle, a time of about $500\,\mathrm{ms}$ is needed. After a standard MOT loading time of $5\,\mathrm{s}$, the compression stage starts with typically $6.5 \cdot 10^7$ Li atoms. The compression stage consists of a first period of simulations linear parameter ramps and a consecutive holding phase for thermalization, before the MOT beams and gradient field are finally switched off. During the $50\,\mathrm{ms}$ ramp, the gradient is increased from $6\,\mathrm{G/cm}$ to $15\,\mathrm{G/cm}$, cooler / repumper are being detuned to $\approx -\Gamma/2$, and their light levels are reduced to $0.4\,\mathrm{I_{sat}}$ / $0.05\,\mathrm{I_{sat}}$. The magnetic offset fields are tuned as well during the compression ramp to match the position of the CBODT. After the ramps have ended, the final parameter values reached are hold for another $10\,\mathrm{ms}$ for thermalization. At

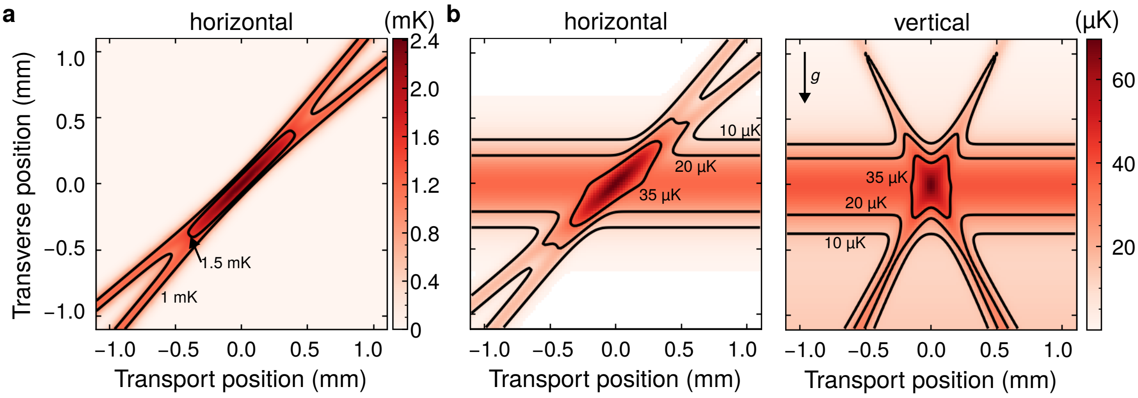

**Figure 6.8** **CBODT simulation. a.** Simulated trap depth in the horizontal plane for two $145\,\mathrm{W}$ crossed beams with $70\,\mu\mathrm{m}$ waists. **b.** Comparison of horizontally and vertically oriented CBODTs at low power for atom handover into the transport beams. Left: same as a., but with a power, that matches the trap depth of the transport. Right: Vertical orientation of the same beams with a crossing angle of $53°$.

---

[3] The simulations are based on waists of $70\,\mu\mathrm{m}$ to account for imperfections.

the end of the hold time, the repumper beam is switched off $5\,\mu\mathrm{s}$ prior to the cooler beam, to pump the atoms in the $F = 1/2$ ground state. When the compression stage has ended, $2.9 \cdot 10^6$ atoms have accumulated in the center of the CBODT with another $\sim 3 \cdot 10^6$ in the wings of the trap. The beams of the CBODT have been switched on $3\,\mathrm{s}$ before the start of the cMOT, to have settled motion due to thermal drifts.

Loading to the CBODT was characterized for varying experimental parameters. The results are shown in Fig. 6.9. Investigating the atom number for increasing trap depths shows a small rise at low trap depths, followed by a linear growth up to the maximum trap depth achievable. Saturation in trap depth is therefore not reached yet. Having the laser run on higher output powers, to get a deeper trap alters the optical output mode and was therefore not tested. Varying the atom number loaded in the MOT prior to the compression stage shows, that a maximum of $3.3 \cdot 10^6$ can be transferred to the trap. The atom number in the CBODT starts saturating for $\sim 10^8$ atoms in the MOT. The transfer efficiency to the CBODT drops from $\sim 8\%$ for low atom numbers to below $3\%$ at saturation. When the atoms are being held in the trap, an initial fast decay of the atom number for $\sim 1\,\mathrm{s}$ is observed. After that a $1/e$-lifetime of $15\,\mathrm{s}$ is recorded. For this reason, the atom numbers stated before were obtained for a holding time of $0.5\,\mathrm{s}$.

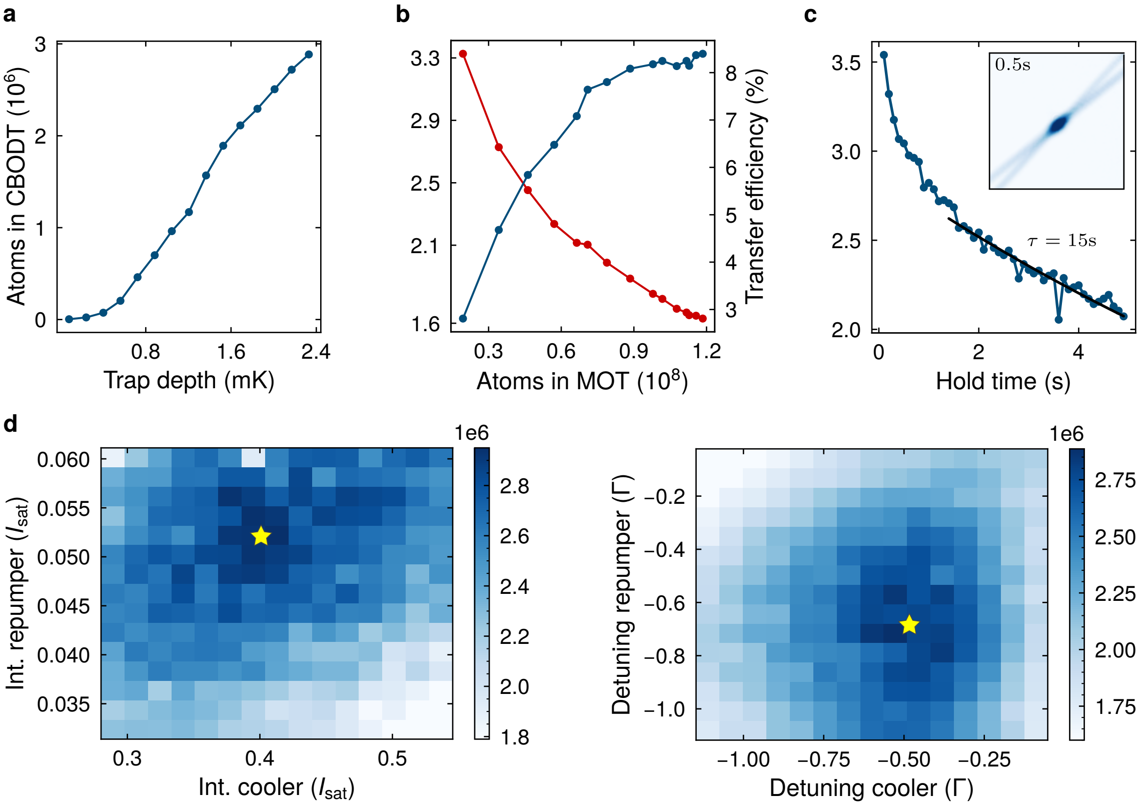

**Figure 6.9** **CBODT loading characterization. a.** Atom number loaded to the CBODT for varying trap depths. **b.** Transfer efficiency and atom number loaded to the CBODT for varying atom numbers in the MOT. **c.** Atom number for varying holding times in the CBODT. The inset shows a typical absorption image. A $15\,\mathrm{s}$ 1/e-lifetime is extracted from an exponential fit (black). **d.** Atom number loaded to the trap for varying final cooler and repumper intensities (left) and detunings (right) of the cMOT stage.

## 6.4 Optical transport of Li

Having the atoms loaded to the CBODT in the Li MOT chamber, a distance of $1\,\mathrm{m}$ to the science chamber has to be overcome. Long distance transport of ultracold atoms have been demonstrated with multiple techniques. Magnetic transport, where an array of spatially overlapped gradient coils are switched sequentially to make the atoms move, is not feasible for our mixture experiment [222]. The highly magnetic Er atoms are very prone to gradient fields. They would therefore be easily disturbed by the magnetic transport of Li. Transport of the atoms with ODTs is an approach, that fits better to our system. There are two common approaches for optical transport of the atomic clouds. In one of them, moving focus traps are employed. Having the atoms trapped in the focus, they move as the focal point is tuned. With focus tunable lenses [223], or focusing lenses mounted on translation stages [224], transport distances of almost half a meter have been demonstrated. Liquid-based focus tunable lenses are prone to drifts and thermal lensing, which does not qualify for applications with high-power laser beams. Even though, focus shifting with translation stages has been successfully demonstrated for transporting a BEC over $44\,\mathrm{cm}$, avoiding fast movements on the experimental table is generally advisable. We therefore decided for a running lattice transport approach, which does not rely on a physically moving parts.

In this technique, the atoms are first loaded to a standing 1D lattice formed by counterpropagating laser beams. In a consecutive step, the interference pattern is shifted by detuning the two beams. Controlling the detuning $\Delta f$, the atoms are moved along the lattice to the desired position. This technique has been demonstrated for a lattice formed by two laser beams of displaced foci in [225]. Our setup (see againFig. 5.12) follows their design, with the seed light being tuned before a consecutive amplification stage.

The optical potential of our transport lattice is provided by two laser beams of $1064\,\mathrm{nm}$ light with $80\,\mathrm{W}$ and $23\,\mathrm{W}$ of power. The beams connect the centers of the Li MOT chamber, the Er MOT chamber and the science chamber. A simulation of the trap depth and lattice depth along this connecting line is shown in Fig. 6.10. The lattice depth $V_0$ gives the height of the potential between neighboring lattice sites. It is different from the total trap depth, because the two interfering beams are not identical. Both, the lattice depth and the trap depth vary strongly from one end to the other. In the Li chamber, the transport lattice provides a total depth of $36\,\mu\mathrm{K}$ and a lattice potential of $V_0 = 19\,\mu\mathrm{K}$. When loaded to the CBODT, the atomic cloud is at $300\,\mu\mathrm{K}$. The atoms are evaporated into the transport lattice in a 3 s linear ramp to zero power. During the evaporation, the Feshbach field is set to $330\,\mathrm{G}$ to increase elastic scattering of the atoms, needed for fast thermalization. Typical atom numbers and temperatures of the Li atoms recorded for various points along the evaporation trajectory are presented in Fig. 6.10b. The evaporation ramp shown stops at about double the trap depth of the transport lattice, because the handover process starts dominating around this point. As the trap depth is lowered continuously, the temperature of the atoms drops linearly. However, the atom number in the CBODT stays constant until $1/3$ of the maximum trap depth is reached. The reason for this is atoms being evaporated into the overlap region of the cross trap from the single beam arms. Starting from $1.8 \cdot 10^6$ atoms at $300\,\mu\mathrm{K}$, $6.5 \cdot 10^5$ atoms at $5\,\mu\mathrm{K}$ are handed over to the transport lattice after the evaporation ramp.

Having the atoms loaded to the lattice, the transport is started immediately. When held in the optical lattice in the Li chamber, a fast spread of the atoms is observed (Fig. 6.11). The initially round cloud of $80\,\mu\mathrm{m}$ waist spreads with about $2.6\,\mu\mathrm{m/ms}$ in both directions due to tunneling. In the transport lattice of spacing $d_l = \lambda/2$, the recoil energy is given

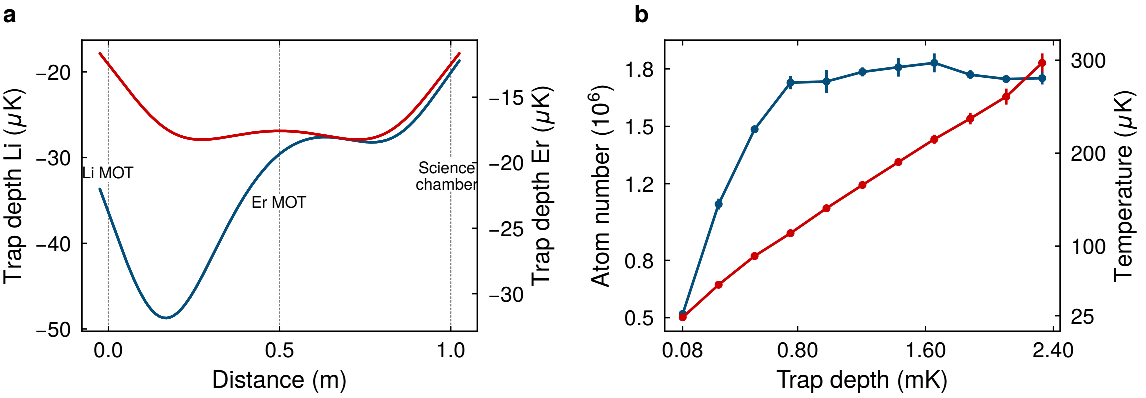

**Figure 6.10 Transport potential and loading. a.** Simulated trapping potential (blue) and lattice depth (red) of the transport beams of $80\,\mathrm{W}$ and $23\,\mathrm{W}$. **b.** Atom number (blue) and temperature (red) of the atoms during the evaporation trajectory of $3\,\mathrm{s}$ in the CBODT. The atom number in the crossed region stays constant over a long period due to atoms entering from the arms.

by $E_r = h^2/8md_l^2$ [22]. The onsite vibrational energy spacing along the lattice is given by $E_l = hf_l = 2E_r\sqrt{V_0/E_r}$, with the trap frequency $f_l$. The energy of the harmonic oscillator ground state is $E_l/2 = 5\,\mu\mathrm{K}$. This means, that Li is mostly in the lowest vibrational state of the transport lattice. The tunneling matrix element

$$J = E_r\frac{4}{\sqrt{\pi}}\left(\frac{V_0}{E_r}\right)^{3/4}\exp\left[-2\left(\frac{V_0}{E_r}\right)^{1/2}\right] \tag{6.11}$$

critically depends on the local lattice depth. The group velocity of the lowest band is given by $v_{g,0} = 2Jd_l/\hbar$. In the Li chamber, a group velocity of $2\,\mu\mathrm{m/ms}$ for $V_0 = 19\,\mu\mathrm{K}$ is calculated. The observed spread of $2.6\,\mu\mathrm{m/ms}$ matches a lattice potential of $V_0 = 17.5\,\mu\mathrm{K}$, which is within the range of the experimental precision at that point.

In order to avoid spreading of Li over the lattice, transport is started right after the atoms have been loaded. The velocity of the transport lattice $v$ is proportional to the detuning: $v = \Delta f\lambda/2$. Tuning the seed AOM driving frequency by up to $2 \cdot 8.5\,\mathrm{MHz}$, a maximum velocity of $9\,\mathrm{m/s}$ is reached[4]. The atoms are accelerated and later decelerated by linear frequency ramps. Here it was found, that using a fast updated cycle ($1\,\mu\mathrm{s}$) of the DDS is crucial to minimize heating of the atoms. Atom numbers transported to the science chamber for varying acceleration and velocity are shown in Fig. 6.11c. Here, the acceleration is given in the "natural" unit $a_{\mathrm{nat}} = a_{\mathrm{ho}}f_{\mathrm{ho}}^2$ of the lattice, with the harmonic oscillator length $a_{\mathrm{ho}}$ and frequency $f_{\mathrm{ho}}$. The best transport efficiency of $74\%$ is found for transporting at maximum velocity and an acceleration of about $a_{\mathrm{nat}}/2$. Due to the high acceleration[5] of $1.4\,\mathrm{km/s^2}$, the constant travel velocity is reached in $6\,\mathrm{ms}$. After $104\,\mathrm{ms}$ the atoms are decelerated again and reach the glass cell after a total travel time of $116\,\mathrm{ms}$. For optimized transport conditions, a total of $4.8 \cdot 10^5$ Li atoms at $8.4\,\mu\mathrm{K}$ reach the science chamber.

---

[4] In the end only one of the two seed AOMs is used for detuning the lattice beams. The reason for this is a peculiarity for frequency ramping with the DDS. Here, always first a positive and then the negative frequency ramp is executed. This circumstance is usually effectively mitigated by a very fast positive frequency ramp before the negative frequency ramp. Unfortunately, this "trick" can not be made use of, since it leads to significant heating of the atoms trapped in the transport lattice.

[5] $1.4\,\mathrm{km/s^2} = 140\,\mathrm{g}$, with the earth's acceleration $g$. Typical accelerations in roller coasters are $6\,\mathrm{g}$.

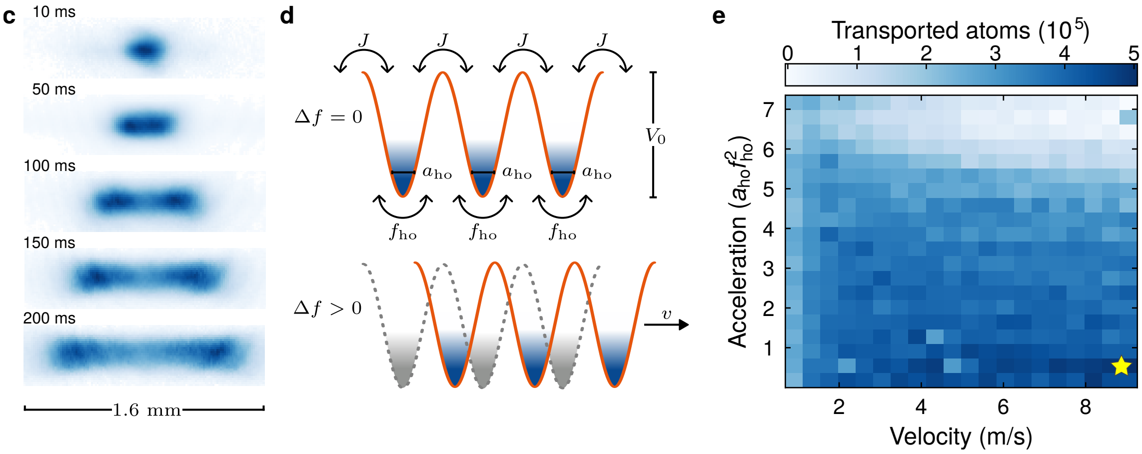

**Figure 6.11** **Optical transport of Li. a.** Absorption images showing tunneling of the Li atoms loaded into the transport lattice for different holding times. A settle time of $10\,\mathrm{ms}$ for the Feshbach field is needed to take a clean absorption image. **b.** Sketch of atoms loaded to the standing transport lattice (top) and the relevant parameters. In the bottom illustration, the lattice runs due to a detuning of the lattice beams. **c.** Number of transported atoms with respect to the acceleration and maximum velocity during transport. The acceleration is given in the natural units of the lattice ($a_{\rm ho} f_{\rm ho}^2$).

In a combined sequence, Li is first transported to the Er chamber in about $50\,\mathrm{ms}$. There Er is loaded to the transport lattice as well by a cMOT stage on the narrow $583\,\mathrm{nm}$ line [74]. After a total hold time of $560\,\mathrm{ms}$ for Li, the mixture is transported to the science chamber. During transport with Er, a magnetic gradient field of $4.2\,\mathrm{G/cm}$ is applied over the remaining transport distance. Employing the gradient field is required to levitate Er, since the radial confinement of the transport lattice can not hold against gravity. Due to higher lattice depths along the transport, a spread of the arriving Li cloud in the glass cell is suppressed. In the combined sequence, the Li atom number transported is reduced by about $50\%$ to $2.5 \cdot 10^5$. The temperature of the transported cloud stays unaffected.

# Chapter 7

# ErLi mixture

This chapter represents ongoing work and preliminary results of an ultracold mixture of ErLi. First measurements on lifetimes and thermalization of ErLi in $1064\,\mathrm{nm}$ ODTs are presented. Furthermore, promising results for sympathetic cooling of Li by Er below the Fermi temperature by double-species evaporation and the observation of an Er BEC in single-species evaporation are shown.

When Er and Li arrive in the glass cell after the optical transport has stopped, they are loaded to $1064\,\mathrm{nm}$ ODTs there (see again Fig. 5.15 for optical setup). In the final experimental sequence, it was found, that employing only the front and the cross beam for trapping the atoms provides the best performance. The front beam, which is sent to the atoms along the transport direction has $2.9\,\mathrm{W}$ of power and horizontal / vertical waists of $(w_h, w_v) = (30\,\mu\mathrm{m}, 48\,\mu\mathrm{m})$. The optical power of the cross beam is $20\,\mathrm{W}$. It is strongly elliptic with horizontal / vertical waists of $(w_h, w_v) = (360\,\mu\mathrm{m}, 43\,\mu\mathrm{m})$. The two beams are sent horizontally onto the atoms and cross at an angle of about $80\,^\circ$.
The combination of the front and cross beams provide a trap depth of $U_{\mathrm{Er}} = 69\,\mu\mathrm{K}$ for Er and $U_{\mathrm{Li}} = 130\,\mu\mathrm{K}$ for Li. Even at full power, gravity reduces the trap depth for Er already significantly. Without the gravitational force the trap depth is $83\,\mu\mathrm{K}$ for Er. The trap frequencies were obtained from parametric heating measurements. For Li they are $(\omega_x, \omega_y, \omega_z) = 2\pi \cdot (3324\,\mathrm{Hz}, 256\,\mathrm{Hz}, 2940\,\mathrm{Hz})$ with a geometric mean frequency of $\bar{\omega}_{\mathrm{Li}} = 2\pi \cdot 1357\,\mathrm{Hz}$. The $z-$axis points along the vertical direction. The geometric mean frequency was also obtained from a simulation of the optical potential. A difference of less than $2\%$ to the measured value shows precise alignment of the foci and overlap of the beams. For Er, the trap frequencies are reduced $6.5$-times compared to Li, due to its higher mass and slightly lower polarizability.
Loading Er and Li to the ODTs takes multiple steps of tuning the magnetic field and optical powers. A sketch of the relevant parameter ramps during the hand-over process is presented in Fig. 7.1. When the atoms have arrived in the glass cell, an optimized offset field for holding the atoms is applied while the gradient field of $4.2\,\mathrm{G/cm}$ for levitating Er atoms during transport is still present. Then the front and cross beams are ramped up to full power in $200\,\mathrm{ms}$. Now, that confinement against gravity is provided by the optical traps, the gradient field is ramped down during another $200\,\mathrm{ms}$. Meanwhile, the offset field is tuned to $B_z = 1.4\,\mathrm{G}$ for ideal holding conditions of Er. As a last step, the optical power of the transport beams are fully ramped down in $40\,\mathrm{ms}$.
The atoms are now placed in a well-isolated part of the vacuum system with large optical access. Er is spin-polarized to all atoms in $m_J = -6$ and Li is in a spin-mixture of the two energetically lowest Zeeman states $|1\rangle$ and $|2\rangle$. In order to obtain a purified Li cloud of all atoms occupying $|1\rangle$, a two-step state preparation process is applied. First the state $|2\rangle$

population is transferred to $|3\rangle$ with an adiabatic rapid passage [82]. For this, the driving frequency of an rf-coil oriented along the horizontal direction is swept over $(225.4\ \pm 0.175\ )\mathrm{kHz}$ in $55\,\mathrm{ms}$. Then the offset field is turned to point along the imaging direction, before a short $30\,\mu\mathrm{s}$ pulse of the circular polarized imaging light driving the $F = 3/2, m_F = 3/2$ to $F' = 5/2, m_{F'} = 5/2$ transition of the $D_2$-line is applied. With the resonant pulse, the atoms in state $|3\rangle$ are heated and a significant fraction, but not all of them, are removed from the system. Imperfect polarization of the imaging beam together with the narrow hyperfine splitting of the excited state are suspected to be the reason for pumping some atoms back to state $|2\rangle$. After repeating the purification process two more times, no atoms in $|2\rangle$ or $|3\rangle$ are detectable anymore. The state preparation process takes $400\,\mathrm{ms}$ and does not reduce the atom number of Li in state $|1\rangle$.

For the following experimental steps either a spin-mixture of Li in $|1\rangle$, $|2\rangle$ of $2 \cdot 10^4$ atoms or a spin-polarized cloud of Li in $|1\rangle$ with $1 \cdot 10^4$ is prepared. With about $3 \cdot 10^5$, the number of Er atoms loaded to the ODTs is about one order of magnitude higher. The hand-over sequence to the glass cell ODTs was optimized for highest Er atom numbers, since it used for sympathetic cooling of Li in later experimental steps. Using the sequence for loading Li in absence of Er yields a significantly reduced amount of loaded atoms. As in the Li chamber, the atoms quickly disperse along the transport lattice in the glass cell.

The atom numbers of Er and Li in the ODTs for varying holding times in the trap and for different mixtures were investigated. Er and Li atom numbers were found to behave very differently while held in the traps. For Er (with and without Li) an exponential decay was observed. In contrary to these findings, when loaded together with Er, the atom number for Li (spin-polarized and spin-mixture) stays basically constant[1] over the entire holding time period of more than $100\,\mathrm{s}$. This indicates, that the thermalization time of ErLi is much shorter than the lifetime of Li alone[2]. In the ErLi mixture, only the high-energy Er atoms are lost, due to the lower trap depth for Er. The heat load on Li is paid for in Er atoms alone for the investigated atom number regime.

With an exponential fit to the Er atom number:

$$N_{\mathrm{Er}}(t) = N_{\mathrm{Er},0} \cdot e^{-t/\tau}, \tag{7.1}$$

the $1/e$-lifetime was extracted for Er alone, for Er in presence of spin-polarized Li and for Er in presence of a spin-mixture of Li. The observed total lifetime consists of three different contributions:

$$1/\tau = 1/\tau_{Er} + N_{\mathrm{Li}|1\rangle}/\tau_{\mathrm{ErLi}|1\rangle} + N_{\mathrm{Li}|2\rangle}/\tau_{\mathrm{ErLi}|2\rangle}. \tag{7.2}$$

The atom numbers of the two Li Zeeman states $|1\rangle$ and $|2\rangle$ are denoted with $N_{\mathrm{Li}|1\rangle}$ and $N_{\mathrm{Li}|2\rangle}$ and their associated decay rates with $1/\tau_{\mathrm{ErLi}|1\rangle}$ and $1/\tau_{\mathrm{ErLi}|2\rangle}$.

In absence of Li, $\tau$ is simply given by the single species lifetime $\tau_{Er} = 139 \pm 7\,\mathrm{s}$. Having $N_{\mathrm{Li}|1\rangle} = 2.6 \cdot 10^4$ atoms of Li in $|1\rangle$ present, reduces the observed lifetime to $63 \pm 4\,\mathrm{s}$. In the spin-mixture with $N_{\mathrm{Li}|1\rangle} = N_{\mathrm{Li}|2\rangle} = 2.2 \cdot 10^4$, the lifetime is again significantly lowered to $39 \pm 1\,\mathrm{s}$. With this, the decay rates per atom number of Li in $|1\rangle$ and $|2\rangle$ are obtained:

$$1/\tau_{\mathrm{ErLi}|1\rangle} = 3.4 \pm 0.4\,\mathrm{mHz}/10^4 \quad \text{and} \quad 1/\tau_{\mathrm{ErLi}|2\rangle} = 5.4 \pm 0.5\,\mathrm{mHz}/10^4. \tag{7.3}$$

---

[1] For short holding times, the Li atom number even rises in the set Region Of Interest (ROI), as previously highly energetic Li atoms in the wings are cooled into the trap by Er.

[2] In other measurements the lifetime of Li in the glass cell ODTs was found to be $\sim 120\,\mathrm{s}$ in a spin-mixture or spin-polarized.

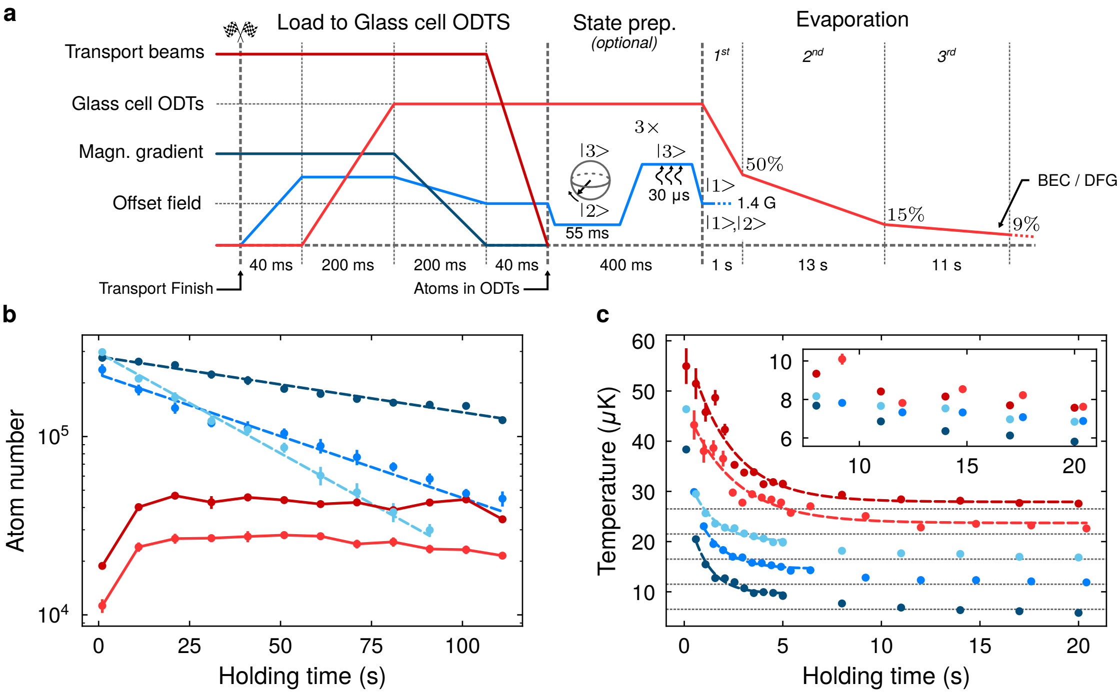

**Figure 7.1** **ErLi mixture in the glass cell ODTs. a.** Representation of the sequence for loading the ErLi mixture from the magnetic gradient supported transport lattice to the ODTs in the science chamber. Subsequent preparation of spin-polarized Li in $|1\rangle$ from a spin-mixture of $|1\rangle$,$|2\rangle$ is done by consecutive rf-transfer from $|2\rangle$ to $|3\rangle$ and removal of $|3\rangle$ by a pulse of resonant imaging light. The evaporation ramps to reach a BEC of Er alone or DFG by sympathetic cooling of Li by Er are also already shown. **b.** Lifetime measurements of Er (dark-blue) without Li, Er (blue) with Li$|1\rangle$ (light-red) and Er (light-blue) with Li$|1\rangle$,$|2\rangle$ (red). Exponential fits are represented by the dotted lines. **c.** Thermalization measurements for the same mixtures as in b. Readability is enhanced by an artificial spacing of $5\,\mu\mathrm{K}$ between the data sets with respect to the one of bare Er (dark-blue). The inset shows the (unshifted) temperatures for long holding times.

With about $2.1 \cdot 10^4$ Li atoms in $|1\rangle$ or about $1.3 \cdot 10^4$ Li atoms in $|2\rangle$ the lifetime of Er halves. The decay rate due to Li in $|1\rangle$ is significantly smaller, than the one due to Li in $|2\rangle$. Heating of Li in $|1\rangle$ and $|2\rangle$ are the same without Er being present. The excess decay rate $1/\tau_{\mathrm{ErLi}|2\rangle} - 1/\tau_{\mathrm{ErLi}|1\rangle} = 2.0 \pm 0.6\,\mathrm{mHz}/10^4$ is expected to originate from dipolar relaxation from Li in $|2\rangle$ decaying to $|1\rangle$, when Er is around. The associated energy of one dipolar relaxation event is $\Delta E_{|2\rangle,|1\rangle} = 2/3\mu_B 1.4\,\mathrm{G} = k_B \cdot 63\,\mu\mathrm{K}$, which does not remove Li from the trap and is absorbed by the Er atoms.

Thermalization of the atomic clouds after being loaded to the ODTs in the glass cell is investigated for the same mixtures as before. Temperatures were obtained with standard ToF thermometry for different holding times (see Fig. 7.1). The temperature of Li is found to be always higher than for Er at the same holding time in the trap. Right after being loaded, the temperature of both Er and Li is about $35\,\mu\mathrm{K}$. Atoms that are not loaded, but still around, bias the obtained temperature for short holding times. For all mixtures, Er and Li thermalize similarly. The $1/e$-thermalization time $\tilde{\tau}$ is obtained from an exponential fit to the temperatures. For Er, an exponential temperature decay is observed for holding times up to $\sim 5\,\mathrm{s}$. Evaporation of Er provides an additional cooling mechanism gradually lowering the temperature for longer holding times. For Li, temperatures for the entire investigated holding time span of $20\,\mathrm{s}$ follow a single exponential decay, since thermalization of Li is provided by the Er bath only. For Er alone the thermalization time is

$$\textbf{Er:}\quad \tilde{\tau}_{\mathrm{ErEr}} = 0.98 \pm 0.15\,\mathrm{s}.$$

In presence of spin-polarized Li in $|1\rangle$, thermalization times for Er and Li are:

$$\textbf{Er:}\quad \tilde{\tau}_{\mathrm{ErLi}|1\rangle} = 1.27 \pm 0.20\,\mathrm{s}\,; \quad \textbf{Li}: \quad \tilde{\tau}_{\mathrm{Li}|1\rangle\mathrm{Er}} = 2.4 \pm 0.4\,\mathrm{s}.$$

In presence of a spin-mixture of Li in $|1\rangle, |2\rangle$, thermalization times for Er and Li are:

$$\textbf{Er:}\quad \tilde{\tau}_{\mathrm{ErLi}|1\rangle|2\rangle} = 1.24 \pm 0.20\,\mathrm{s}\,; \quad \textbf{Li}: \quad \tilde{\tau}_{\mathrm{Li}|1\rangle|2\rangle\mathrm{Er}} = 2.1 \pm 0.3\,\mathrm{s}.$$

Compared to the bare Er case, the thermalization time of Er is increased, when Li is around due to the extra heating source introduced to the system. For the current configuration, the observed thermalization time of Er does not benefit from the enhanced thermal velocity and higher trap frequencies of Li. Thermalization times of Li, spin-polarized or spin-mixture, are found to be the same within the precision of our measurement. Compared to Er, the thermalization time of Li is found to be about double.

For forced evaporation of the ErLi mixture, both atoms are prepared in their ground state. Three sequential linear ramps of the optical potential are employed (see again Fig. 7.1). In a first fast ramp, the optical power of the ODTs is lowered to half in $1\,\mathrm{s}$. Then the optical power is lowered to $15\%$ in $13\,\mathrm{s}$. In the third ramp, the optical power is lowered very slowly with a slope of $-0.5\%/\mathrm{s}$. The evaporation ramps were optimized for Er alone.

Atom numbers and temperatures for Er and Li were recorded along the evaporation trajectory (see Fig. 7.2). During the entire evaporation process, the atom number of Li stays constant with $1.6 \cdot 10^4$ atoms. Cooling of Li is therefore provided by sympathetic cooling of Er only. Compared to the previous measurements, the number of loaded Li is reduced for lower heating. The Er atom number decreases linearly during the evaporation process. Starting with $22 \cdot 10^4$ Er atoms at the beginning of the second ramp, the optical trap for Er has opened due to gravity for powers of less than $9\%$ in the third ramp[3]. During the evaporation process the temperature for Li always stays above the one of Er. At the beginning of the second ramp the temperature of Er is about $5\,\mu\mathrm{K}$ and about $7\,\mu\mathrm{K}$ for Li. The temperature of Li follows the one of Er until about $10\%$ of the initial trap depth is reached. Here the gravitational sag is about $18\,\mu\mathrm{m}$ and the waist of Er has reduced to $9\,\mu\mathrm{m}$. At his point, thermalization and with this sympathetic cooling fades out due to a loss of overlap between the Er and Li atomic clouds. The highest degeneracy achieved for Li is $T/T_F = 0.77 \pm 0.10$. With Li being present, condensation of Er at the end of the evaporation trajectory is observed. The atom number in the BEC is reduced by $2/3$, compared to the single-species evaporation and overlap of the clouds are lost due to the gravitational sag.

In absence of Li, an Er BEC of $1.9 \cdot 10^4$ atoms with a condensed fraction of $31\,\%$ forms after $9\,\mathrm{s}$ in the third ramp. Right before the atoms are lost, a BEC of $2 \cdot 10^4$ atoms with an undetectable classical fraction is observed. The condensed fraction was extracted with a bimodal fit of a Gaussian and an integrated Thomas-Fermi distribution (Eq. (2.62)).

Temperatures for the ErLi evaporation were extracted with standard ToF thermometry, which eventually fails to provide the correct temperature of the system around the onset of degeneracy. Independent thermometry with a Fermi fit (Eq. (2.48)) to $9 \cdot 10^3$ Li atoms in a spin-mixture with $4\,\mathrm{ms}$ ToF was performed after sympathetic cooling with Er. Here, a temperature of $T/T_F = 0.49^{0.71}_{0.35}$ was found, which agrees well with $T/T_F = 0.77 \pm 0.10$ within

---

[3] Right before this point a BEC of Er is obtained in the single species evaporation.

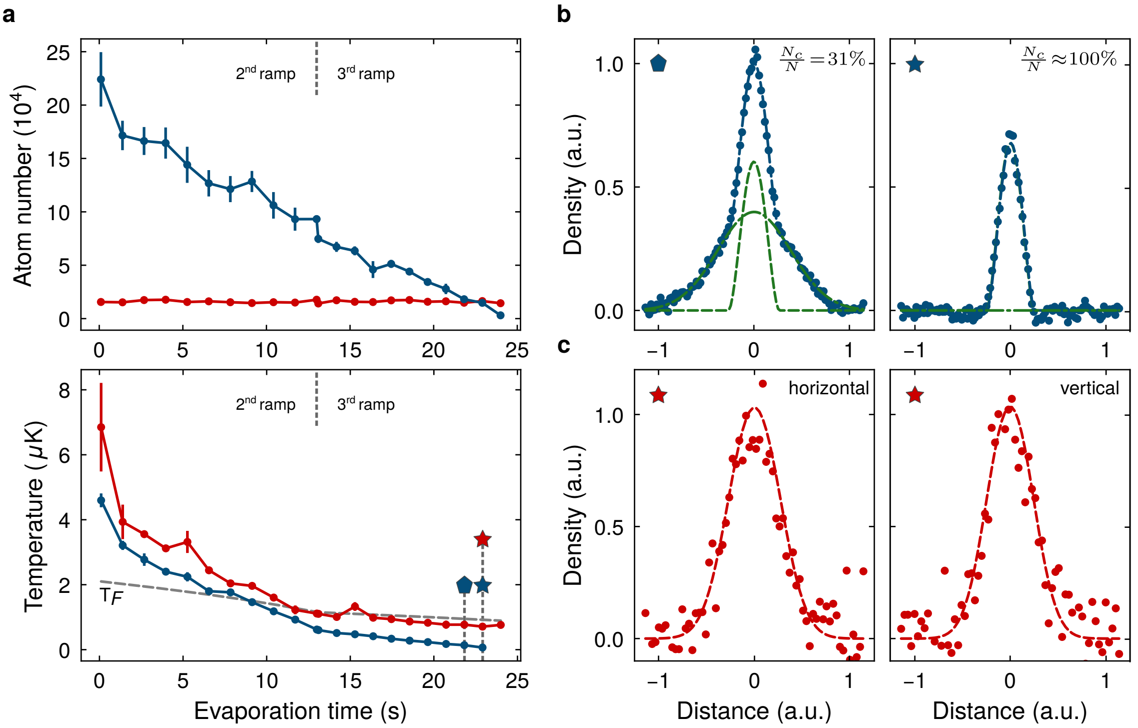

**Figure 7.2 Sympathetic cooling of Li by Er. a.** Atom numbers and temperatures of Er (blue) and Li (red) along the evaporation trajectory. Sympathetic cooling of Li by Er is demonstrated as the Li atom number stays constant until Er is lost. The red star marks the point of highest degeneracy of Li with $T/T_F = 0.77 \pm 0.10$. The blue pentagon and star mark the point in the trajectory, where Er forms a BEC in a single species evaporation. **b.** 1D integrated density profiles of Er BECs with a bi-modal fit (blue dashed) consisting of a Thomas-Fermi (green dashed) and a Gaussian (green dash dotted) distribution. **c.** 1D cuts of the atomic density of $9 \cdot 10^3$ Li atoms in a spin-mixture after $4\,\mathrm{ms}$ ToF. With a 2D Fermi fit (dashed line) $T/T_F = 0.49^{0.71}_{0.35}$ is found.

the achieved error. The fitted Fermi profile still closely resembles a Gaussian distribution at these comparably low degeneracies. A flat top is slowly becoming apparent in the observed atomic density distribution.

Enhanced performance in evaporating Er and sympathetic cooling of Li is expected to be obtained for optical traps providing higher trap frequencies. Tighter confinement in the vertical direction helps to reduce the gravitational sag of Er. Thereby thermal contact between Er and Li is expected to persist at ultra-low temperatures and Li clouds of even higher degeneracies could be achieved. The evaporation speed will also benefit from increased trap frequencies. For the current configuration, the trap frequency along the y-direction strongly reduces the geometric mean trap frequency. With faster evaporation, the effect of time independent heating mechanisms, such as off-resonant scattering, are reduced as well. The experimental cycle time also benefits from faster evaporation, since it makes up the longest part of the sequence.

In the future, additional ODTs at the tune-out wavelength near $841\,\mathrm{nm}$ of Er can be employed [64]. Providing higher trap frequencies for Li, the Fermi temperature of the system is increased leading to higher degeneracies for the same temperature. As the tune-out ODTs provide species selective trapping, spatial overlap of the clouds can be kept by dynamical adjustments of the trap centres.

# Chapter 8

# Summary and outlook

## 8.1 Summary

In this thesis a new dual-species quantum gas experiment for bosonic $^{166}$Er and fermionic $^{6}$Li is presented. The focus of this work is on the experimental parts of the laser and vacuum system for providing an ultracold gas of Li. The generation of the ultracold Li gas is discussed and characterized in detail, making use of standard and further developed laser cooling techniques. First results of sympathetic cooling of Li below the Fermi temperature by Er in a well-isolated glass cell providing high optical access are promising steps towards the exploration of highly degenerate Fermi systems.

After introducing properties of degenerate quantum gases of fermions and bosons in harmonic potentials, issues on thermometry of Fermi gases by fitting Fermi distributions below $T/T_F = 0.2$ and a stop of efficient thermalization below $T/T_F = 0.15$ due the closing Fermi seas in spin-mixtures are discussed. Approaches for addressing both problems in a Fermi-Bose mixture of Li and Er is presented and approaches on keeping efficient sympathetic cooling below $T/T_F = 0.01$ are introduced.
A comprehensive overview and comparison of the level structures and ground state properties focusing on laser cooling characteristics of the alkali-metal Li and lanthanide Er are provided. Here, especially the difference in magnetic moments of the ground states (Li: $1\mu_B$, Er: $7\mu_B$) and the laser cooling limits of commonly used optical transitions (Li: $D_1$&$D_2$ at $671\,\mathrm{nm}$, Er: $401\,\mathrm{nm}$, $583\,\mathrm{nm}$ and $841\,\mathrm{nm}$) are pointed out.
After a global overview on the vacuum system of the ErLi experiment is given, the focus is set on the single species Li arm. Subsystems are presented individually together with laser cooling steps for efficient loading of the MOT. A boost of the MOT loading rate by one order of magnitude is demonstrated and characteristiced with a combined technique of Optical Pumping / Transversal Cooling (OP/TC) of the atomic beam right after the oven. Typically, $6.5 \cdot 10^{7}$ atoms are provided for further cooling steps after $5\,\mathrm{s}$ of MOT loading.
The laser system providing resonant light at $671\,\mathrm{nm}$ for laser cooling of Li is presented. It is based on three homebuilt External Cavity Diode Lasers (ECDLs) with one master laser locked to an Ultra Low Expansion (ULE) cavity and the other two beat-locked to it. Sufficient optical power is provided with amplification by Injection-Locks (ILs) and stable operation is ensured by a new-developed and characterized optimization algorithm. The laser systems for providing Optical Dipole Traps (ODTs) at $1064\,\mathrm{nm}$ and $1070\,\mathrm{nm}$ for trapping and transporting of Er and Li are presented as well.
Starting from the loaded MOT, a non-standard intensity ramped free space Gray Molasses-technique providing temperatures as low as $13\,\mu\mathrm{K}$ is demonstrated. It is characteristiced and compared to the standard pulsed approach, reaching only $40\,\mu\mathrm{K}$ - $50\,\mu\mathrm{K}$ for Li. In the

final experimental sequence for overlapping Er and Li, a horizontally oriented Crossed Beam Optical Dipole Trap (CBODT) is loaded directly from the cMOT. Starting form $1.8 \cdot 10^6$ atoms in the trap center, $6.5 \cdot 10^5$ Li atoms at $5\,\mu\mathrm{K}$ are handed over by evaporation into the 1D transport lattice, formed by two high-power counterpropagating single mode laser beams at $1064\,\mathrm{nm}$. By detuning one of the transport laser beams, subsequent optical transport over $1\,\mathrm{m}$ to the science chamber with an efficiency of $74\%$ is demonstrated.
In a combined ErLi sequence, the Li atoms are first transported to the Er chamber, where the Er atoms are loaded on top with a cMOT at $583\,\mathrm{nm}$. Further optical transport to the $0.5\,\mathrm{m}$ away science chamber is supported by an additional $4.2\,\mathrm{G/cm}$ magnetic gradient field for levitating Er. After transport, the atoms are loaded to $1064\,\mathrm{nm}$ ODTs and the gradient field is switched-off. In the ODTs, typically $3 \cdot 10^5$ Er atoms and $4.4 \cdot 10^4$ Li atoms in a spin-mixutre of $|1\rangle$, $|2\rangle$ or $2.2 \cdot 10^4$ of Li in the lowest Zeeman state $|1\rangle$ are loaded. By simply holding the atoms in the ODTs, a reduced lifetime of Er in the ErLi-mixtures compared to Er alone $(139\,\mathrm{s})$ due to additional heating by Li is observed. Atom numbers of Li in the ErLi mixtures are found to stay constant, due thermal contact to Er, which experiences a lower trap depth than Li. In the current configuration, thermalization of the Er atoms after being loaded is about $1\,\mathrm{s}$ and about $2\,\mathrm{s}$ for Li. By forced evaporation of Er alone, a BEC of $2 \cdot 10^4$ atoms is created. For the same evaporation trajectory in the ErLi mixture the Li atom number stays constant and sympathetic cooling of Li by Er to $T/T_F = 0.77 \pm 0.10$ is demonstrated. Here also a BEC with a reduced atom number by $2/3$ is observed. Due to the gravitational sag, the two degenerate clouds are not spatially overlapped at this point anymore.

## 8.2 Outlook

The presented work provides first promising results on an ultracold quantum gas mixture of fermionic $^6$Li and bosonic $^{166}$Er. In the following, experimental and technical improvements are discussed to refine the control of the system in pursuit of exploring fascinating quantum phenomena.

### Upgrading the ODTs at the glass cell

*Tightening $1064\,\mathrm{nm}$ ODTs* Gravitational sagging and slow thermalization of the atoms in the glass cell ODTs described in this thesis are limiting the performance and spatial overlap of the degenerate clouds. An improved ODT setup at the glass cell is being worked on by the junior PhD-students while writing of this thesis is coming to and end. In pursuit of achieving a double-degenerate system of a DFG of Li and a BEC of Er, the optics of the $1064\,\mathrm{nm}$ traps are adapted to have tighter confinement and an additional $1064\,\mathrm{nm}$ ODT is implemented to further increase the trap frequencies. In resent measurements, a BEC of Er was already achieved after $8\,\mathrm{s}$ of evaporation only, cutting the required time by factor 3. The new implemented trap conditions are similar to the one realized in [105], where $T/T_F = 0.08$ was achieved by sympathetic cooling in a Bose-Fermi mixture of $^6$Li$^{174}$Yb.

*Differential trapping* The displacement of the clouds due to the gravitational sag can only be minimized by tighter trapping, but it can not be fully compensated for in single-color ODTs. Employing ODTs for Li at the tune-out wavelength for Er near its narrow $841\,\mathrm{nm}$

line, allows for species selective trapping without introducing significant heating to Er [64]. Characterization of the unisotropic tune-out wavelength was carried out in the framework of this thesis. Details are provided in thesis of Alexandre De Martino [74]. Dynamical motional control of the trap centers is planned to be achieved with the precise tip/tilt-stages already built in the setup. Having the clouds thermalized and overlapped, precise thermometry of the DFG by the non-condensed fraction of Er can be achieved [85].

*Tuning the onset of condensation* Next to differential control of the position of the atoms, trapping of Li at the tune-out wavelength of Er is planned to also benefit the ratio of $T_F/T_c$, by increasing the trap frequencies for Li. Sympathetic cooling is expected to stay efficient below $T/T_F = 0.01$, by increasing the trap frequencies for Li by a factor $2$ to $3$ only. Generating Li clouds of these high degeneracies would beat the $10$ year old temperature record of $T/T_F = 0.03$ in $^6$Li$^7$Li [56].

*Size-matching the DFG and BEC* Being trapped in the same $1064\,\mathrm{nm}$ ODTs, the size of the Er BEC is only a fraction of the DFG. Here, again tighter confinement of Li by employing ODTs at the tune-out wavelength enables to match the sizes of the two. By increasing the trap frequencies for Li by one order of magnitude, the spatial extent of the BEC and DFG are similiar.

### Exploring polaron phyiscs

Having the ODTs upgraded, paths for exploring new phenomena open. The ErLi mixture has great prerequisites for studying (heavy-light) impurity physics. In a large Er BEC, few Li atoms immersed can be treated as impurities. In such a system, interactions of the impurities with the bosonic background can form so-called Bose polarons. The effective mass of these quasiparticles rise with the interaction strength between the impurity and the bath. Recent ideas are to realize and observe non-equilibrium dynamics in the form of polaron oscillations [68]. Similar to an approach in a 1D system [226], we want to excite a centre of mass motion of the polarons in a 3D system. It is theoretically predicted, that the characteristic oscillation frequency is renormalized with the effective mass of the polaron, which was not observed in the 1D case.

### Quantum gas microscope and optical lattice

Lowering the atom numbers, at one point the resolution and sensitivity of absorption imaging will be limiting. A high-NA objective is already installed for the realization of a quantum gas microscope [168]. A setup for trapping the Li atoms in near-resonant optical tweezers at $675\,\mathrm{nm}$ is worked on currently. The light for generating the tweezers with a Spatial Light Modulator (SLM) [227] is planned to be sent through, and the fluorescence from in-tweezer GM cooling is planned to be collected by the objective. In a similar setup with tweezers of $1064\,\mathrm{nm}$ light, imaging of Li with great survival rates have been demonstrated [228]. Our aporoach of near-resonant tweezers benefits from low optical powers needed for achieving the same trap depths and higher resolution due to the smaller wavelength compared to the $1064\,\mathrm{nm}$ case. The strong cooling power of the in-tweezer GM is calculated to suppress atom loss from heating by off-resonant scattering of the tweezer light.

Another project, that was started to being worked on recently is the implementation of a $841\,\mathrm{nm}$ optical lattice for Li at the tune-out wavelength for Er. Sympathetic cooling of Li into the lattice by Er trapped in $1064\,\mathrm{nm}$ ODTs is a promising approach for the preparation of a Fermi-Hubbard systems at ultra-low temperatures. Imaging of every second lattice site can be carried of with the near-resonant tweezers. Gradient coils for spin-resolved imaging are built in the system already [33].

# Acronyms

**AMO** Atomic, Molecular, and Optical Physics.
**AOM** Acousto-Optic Modulator.

**BEC** Bose–Einstein condensate.
**BL** Beat Lock.

**CBODT** Crossed Beam Optical Dipole Trap.
**cMOT** compressed Magneto-Optical Trap.

**DDI** Dipole-Dipole Interaction.
**DDS** Direct digital synthesizer.
**DFG** Degenerate Fermi Gas.

**ECDL** External Cavity Diode Laser.
**EOM** Electro–Optic Modulator.

**FI** Faraday Isolator.
**FP** Fabry-Pérot.
**FSR** Free Spectral Range.

**GM** Gray Molasses.

**HF** Hyperfine.

**IL** Injection-Lock.
**ILA** Injection Lock Algorithm.
**IR** Infrared.

**LD** Laser Diode.

**MOT** Magneto-Optical Trap.

**NEG** Non-Evaporative Getter.

**ODT** Optical Dipole Trap.

**OP/TC** Optical Pumping / Transversal Cooling.

**OSA** Optical Spectrum Analyzer.

**PBS** Polarizing BeamSplitter.

**PD** Photo Diode.

**PDH** Pound–Drever–Hall.

**PID** Proportional–Integral–Derivative.

**PSD** Phase-Space Density.

**RIN** Relative Intensity Noise.

**ROI** Region Of Interest.

**SIP** Sputter Ion Pump.

**SLM** Spatial Light Modulator.

**TA** Tapered Amplifier.

**ToF** Time-of-Flight.

**TSP** Titanium Sublimation Pump.

**UHV** Ultra-High Vacuum.

**ULE** Ultra Low Expansion.

**UV** Ultraviolet.

**VCO** Voltage-Controlled Oscillator.

**VSCPT** Velocity-Selective Coherent Population Trapping.

**WM** Wave-Meter.

**ZS** Zeeman Slowing.

# Appendix A

# Appendix

## A.1 Li oven refilling and final setup

### Oven refilling procedure

Commonly purified Li comes in chunks submerged in oil, preventing it from oxidation. To achieve low vacuum pressure, the oil has to be removed rigorously from the chunks. As a first step, this is done by cleaning the chunks multiple times with cyclohexane ($\geq 99.9\%$). The chunks appear silverish with dark spots. The surface and especially the dark sports of the chunks are cut away with a common kitchen knife. Then the chunks are cleaned again with cyclohexane and cut in longish pieces, that fit through the nozzle. For us from initially $20\,\mathrm{g}$ enriched $^6$Li (Sigma-Aldrich 340421-10G) we were left with $13\,\mathrm{g}$ to fill the oven. In principle the reservoir of the oven is capable of holding at least $70\,\mathrm{g}$ of it.
During the cleaning process working in a clean environment is important. Having all tools already prepared before starting the process is advantageous as Li oxidizes quickly when exposed to air.
When the oven is filled, it is pumped with a turbo pump and heated up like in the experiment. We pumped it until the pressure reached $5 \cdot 10^{-9}\,\mathrm{mbar}$. After the cool down, we flooded it with argon and closed it again until it was mounted to the experimental apparatus. In order to keep the stop in machine operation time as small as possible, a second Li oven is held in stock. Over a period of more than $3.5$ years of operation no refilling of the Li oven was necessary.

### Final installation

After the oven was mounted to the vacuum system and a successful bake-out, the heat cap of the reservoir and the heat ring for heating the nozzle were attached. Commercial heat clamps (ERGE-Elektrowärmetechnik Franz Messer GmbH: 80751305 (reservoir), 31-15682 (nozzle)) were mounted around them and covered with isolation material. Additionally, two water cooled copper plates were attached to the oven. One was mounted right after the CF40 flange of the oven. Its tight fit around the oven allows for great thermal isolation of the flange connection to the hot oven. Under constant operation of the oven, the flange is at $\sim 30\,^\circ\mathrm{C}$ only.
Another cooling plates was initially mounted between the nozzle and the reservoir to also thermally isolate those parts of the oven. During operation, we saw, that this suppressed the reservoir temperature dependence of the MOT loading rate above $\sim 320\,^\circ\mathrm{C}$. Removing the cold plate, the vacuum pressure in the section increased tremendously as all kind of

impurities, that accumulated at the cold spot were suddenly released into the vacuum. Fortunately, this pressure burst did not saturate the ion pump of Li division. Even without the extra cooling plate, the reservoir and nozzle temperatures can be controlled almost independently.

A copper housing, that is attached to the cooper cooling plate provides isolation to the optical table environment. Pictures of the final setup are shown in Fig. A.1.

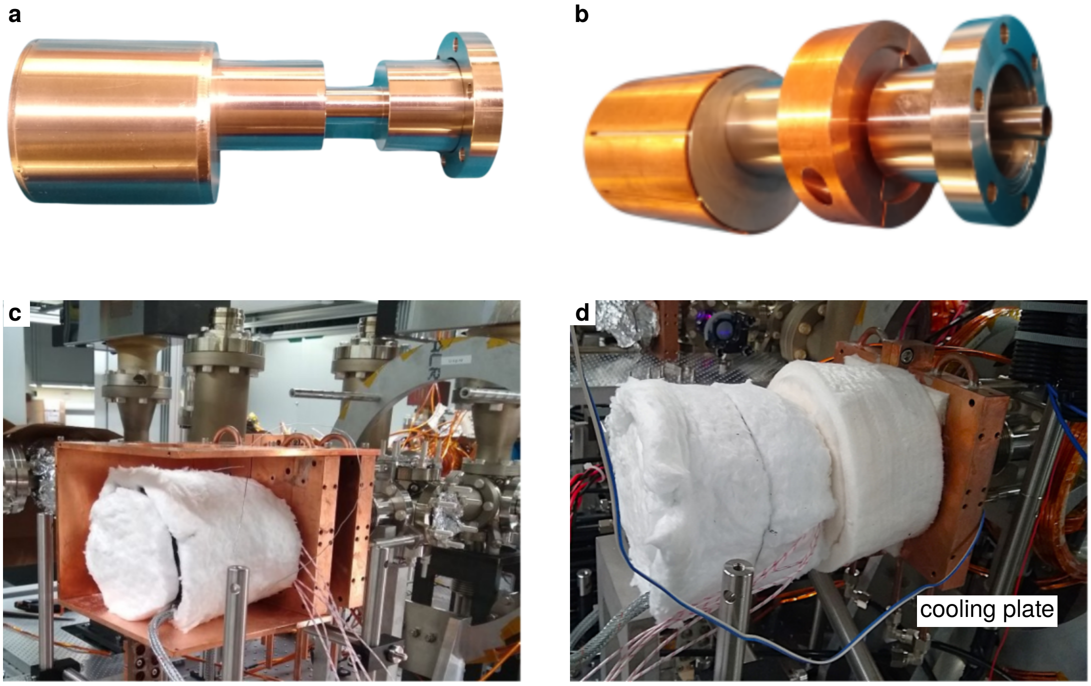

**Figure A.1** **Li oven pictures a.** Bare Li oven vacuum piece. **b.** Li oven with heat cap and heat ring made out of copper. **c.** Li oven mounted to the vacuum system and covered with isolation material (initial installation). The the oven's copper housing is partially opened. Here, both cooling plates are still mounted. **d.** Final oven configuration with only one cooling plate. The copper housing was removed at the time the picture was taken.

## A.2 Optical coatings

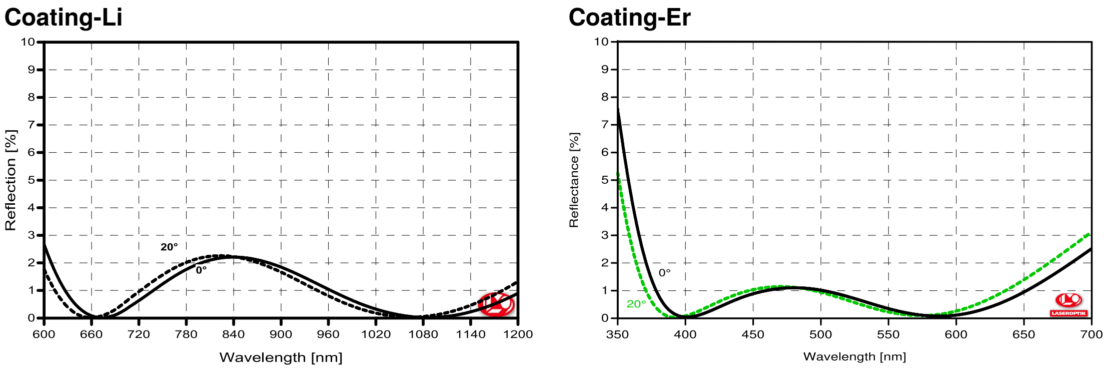
**Coating-Li**

**Coating-Er**

B-07158: AR671nm+1064nm/0-20° on UHV

B-18077: AR401nm+583nm/0-20° on UHV

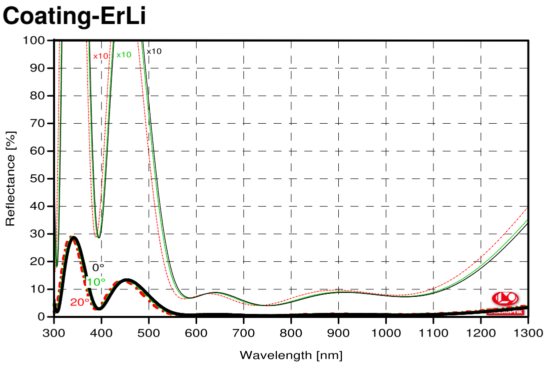
**Coating-ErLi**

B-18076: HT401 AR583+671+810-850+1064-1070nm/0-20° on UHV

**Figure A.2 Optical coatings of the vacuum viewports.** Coatings

## A.3 View ports

| | Location | # | Magnetic | Size/Type | Coating- |
|---|---|---|---|---|---|
| **Li section** | | | | | |
| | OP/TC | 4 | mag. | CF40 | Li |
| | Shutter stick | 1 | mag. | CF40 | - |
| Main chamber Li | | | | | |
| | MOT horizontal | 4 | non-mag. | CF64 | Li |
| | MOT vertical | 2 | non-mag. | Bucket | ErLi |
| | Zeeman window | 1 | mag. | CF40 | Er |
| | Transport | 1 | non-mag. | CF40 | Li |
| **Er section** | | | | | |
| | TC | 4 | mag. | CF40 | Er |
| | Shutter stick | 1 | mag. | CF40 | Er |
| Main chamber Er | | | | | |
| | MOT horizontal | 3 | non-mag. | CF64 | ErLi |
| | | 1 | non-mag. | CF40 | ErLi |
| | MOT vertical | 2 | non-mag. | Bucket | ErLi |
| | Zeeman window | 1 | mag. | CF40 | Er |

**Table A.1** **Viewports of the ErLi experiment and their properties.** CF40 mag.: Hositrad HOVPZ38Q, CF40 non-mag.: Hositrad HOVPZ38Q-NM, CF64 non-mag.: Hositrad HOVPZ64Q-NM, Buckets see (LINK). Coatings as in Fig. A.2.
*Comment:* Due to broken viewports in the bake-out process, the viewport to the Zeeman mirror of Li has not the intended "Coating-Li". And one of the horizontal MOT viewports on the Er chamber is smaller than planned (CF40 instead of CF64).

## A.4 High current circuits

Fast switching and precise control of magnetic fields are important experimental parameters for many steps of the ErLi experiment. In the following two high current circuits, that control the jump coil of the Li chamber and the Feshbach coil of the science cell are presented (see Fig. A.3). The implemented circuits are adapted from [229], where they are discussed in detail.

The circuit for the jump coils is designed for a fast switch-off. Here, the current for driving the coils is controlled with the power supply in "current mode". During the normal operation, the fast recovery diode blocks current flow through the resistor. For switching the field off, the IGBT opens the circuit in microseconds. The inductance of the coil induces a voltage, that counteracts the field change in the coil. For the reversed polarity the fast recovery diode opens and the high voltage capacitor is charged. Oscillations of the LC circuit are blocked by the fast recovery diode after a quarter of a period ($T/4$). The field energy of the coils is thereby effectively transferred to the electric field energy of the capacitor. The timescale of this process is $T/4 = \pi/2\sqrt{LC}$, with the capacity $C$ and inductance $L$. Typical values are in the $\sim 100\,\mu$s regime. The capacitor is then "slowely" discharged by the parallel high power resistor. The typical discharge time is $\tau = RC = 1.4\,$s for the implemented circuit, with the resistance $R$. This timescale has to be shorter than the typical experimental cycling time. The power supply is protected from the high voltage spikes of the fast switch-off process by a standard high power and low voltage drop diode.

The circuit controlling the current of the science chamber's Feshbach coil only differs from the one just discussed in one aspect. Here, the control of the current is provided with MOSFETs, that are controlled by a PI controller. The current value is provided by a high precision current transducer (CT) fed to the PI controller. The power supply is set to "voltage mode" here.

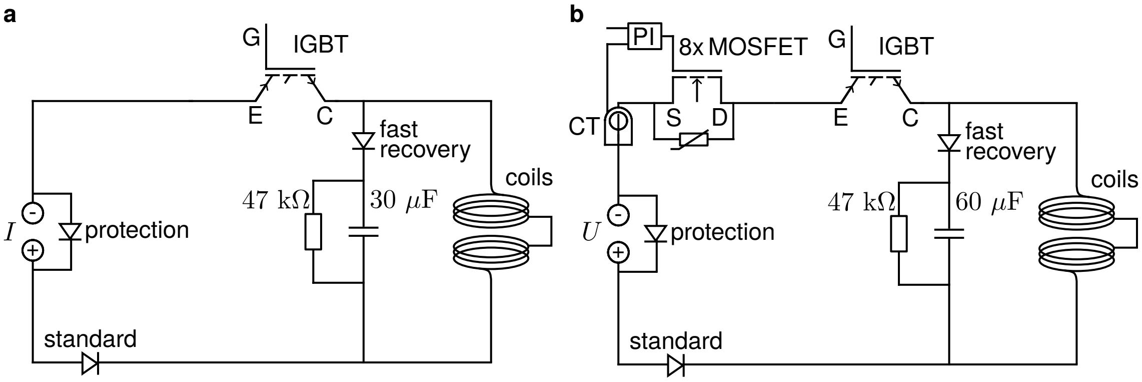

**Figure A.3 High current switching circuits. a.** High current switch-off circuit of the Li chamber's jump coils. Key components: IGBT: SEMIKRON SKM800GA176D, standard diode: Vishay VS-SD1100C25C, fast recovery diode: Vishay SD1053C22S20L, capacitor Wima GTO MKP 30muF, protection diode: TVS diode. **b.** High current switch-off and precision stabilization circuit of the science chamber's Fesbach coils. Additional key components added to a.: MOSFET: IXFN 200N10P, CT: DANISENSE DS300ID.

## A.5 Air-baking of the main chamber

Air-baking of the main chamber, the Zeeman slower vacuum tubes and the Zeeman cross pieces were done in the oven of the glassblowing workshop on campus. After 24 h at 400 °C an oxidation layer has formed. The layer visibly changed the color of the chamber (316LN/1.4429esu and 316L/1.4404) from silverish to almost copper like (see Fig. A.4). The standard stainless steel 304/1.4301 flanges used to protect the knife edges from oxidation during the baking process turned to a brass like color. As for all backing procedures, silver coated screws, washers and nuts were employed to prevent them from sticking to the corpus.

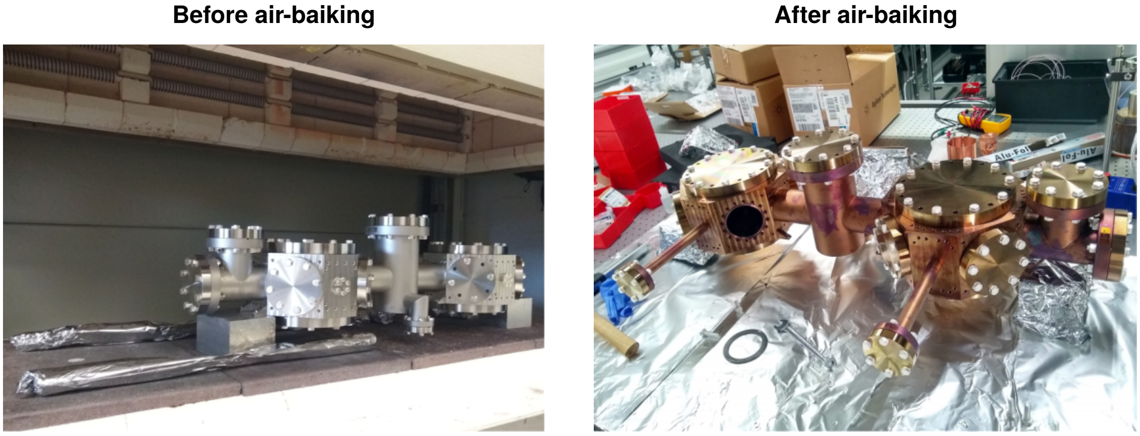

**Before air-baiking**

**After air-baiking**

**Figure A.4 Chamber before and after air-baking.**

## A.6 Fabry-Pérot cavity

The Fabry-Pérot (FP) cavity is an optical resonator used for high-resolution spectroscopy. We use it for detection of multi-mode lasing of the ECDLs. In our setup (see Fig. A.5a for schematics), the optical cavity consists of two curved mirrors. One of these mirrors is mounted on a piezo actuator allowing to scan the cavity resonance by many Free Spectral Range (FSR). The FSR of our cavity is $\sim 1.5\,\mathrm{GHz}$. The light is coupled to the cavity with a pair of mirrors only. Adjusting the collimation for mode matching is not needed as the Finesse of the cavity is quite low. The transmission of the light is monitored with a PD placed on the output side of the cavity.

Characteristic signals of the transmitted light with respect to the cavity length is shown in Fig. A.5b. The signal for single mode light shows evenly spaced and symmetric transmission peaks. Unwanted multi-mode lasing results in a signal with reduced main peaks and the appearance of side peaks from the additional frequency components.

From day-to-day operation, we saw that for some lasers running multi-mode is better indicated by a reduction of the main peak, whereas for some others the appearance of side peaks is a better indicator.

When the ECDL is lasing multi-mode, single mode operation is easily recovered by slight adjustments on the laser body's temperature and also the current applied to the LD if needed.

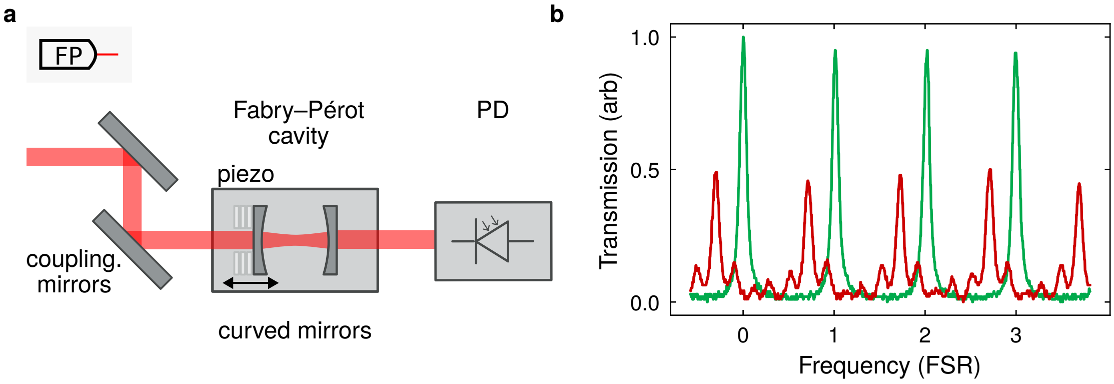

**Figure A.5 Fabry–Pérot setup and signals. a.** Schematic structure of the FP to detect multi-mode lasing. The setup is represented by the upper left corner symbol (see Fig. 5.1). **b.** Characteristic signals of light from a laser running single mode (green) or multi-mode (red).

# Bibliography

[1] *FAKSIMILE AUS DEN VERHANDLUNGEN DER DEUTSCHEN PHYSIKALISCHEN GESELLSCHAFT 2 (1900) S. 237: Zur Theorie des Gesetzes der Energieverteilung im Normalspectrum; von M. Planck*, Physikalische Blätter **4**., 146–151 (1948). DOI: https://doi.org/10.1002/phbl.19480040404 (cit. on p. 1).

[2] Einstein, A. *Über einen die Erzeugung und Verwandlung des Lichtes betreffenden heuristischen Gesichtspunkt*, Annalen der Physik **322**., 132–148 (1905). DOI: https://doi.org/10.1002/andp.19053220607 (cit. on p. 1).

[3] Heisenberg, W. *Über quantentheoretische Umdeutung kinematischer und mechanischer Beziehungen.*, Zeitschrift für Physik **33**., 879–893 (Dec. 1925). DOI: 10.1007/BF01328377 (cit. on p. 1).

[4] Schrödinger, E. *Quantisierung als Eigenwertproblem*, Annalen der Physik **385**., 437–490 (1926). DOI: 10.1002/andp.19263840602 (cit. on p. 1).

[5] Einstein, A., B. Podolsky, and N. Rosen. *Can Quantum-Mechanical Description of Physical Reality Be Considered Complete?* Physical Review **47**, 777–780 (May 1935). DOI: 10.1103/PhysRev.47.777 (cit. on p. 1).

[6] Wiesner, S. *Conjugate coding*, SIGACT News **15**., 78–88 (Jan. 1983). DOI: 10.1145/1008908.1008920 (cit. on p. 1).

[7] Ekert, A. K. *Quantum cryptography based on Bell's theorem*, Physical Review Letters **67**, 661–663 (Aug. 1991). DOI: 10.1103/PhysRevLett.67.661 (cit. on p. 1).

[8] Yin, J. *et al. Satellite-based entanglement distribution over 1200 kilometers*, Science **356**., 1140–1144 (2017). DOI: 10.1126/science.aan3211 (cit. on p. 1).

[9] Kinoshita, T. *Ground state of the helium atom*, Physical Review **105**., 1490 (1957) (cit. on p. 1).

[10] Georgescu, I. M., S. Ashhab, and F. Nori. *Quantum simulation*, Reviews of Modern Physics **86**, 153–185 (Mar. 2014). DOI: 10.1103/RevModPhys.86.153 (cit. on p. 1).

[11] Troyer, M. and U.-J. Wiese. *Computational Complexity and Fundamental Limitations to Fermionic Quantum Monte Carlo Simulations*, Physical Review Letters **94**, 170201 (May 2005). DOI: 10.1103/PhysRevLett.94.170201 (cit. on p. 1).

[12] Feynman, R. P. *Simulating physics with computers*, International Journal of Theoretical Physics **21**., 467–488 (June 1982). DOI: 10.1007/BF02650179 (cit. on p. 1).

[13] Ladd, T. D., F. Jelezko, R. Laflamme, Y. Nakamura, C. Monroe, and J. L. O'Brien. *Quantum computers*, Nature **464**., 45–53 (Mar. 2010). DOI: 10.1038/nature08812 (cit. on p. 1).

[14] Barenco, A., C. H. Bennett, R. Cleve, D. P. DiVincenzo, N. Margolus, P. Shor, T. Sleator, J. A. Smolin, and H. Weinfurter. *Elementary gates for quantum computation*, Physical Review A **52**, 3457–3467 (Nov. 1995). DOI: 10.1103/PhysRevA.52.3457 (cit. on p. 1).

[15] Deutsch, D. *Quantum theory, the Church–Turing principle and the universal quantum computer*, Proceedings of the Royal Society of London. A. Mathematical and Physical Sciences **400**., 97–117 (1985). DOI: 10.1098/rspa.1985.0070 (cit. on p. 1).

[16] Cirac, J. I. and P. Zoller. *Goals and opportunities in quantum simulation*, Nature Physics **8**., 264–266 (Apr. 2012). DOI: 10.1038/nphys2275 (cit. on p. 1).

[17] Fauseweh, B. *Quantum many-body simulations on digital quantum computers: State-of-the-art and future challenges*, Nature Communications **15**., 2123 (Mar. 2024). DOI: 10.1038/s41467-024-46402-9 (cit. on p. 1).

[18] Shor, P. W. *Scheme for reducing decoherence in quantum computer memory*, Physical Review A **52**, R2493–R2496 (Oct. 1995). DOI: 10.1103/PhysRevA.52.R2493 (cit. on p. 1).

[19] Acharya, R. *et al. Quantum error correction below the surface code threshold*, Nature **638**., 920–926 (Feb. 2025). DOI: 10.1038/s41586-024-08449-y (cit. on p. 1).

[20] Preskill, J. *Reliable quantum computers*, Proceedings of the Royal Society of London. Series A: Mathematical, Physical and Engineering Sciences **454**., 385–410 (1998) (cit. on p. 1).

[21] Preskill, J. *Quantum Computing in the NISQ era and beyond*, Quantum **2**, 79 (Aug. 2018). DOI: 10.22331/q-2018-08-06-79 (cit. on p. 2).

[22] Bloch, I., J. Dalibard, and W. Zwerger. *Many-body physics with ultracold gases*, Reviews of Modern Physics **80**, 885–964 (July 2008). DOI: 10.1103/RevModPhys.80.885 (cit. on pp. 2, 28, 103).

[23] Bloch, I., J. Dalibard, and S. Nascimbène. *Quantum simulations with ultracold quantum gases*, Nature Physics **8**., 267–276 (Apr. 2012). DOI: 10.1038/nphys2259 (cit. on p. 2).

[24] Esslinger, T. *Fermi-Hubbard Physics with Atoms in an Optical Lattice*, Annual Review of Condensed Matter Physics **1**., 129–152 (Aug. 2010). DOI: 10.1146/annurev-conmatphys-070909-104059 (cit. on p. 2).

[25] Hubbard, J. *Electron correlations in narrow energy bands*, Proceedings of the Royal Society of London. Series A. Mathematical and Physical Sciences **276**., 238–257 (1963). DOI: 10.1098/rspa.1963.0204 (cit. on p. 2).

[26] Hubbard, J. *Electron Correlations in Narrow Energy Bands. II. The Degenerate Band Case*, Proceedings of the Royal Society of London. Series A, Mathematical and Physical Sciences **277**., 237–259 (1964). DOI: 10.1098/rspa.1964.0019 (cit. on p. 2).

[27] Jaksch, D. and P. Zoller. *The cold atom Hubbard toolbox*, Annals of Physics. Special Issue **315**., 52–79 (Jan. 2005). DOI: 10.1016/j.aop.2004.09.010 (cit. on p. 2).

[28] Chin, C., R. Grimm, P. Julienne, and E. Tiesinga. *Feshbach resonances in ultracold gases*, Reviews of Modern Physics **82**, 1225–1286 (Apr. 2010). DOI: 10.1103/RevModPhys.82.1225 (cit. on pp. 2, 18).

[29] Cheuk, L. W., M. A. Nichols, M. Okan, T. Gersdorf, V. V. Ramasesh, W. S. Bakr, T. Lompe, and M. W. Zwierlein. *Quantum-Gas Microscope for Fermionic Atoms*, Physical Review Letters **114**, 193001 (May 2015). DOI: 10.1103/PhysRevLett.114.193001 (cit. on p. 2).

[30] Omran, A., M. Boll, T. A. Hilker, K. Kleinlein, G. Salomon, I. Bloch, and C. Gross. *Microscopic Observation of Pauli Blocking in Degenerate Fermionic Lattice Gases*, Physical Review Letters **115**., 263001 (Dec. 2015). DOI: 10.1103/PhysRevLett.115.263001 (cit. on p. 2).

[31] Parsons, M. F., F. Huber, A. Mazurenko, C. S. Chiu, W. Setiawan, K. Wooley-Brown, S. Blatt, and M. Greiner. *Site-Resolved Imaging of Fermionic* $^6$Li *in an Optical Lattice*, Physical Review Letters **114**, 213002 (May 2015). DOI: 10.1103/PhysRevLett.114.213002 (cit. on p. 2).

[32] Preiss, P. M., R. Ma, M. E. Tai, J. Simon, and M. Greiner. *Quantum gas microscopy with spin, atom-number, and multilayer readout*, Physical Review A **91**., 041602 (Apr. 2015). DOI: 10.1103/PhysRevA.91.041602 (cit. on p. 2).

[33] Boll, M., T. A. Hilker, G. Salomon, A. Omran, J. Nespolo, L. Pollet, I. Bloch, and C. Gross. *Spin- and density-resolved microscopy of antiferromagnetic correlations in Fermi-Hubbard chains*, Science **353**., 1257–1260 (Sept. 2016). DOI: 10.1126/science.aag1635 (cit. on pp. 2, 113).

[34] Gross, C. and I. Bloch. *Quantum simulations with ultracold atoms in optical lattices*, Science **357**., 995–1001 (Sept. 2017). DOI: 10.1126/science.aal3837 (cit. on p. 2).

[35] Bardeen, J., L. N. Cooper, and J. R. Schrieffer. *Theory of Superconductivity*, Physical Review **108**, 1175–1204 (Dec. 1957). DOI: 10.1103/PhysRev.108.1175 (cit. on p. 2).

[36] Hartke, T., B. Oreg, C. Turnbaugh, N. Jia, and M. Zwierlein. *Direct observation of nonlocal fermion pairing in an attractive Fermi-Hubbard gas*, Science **381**., 82–86 (July 2023). DOI: 10.1126/science.ade4245 (cit. on p. 2).

[37] Jördens, R., N. Strohmaier, K. Günter, H. Moritz, and T. Esslinger. *A Mott insulator of fermionic atoms in an optical lattice*, Nature **455**., 204–207 (Sept. 2008). DOI: 10.1038/nature07244 (cit. on p. 2).

[38] Schneider, U., L. Hackermüller, S. Will, T. Best, I. Bloch, T. A. Costi, R. W. Helmes, D. Rasch, and A. Rosch. *Metallic and Insulating Phases of Repulsively Interacting Fermions in a 3D Optical Lattice*, Science **322**., 1520–1525 (Dec. 2008). DOI: 10.1126/science.1165449 (cit. on p. 2).

[39] Mott, N. *Metal-insulator transitions*. CRC Press, 2004 (cit. on p. 2).

[40] Mazurenko, A., C. S. Chiu, G. Ji, M. F. Parsons, M. Kanász-Nagy, R. Schmidt, F. Grusdt, E. Demler, D. Greif, and M. Greiner. *A cold-atom Fermi–Hubbard antiferromagnet*, Nature **545**., 462–466 (2017). DOI: 10.1038/nature22362 (cit. on p. 2).

[41] White, S. R. and D. J. Scalapino. *Density Matrix Renormalization Group Study of the Striped Phase in the 2D* $t - J$ *Model*, Physical Review Letters **80**, 1272–1275 (Feb. 1998). DOI: 10.1103/PhysRevLett.80.1272 (cit. on p. 2).

[42] Wietek, A., Y.-Y. He, S. R. White, A. Georges, and E. M. Stoudenmire. *Stripes, Antiferromagnetism, and the Pseudogap in the Doped Hubbard Model at Finite Temperature*, Physical Review X **11**, 031007 (July 2021). DOI: 10.1103/PhysRevX.11.031007 (cit. on p. 2).

[43] Hofstetter, W., J. I. Cirac, P. Zoller, E. Demler, and M. D. Lukin. *High-Temperature Superfluidity of Fermionic Atoms in Optical Lattices*, Physical Review Letters **89**., 220407 (Nov. 2002). DOI: 10.1103/PhysRevLett.89.220407 (cit. on p. 2).

[44] Keimer, B., S. A. Kivelson, M. R. Norman, S. Uchida, and J. Zaanen. *From quantum matter to high-temperature superconductivity in copper oxides*, Nature **518**., 179–186 (Feb. 2015). DOI: 10.1038/nature14165 (cit. on p. 2).

[45] Vilk, Y. and A.-M. Tremblay. *Non-perturbative many-body approach to the Hubbard model and single-particle pseudogap*, Journal de Physique I **7**., 1309–1368 (1997). DOI: 10.1051/jp1:1997135 (cit. on p. 2).

[46] Šimkovic, F., R. Rossi, A. Georges, and M. Ferrero. *Origin and fate of the pseudogap in the doped Hubbard model*, Science **385**., eade9194 (Sept. 2024). DOI: 10.1126/science.ade9194 (cit. on p. 2).

[47] Kendrick, L. H., A. Kale, Y. Gang, A. D. Deters, M. Lebrat, A. W. Young, and M. Greiner. *Pseudogap in a Fermi-Hubbard quantum simulator*, (2025). DOI: 10.48550/arXiv.2509.18075 (cit. on p. 2).

[48] Chu, S. *Nobel Lecture: The manipulation of neutral particles*, Reviews of Modern Physics **70**., 685–706 (July 1998). DOI: 10.1103/RevModPhys.70.685 (cit. on pp. 2, 35).

[49] Phillips, W. D. *Nobel Lecture: Laser cooling and trapping of neutral atoms*, Reviews of Modern Physics **70**, 721–741 (July 1998). DOI: 10.1103/RevModPhys.70.721 (cit. on p. 2).

[50] Cohen-Tannoudji, C. N. *Nobel Lecture: Manipulating atoms with photons*, Reviews of Modern Physics **70**, 707–719 (July 1998). DOI: 10.1103/RevModPhys.70.707 (cit. on p. 2).

[51] Ketterle, W., D. S. Durfee, and D. M. Stamper-Kurn. *Making, probing and understanding Bose-Einstein condensates*, (1999). DOI: 10.48550/arXiv.cond-mat/9904034 (cit. on pp. 2, 18, 22, 89).

[52] Grimm, R., M. Weidemüller, and Y. B. Ovchinnikov. *Optical dipole traps for neutral atoms*, (1999). DOI: 10.48550/arXiv.physics/9902072 (cit. on pp. 2, 6, 27).

[53] Geist, W. and T. A. B. Kennedy. *Evaporative cooling of mixed atomic fermions*, Physical Review A **65**., 063617 (June 2002). DOI: 10.1103/PhysRevA.65.063617 (cit. on pp. 2, 18, 19).

[54] Onofrio, R. *Cooling and thermometry of atomic Fermi gases*, Physics-Uspekhi **59**., 1129–1153 (Nov. 2016). DOI: 10.3367/UFNe.2016.07.037873 (cit. on pp. 2, 18).

[55] Hadzibabic, Z., S. Gupta, C. A. Stan, C. H. Schunck, M. W. Zwierlein, K. Dieckmann, and W. Ketterle. *Fiftyfold Improvement in the Number of Quantum Degenerate Fermionic Atoms*, Physical Review Letters **91**., 160401 (Oct. 2003). DOI: 10.1103/PhysRevLett.91.160401 (cit. on pp. 2, 21).

[56] Delehaye, M., S. Laurent, I. Ferrier-Barbut, S. Jin, F. Chevy, and C. Salomon. *Critical Velocity and Dissipation of an Ultracold Bose-Fermi Counterflow*, Physical Review Letters **115**., 265303 (Dec. 2015). DOI: 10.1103/PhysRevLett.115.265303 (cit. on pp. 2, 21, 112).

[57] Brown-Hayes, M., Q. Wei, C. Presilla, and R. Onofrio. *Thermodynamical approaches to efficient sympathetic cooling in ultracold Fermi-Bose atomic mixtures*, Physical Review A **78**., 013617 (July 2008). DOI: 10.1103/PhysRevA.78.013617 (cit. on pp. 2, 20).

[58] Presilla, C. and R. Onofrio. *Cooling Dynamics of Ultracold Two-Species Fermi-Bose Mixtures*, Physical Review Letters **90**., 030404 (Jan. 2003). DOI: 10.1103/PhysRevLett.90.030404 (cit. on pp. 2, 21).

[59] Onofrio, R. and C. Presilla. *Reaching Fermi Degeneracy in Two-Species Optical Dipole Traps*, Physical Review Letters **89**, 100401 (Aug. 2002). DOI: 10.1103/PhysRevLett.89.100401 (cit. on pp. 2, 22).

[60] Granade, S. R., M. E. Gehm, K. M. O'Hara, and J. E. Thomas. *All-Optical Production of a Degenerate Fermi Gas*, Physical Review Letters **88**, 120405 (Mar. 2002). DOI: 10.1103/PhysRevLett.88.120405 (cit. on p. 2).

[61] Aikawa, K., A. Frisch, M. Mark, S. Baier, A. Rietzler, R. Grimm, and F. Ferlaino. *Bose-Einstein Condensation of Erbium*, Physical Review Letters **108**, 210401 (May 2012). DOI: 10.1103/PhysRevLett.108.210401 (cit. on pp. 2, 75).

[62] Krstaji ć, M., P. Juhász, J. ř. Ku čera, L. R. Hofer, G. Lamb, A. L. Marchant, and R. P. Smith. *Characterization of three-body loss in* $^{166}$Er *and optimized production of large Bose-Einstein condensates*, Physical Review A **108**, 063301 (Dec. 2023). DOI: 10.1103/PhysRevA.108.063301 (cit. on pp. 2, 36).

[63] Ban, H. Y., M. Jacka, J. L. Hanssen, J. Reader, and J. J. McClelland. *Laser cooling transitions in atomic erbium*, Optics Express **13**., 3185–3195 (Apr. 2005). DOI: 10.1364/OPEX.13.003185 (cit. on p. 2).

[64] Kiesel, F., A. De Martino, J. Auch, K. Karpov, and C. Gross. *Dissipationless tune-out trapping for a lanthanide–alkali-metal quantum gas mixture*, Physical Review A **112**, L051304 (Nov. 2025). DOI: 10.1103/rykg-qn6s (cit. on pp. 2, 10, 22, 26, 27, 109, 112).

[65] Grusdt, F. and E. Demler. *New theoretical approaches to Bose polarons*, *Quantum matter at ultralow temperatures*. IOS Press, 2016, pp. 325–411. DOI: 10.48550/arXiv.1510.04934 (cit. on p. 3).

[66] Scazza, F., M. Zaccanti, P. Massignan, M. M. Parish, and J. Levinsen. *Repulsive Fermi and Bose Polarons in Quantum Gases*, Atoms **10**. (2022). DOI: 10.3390/atoms10020055 (cit. on p. 3).

[67] Massignan, P., M. Zaccanti, and G. M. Bruun. *Polarons, dressed molecules and itinerant ferromagnetism in ultracold Fermi gases*, Reports on Progress in Physics **77**., 034401 (2014). DOI: 10.1088/0034-4885/77/3/034401 (cit. on p. 3).

[68] Grusdt, F., N. Mostaan, E. Demler, and L. A. P. Ardila. *Impurities and polarons in bosonic quantum gases: a review on recent progress*, Reports on Progress in Physics **88**., 066401 (June 2025). DOI: 10.1088/1361-6633/add94b (cit. on pp. 3, 112).

[69] Goold, J., T. Fogarty, N. Lo Gullo, M. Paternostro, and T. Busch. *Orthogonality catastrophe as a consequence of qubit embedding in an ultracold Fermi gas*, Physical Review A **84**, 063632 (Dec. 2011). DOI: 10.1103/PhysRevA.84.063632 (cit. on p. 3).

[70] Knap, M., A. Shashi, Y. Nishida, A. Imambekov, D. A. Abanin, and E. Demler. *Time-Dependent Impurity in Ultracold Fermions: Orthogonality Catastrophe and Beyond*, Physical Review X **2**, 041020 (Dec. 2012). DOI: 10.1103/PhysRevX.2.041020 (cit. on p. 3).

[71] Pires, R., J. Ulmanis, S. Häfner, M. Repp, A. Arias, E. D. Kuhnle, and M. Weidemüller. *Observation of Efimov Resonances in a Mixture with Extreme Mass Imbalance*, Physical Review Letters **112**, 250404 (June 2014). DOI: 10.1103/PhysRevLett.112.250404 (cit. on p. 3).

[72] Naidon, P. and S. Endo. *Efimov physics: a review*, Reports on Progress in Physics **80**., 056001 (2017). DOI: 10.1088/1361-6633/aa50e8 (cit. on p. 3).

[73] Oi, K. and S. Endo. *Universal Efimov spectra and fermionic doublets in highly mass-imbalanced cold-atom mixtures with van der Waals and dipole interactions*, Physical Review Research **7**, 033236 (Sept. 2025). DOI: 10.1103/z5rx-51yx (cit. on p. 3).

[74] De Martino, A. “A new apparatus for quantum mixtures of Er and Li.” PhD thesis. University of Tübingen, expected to be published in 2025/2026 (cit. on pp. 3, 4, 30, 34, 57, 75, 82, 104, 112).

[75] Ashkin, A., J. M. Dziedzic, J. E. Bjorkholm, and S. Chu. *Observation of a single-beam gradient force optical trap for dielectric particles*, Optics Letters **11**., 288–290 (May 1986). DOI: 10.1364/OL.11.000288 (cit. on p. 7).

[76] Ashkin, A. and J. M. Dziedzic. *Optical Trapping and Manipulation of Viruses and Bacteria*, Science **235**., 1517–1520 (1987). DOI: 10.1126/science.3547653 (cit. on p. 7).

[77] Cohen-Tannoudji, C. and D. guéry-odelin. *Advances in Atomic Physics: An Overview*. Nov. 2011, pp. 1–767. DOI: 10.1142/6631 (cit. on pp. 8, 25).

[78] King, B. E. *Angular Momentum Coupling and Rabi Frequencies for Simple Atomic Transitions*, (2008). DOI: 10.48550/arXiv.0804.4528 (cit. on p. 9).

[79] Takamoto, M., F.-L. Hong, R. Higashi, and H. Katori. *An optical lattice clock*, Nature **435**., 321–324 (May 2005). DOI: 10.1038/nature03541 (cit. on p. 10).

[80] Foot, C. J. *Atomic physics*. 7. Oxford: Oxford Univ. Press, 2011. 331 pp. (cit. on pp. 10, 32, 34, 51).

[81] Goodstein, D. L. *States of matter*. Courier Corporation, 2013 (cit. on p. 11).

[82] Ketterle, W. and M. W. Zwierlein. *Making, probing and understanding ultracold Fermi gases*, La Rivista del Nuovo Cimento **31**., 247–422 (May 2008). DOI: 10.1393/ncr/i2008-10033-1 (cit. on pp. 12, 15, 18, 23, 26, 106).

[83] Goncharov, A. B. “Polylogarithms in Arithmetic and Geometry,” *Proceedings of the International Congress of Mathematicians*. Ed. by Chatterji, S. D. Basel: Birkhäuser Basel, 1995, pp. 374–387. DOI: 10.1007/978-3-0348-9078-6_31 (cit. on p. 13).

[84] McKay, D. and B. DeMarco. *Cooling in strongly correlated optical lattices: prospects and challenges*, Reports on Progress in Physics **74**, 054401 (2010). DOI: 10.1088/0034-4885/74/5/054401 (cit. on p. 16).

[85] Lous, R. S., I. Fritsche, M. Jag, B. Huang, and R. Grimm. *Thermometry of a deeply degenerate Fermi gas with a Bose-Einstein condensate*, Physical Review A **95**., 053627 (May 2017). DOI: 10.1103/PhysRevA.95.053627 (cit. on pp. 16, 112).

[86] Stellmer, S., B. Pasquiou, R. Grimm, and F. Schreck. *Laser Cooling to Quantum Degeneracy*, Physical Review Letters **110**., 263003 (June 2013). DOI: 10.1103/PhysRevLett.110.263003 (cit. on p. 18).

[87] Duarte, P. M., R. A. Hart, J. M. Hitchcock, T. A. Corcovilos, T.-L. Yang, A. Reed, and R. G. Hulet. *All-optical production of a lithium quantum gas using narrow-line laser cooling*, Physical Review A **84**., 061406 (Dec. 2011). DOI: 10.1103/PhysRevA.84.061406 (cit. on pp. 18, 35, 91).

[88] Gross, C., H. C. J. Gan, and K. Dieckmann. *All-optical production and transport of a large Li 6 quantum gas in a crossed optical dipole trap*, Physical Review A **93**., 053424 (May 2016). DOI: 10.1103/PhysRevA.93.053424 (cit. on pp. 18, 19).

[89] Anderson, M. H., J. R. Ensher, M. R. Matthews, C. E. Wieman, and E. A. Cornell. *Observation of Bose-Einstein Condensation in a Dilute Atomic Vapor*, Science **269**., 198–201 (July 1995). DOI: 10.1126/science.269.5221.198 (cit. on p. 18).

[90] Davis, K. B., M. .-. Mewes, M. R. Andrews, N. J. Van Druten, D. S. Durfee, D. M. Kurn, and W. Ketterle. *Bose-Einstein Condensation in a Gas of Sodium Atoms*, Physical Review Letters **75**., 3969–3973 (Nov. 1995). DOI: 10.1103/PhysRevLett.75.3969 (cit. on p. 18).

[91] Lu, M., N. Q. Burdick, and B. L. Lev. *Quantum Degenerate Dipolar Fermi Gas*, Phys. Rev. Lett. **108**, 215301 (May 2012). DOI: 10.1103/PhysRevLett.108.215301 (cit. on p. 18).

[92] Aikawa, K. *Reaching Fermi Degeneracy via Universal Dipolar Scattering*, Physical Review Letters **112**. (2014). DOI: 10.1103/PhysRevLett.112.010404 (cit. on p. 18).

[93] Holland, M. J., B. DeMarco, and D. S. Jin. *Evaporative cooling of a two-component degenerate Fermi gas*, Physical Review A **61**., 053610 (Apr. 2000). DOI: 10.1103/PhysRevA.61.053610 (cit. on pp. 18, 19).

[94] Crescimanno, M., C. G. Kaoy, and R. Peterson. *Limits to sympathetic evaporative cooling of a two-component Fermi gas*, Physical Review A **61**., 053602 (Apr. 2000). DOI: 10.1103/PhysRevA.61.053602 (cit. on p. 19).

[95] Gehm, M. E., S. L. Hemmer, K. M. O'Hara, and J. E. Thomas. *Unitarity-limited elastic collision rate in a harmonically trapped Fermi gas*, Physical Review A **68**., 011603 (July 2003). DOI: 10.1103/PhysRevA.68.011603 (cit. on p. 19).

[96] Smale, S., P. He, B. A. Olsen, K. G. Jackson, H. Sharum, S. Trotzky, J. Marino, A. M. Rey, and J. H. Thywissen. *Observation of a transition between dynamical phases in a quantum degenerate Fermi gas*, Science Advances **5**., eaax1568 (Aug. 2019). DOI: 10.1126/sciadv.aax1568 (cit. on p. 19).

[97] Fukuhara, T., Y. Takasu, M. Kumakura, and Y. Takahashi. *Degenerate Fermi Gases of Ytterbium*, Physical Review Letters **98**., 030401 (Jan. 2007). DOI: 10.1103/PhysRevLett.98.030401 (cit. on p. 20).

[98] DeSalvo, B. J., M. Yan, P. G. Mickelson, Y. N. Martinez de Escobar, and T. C. Killian. *Degenerate Fermi Gas of* $^{87}$Sr, Physical Review Letters **105**, 030402 (July 2010). DOI: 10.1103/PhysRevLett.105.030402 (cit. on p. 20).

[99] Krauser, J. S., J. Heinze, S. Götze, M. Langbecker, N. Fläschner, L. Cook, T. M. Hanna, E. Tiesinga, K. Sengstock, and C. Becker. *Investigation of Feshbach resonances in ultracold* $^{40}$**K** *spin mixtures*, Physical Review A **95**, 042701 (Apr. 2017). DOI: 10.1103/PhysRevA.95.042701 (cit. on p. 20).

[100] DeMarco, B. and D. S. Jin. *Onset of Fermi Degeneracy in a Trapped Atomic Gas*, Science **285**., 1703–1706 (1999). DOI: 10.1126/science.285.5434.1703 (cit. on p. 20).

[101] Truscott, A. G., K. E. Strecker, W. I. McAlexander, G. B. Partridge, and R. G. Hulet. *Observation of Fermi Pressure in a Gas of Trapped Atoms*, Science **291**., 2570–2572 (2001). DOI: 10.1126/science.1059318 (cit. on p. 21).

[102] Schreck, F., L. Khaykovich, K. L. Corwin, G. Ferrari, T. Bourdel, J. Cubizolles, and C. Salomon. *Quasipure Bose-Einstein Condensate Immersed in a Fermi Sea*, Physical Review Letters **87**, 080403 (Aug. 2001). DOI: 10.1103/PhysRevLett.87.080403 (cit. on p. 21).

[103] Becher, J. H., S. Baier, K. Aikawa, M. Lepers, J.-F. Wyart, O. Dulieu, and F. Ferlaino. *Anisotropic polarizability of erbium atoms*, Physical Review A **97**, 012509 (Jan. 2018). DOI: 10.1103/PhysRevA.97.012509 (cit. on pp. 21, 35).

[104] Kiruga, A., C. Cheung, D. Filin, P. Barakhshan, A. Bhosale, V. Badhan, B. Arora, R. Eigenmann, and M. S. Safronova. *Portal for High-Precision Atomic Data and Computation*. 2025 (cit. on p. 21).

[105] Hara, H., Y. Takasu, Y. Yamaoka, J. M. Doyle, and Y. Takahashi. *Quantum Degenerate Mixtures of Alkali and Alkaline-Earth-Like Atoms*, Physical Review Letters **106**, 205304 (May 2011). DOI: 10.1103/PhysRevLett.106.205304 (cit. on pp. 21, 111).

[106] Giorgini, S., L. P. Pitaevskii, and S. Stringari. *Condensate fraction and critical temperature of a trapped interacting Bose gas*, Physical Review A **54**, R4633–R4636 (Dec. 1996). DOI: 10.1103/PhysRevA.54.R4633 (cit. on p. 23).

[107] Mølmer, K. *Bose Condensates and Fermi Gases at Zero Temperature*, Physical Review Letters **80**, 1804–1807 (Mar. 1998). DOI: 10.1103/PhysRevLett.80.1804 (cit. on p. 23).

[108] Modugno, G., G. Roati, F. Riboli, F. Ferlaino, R. J. Brecha, and M. Inguscio. *Collapse of a Degenerate Fermi Gas*, Science **297**., 2240–2243 (2002). DOI: 10.1126/science.1077386 (cit. on p. 23).

[109] Côté, R., R. Onofrio, and E. Timmermans. *Sympathetic cooling route to Bose-Einstein condensate and Fermi-liquid mixtures*, Physical Review A **72**., 041605 (Oct. 2005). DOI: 10.1103/PhysRevA.72.041605 (cit. on p. 24).

[110] Timmermans, E. *Degenerate Fermion Gas Heating by Hole Creation*, Physical Review Letters **87**., 240403 (Nov. 2001). DOI: 10.1103/PhysRevLett.87.240403 (cit. on p. 25).

[111] Bali, S., K. M. O'Hara, M. E. Gehm, S. R. Granade, and J. E. Thomas. *Quantum-diffractive background gas collisions in atom-trap heating and loss*, Physical Review A **60**., R29–R32 (July 1999). DOI: 10.1103/PhysRevA.60.R29 (cit. on p. 25).

[112] Ulitzsch, J., D. Babik, R. Roell, and M. Weitz. *Bose-Einstein condensation of erbium atoms in a quasielectrostatic optical dipole trap*, Physical Review A **95**, 043614 (Apr. 2017). DOI: 10.1103/PhysRevA.95.043614 (cit. on pp. 26, 36).

[113] Hensler, S., J. Werner, A. Griesmaier, P. O. Schmidt, A. Goerlitz, T. Pfau, S. Giovanazzi, and K. Rzazewski. *Dipolar Relaxation in an ultra-cold Gas of magnetically trapped chromium atoms*, Applied Physics B **77**., 765–772 (Dec. 2003). DOI: 10.1007/s00340-003-1334-0 (cit. on p. 26).

[114] Lepers, M., J.-F. Wyart, and O. Dulieu. *Anisotropic optical trapping of ultracold erbium atoms*, Physical Review A **89**, 022505 (Feb. 2014). DOI: 10.1103/PhysRevA.89.022505 (cit. on p. 27).

[115] Gehm, M. E., K. M. O'Hara, T. A. Savard, and J. E. Thomas. *Dynamics of noise-induced heating in atom traps*, Physical Review A **58**., 3914–3921 (Nov. 1998). DOI: 10.1103/PhysRevA.58.3914 (cit. on p. 27).

[116] Partes, C. "FPGA-based laser intensity stabilization for the suppression of noise-induced atom heating in optical lattices." Bachelor's thesis. University of Tübingen, 2025 (cit. on p. 28).

[117] Park, A. J., J. Trautmann, N. Šanti ć, V. Klüsener, A. Heinz, I. Bloch, and S. Blatt. *Cavity-Enhanced Optical Lattices for Scaling Neutral Atom Quantum Technologies to Higher Qubit Numbers*, PRX Quantum **3**, 030314 (July 2022). DOI: 10.1103/PRXQuantum.3.030314 (cit. on p. 28).

[118] Tricot, F., D. H. Phung, M. Lours, S. Guérandel, and E. de Clercq. *Power stabilization of a diode laser with an acousto-optic modulator*, Review of Scientific Instruments **89**., 113112 (Nov. 2018). DOI: 10.1063/1.5046852 (cit. on p. 28).

[119] Takahashi, K., M. Ando, and K. Tsubono. *Stabilization of laser intensity and frequency using optical fiber*, Journal of Physics: Conference Series **122**., 012016 (July 2008). DOI: 10.1088/1742-6596/122/1/012016 (cit. on p. 28).

[120] Ehrenfest, P. and J. R. Oppenheimer. *Note on the Statistics of Nuclei*, Physical Review **37**, 333–338 (Feb. 1931). DOI: 10.1103/PhysRev.37.333 (cit. on p. 30).

[121] Scherf, W., O. Khait, H. Jäger, and L. Windholz. *Re-measurement of the transition frequencies, fine structure splitting and isotope shift of the resonance lines of lithium, sodium and potassium*, Zeitschrift für Physik D Atoms, Molecules and Clusters **36**., 31–33 (Mar. 1996). DOI: 10.1007/BF01437417 (cit. on pp. 30, 36).

[122] McAlexander, W. I., E. R. I. Abraham, and R. G. Hulet. *Radiative lifetime of the* $2P$ *state of lithium*, Physical Review A **54**, R5–R8 (July 1996). DOI: 10.1103/PhysRevA.54.R5 (cit. on p. 30).

[123] Zürn, G., T. Lompe, A. N. Wenz, S. Jochim, P. S. Julienne, and J. M. Hutson. *Precise Characterization of* $^6$Li *Feshbach Resonances Using Trap-Sideband-Resolved RF Spectroscopy of Weakly Bound Molecules*, Physical Review Letters **110**, 135301 (Mar. 2013). DOI: 10.1103/PhysRevLett.110.135301 (cit. on pp. 30, 31).

[124] Frisch, A. “Dipolar Quantum Gases of Erbium.” PhD thesis. University of Innsbruck, 2014 (cit. on pp. 32, 34, 36, 43).

[125] Gehm, M. E. “Preparation of an Optically-Trapped Degenerate Fermi Gas of $^6$Li: Finding the Route to Degeneracy.” PhD thesis. Duke University, 2003 (cit. on pp. 33, 40, 47).

[126] Judd, B. R. and I. Lindgren. *Theory of Zeeman Effect in the Ground Multiplets of Rare-Earth Atoms*, Physical Review **122**., 1802–1812 (June 1961). DOI: 10.1103/PhysRev.122.1802 (cit. on p. 33).

[127] Conway, J. G. and B. G. Wybourne. *Low-Lying Energy Levels of Lanthanide Atoms and Intermediate Coupling*, Physical Review **130**, 2325–2332 (June 1963). DOI: 10.1103/PhysRev.130.2325 (cit. on p. 33).

[128] R. Weast, M. A. and e. W. Beyer. *CRC handbook of chemistry and physics*. CRC Press, Boca Ratons, 64th edition (1983) (cit. on p. 33).

[129] A. M. James, M. L. *Macmillan’s chemical and physical data*. Macmillan, 1992 (cit. on p. 33).

[130] Zhang, Y., J. R. G. Evans, and S. Yang. *Corrected Values for Boiling Points and Enthalpies of Vaporization of Elements in Handbooks*, Journal of Chemical & Engineering Data **56**., 328–337 (Feb. 2011). DOI: 10.1021/je1011086 (cit. on p. 33).

[131] *National Nuclear Data Center, information extracted from the NuDat database*. DOI: https://www.nndc.bnl.gov/nudat/ (cit. on p. 33).

[132] Arimondo, E., M. Inguscio, and P. Violino. *Experimental determinations of the hyperfine structure in the alkali atoms*, Reviews of Modern Physics **49**., 31–75 (Jan. 1977). DOI: 10.1103/RevModPhys.49.31 (cit. on p. 33).

[133] Phelps, G. A. “A dipolar quantum gas microscope.” PhD thesis. Harvard University, 2019 (cit. on pp. 34, 43).

[134] Seo, B., P. Chen, Z. Chen, W. Yuan, M. Huang, S. Du, and G.-B. Jo. *Efficient production of a narrow-line erbium magneto-optical trap with two-stage slowing*, Physical Review A **102**, 013319 (July 2020). DOI: 10.1103/PhysRevA.102.013319 (cit. on p. 34).

[135] Loftus, T. H., T. Ido, M. M. Boyd, A. D. Ludlow, and J. Ye. *Narrow line cooling and momentum-space crystals*, Physical Review A **70**., 063413 (Dec. 2004). DOI: 10.1103/PhysRevA.70.063413 (cit. on p. 34).

[136] Heidt, E. “Optimization of the Erbium laser system and implementation of a narrow-line magneto-optical trap for the ErLi experiment.” Master’s thesis. University of Tübingen, 2025 (cit. on pp. 35, 70).

[137] Omran, A. “A Microscope for Fermi Gases.” PhD thesis. Ludwig Maximilian University of Munich, 2016 (cit. on pp. 35, 76, 81).

[138] Den Hartog, E. A., J. P. Chisholm, and J. E. Lawler. *Radiative lifetimes of neutral erbium*, Journal of Physics B: Atomic, Molecular and Optical Physics **43**., 155004 (July 2010). DOI: 10.1088/0953-4075/43/15/155004 (cit. on p. 36).

[139] Ban, H. Y., M. Jacka, J. L. Hanssen, J. Reader, and J. J. McClelland. *Laser cooling transitions in atomic erbium*, Optics Express **13**., 3185 (2005). DOI: 10.1364/OPEX.13.003185 (cit. on pp. 36, 75).

[140] Frisch, A., M. Mark, K. Aikawa, F. Ferlaino, J. L. Bohn, C. Makrides, A. Petrov, and S. Kotochigova. *Quantum chaos in ultracold collisions of gas-phase erbium atoms*, Nature **507**., 475–479 (Mar. 2014). DOI: 10.1038/nature13137 (cit. on p. 36).

[141] Weber, T., J. Herbig, M. Mark, H.-C. Nägerl, and R. Grimm. *Three-Body Recombination at Large Scattering Lengths in an Ultracold Atomic Gas*, Physical Review Letters **91**, 123201 (Sept. 2003). DOI: 10.1103/PhysRevLett.91.123201 (cit. on p. 36).

[142] Patscheider, A., L. Chomaz, G. Natale, D. Petter, M. J. Mark, S. Baier, B. Yang, R. R. W. Wang, J. L. Bohn, and F. Ferlaino. *Determination of the scattering length of erbium atoms*, Physical Review A **105**, 063307 (June 2022). DOI: 10.1103/PhysRevA.105.063307 (cit. on p. 36).

[143] Chomaz, L. *et al. Long-Lived and Transient Supersolid Behaviors in Dipolar Quantum Gases*, Physical Review X **9**, 021012 (Apr. 2019). DOI: 10.1103/PhysRevX.9.021012 (cit. on p. 36).

[144] González-Martínez, M. L. and P. S. Żuchowski. *Magnetically tunable Feshbach resonances in Li+Er*, Physical Review A **92**, 022708 (Aug. 2015). DOI: 10.1103/PhysRevA.92.022708 (cit. on p. 36).

[145] Schäfer, F., N. Mizukami, and Y. Takahashi. *Feshbach resonances of large-mass-imbalance Er-Li mixtures*, Physical Review A **105**, 012816 (Jan. 2022). DOI: 10.1103/PhysRevA.105.012816 (cit. on p. 36).

[146] Kalia, J., J. Rivera, R. R. Emran, W. J. S. Hernandez, K. Kwon, and R. J. Fletcher. *Creation of a degenerate Bose-Bose mixture of erbium and lithium atoms*. May 2025. DOI: 10.48550/arXiv.2506.00177 (cit. on p. 36).

[147] Mosk, A., S. Kraft, M. Mudrich, K. Singer, W. Wohlleben, R. Grimm, and M. Weidemüller. *Mixture of ultracold lithium and cesium atoms in an optical dipole trap*, Applied Physics B **73**., 791–799 (Dec. 2001). DOI: 10.1007/s003400100743 (cit. on p. 37).

[148] Slater, J. C. *Atomic Radii in Crystals*, The Journal of Chemical Physics **41**., 3199–3204 (Nov. 1964). DOI: 10.1063/1.1725697 (cit. on p. 40).

[149] O'Hanlon, J. F. *A User's Guide to Vacuum Technology*. John Wiley & Sons, 2003 (cit. on p. 40).

[150] Ho, C. Y., R. W. Powell, and P. E. Liley. *Thermal conductivity of selected materials, part 2,* (1968) (cit. on p. 40).

[151] Balykin, V. I. and A. I. Sidorov. *Collimation and decollimation of atomic beams by laser radiation*, Applied Physics B **42**., 51–54 (Jan. 1987). DOI: 10.1007/BF00694774 (cit. on p. 42).

[152] Chakravarthy, R., J. Agil, A. Sharma, J. B. Kim, and D. Budker. *Hyperfine and Zeeman Optical Pumping and Transverse Laser Cooling of a Thermal Atomic Beam of Dysprosium Using a Single 421 nm Laser,* (Feb. 2025). DOI: 10.48550/arXiv.2502.17310 (cit. on p. 43).

[153] Lison, F., P. Schuh, D. Haubrich, and D. Meschede. *High-brilliance Zeeman-slowed cesium atomic beam*, Physical Review A **61**. (Dec. 1999). DOI: 10.1103/physreva.61.013405 (cit. on p. 43).

[154] Stellmer, S., R. Grimm, and F. Schreck. *Production of quantum-degenerate strontium gases*, Physical Review A **87**. (Jan. 2013). DOI: 10.1103/physreva.87.013611 (cit. on p. 43).

[155] Lafferty, J. M. and L. G. Rubin. *Foundations of vacuum science and technology*. American Institute of Physics, 1999 (cit. on p. 45).

[156] Marti, G. E., R. Olf, E. Vogt, A. Öttl, and D. M. Stamper-Kurn. *Two-element Zeeman slower for rubidium and lithium*, Physical Review A **81**., 043424 (Apr. 2010). DOI: 10.1103/PhysRevA.81.043424 (cit. on p. 46).

[157] Phillips, W. D. and H. Metcalf. *Laser Deceleration of an Atomic Beam*, Physical Review Letters **48**, 596–599 (Mar. 1982). DOI: 10.1103/PhysRevLett.48.596 (cit. on p. 46).

[158] Joffe, M. A., W. Ketterle, A. Martin, and D. E. Pritchard. *Transverse cooling and deflection of an atomic beam inside a Zeeman slower*, Journal of the Optical Society of America B **10**., 2257 (Dec. 1993). DOI: 10.1364/JOSAB.10.002257 (cit. on p. 49).

[159] Hilker, T. *Laser Cooling of Bosonic and Fermionic Lithium*. Diploma thesis. 2012 (cit. on p. 49).

[160] Phillips, W. *Historical foreword: Jean Dalibard, the magneto-optical trap, and the ascent of physics with cold atomic gases*, Comptes Rendus. Physique **24**, 5–13 (May 2024). DOI: 10.5802/crphys.172 (cit. on p. 51).

[161] Raab, E. L., M. Prentiss, A. Cable, S. Chu, and D. E. Pritchard. *Trapping of Neutral Sodium Atoms with Radiation Pressure*, Physical Review Letters **59**., 2631–2634 (Dec. 1987). DOI: 10.1103/PhysRevLett.59.2631 (cit. on p. 51).

[162] Harold Metcalf, P. v. d. S. *Laser Cooling and Trapping*. Springer, 1999 (cit. on p. 51).

[163] Bills, D. G. *Ultimate Pressure Limitations*, Journal of Vacuum Science and Technology **6**., 166–173 (Jan. 1969). DOI: 10.1116/1.1492650 (cit. on p. 56).

[164] Patscheider, A., B. Yang, G. Natale, D. Petter, L. Chomaz, M. J. Mark, G. Hovhannesyan, M. Lepers, and F. Ferlaino. *Observation of a narrow inner-shell orbital transition in atomic erbium at 1299 nm*, Physical Review Research **3**, 033256 (Sept. 2021). DOI: 10.1103/PhysRevResearch.3.033256 (cit. on p. 58).

[165] Boll, M. "Spin and density resolved microscopy of Hubbard chains." PhD thesis. Ludwig Maximilian University of Munich, 2016 (cit. on p. 60).

[166] Boll, M., T. A. Hilker, G. Salomon, A. Omran, J. Nespolo, L. Pollet, I. Bloch, and C. Gross. *Spin- and density-resolved microscopy of antiferromagnetic correlations in Fermi-Hubbard chains*, Science **353**., 1257–1260 (Sept. 2016). DOI: 10.1126/science.aag1635 (cit. on p. 60).

[167] Koepsell, J., S. Hirthe, D. Bourgund, P. Sompet, J. Vijayan, G. Salomon, C. Gross, and I. Bloch. *Robust Bilayer Charge Pumping for Spin- and Density-Resolved Quantum Gas Microscopy*, Physical Review Letters **125**. (July 2020). DOI: 10.1103/physrevlett.125.010403 (cit. on p. 60).

[168] Gross, C. and W. S. Bakr. *Quantum gas microscopy for single atom and spin detection*, Nature Physics **17**., 1316–1323 (Dec. 2021). DOI: 10.1038/s41567-021-01370-5 (cit. on pp. 60, 112).

[169] Satter, C. L., S. Tan, and K. Dieckmann. *Comparison of an efficient implementation of gray molasses to narrow-line cooling for the all-optical production of a lithium quantum gas*, Physical Review A **98**, 023422 (Aug. 2018). DOI: 10.1103/PhysRevA.98.023422 (cit. on p. 65).

[170] Duda, M. "A Laser System for Cooling and Trapping Potassium-39." Master's thesis. Ludwig Maximilian University of Munich, 2017 (cit. on p. 68).

[171] Hirthe, S. "A Laser Setup for Two-Photon Rydberg Excitation of Potassium." Master's thesis. Ludwig Maximilian University of Munich, 2018 (cit. on p. 68).

[172] McCarron, D. J., S. A. King, and S. L. Cornish. *Modulation transfer spectroscopy in atomic rubidium*, Measurement Science and Technology **19**., 105601 (Aug. 2008). DOI: 10.1088/0957-0233/19/10/105601 (cit. on p. 70).

[173] Young, B. C., F. C. Cruz, W. M. Itano, and J. C. Bergquist. *Visible Lasers with Subhertz Linewidths*, Physical Review Letters **82**, 3799–3802 (May 1999). DOI: 10.1103/PhysRevLett.82.3799 (cit. on p. 70).

[174] Jiang, Y., A. Ludlow, N. D. Lemke, R. W. Fox, J. A. Sherman, L.-S. Ma, and C. W. Oates. *Making optical atomic clocks more stable with 10- 16-level laser stabilization*, Nature Photonics **5**., 158–161 (2011). DOI: 10.1038/nphoton.2010.313 (cit. on p. 70).

[175] Riehle, F. *Frequency standards: basics and applications*. John Wiley & Sons, 2006 (cit. on p. 70).

[176] Müller, L. "Stabilization of a diode laser to a high finesse four bore ultra low expansion cavity." Bachelor's thesis. University of Tübingen, 2021 (cit. on p. 70).

[177] Auch, J. "Creation and characterization of an Erbium MOT." Master's thesis. University of Tübingen, 2023 (cit. on p. 70).

[178] Lorenz, N. "A Rydberg Tweezer Platform with Potassium Atoms." PhD thesis. Ludwig Maximilian University of Munich, 2021 (cit. on p. 70).

[179] Sabia, R., M. J. Edwards, R. VanBrocklin, and B. Wells. *Corning 7972 ULE material for segmented and large monolithic mirror blanks*, **6273**. Ed. by Atad-Ettedgui, E., J. Antebi, and D. Lemke, 627302 (2006). DOI: 10.1117/12.672059 (cit. on p. 71).

[180] Wang, Z., Y. Ye, J. Chang, J. Zhang, Y. Sun, L. He, Q. Wu, Z. Lu, and J. Zhang. *Single step zero-thermal-expansion temperature measurement of optical reference cavities*, Optics Express **29**., 30567–30578 (Sept. 2021). DOI: 10.1364/OE.436112 (cit. on p. 71).

[181] Pound, R. V. *Electronic Frequency Stabilization of Microwave Oscillators*, Review of Scientific Instruments **17**., 490–505 (Nov. 1946). DOI: 10.1063/1.1770414 (cit. on p. 72).

[182] Drever, R. W. P., J. L. Hall, F. V. Kowalski, J. Hough, G. M. Ford, A. J. Munley, and H. Ward. *Laser phase and frequency stabilization using an optical resonator*, Applied Physics B **31**., 97–105 (June 1983). DOI: 10.1007/BF00702605 (cit. on p. 72).

[183] Mäusezahl, M., F. Munkes, and R. Löw. *Tutorial on laser locking techniques and the manufacturing of vapor cells for spectroscopy*, New Journal of Physics **26**., 105002 (Nov. 2024). DOI: 10.1088/1367-2630/ad42c6 (cit. on p. 72).

[184] Black, E. D. *An introduction to Pound–Drever–Hall laser frequency stabilization*, American Journal of Physics **69**., 79–87 (Jan. 2001). DOI: 10.1119/1.1286663 (cit. on p. 72).

[185] Balakier, K., L. Ponnampalam, M. J. Fice, C. C. Renaud, and A. J. Seeds. *Integrated Semiconductor Laser Optical Phase Lock Loops*, IEEE Journal of Selected Topics in Quantum Electronics **24**., 1–12 (2018). DOI: 10.1109/JSTQE.2017.2711581 (cit. on p. 73).

[186] Adler, R. *A Study of Locking Phenomena in Oscillators*, Proceedings of the IRE **34**., 351–357 (1946). DOI: 10.1109/JRPROC.1946.229930 (cit. on pp. 75, 79).

[187] Paciorek, L. *Injection locking of oscillators*, Proceedings of the IEEE **53**., 1723–1727 (1965). DOI: 10.1109/PROC.1965.4345 (cit. on p. 75).

[188] Hong, B. and A. Hajimiri. *A General Theory of Injection Locking and Pulling in Electrical Oscillators—Part I: Time-Synchronous Modeling and Injection Waveform Design*, IEEE Journal of Solid-State Circuits **54**., 2109–2121 (2019). DOI: 10.1109/JSSC.2019.2908753 (cit. on p. 75).

[189] Stover, H. L. and W. H. Steier. *LOCKING OF LASER OSCILLATORS BY LIGHT INJECTION*, Applied Physics Letters **8**., 91–93 (Feb. 1966). DOI: 10.1063/1.1754502 (cit. on p. 75).

[190] Liu, Z. and R. Slavík. *Optical Injection Locking: From Principle to Applications*, Journal of Lightwave Technology **38**., 43–59 (Jan. 2020). DOI: 10.1109/JLT.2019.2945718 (cit. on pp. 75, 76).

[191] Winkelmann, L. *et al. Injection-locked single-frequency laser with an output power of 220 W*, Applied Physics B **102**., 529–538 (Mar. 2011). DOI: 10.1007/s00340-011-4411-9 (cit. on p. 75).

[192] Takasu, Y., K. Maki, K. Komori, T. Takano, K. Honda, M. Kumakura, T. Yabuzaki, and Y. Takahashi. *Spin-Singlet Bose-Einstein Condensation of Two-Electron Atoms*, Physical Review Letters **91**, 040404 (July 2003). DOI: 10.1103/PhysRevLett.91.040404 (cit. on p. 75).

[193] Stellmer, S., M. K. Tey, B. Huang, R. Grimm, and F. Schreck. *Bose-Einstein Condensation of Strontium*, Physical Review Letters **103**, 200401 (Nov. 2009). DOI: 10.1103/PhysRevLett.103.200401 (cit. on p. 75).

[194] Das, D., S. Barthwal, A. Banerjee, and V. Natarajan. *Absolute frequency measurements in Yb with* $0.08$ ppb *uncertainty: Isotope shifts and hyperfine structure in the* $399{-}\mathrm{nm}\ {}^1S_0 \rightarrow {}^1P_1$ *line*, Physical Review A **72**, 032506 (Sept. 2005). DOI: 10.1103/PhysRevA.72.032506 (cit. on p. 75).

[195] Courtillot, I., A. Quessada-Vial, A. Brusch, D. Kolker, G. D. Rovera, and P. Lemonde. *Accurate spectroscopy of Sr atoms*, The European Physical Journal D - Atomic, Molecular, Optical and Plasma Physics **33**., 161–171 (May 2005). DOI: 10.1140/epjd/e2005-00058-0 (cit. on p. 75).

[196] Saxberg, B., B. Plotkin-Swing, and S. Gupta. *Active stabilization of a diode laser injection lock*, Review of Scientific Instruments **87**., 063109 (June 2016). DOI: 10.1063/1.4953589 (cit. on pp. 75, 77).

[197] Niederriter, R. D., I. Marques Van Der Put, and P. Hamilton. *Polarization purity for active stabilization of diode laser injection lock*, Review of Scientific Instruments **92**., 083004 (Aug. 2021). DOI: 10.1063/5.0059824 (cit. on p. 75).

[198] Pagett, C. J. H., P. H. Moriya, R. Celistrino Teixeira, R. F. Shiozaki, M. Hemmerling, and P. W. Courteille. *Injection locking of a low cost high power laser diode at 461 nm*, Review of Scientific Instruments **87**., 053105 (May 2016). DOI: 10.1063/1.4947462 (cit. on p. 75).

[199] Kiesel, F., K. Karpov, A. De Martino, J. Auch, and C. Gross. *Long-term stable laser injection locking for quasi-CW applications*, EPJ Techniques and Instrumentation **12**., 1 (Jan. 2025). DOI: 10.1140/epjti/s40485-024-00113-z (cit. on p. 75).

[200] Schreck, F. "Mixtures of ultracold gases: Fermi sea and Bose-Einstein condensate of Lithium isotopes." PhD thesis. Pierre and Marie Curie University, 2002 (cit. on p. 76).

[201] Mogensen, F., H. Olesen, and G. Jacobsen. *Locking conditions and stability properties for a semiconductor laser with external light injection*, IEEE Journal of Quantum Electronics **21**., 784–793 (1985). DOI: 10.1109/JQE.1985.1072760 (cit. on p. 79).

[202] Ottenstein, T. B. "Few-body physics in ultracold Fermi gases." PhD thesis. Ruperto-Carola-University of Heidelberg, 2010 (cit. on p. 81).

[203] Kerkmann, A. "A novel Apparatus for Quantum Gas Microscopy of Lithium Atoms." PhD thesis. University of Hamburg, 2019 (cit. on p. 81).

[204] Jin, S. "New Generation Experiment for the Study of Strongly Interacting Fermi Gases." PhD thesis. Paris Sciences et Lettres University, 2019 (cit. on p. 81).

[205] Smith, D. A., S. Aigner, S. Hofferberth, M. Gring, M. Andersson, S. Wildermuth, P. Krüger, S. Schneider, T. Schumm, and J. Schmiedmayer. *Absorption imaging of ultracold atoms on atom chips*, Optics Express **19**., 8471–8485 (Apr. 2011). DOI: 10.1364/OE.19.008471 (cit. on p. 89).

[206] Dalibard, J. and C. Cohen-Tannoudji. *Laser cooling below the Doppler limit by polarization gradients: simple theoretical models*, Journal of the Optical Society of America B **6**., 2023–2045 (Nov. 1989). DOI: 10.1364/JOSAB.6.002023 (cit. on p. 91).

[207] Weiss, D. S., E. Riis, Y. Shevy, P. J. Ungar, and S. Chu. *Optical molasses and multilevel atoms: experiment*, Journal of the Optical Society of America B **6**., 2072–2083 (Nov. 1989). DOI: 10.1364/JOSAB.6.002072 (cit. on p. 91).

[208] Phillips, W. D., P. D. Lett, S. L. Rolston, C. E. Tanner, R. N. Watts, C. I. Westbrook, C. Salomon, J. Dalibard, A. Clairon, and S. Guellati. *Optical Molasses: The Coldest Atoms Ever*, Physica Scripta **1991**, 20 (Jan. 1991). DOI: 10.1088/0031-8949/1991/T34/003 (cit. on p. 91).

[209] McKay, D. C., D. Jervis, D. J. Fine, J. W. Simpson-Porco, G. J. A. Edge, and J. H. Thywissen. *Low-temperature high-density magneto-optical trapping of potassium using the open* $4S \rightarrow 5P$ *transition at 405 nm*, Physical Review A **84**, 063420 (Dec. 2011). DOI: 10.1103/PhysRevA.84.063420 (cit. on p. 91).

[210] Weidemüller, M., T. Esslinger, M. A. Ol'shanii, A. Hemmerich, and T. W. Hänsch. *A Novel Scheme for Efficient Cooling below the Photon Recoil Limit*, Europhysics Letters **27**., 109 (July 1994). DOI: 10.1209/0295-5075/27/2/006 (cit. on p. 91).

[211] Boiron, D., C. Triché, D. R. Meacher, P. Verkerk, and G. Grynberg. *Three-dimensional cooling of cesium atoms in four-beam gray optical molasses*, Physical Review A **52**., R3425–R3428 (Nov. 1995). DOI: 10.1103/PhysRevA.52.R3425 (cit. on p. 91).

[212] Alzetta, G., A. Gozzini, L. Moi, and G. Orriols. *An experimental method for the observation of rf transitions and laser beat resonances in oriented Na vapour*, Il Nuovo Cimento B **36**., 5–20 (Nov. 1976). DOI: 10.1007/BF02749417 (cit. on p. 91).

[213] Shahriar, M. S., P. R. Hemmer, M. G. Prentiss, P. Marte, J. Mervis, D. P. Katz, N. P. Bigelow, and T. Cai. *Continuous polarization-gradient precooling-assisted velocity-selective coherent population trapping*, Physical Review A **48**, R4035–R4038 (Dec. 1993). DOI: 10.1103/PhysRevA.48.R4035 (cit. on p. 91).

[214] Grier, A. T., I. Ferrier-Barbut, B. S. Rem, M. Delehaye, L. Khaykovich, F. Chevy, and C. Salomon. *$\Lambda$-enhanced sub-Doppler cooling of lithium atoms in $D_1$ gray molasses*, Phys. Rev. A **87**, 063411 (June 2013). DOI: 10.1103/PhysRevA.87.063411 (cit. on p. 93).

[215] Papoff, F., F. Mauri, and E. Arimondo. *Transient velocity-selective coherent population trapping in one dimension*, Journal of the Optical Society of America B **9**., 321–331 (Mar. 1992). DOI: 10.1364/JOSAB.9.000321 (cit. on p. 92).

[216] Phatak, S. S., K. N. Blodgett, D. Peana, M. R. Chen, and J. D. Hood. *Generalized theory for optical cooling of a trapped atom with spin*, Physical Review A **110**., 043116 (Oct. 2024). DOI: 10.1103/PhysRevA.110.043116 (cit. on p. 93).

[217] Sievers, F., N. Kretzschmar, D. R. Fernandes, D. Suchet, M. Rabinovic, S. Wu, C. V. Parker, L. Khaykovich, C. Salomon, and F. Chevy. *Simultaneous sub-Doppler laser cooling of fermionic* $^6$Li *and* $^{40}$K *on the $D_1$ line: Theory and experiment*, Physical Review A **91**, 023426 (Feb. 2015). DOI: 10.1103/PhysRevA.91.023426 (cit. on pp. 94, 95).

[218] Colzi, G., G. Durastante, E. Fava, S. Serafini, G. Lamporesi, and G. Ferrari. *Sub-Doppler cooling of sodium atoms in gray molasses*, Physical Review A **93**, 023421 (Feb. 2016). DOI: 10.1103/PhysRevA.93.023421 (cit. on p. 94).

[219] Kim, K., S. Huh, K. Kwon, and J.-y. Choi. *Rapid production of large Li 7 Bose-Einstein condensates using D 1 gray molasses*, Physical Review A **99**., 053604 (May 2019). DOI: 10.1103/PhysRevA.99.053604 (cit. on p. 95).

[220] Gerken, M. "Gray molasses cooling of lithium-6 towards a degenerate fermi gas." Master's thesis. Ruperto-Carola-University of Heidelberg, 2016 (cit. on p. 95).

[221] Burchianti, A., G. Valtolina, J. A. Seman, E. Pace, M. De Pas, M. Inguscio, M. Zaccanti, and G. Roati. *Efficient all-optical production of large* $^6$Li *quantum gases using $D_1$ gray-molasses cooling*, Physical Review A **90**., 043408 (Oct. 2014). DOI: 10.1103/PhysRevA.90.043408 (cit. on p. 98).

[222] Minniberger, S., F. Diorico, S. Haslinger, C. Hufnagel, C. Novotny, N. Lippok, J. Majer, C. Koller, S. Schneider, and J. Schmiedmayer. *Magnetic conveyor belt transport of ultracold atoms to a superconducting atomchip*, Applied Physics B **116**., 1017–1021 (2014) (cit. on p. 102).

[223] Léonard, J., M. Lee, A. Morales, T. M. Karg, T. Esslinger, and T. Donner. *Optical transport and manipulation of an ultracold atomic cloud using focus-tunable lenses*, New Journal of Physics **16**., 093028 (Sept. 2014). DOI: 10.1088/1367-2630/16/9/093028 (cit. on p. 102).

[224] Gustavson, T. L., A. P. Chikkatur, A. E. Leanhardt, A. Görlitz, S. Gupta, D. E. Pritchard, and W. Ketterle. *Transport of Bose-Einstein Condensates with Optical Tweezers*, Physical Review Letters **88**, 020401 (Dec. 2001). DOI: 10.1103/PhysRevLett.88.020401 (cit. on p. 102).

[225] Matthies, A. J., J. M. Mortlock, L. A. McArd, A. P. Raghuram, A. D. Innes, P. D. Gregory, S. L. Bromley, and S. L. Cornish. *Long-distance optical-conveyor-belt transport of ultracold* $^{133}\mathrm{Cs}$ *and* $^{87}\mathrm{Rb}$ *atoms*, Physical Review A **109**, 023321 (Feb. 2024). DOI: 10.1103/PhysRevA.109.023321 (cit. on p. 102).

[226] Catani, J., G. Lamporesi, D. Naik, M. Gring, M. Inguscio, F. Minardi, A. Kantian, and T. Giamarchi. *Quantum dynamics of impurities in a one-dimensional Bose gas*, Physical Review A **85**, 023623 (Feb. 2012). DOI: 10.1103/PhysRevA.85.023623 (cit. on p. 112).

[227] McGloin, D., G. Spalding, H. Melville, W. Sibbett, and K. Dholakia. *Applications of spatial light modulators in atom optics*, Optics Express **11**., 158–166 (Jan. 2003). DOI: 10.1364/OE.11.000158 (cit. on p. 112).

[228] Blodgett, K. N., D. Peana, S. S. Phatak, L. M. Terry, M. P. Montes, and J. D. Hood. *Imaging a* $^{6}\mathrm{Li}$ *Atom in an Optical Tweezer 2000 Times with* $\Lambda$*-Enhanced Gray Molasses*, Physical Review Letters **131**, 083001 (Aug. 2023). DOI: 10.1103/PhysRevLett.131.083001 (cit. on p. 112).

[229] Gantner, T. “Magnetic Trapping of Lithium-6 and Lithium-7.” Master’s thesis. Technical University of Munich, 2012 (cit. on p. 121).

# Danksagung

Thinking about the last five and a half years, that have passed, many memories come to my mind: The first enthusiastic introduction to the ideas and prospects of the ErLi mixture by Christian at his white board. First meeting in person with my con-PhD Alex, who seemed to know already everything about Er. Winding the more than 40 coils of the experiment with the old winding machine in the basement. The flying optical tables, when the rest of the Garching team with their apparatus arrived and a big hail storm started right after the last table was safely in place. Seeing a digitally planned vacuum system become a real machine and the hot isopropanol steam from cleaning the parts, that made the brain rod a bit every time the next batch was taken out. Hard soldering the water connections and becoming a plumber and electrician when needed. The heart attack, when the ion pumps were saturated by reactivating the NEGs and the relief, when vacuum dropped again after baking them worked out. The first MOT signals, the first signals in the glass cell and the first degenerate clouds of Li and Er. These memories are only a small selection of many.
The work and progress achieved in the last years were contributed to by many people in different ways.
I want to say thank you to / Ich möchte mich bedanken bei

- Christian for the great trust he set in Alex and me to build this crazy machine, for encouragement, patients, advice, hands-on help whenever needed, his everlasting optimism and his truly contagious enthusiasm for physics.
- Alex for being a good and reliable (team-)mate, the endurance, helping me with all kind of damn computer stuff, proofreading this thesis and all the croissants he handed out in the office. For me you are Mr. Erbium.
- the junior PhDs: Jonas, Kirill and Edu for working hard on the experiment, great discussions, joking about everything, proofreading this thesis and keeping the ErLi team spirit up.
- all the Bachelor and Master students, that contributed to the experiment with their work: Roxana Wedowski for testing and understanding of the first injection locks, Liam Crane for first transport testing, Max Hassunah for building major parts of the Li laser system and delivery of delicious pain au chocolat, Eduard Heidt for further transport testing and achieving a narrow-line MOT, Jonas Auch for massaging the Vexlum laser and bringing the blue MOT, Ludwig Müller for the ULE setup, Gregor Winkler for fighting with the blue laser system, Isabel Horrer for taming the Ti:Sa, Magnus Rusch for starting with the tweezer setup and intense optical filtering, and Christian Partes for a new intensity PI-controller. ...they did a lot of work!
- the precision mechanics workshop (Stocky, Matze and Lars) of the institute for the various simple and complex parts they provided us with for the experiment, for their technical advice and their openness for new ideas.

- the K-team and Sr-team for sharing useful expertise and for letting me steal equipment from them, whenever needed.
- the electronics workshop (Michael, Matthias and Michael) for providing us with usefull electronics for the experiment.
- meinen Eltern und meiner Schwester für den immer offenen und unbeschwerten Rückzugsort in der Stettener Heimat, und dass sie nie gefragt haben wann ich *endlich* fertig werde.
- meiner Frau Lisa für alles.

*Vivat, crescat, floreat, rex!*